

Schlieren photograph of the laminar separation and turbulent reattachment on the hemisphere nose body. Flow is from left to right. Maximum height of the separated region is approximately 0.01 inches. $Re_D = 2.6 \times 10^5$. Body diameter is two inches.

THE INFLUENCE OF FREESTREAM TURBULENCE,
FREESTREAM NUCLEI POPULATIONS
AND A DRAG-REDUCING POLYMER
ON CAVITATION INCEPTION ON TWO AXISYMMETRIC BODIES

Thesis by
Edward M. Gates

In Partial Fulfillment of the Requirements

For the Degree of
Doctor of Philosophy

California Institute of Technology
Pasadena, California

1977

(Submitted February 28, 1977)

ACKNOWLEDGMENTS

My first thanks go to my advisor, Professor A.J. Acosta, for his guidance and support during the course of this research. Thanks are also due to Drs. Brennen and Sabersky for their continuing interest in and helpful comments about my work. Dr. N. George is deserving of special thanks for his generosity in time and equipment during the construction of the cavitation nuclei counter.

I would like to gratefully acknowledge the many sources of financial support which have made this work possible. The support provided by the Daniel and Florence Guggenheim and the F. J. Cole Fellowships and the Tutorial Assistantship awarded to me by the Institute is gratefully noted. The support of the Office of Naval Research and the Naval Ship Research and Development Center is also gratefully acknowledged.

I would especially like to thank Elton Daly and Joe Fontana for their patient help in building much of the experimental equipment; George Lundgren for machining the test bodies; Clarence Hemphill and Vince Sodha for their help in designing, building and debugging the necessary electronic equipment; Harry Hamaguchi for his aid in doing the photographic work; and Tom Ward, Jack Kingam and Rich Eastvedt for their help with experiments in the HSWT. Thanks are also due to the students who helped in carrying out the experiments: Jack Bacon, Mike Smyth, Peter Chang and Dave Faulkner.

I would like to thank Sigrid Kite for her meticulous typing and organization of the manuscript and Dave Byrun for preparation of the drawings. Barbara Hawk and Michele Suggs are also deserving of much thanks for not only helping with administrative chores but also for their continuous encouragement.

Finally I would like to reserve my deepest thanks for Ms. Karla Schokman whose patience, understanding and constant encouragement considerably reduced the frustration and lightened the responsibilities encountered during the completion of this work.

ABSTRACT

The influence upon the basic viscous flow about two axisymmetric bodies of (i) freestream turbulence level and (ii) the injection of small amounts of a drag-reducing polymer (Polyox WSR 301) into the test model boundary layer was investigated by the schlieren flow visualization technique. The changes in the type and occurrence of cavitation inception caused by the subsequent modifications in the viscous flow were studied. A nuclei counter using the holographic technique was built to monitor freestream nuclei populations and a few preliminary tests investigating the consequences of different populations on cavitation inception were carried out.

Both test models were observed to have a laminar separation over their respective test Reynolds number ranges. The separation on one test model was found to be insensitive to freestream turbulence levels of up to 3.75 percent. The second model was found to be very susceptible having its critical velocity reduced from 30 feet per second at a 0.04 percent turbulence level to 10 feet per second at a 3.75 percent turbulence level. Cavitation tests on both models at the lowest turbulence level showed the value of the incipient cavitation number and the type of cavitation were controlled by the presence of the laminar separation. Cavitation tests on the second model at 0.65 percent turbulence level showed no change in the inception index, but the appearance of the developed cavitation was altered.

The presence of Polyox in the boundary layer resulted in a

cavitation suppression comparable to that found by other investigators. The elimination of the normally occurring laminar separation on these bodies by a polymer-induced instability in the laminar boundary layer was found to be responsible for the suppression of inception.

Freestream nuclei populations at test conditions were measured and it was found that if there were many freestream gas bubbles the normally present laminar separation was eliminated and travelling bubble type cavitation occurred — the value of the inception index then depended upon the nuclei population. In cases where the laminar separation was present it was found that the value of the inception index was insensitive to the freestream nuclei populations.

LIST OF FIGURE CAPTIONS

- Fig. 1 Cavitation inception number versus velocity for a series of six hemisphere nose bodies. (Ref. 128)
- Fig. 2 Results of a comparative cavitation inception test on a modified ellipsoidal headform sponsored by the International Towing Tank Conference. Taken from Fig. 8 of Ref. 4.
- Fig. 3 Photographs of incipient cavitation on the ITTC headform in various facilities. Taken from Ref. 5.
- Fig. 4 Diagrams of the test bodies showing the geometric details.
(a) hemisphere nose body
(b) NSRDC body
- Fig. 5 Schlieren photographs of the laminar separation and cavitation inception on the hemisphere nose body. The photographs illustrate the development of cavitation from "steady bubble" type to "band type" cavitation. Inception can clearly be seen to start in the reattachment zone of the separation. Flow is from right to left. $Re_D = 3.3 \times 10^5$, $\sigma = 0.66$ for each photograph.
- Fig. 6 Schematic diagram of the LTWT.
- Fig. 7 Photograph of nozzle and stagnation section of the LTWT. Panels in the lower right of the picture are the tunnel power and velocity controls. On top of the stagnation section is the expansion pot and the piping to the vacuum pump and drain.
- Fig. 8 Schematic diagram of the details and positions of the turbulence manipulators in the Low Turbulence Water Tunnel.
- Fig. 9 The second honeycomb located in LTWT stagnation section.
(a) View of honeycomb in its supporting frame. Honeycomb

is $4' \times 4' \times 2''$ deep. (b) Close-up view of $1/8''$ hexagonal cells.

- Fig. 10 One of the three turbulence damping screens located in the stagnation section of the LTWT. (a) View of screen on its frame. Screen is $4' \times 4'$. (b) Close-up view of screen. Screen is made of $0.0075''$ diameter stainless steel wire and has 22 mesh/lineal inch.
- Fig. 11 Photograph of turbulence damping screen being installed in the stagnation section of the LTWT.
- Fig. 12 Photograph of turbulence generating grid being installed in the test section entrance of the LTWT.
- Fig. 13 Photograph of the Disa hot-film probe used to measure turbulence levels in the LTWT.
- Fig. 14 Photograph of the hot-film probe mounted in the LTWT. Flow is from right to left.
- Fig. 15 Summary of the turbulence level measurements in the LTWT.
- Fig. 16 Schematic diagram of the schlieren flow visualization system.
- Fig. 17 Photograph of the schlieren light sources. The silver box is a Hg arc lamp used for steady observation. The removable mirror reflects the light along the optical axis of the schlieren system. The black cylinder in the right of the photograph is the spark gap light source.
- Fig. 18 The camera side of the schlieren system. The lens simultaneously focuses the collimated beam on the knife edge and the image of the model on the film. The camera box is about 80 inches long giving an overall magnification of about 8 times.

- Fig. 19 Light source side of schlieren system mounted at HSWT.
- Fig. 20 Camera side of schlieren system mounted at HSWT. System is suspended from ceiling to isolate it from tunnel vibration.
- Fig. 21 Example of quality of schlieren photography obtained in LTWT which has flat glass test section windows. Flow is from left to right on hemisphere nose body. $Re_D = 2.6 \times 10^5$.
- Fig. 22 Example of quality of schlieren photography obtained in HSWT which has curved plexiglass test section windows. Note loss of detail in reattachment zone as compared to Fig. 21. Flow is from left to right on a hemisphere nose body. $Re_D = 4.2 \times 10^5$.
- Fig. 23 Schematic diagram of the injection system.
- Fig. 24 Photograph of the injection system at the LTWT showing the holding tank and the flowmeter.
- Fig. 25 Schematic drawing showing the injector mounted inside the hemisphere nose body.
- Fig. 26 Photograph of injector installed in hemisphere nose body.
- Fig. 27 Photograph of dismantled injector showing porous foam and sintered disc used to help smooth the injection flow.
- Fig. 28 Schlieren photograph of an example of stable injection of water at stagnation point of hemisphere nose body.
 $U_1 / U_\infty = 0.16$, $U_\infty = 12.2$ feet per second. Freestream flow is from right to left.
- Fig. 29 Schlieren photograph of an example of unstable injection of water at stagnation point of hemisphere nose body.
 $U_1 / U_\infty = 0.29$, $U_\infty = 12.2$ feet per second. Freestream flow

is from right to left.

Fig. 30 Plot of the regions of stable and unstable injection with water on the hemisphere nose body for two injection tube diameters.

Fig. 31 Schematic drawing of holocamera: A) dielectric mirror B) iris C) spectrophotometer cell D) ruby-flash lamp assembly E) iris F) dielectric mirror G) beamsplitter H) neutral density filter I) 1.6 cm focal length lens J) 25 μ pinhole K) 43.2 cm focal length collimating lens L) front surface mirror M) pin diode N) filmholder.

Fig. 32 Schematic drawing of the reconstruction system.

Fig. 33 Photographs of the components of the nuclei counting system. (a) holocamera set-up at the LTWT. (b) the reconstruction system. On the monitor screen can be seen the reconstructed images of some 100 μ diameter polystyrene spheres.

Fig. 34 Schematic drawings showing the definitions of the laminar separation dimensions.

Fig. 35 Effect of freestream turbulence level upon laminar separation on hemisphere nose body. Flow is from right to left.

$$Re_D = 2.6 \times 10^5.$$

$$(a) u'/U = 0.05\% \quad (b) u'/U = 1.2\%$$

$$(c) u'/U = 2.3\% \quad (d) u'/U = 3.6\%$$

Fig. 36 Effect of freestream turbulence level upon the laminar separation on the NSRDC body. Flow is from right to left.

$$Re_D = 1.6 \times 10^5.$$

$$(a) u'/U = 0.05\% \quad (b) u'/U = 0.65\% \quad (c) u'/U = 1.1\%$$

(d) $u'/U = 2.3\%$ (e) $u'/U = 3.6\%$

Fig. 37 Effect of freestream turbulence level on the laminar separation on the NSRDC body. Flow is from right to left.

$$Re_0 = 2.5 \times 10^5.$$

(a) $u'/U = 0.05\%$ (b) $u'/U = 0.65\%$ (c) $u'/U = 1.1\%$
(d) $u'/U = 2.3\%$ (e) $u'/U = 3.6\%$

Fig. 38 Effect of freestream turbulence level on the length of the separated region on the hemisphere nose body.

Fig. 39 Effect of freestream turbulence level on the length of the laminar separation on the NSRDC body.

Fig. 40 Effect of freestream turbulence level on the height of the separated region on the hemisphere nose body.

Fig. 41 Effect of freestream turbulence level on the height of the separated region on the NSRDC body.

Fig. 42 Effect of freestream turbulence level on the position of separation for both the hemisphere nose body and the NSRDC body.

Fig. 43 Comparison of calculated and measured values of the critical Reynolds number for the hemisphere nose and NSRDC bodies.

Fig. 44 Effect of injection of water on the laminar separation on the hemisphere nose body. Flow is from right to left.

$$Re_0 = 3.9 \times 10^5.$$

(a) Q (injection rate) = 0.0 ml/sec (b) $Q = 3.57$ ml/sec
(c) $Q = 8.35$ ml/sec (d) $Q = 13.21$ ml/sec

Fig. 45 Effect of injection of water on the laminar separation on the NSRDC body. Flow is from right to left. $Re_D = 3.2 \times 10^5$.

- (a) Q (injection rate) = 0.0 ml/sec (b) $Q = 1.80$ ml/sec
(c) $Q = 3.60$ ml/sec (d) $Q = 6.60$ ml/sec (e) $Q = 9.80$ ml/sec

Fig. 46 Effect of injection of Polyox (WSR 301) on the laminar separation on the hemisphere nose body. Flow is from right to left. $Re_D = 4.2 \times 10^5$. Concentration = 500 wppm.

- (a) Q (injection rate) = 0.0, $G = 0.0$
(b) $Q = 0.1$ ml/sec, $G = 0.47 \times 10^{-6}$
(c) $Q = 0.3$ ml/sec, $G = 1.40 \times 10^{-6}$
(d) $Q = 0.5$ ml/sec, $G = 2.34 \times 10^{-6}$
(e) $Q = 2.0$ ml/sec, $G = 9.35 \times 10^{-6}$

Fig. 47 Effect of injection of Polyox (WSR 301) on the laminar separation on the hemisphere nose body. Flow is from right to left. $Re_D = 3.9 \times 10^5$. Concentration = 100 wppm.

- (a) Q (injection rate) = 0.0 ml/sec, $G = 0.0$
(b) $Q = 0.53$ ml/sec, $G = 0.5 \times 10^{-6}$
(c) $Q = 1.10$ ml/sec, $G = 1.1 \times 10^{-6}$
(d) $Q = 1.75$ ml/sec, $G = 1.7 \times 10^{-6}$
(e) $Q = 3.00$ ml/sec, $G = 2.9 \times 10^{-6}$

Fig. 48 Effect of injection of Polyox (WSR 301) on the laminar separation on the NSRDC body. Flow is from right to left.

$Re_D = 1.6 \times 10^5$. Concentration = 500 wppm.

- (a) Q (injection rate) = 0.0 ml/sec, $G = 0.0$
(b) $Q = 0.1$ ml/sec, $G = 0.5 \times 10^{-6}$
(c) $Q = 0.3$ ml/sec, $G = 1.5 \times 10^{-6}$

(d) $Q = 0.5 \text{ ml/sec}$, $G = 2.5 \times 10^{-6}$

Fig. 49 Effects of injection of Polyox (WSR 301) on the laminar separation on the NSRDC body. Flow is from right to left.

$Re_D = 3.4 \times 10^5$. Concentration = 500 wppm.

(a) Q (injection rate) = 0.0 ml/sec, $G = 0.0$

(b) $Q = 0.1 \text{ ml/sec}$, $G = 0.36 \times 10^{-6}$

(c) $Q = 0.3 \text{ ml/sec}$, $G = 1.08 \times 10^{-6}$

Fig. 50 Effect of injection of Polyox (WSR 301) on the length of the laminar separation on the hemisphere nose body.

Fig. 51 Effect of injection of Polyox (WSR 301) on the length of the laminar separation on the NSRDC body.

Fig. 52 Effect of injection of Polyox (WSR 301) on the height of the laminar separation on the hemisphere nose body.

Fig. 53 Effect of the injection of Polyox (WSR 301) on the height of the laminar separation on the NSRDC body.

Fig. 54 Effect of injection of Polyox (WSR 301) on the position of separation on both the hemisphere nose and the NSRDC bodies.

Fig. 55 The estimated additional boundary layer disturbance amplification caused by the presence of Polyox (WSR 301).

Fig. 56 Photographs of the physical appearance of cavitation on the NSRDC body at two turbulence levels. Flow is from right to left. $Re_D = 3.4 \times 10^5$.

(a) $u'/U = 0.05\%$, $\sigma = 0.44$ (b) $u'/U = 0.65\%$, $\sigma = 0.36$

(c) $u'/U = 0.65\%$, $\sigma = 0.36$ (d) $u'/U = 0.65\%$, $\sigma = 0.35$

Fig. 57 The effect of freestream turbulence level upon the cavitation inception number on the NSRDC body.

Fig. 58 Photographs of the physical appearance of cavitation on the hemisphere nose body with polymer injection. Flow is from

left to right. $Re_D = 6.7 \times 10^5$, $\sigma = 0.59$.

Concentration = 500 wppm.

(a) Q (injection rate) = 0.0 ml/sec, $G = 0.0$

(b) $Q = 0.51$ ml/sec, $G = 1.88 \times 10^{-6}$

(c) $Q = 1.12$ ml/sec, $G = 4.14 \times 10^{-6}$

(d) $Q = 1.42$ ml/sec, $G = 5.24 \times 10^{-6}$

Fig. 59 Photographs of the physical appearance of cavitation on the NSRDC body with polymer injection. Flow is from right to left. $Re_D = 3.4 \times 10^5$.

(a) \dot{Q} (injection rate) = 0.0 ml/sec., $G = 0.0$, $\sigma = 0.44$

(b) $\dot{Q} = 2.40$ ml/sec., c (concentration) = 20 wwpm,
 $G = 0.34 \times 10^{-6}$, $\sigma = 0.45$

(c) $\dot{Q} = 2.40$ ml/sec., $c = 20$ wppm, $G = 0.34 \times 10^{-6}$,
 $\sigma = 0.34$

(d) $\dot{Q} = 2.00$ ml/sec., $c = 500$ wppm, $G = 7.11 \times 10^{-6}$,
 $\sigma = 0.34$

Fig. 60 The effect of injection of Polyox (WSR 301) upon cavitation inception number on the hemisphere nose body.

Fig. 61 The effect of injection of Polyox (WSR 301) on the cavitation inception number on the NSRDC body.

Fig. 62 The effect of injection of Polyox (WSR 301) on the cavitation inception number on the hemisphere nose body as a function of injection rate for two concentrations. $Re_D = 7.5 \times 10^5$.

Fig. 63 The same data as presented in Fig. 62 but now plotted versus the parameter G to show the correlation of the cavitation suppression with the amount of polymer injected into the boundary

layer.

- Fig. 64 Comparison of the cavitation suppression results of the present study with those of several other investigations.
- Fig. 65 Comparison of nuclei number density distribution functions derived from the experimental results of several investigations.
- Fig. 66 Schlieren photographs of the effect of increasing numbers of freestream bubbles on the laminar separation on the hemisphere nose body. Flow is from left to right. $Re_D = 3.5 \times 10^5$.
- Fig. 67 Some nuclei distributions obtained in the LTWT during the present investigations and one distribution obtained in the NSRDC facility by Peterson [15]. The holographic technique was used in both investigations.

LIST OF SYMBOLS

U, U_{∞}	—	freestream tunnel velocity
U_e	—	local velocity at the edge of the boundary layer
U'_e	—	local velocity gradient at the edge of the boundary layer
U_i	—	injectant velocity
u'	—	root mean square value of the longitudinal freestream velocity fluctuations
ρ	—	liquid density
μ	—	coefficient of absolute viscosity
ν	—	coefficient of kinematic viscosity
p	—	local static pressure
p_{∞}	—	freestream tunnel static pressure
p_v	—	vapor pressure of liquid at the bulk temperature
s	—	streamwise body coordinate measured from the stagnation point
$(S/D)_s$	—	streamwise body coordinate at the position of separation
x	—	body coordinate measured along body axis of revolution from the stagnation point
$r_0(x)$	—	local body radius of revolution
L	—	length of laminar separation bubble

H	—	height of laminar separation bubble
D	—	diameter of test body
R	—	nuclei radius
θ	—	boundary layer momentum thickness
δ^*	—	boundary layer displacement thickness
δ_s^*	—	boundary layer displacement thickness at the position of separation
Re_D	—	Reynolds number defined by UD/ν
Re_{δ^*}	—	Reynolds number defined by $U\delta^*/\nu$
Re_c	—	critical Reynolds number at which the position of transition and separation coincide
σ	—	cavitation number defined by $(p_\infty - p_v)/\frac{1}{2}\rho U_\infty^2$
σ_i	—	incipient cavitation number
σ_d	—	desinent cavitation number
c_p	—	pressure coefficient defined by $(p - p_\infty)/\frac{1}{2}\rho U_\infty^2$
$c_{p_{min}}$	—	minimum pressure coefficient
\dot{Q}	—	polymer solution injection rate
c	—	polymer solution concentration
G	—	ratio of polymer flow rate to the total boundary layer flow rate at the position of separation

$N(R)$	—	nuclei number density distribution function
β	—	Hartree dimensionless pressure parameter
H_s	—	δ^*/θ
A_{\max}	—	maximum boundary layer disturbance amplification
ω	—	frequency
ω_r	—	dimensionless frequency defined by $\omega\nu/U_e^2$
α_i	—	imaginary part of the dimensional wave number associated with a Tollmien-Schlichting disturbance
λ	—	Thwaites parameter defined by $\theta^2 U_e' / \nu$
T	—	polymer molecule relaxation time
λ_θ	—	Polhausen parameter defined by $-\frac{\delta^{*2}}{\mu U_e} \frac{dp}{ds}$

TABLE OF CONTENTS

	<u>Page</u>
ACKNOWLEDGMENTS	ii
ABSTRACT	iii
LIST OF FIGURES CAPTIONS	v
LIST OF SYMBOLS	xiv
I. INTRODUCTION	1
I. 1 Background	1
I. 2 Cavitation Inception – Some Physical Considerations	5
I. 3 Surface Nuclei and Inception	7
I. 4 Freestream Nuclei and Inception	9
I. 5 Cavitation Inception – Theories	14
I. 6 Summary of Cavitation Inception Theories	18
I. 7 Viscous Effects and Cavitation Inception	19
I. 8 Freestream Turbulence Level and Cavitation Inception	22
I. 9 Polymer Additives and Cavitation Inception	24
I. 10 Definition of Cavitation Inception	27
I. 11 Scope of Present Work	29
II. EXPERIMENTAL EQUIPMENT	31
II. 1 Low Turbulence Water Tunnel	31
II. 2 Flow Visualization	35
II. 3 Injection System	37
II. 4 Models	41
II. 5 Nuclei Counter	41

II. 5. 1	Holocamera	44
II. 5. 2	Reconstructor	45
III.	EXPERIMENTAL PROCEDURES AND REDUCTION OF DATA	47
III. 1	Preparation of Polymer Solution	47
III. 2	Preparation of Tunnel Water	48
III. 3	Photography and Holography	50
III. 4	Test Procedure – LTWT	50
III. 5	Test Procedure – HSWT	51
III. 6	Calculation of Tunnel Velocity and the Cavitation Number	51
IV.	PRESENTATION AND DISCUSSION OF THE FULLY WETTED RESULTS	52
IV. 1	Freestream Turbulence Level – Presentation of Results	52
IV. 2	Transition Prediction	53
IV. 3	Results of Transition Calculations and Comparison with Present Experimental Results	55
IV. 4	Boundary Layer – Freestream Turbulence Interaction	56
IV. 5	Influence of Polymer Injection on the Fully Wetted Flow – Presentation of Results	58
IV. 6	Comparison of Present Results with Those of van der Meulen	60
IV. 7	Other Work	62
IV. 8	Flow of Polymer Solutions Past Lifting Surfaces	63
IV. 9	Stability of Polymer Flows – Experimental	65
IV. 10	Stability of Polymer Flows – Theoretical	68
IV. 11	A Correlation Between Disturbance Amplification and G	69

IV.12	Polymer Mechanism	70
V.	PRESENTATION AND DISCUSSION OF CAVITATION RESULTS	74
V.1	Freestream Turbulence Level and Cavitation Inception – Presentation of Results	74
V.1.1	Visual Observations – Hemisphere Nose Body	74
V.1.2	Visual Observations – NSRDC Body	74
V.2	LTWT Limitations	75
V.3	Discussion	75
V.4	Comparison with Other Investigations	76
V.5	Polymer Additives and Cavitation Inception	78
V.5.1	Visual Observations – Hemisphere Nose Body	78
V.5.2	Visual Observations – NSRDC Body	79
V.6	Discussion	80
V.7	Comparison with Boundary Layer Trip Experiments	82
VI.	FREESTREAM NUCLEI AND CAVITATION INCEPTION	85
VI.1	Presentation of Results	85
VI.2	Comparison of Nuclei Distributions	85
VI.3	Freestream Nuclei and Cavitation Inception Tests in the LTWT	87
VI.4	Discussion of Nuclei Tests in the LTWT	88
VI.5	Cavitation Nuclei and Boundary Layer Interaction	93
VII.	SUMMARY AND CONCLUSIONS	95
	REFERENCES	98
	FIGURES	109

APPENDIX I.	MEASUREMENT OF FREESTREAM TURBULENCE LEVEL IN THE LTWT	169
I. 1	Flow Measuring Equipment	169
I. 2	Data Recording	170
I. 3	Data Reduction	171
I. 4	Comparison of Results	172
I. 5	Estimate of the Error in the Turbu- lence of Level Measurements	172
APPENDIX II.	TUNNEL CALIBRATION PROCEDURE	181
APPENDIX III.	BOUNDARY LAYER CALCULATIONS	188
III. 1	Laminar Boundary Layer Growth	188
III. 2	Approximate Calculation of Spatial Amplification of Boundary Disturbances	190
III. 2. 1	Present Computational Method	191

Chapter I

INTRODUCTION

I. 1 Background

The capacity to withstand tensile forces is a property normally associated with solids only. Liquids, however, are also capable of sustaining tensile stresses and theoretical estimates for a pure, homogeneous liquid predict ultimate strengths of thousands of atmospheres [1]*. Yet, the most careful experiments yield strengths of only a few hundred atmospheres [1]. To explain this discrepancy it is postulated that weak spots or "nuclei" exist in the liquid samples. The study of the "breaking" of the liquid (the formation of a hole or cavity) at a nucleus site and the subsequent growth and eventual collapse of the cavity is called "cavitation." If the resulting cavity is filled predominantly with gases formerly dissolved in the liquid, the process is called "gaseous" cavitation.

Liquids are usually "broken" either by heating at constant pressure (boiling) or by reducing the pressure at constant temperature. It is the latter case which is of concern to hydraulic engineers. Hydraulic machines (such as propellers, pumps, and turbines), valves, hydrofoils, and any hydraulic device in which the dynamically reduced pressure falls to a "low enough" value are susceptible to cavitation. The presence of cavitation (unless specifically designed for) causes a loss

* Numbers in brackets refer to References at the end of the paper.

of performance, erosion damage and noise. Thus it becomes desirable to be able to predict the set of operating conditions for a particular device which form the boundary between cavitating and non-cavitating regions.

The impracticality of observing a full scale device in operation has led to the development of facilities for model testing. The boundary between the cavitating and non-cavitating regions can then be determined for the model. To transfer these model results to a prototype operating at dynamically similar conditions requires knowledge of appropriate similarity parameters and scaling laws. A great deal of theoretical and experimental work has been done to determine what these significant parameters and their scaling laws are. However, at the present time the process of cavitation onset (or inception) and the factors controlling the process are not fully understood [2, 3].

The main parameter used to describe a cavitating condition is the cavitation number, σ . It is defined as:

$$\sigma = \frac{p_{\infty} - p_v}{\frac{1}{2} \rho U_{\infty}^2}$$

where p_{∞} and U_{∞} are the reference pressure and velocity respectively; ρ and p_v are respectively the liquid density and vapor pressure at its bulk temperature. In water tunnel testing, p_{∞} and U_{∞} are the test section static pressure and velocity measured at some distance from the body. Standard procedure at most water tunnel facilities during cavitation tests is to fix the water velocity and slowly reduce the

pressure until cavitation occurs. The value of σ at which cavitation first occurs is called the "incipient" cavitation number and is denoted σ_i . By raising the tunnel pressure the cavitation can be made to disappear. The value of σ at which it first disappears is called the "desinent" cavitation number and is denoted σ_d . In almost all cases a hysteresis exists and $\sigma_d \geq \sigma_i$. Now if σ was the only significant parameter involved in the inception process, then a geometrically similar model operating at a dynamically similar condition should have the same value of σ at inception. The results presented in Fig. 1 show this is not the case and it can be seen in this figure that the value of σ_i depends on body diameter and freestream velocity. Thus σ is not the only pertinent parameter and a complete set of governing parameters is yet to be found [2]. The dependence of σ on such variables as body size, freestream velocity, and liquid properties is called "scale effect."

Research on the mechanism of cavitation inception and scale effects is conducted in many facilities worldwide. Each of these facilities has its characteristic environment of the test section. For example, some water tunnels have resorbers which put back into solution the gases brought out by the cavitation. These facilities usually have very few freestream bubbles present in the test section, while water tunnels without resorbers typically have a very bubbly test section environment. To compare cavitation inception in these various facilities the International Towing Tank Committee (ITTC) organized a comparative test [4]. Each facility, using its own standard procedure, measured cavitation inception on a model of prescribed geometry. Some results of these tests are presented in Fig. 2. Neither the quantitative nor the qualitative agreement between the facilities is acceptable.

Associated with the large variance in the values of σ_i is an equally disconcerting variation of the physical appearance of the cavitation. Figure 3 shows a number of photographs of cavitation inception on the ITTC standard headform body taken in different facilities [5]. Photographs 4, 5, 9 show "band" type cavitation inception. It usually occurs suddenly without any warning, precursor bubbles forming an attached "sheet" cavity. Photograph 6 is an example of "spot" type cavitation inception. It starts at a fixed spot near $c_{p_{min}}$ and has a region of V-shaped attached cavitation behind it [3]. Photographs 1, 3, 7, 8 show "traveling bubble" type inception. These three types of incipient cavitation are the ones that typically occur on smooth two-dimensional bodies and can occur singly or in any combination [3]. It should be expected that the cavitation indices of these various forms will differ greatly and the type that does occur depends upon the liquid environment. It is then obvious that it is necessary to document the liquid environment during cavitation inception experiments — a fact recognized but not extensively practiced at the present time.

Scale effects and liquid environment effects by themselves are the source of formidable experimental problems. Yet, recently another consideration has been added by the introduction of small amounts of drag-reducing polymers into the liquid. This has been motivated by the discovery that certain naturally occurring organisms (such as algae) secrete drag-reducing chemicals into the environment [6] and also by the intentional introduction of polymers into the fluid to reduce viscous drag on a vehicle. Thus the propulsive system of a vehicle (usually a propeller, but in the case of a jet boat a pump) may operate

in a drag-reducing solution. Tests to determine the cavitation characteristics of the propulsive system in a drag-reducing environment must then be carried out. However before discussing the preceding topics in detail it is a good idea to digress slightly and consider some physical aspects of cavitation inception.

I.2 Cavitation Inception — Some Physical Considerations

Previously it was mentioned that cavitation started at "weak spots" or nuclei in the liquid. And since, in essentially all cases of engineering concern, cavitation would not occur if it were not for the presence of cavitation nuclei, it is worthwhile giving them a great deal of consideration. There are three questions of interest about nuclei: namely, what is their physical nature, their origin, and their role in the inception process. First, what are the nuclei? Since it is an obvious candidate for the physical model of a nucleus, the free gas bubble has received the most attention. However, Epstein and Plesset [7] showed that theory predicts free gas bubbles will disappear from an undersaturated liquid either by dissolving or by rising to the high points of the system. Yet, in the most careful experiments where a water sample has been carefully treated to remove any free gas bubbles, the sample still "breaks" or cavitates at tensions much less than theoretically predicted [1]. To explain the evident persistence of the nuclei, several additional models have been proposed.

Since these models have been discussed extensively in the literature, the comments here will be limited to a brief description of the model and its current rating among cavitation investigators. Fox

and Herzfeld [8] suggested that an organic skin protects the gas bubble by preventing diffusion. Pease and Blinks [9] discarded the gas bubble completely and postulated that the nucleus consists of a solid, hydrophobic particle. Both these models have been considered by Plesset [1] and Holl [10] and for various reasons they have given unfavorable opinions as to their significance. The model presently considered with the most favor is that proposed by Harvey et al [11]. Harvey suggested that undissolved gas could exist in pockets or pores of microscopic, hydrophobic crevices in container walls or in freely suspended solid particles. These gas pockets would then be the nuclei. Experiments by Keller [12, 13] and Knapp [14] have provided some indirect evidence supporting this model. However, the absolute evidence as to what the nuclei actually are that could be provided by direct observation is unavailable. This is so because of the extreme difficulties encountered in trying to observe the very small nuclei (usually less than 100 microns in diameter) as they are moving at high velocities (normally greater than 20 feet per second). The only presently available observations of cavitation nuclei under test conditions are those made by pulsed laser holography [15, 16, 17]. In these investigations it was found that both gas bubbles and solid particles were present. However, the resolution was insufficient to determine if the solid particles had any pockets of trapped gas. Thus, at the present time a complete description of the cavitation nucleus is still not available.

The second question that we asked about nuclei was: what are their origins? This can be answered easily (if somewhat superficially) for experimental facilities. There are two sources of cavitation nuclei

in a water tunnel — the incoming flow and the test body itself. These are referred to as "freestream" and "surface" nuclei respectively. The third question was: what roles do these surface and freestream nuclei play in the inception process? First consider surface nuclei and then freestream nuclei.

I.3 Surface Nuclei and Inception

Assuming that surface characteristics control surface nuclei behavior, several investigations have been conducted on the influence of surface nuclei in cavitation inception by controlling the test body surface quality. In these investigations roughness effects were not a consideration. Acosta and Hamaguchi [18] dipped the nose of the ITTC test body into a mixture of silicon oil and solvent. Since silicon oils have the ability to dissolve large amounts of air, the effect of the dipping was to create a layer of potential nuclei on the surface of the model. Ensuing inception tests showed the incipient cavitation indices to be systemically higher than for the pure water case. But as the coating aged and became deaerated by the evolution of cavitation bubbles, the values of the cavitation index fell below those for pure water and the appearance of the cavitation changed. This latter result was never resolved by the investigators.

Holl and Treaster [19], Holl [20], Reed [21], and Gupta [22] studied cavitation inception on hemisphere nose bodies having surface finishes of smooth stainless steel, sandblasted stainless steel, waxed ("simonized") stainless steel, teflon, nylon, and glass. They found that whereas teflon could be made to cavitate easily, glass could be

made to cavitate only with difficulty and the simonized stainless steel was harder to cavitate than the smooth stainless steel surface. These observations led Holl [2] to suggest that surface porosity is the controlling factor.

Van der Meulen [23, 24] also studied inception and desinence on stainless steel and teflon hemisphere nose bodies. He found, like Holl [20], that the teflon body was easier to cavitate than the stainless steel one and that the cavitation appearance was different for the different materials. He suggested that whereas surface nuclei were responsible for cavitation on the teflon body, freestream nuclei were responsible for cavitation on the stainless steel model.

Further tests of this type were carried out by Peterson [25] on a modified ellipsoidal(NSRDC^{*})body(see Fig. 4) which was first cleaned with acetone and then air dried. When tested, it produced a cavitation index of 0.780 at 20 feet per second. The headform was then soaked in acetone for 65 hours, washed in distilled water, quickly pressurized to 19,000 psi and installed in the filled water tunnel. All steps were carried out so that the model was never exposed to the atmosphere. The average incipient cavitation index after this treatment was 0.625 at 20 feet per second and was found to be the same five days later after continuous submergence. The headform was then air dried and retested. The value of the cavitation index then returned to its initial value of 0.780.

As a summary of the above review, it can be concluded that not only the surface characteristics but also the pressure-time history

* David W. Taylor Naval Ship Research & Development Center

experienced by the surface are important in determining the occurrence of cavitation. These observations, though, are for cases where surface nuclei control inception. What about the cases where freestream nuclei control inception?

I.4 Freestream Nuclei and Inception

Before discussing the role of freestream nuclei in cavitation, let us briefly return to the nature of these nuclei. In Section I.2 it was pointed out that a free gas bubble should be eliminated from consideration as a nucleus since it will either dissolve or rise to the high points of the system and be removed. However, this statement assumes that the gas-water system is in equilibrium. This is hardly the case in a water tunnel under test conditions where free gas bubbles are being generated throughout the circuit — especially at the tunnel pump [28]. Also recall that the holographic observations of freestream nuclei mentioned earlier showed both free gas bubbles and solid particles to be present. Therefore, the free gas bubble will be brought back into contention as a model for the cavitation nucleus. And as we shall soon see, until very recently the free gas bubble was the major model used as the cavitation nucleus in experimental and theoretical investigations. Therefore before reviewing these investigations it is helpful to briefly discuss some aspects of the growth of a free gas bubble.

An analysis of the static stability of a stationary spherical gas bubble containing the liquid vapor and a small amount of permanent gas shows (see for example Knapp et al [26]) that for an initial bubble radius R_0 there exists a critical ambient pressure p_c below which the bubble cannot be in static equilibrium. If the ambient pressure falls

below this value, the bubble will grow dynamically under the conditions of constant vapor pressure and gas content. In this case the bubble is said to grow by "vaporous" cavitation. As the initial size of the bubble increases, the critical pressure p_c approaches the fluid vapor pressure asymptotically. Thus in order for vaporous cavitation to occur, the local ambient pressure must be below the vapor pressure. And if the initial bubble is very small, it may actually be necessary to impose a tension on the liquid before the bubble becomes unstable.

As can be seen from the experimental results of Fig. 2, cavitation also occurs when the liquid pressure is above the vapor pressure. This can't be vaporous cavitation and it has been suggested by Holl [2] that gaseous diffusion is responsible for the bubble growth. "Gaseous" cavitation, as this process is called, can occur anytime the ambient liquid is supersaturated with respect to the partial pressure of the gas in the bubble. Thus bubbly growth by diffusion is possible even when the ambient pressure is above the vapor pressure. Vaporous cavitation is a much faster phenomenon compared to gaseous cavitation. Typical times for vaporous growth are of the order of milliseconds [27], whereas gaseous growth may be the order of a few seconds [7]. However, to differentiate between vaporous and gaseous cavitation in a test situation is often difficult.

Now let us begin the discussion of freestream nuclei and their role in cavitation inception. Ripken and Killen [28] studied the influence of freestream gas bubbles on cavitation inception. Using an acoustic technique to measure free gas volume they tried to relate the free gas volume to the occurrence of inception. They found that many of the tests

did not correlate well with free gas content and suggested that a measurement of the gas bubble size and number distribution would be more meaningful. They further concluded that the principal bubble source is the pump and that the resulting bubble numbers and sizes at the test section would be determined by the time-pressure characteristics of the flow circuit, i. e. each facility will produce its own characteristic bubble spectrum. Killen and Ripken [29] continued work on the acoustic free gas meter to give it the capability of determining bubble sizes and concentrations. Schiebe [30], using this upgraded version, tried to estimate the number of cavitation events that should occur for a given body, tunnel conditions and measured nuclei distribution. He found that the predicted number of events compared poorly with the measured number of events and claimed that insufficient accuracy of the acoustic method was the probable cause.

The problem of accurately determining nuclei concentrations and size distributions has hampered the study of the role of freestream nuclei in the inception process. Morgan [80] has reviewed the existing nuclei counting techniques and has proposed certain criteria which an ideal counter should satisfy. However, most of the present techniques fail to meet these criteria and it has only been with the development of laser technology that more promising methods have become available. One of these new techniques has been used by Keller [12, 13] to investigate the role of freestream nuclei in cavitation inception.

Keller[12, 13, 31, 32]has investigated the effects of nuclei on cavitation inception by the direct measurement of nuclei distributions using an optical technique. Since Keller's nuclei measuring system

was a major advance in this type of work, it is worthy of a brief description before discussing his results. Basically the system determines the size of a nucleus by measuring the intensity of light scattered by the nucleus as it passes through a laser beam. In Keller's configuration, a control volume was defined by the intersection of a small diameter laser beam and the focal volume of the receiving optics. When a nucleus passed through this control volume, it would scatter some of the laser light into the receiving system. In the receiving system the intensity of the scattered light would be measured and from a previous calibration the nucleus size could be determined. Keller connected the output of the receiving system into a recorder where it was stored until the data collection was finished. Then the recorder would provide a nuclei-size histogram.

Using this counting method, Keller [12] measured nuclei populations in four types of water (tap water, degassed tap water, filtered water, degassed-filtered water) and then tested a half body (formed by the potential flow solution of a point source in a uniform flow) in each type. The results of these tests showed that by changing from highly nucleated tap water to a low nuclei population in filtered-degassed water the cavitation number at inception could be reduced by as much as a factor of ten! The kind of cavitation was always of the traveling bubble type.

Unfortunately, Keller's nuclei counter could not distinguish between free gas bubbles and particulates. However, some observations of the effects of various water treatment (degassing, filtering, aging) on the nuclei populations provided some useful conclusions. For example,

Keller found that whereas an "alteration of the total gas content affected the measured nucleus spectrum only moderately, many nuclei were withdrawn from the water by filtering" [13]. He also found, that if the water was slowly circulated for an hour before the cavitation test, the cavitation index could be reduced by a factor of two in tap water whereas it would be reduced by a factor of ten in filtered water. Any longer waiting time before the cavitation test showed no further suppression of cavitation or reduction in the nuclei population. We infer from these results that although free gas bubbles and particulates can both act as nucleation sites, the particulates are more important (at least in Keller's facility). Keller apparently agrees with this inference, since he forwarded an inception theory based on the Harvey "pore" model which will be discussed in a later section.

Keller's work showed very dramatically that the freestream nuclei population is a major factor influencing cavitation inception. Thus, any similarity law cannot be useful if it does not take proper account of the nucleus spectrums of the prototype water and the test water. However, although this fact is generally appreciated in the field, the lack of full understanding of how these nuclei initiate cavitation restricts one to passing only qualitative judgements as to the quantitative effect of these various nuclei populations on the actual cavitation events.

In the previous two sections we have discussed experimental investigations of the role of the cavitation nucleus in the inception process. Theoretical investigations of this problem have also been made. And although the role of cavitation nuclei is still not fully understood, it is worth briefly mentioning these theories to gain insight

into how the thinking about cavitation inception has developed.

I. 5 Cavitation Inception — Theories

From the earlier analysis of the static stability of a spherical gas bubble, it can be shown that for R_0 greater than 250 microns, it would be expected that they would grow vaporously as soon as the pressure in the neighborhood of the body fell to the vapor pressure. And since the lowest pressure available is the minimum pressure on the body it has been customary to set the cavitation inception index equal to the negative of the minimum pressure coefficient. A quick glance at Figs. 1 and 2 show this to be a poor correlation.

An early attempt to more rigorously model the cavitation inception process theoretically was made by Parkin in 1952 [33]. Parkin assumed that cavitation was initiated from small solid particles with stabilized pockets of air and/or vapor. Parkin recognized that a spectrum of nuclei sizes probably existed; but having no experimental or theoretical evidence as to what the spectrum would be, he assumed a constant size. These nuclei were then assumed to travel along the body surface at the local freestream velocity and the nuclei growth was estimated using the Rayleigh-Plesset [34] equation neglecting viscous and thermal terms. Inception was said to have occurred when the nuclei had grown to a 1 millimeter radius. His predicted values of the inception index showed qualitative, but poor quantitative agreement with experiment and Parkin attributed the lack of agreement to the neglect of the influence of the boundary layer.

To investigate what the effects of the boundary layer could be,

Parkin and Kermeen [35] carried out further experiments on a hemisphere nose body. In what is now considered a classic experiment they showed that the boundary layer has a significant influence on cavitation and from their observations they concluded the following events take place at inception. Inception would first occur as a ring of macroscopic bubbles around the body. These macroscopic bubbles are sustained by very small microscopic bubbles which grow in the boundary layer upstream of the macroscopic cavitation. These microscopic bubbles would grow in time at a fixed position until the bubble radius reached a value equal to one half of the boundary layer displacement thickness. Then the microscopic bubble would be entrained by the flow and travel downstream to be distorted into irregular patches which sustained the macroscopic cavitation. A reduction in the tunnel pressure from this point would increase the rate of microscopic bubble evolution and cause more profuse macroscopic cavitation until a clear attached cavity was formed. These interpretations made by Parkin and Kermeen of their observations are very important because they were incorporated into many of the subsequent theories of cavitation — as we shall see.

Holl and Kornhauser [36] carried out an analysis similar to Parkin's [33] but included the effect of initial conditions, stream versus surface nuclei and thermodynamic effects using the complete Rayleigh-Plesset equation. Boundary layer effects were taken into account by assuming that the bubble had a velocity equal to that in the boundary layer at one nuclei radius away from the body surface. Again, inception was said to occur when the bubble diameter reached an arbitrary

diameter — in this case 250 microns. Comparison of theory with experimental results for a hemisphere nose body showed qualitative agreement for diameter and size effects. But theory predicted the incipient cavitation number should decrease with temperature, whereas experiment showed it increased. The discrepancy was attributed to convective heat transfer effects which were neglected in the calculations.

Another theory was proposed by van der Walle [37] who, motivated by Parkin and Kermeen's observations, presented a theory which is concerned mainly with the stabilization of bubbles in the boundary layer under the action of drag, pressure gradient, and adhesion forces and the resulting importance of gaseous cavitation. Taking the above factors into account and doing calculations similar to Parkin, he obtained cavitation inception values for bodies with different pressure gradients. Here too, comparison with experimental results for a hemisphere nose body showed only qualitative agreement.

At about the same time van der Walle presented his theory, Oshima [38] attempted to formulate scaling laws based on similarity ideas. He assumed that bubbles undergo dynamically similar growth as specified by the Rayleigh-Plesset equation and that this growth occurs at geometrically similar locations for geometrically similar bodies. He also assumed that bubbles move with the liquid at a distance from the wall equal to a constant percentage of the boundary layer thickness and inception was assumed to take place when the bubble diameter equalled the local boundary layer displacement thickness. Oshima's results agreed reasonably well with experiments for hemisphere nose

bodies with small diameters but departed from the experimental values as the diameter increased.

The above theories are based on interpretations of Parkin and Kermeen's observations and thus boundary layer considerations play a main part. Johnson and Hsieh [39] introduced a theory in which boundary layer considerations are neglected. They assumed that freestream gas bubbles convected into the minimum pressure region of the body are responsible for cavitation inception. They then calculated bubble trajectories and examined the bubble stability along the trajectory for different combinations of body size, freestream velocity and initial nuclei sizes. The results of the calculations showed a "screening" effect whereby the pressure gradient force deflected the large bubbles away from the minimum pressure region. This "screening" effect was found to be body size and tunnel velocity dependent. Thus for a given body size, tunnel velocity and tunnel pressure, a range of "cavitatable" bubbles was found. Below this range the bubbles were too small to become unstable whereas the bubbles above this range would be deflected away. As the tunnel pressure increased, this range would decrease in size until there would be only one unstable bubble size. Therefore, according to this theory, for a particular velocity and body a unique entrained bubble size should exist whose stability defines inception.

Schiebe [30] used this theory in conjunction with some actual nuclei distributions obtained by using the acoustic method. He estimated the number of cavitation events that would occur for a given body size, velocity and cavitation number. However, comparison with the actual number of events as determined by a hydrophone located in the body

showed only qualitative agreement.

Most recently, Keller [13] has suggested a theory based on the Harvey nucleus. Keller estimated the growth of a pocket of gas trapped in a crevice of a hydrophobic particle as it traveled along the body surface with the local freestream velocity. This was accomplished by considering the growth of a volume equivalent spherical gas bubble and using the Rayleigh-Plesset equation. Inception was said to occur when the radius of the phase boundary arching outside the crevice equalled the crevice radius. He then compared his critical pore size with his measured nuclei spectrum and found it was approximately equal to the largest measured nuclei. Assuming then that the largest nuclei cavitates first, Keller said he had good agreement between his predicted inception and experiment. However, the concept did not work well for the blunter bodies tested, and Keller attributed this to viscous effects inside the crevice walls which were not included in his analysis.

I.6 Summary of Cavitation Inception Theories

In general, the prediction theories reviewed above calculate the growth of a spherical bubble from an initial radius R_0 to a prescribed final radius as it experiences a pressure-time history determined by the tunnel velocity and test model. The bubble growth is estimated by the Rayleigh-Plesset equation and it is assumed that the behavior of a single particle characterizes the problem. Attempts to include viscous effects are based on Parkin and Kermeen's [35] interpretation of their observations made by high-speed photography. However, the theories used this interpretation without any knowledge of the

actual viscous flow over the body. For example, on the hemisphere nose body, Holl and Kornhauser [36] assumed a laminar to turbulent boundary layer transition occurred at the minimum pressure point; Oshima also assumed a laminar to turbulent transition occurred. In the next section it will be shown that not only is this assumption wrong but also that Parkin and Kermeen's interpretation of their observations was incorrect. Thus, it is not too surprising that the quantitative results of these theories do not agree well with experiment.

I.7 Viscous Effects and Cavitation Inception

Even though Parkin and Kermeen urged that further work on boundary layer effects be done, it was not until very recently that a careful investigation of viscous effects was undertaken. Arakeri and Acosta [40, 41] used the schlieren flow visualization technique to observe the fully wetted flow and the inception of cavitation on two axisymmetric bodies (a hemisphere nose body and an ITTC body). Arakeri observed that Holl and Kornhauser's [36] and Oshima's [38] assumption of a laminar to turbulent transition was wrong and that instead a laminar separation existed on the two bodies at all test Reynolds numbers (3.8×10^5 to 9.1×10^5 for the hemisphere nose body and 3.7×10^5 to 8.8×10^5 for the ITTC body). Arakeri also determined that Parkin and Kermeen's interpretation of their observations was incorrect and that the actual sequence of events in the inception process on the hemisphere nose body is as follows: Inception begins in the reattachment zone of the laminar separation and appears as a ring of microscopic and macroscopic bubbles around the body.

Some of the microscopic bubbles were entrained in the reverse flow in the separated region and carried to the separation point where they would then be entrained by the flow external to the separated region and carried downstream within the free shear layer back to the position of the macroscopic cavitation. A few of the microscopic bubbles were observed to grow at a fixed point just downstream of the separation. When these bubbles grew to the height of the separated region, they were entrained into the main flow and carried downstream — as was observed but misinterpreted by Parkin and Kermeen. If the tunnel pressure was then lowered slightly, the cavitation would become more profuse and a clear, attached cavity was formed. This sequence of events from the macroscopic bubble cavitation to "band" type cavitation and its relation to the laminar separation are clearly demonstrated in the schlieren photographs of Fig. 5.

The authors speculated that large pressure fluctuations in the re-attachment were responsible for cavitation inception occurring at that position. Arakeri [42] then measured the pressure fluctuations in this region and obtained values of peak fluctuations of 25 percent of the dynamic head and thus supports their speculation. Further, the authors found a good correlation between the cavitation inception index and the negative of the pressure coefficient at the position of separation ($-c_{p_s}$). However, for the hemisphere nose body it was found that $\sigma_i \geq -c_{p_s}$ whereas for the ITTC body $\sigma_i \leq -c_{p_s}$. The authors had no explanation for this difference in behavior, but speculated that the height of the separated region might be responsible (the height of the separated region on the hemisphere nose body is two to three times greater than on

the ITTC body).

Arakeri and Acosta[44] continued their investigation of viscous effects on bodies with a laminar separation by next considering the effect of removing the separation. They investigated this topic for three axisymmetric bodies: a hemisphere nose, an ITTC, and a modified ellipsoidal body provided by Peterson. The laminar separation was eliminated by stimulating the boundary layer so that an early transition would occur. This was done artificially on the hemisphere nose and ITTC bodies by the addition of a trip ring, whereas a natural transition on the modified ellipsoidal body was obtained by increasing the freestream velocity. The effects of the trips on the hemisphere and ITTC bodies was then to lower the critical Reynolds number to a value easily obtainable in the HSWT. The critical Reynolds number is that value of the Reynolds number at which the positions of laminar separation and transition coincide.

In the subsequent cavitation tests on the tripped hemisphere nose body, the following observations were made. At Reynolds numbers less than the critical value, band type inception took place indicating the presence of a laminar separation. As the Reynolds number approached the critical value from below, the cavity surface changed from smooth to very "rough" and the cavity separation changed from a well defined line to a very "wavy" line. If the Reynolds number was increased further until it was near the critical value, the cavitation became very "patchy" and intermittent. Finally, at supercritical values of the Reynolds number they found that no attached cavitation could be sustained on the model! Similarly dramatic cavitation results were observed on the ITTC and the modified ellipsoidal bodies. These observations plus the original ones [40] show that, on bodies normally

having a laminar separation, the condition of the separated region (i. e. extent, steadiness) is a major factor in determining when and what type of cavitation occurs. This important conclusion will be used extensively in the discussion of the results of the present experiments.

1.8 Freestream Turbulence Level and Cavitation Inception

Since Arakeri and Acosta found, on the axisymmetric bodies they tested, that the type and occurrence of cavitation is controlled by the condition of the fully wetted flow, it should be expected that any factor which would influence the fully wetted flow would also influence the cavitation. One such factor is the freestream turbulence level. It is well known [47, 48] that the laminar to turbulent boundary layer transition is affected by not only the intensity but also by the power spectrum of freestream disturbances. It is suspected then that some of the observed differences between facilities may be caused by different disturbances present in the facility test section. Unfortunately, measurement of turbulence levels in water is difficult and, unlike wind tunnels, there has been no great demand to determine the freestream turbulence levels in water tunnels. Tabulated on page 23 is the freestream turbulence level for the few tunnels that have this information available [49]. Unfortunately scale and spectrum information was not available with these figures.

Whether this variation in turbulence level will influence the fully wetted flow sufficiently to cause the inconsistencies between facilities

TABLE I.1 Turbulence Levels in Some Water Tunnels

Ottawa, Canada	0.75%	ORL	0.8%
Kriloff #2 Leningrad, USSR	0.4%	Pennsylvania State, USA	
NPL #1 Feltham, UK	0.5%	HSWT California Institute of Technology, USA	0.25%
MIT Massachusetts, USA	0.77%	LTWT California Institute of Technology, USA (Present Work)	0.05% 3.75%
6" Tunnel Minnesota, USA	0.8%		

previously noted is unknown and will require an experimental investigation.

I. 9 Polymer Additives and Cavitation Inception

In the preceding sections the effects upon cavitation inception of cavitation nuclei and the fully wetted flow have been discussed. Recently a new factor has been introduced — drag reducing polymers. The addition of a few parts per million by weight of drag-reducing polymers to the liquid environment has been found to suppress the occurrence of cavitation in most situations. Ellis et al [50] carried out experiments in a blowdown tunnel to explore the influence of polymer additives on cavitation inception for two stainless steel hemisphere nose bodies with $\frac{1}{4}$ inch and $\frac{1}{2}$ inch diameters. The polymers tested include Polyox (WSR 301), algae (*Porphyridium aeruginum*), and guar gum (J2FP) at various concentrations. Over the Reynolds number range tested (7×10^4 to 3.1×10^5) the incipient cavitation number was reduced by as much as 50 percent by the addition of polymers. Polyox was observed to be the most effective of the additives in that for a given concentration it produced the greatest suppression.

Similar experiments have been carried out at the Garfield Thomas Water Tunnel (GTWT) as part of a long term investigation of polymer effects in naval hydrodynamics [51, 52, 53, 54]. The results of their tests on hemisphere nose bodies indicate: (1) the presence of Polyox (WSR 301) inhibits cavitation inception— maximum inhibition occurring when the polymer is fresh. (2) there is a definite trend of reduced polymer effectiveness as model size increases (tests on an 8.0

inch diameter hemisphere body did not show a significant effect due to polymers). (3) there seems to be a correlation between reduced drag on a standard body and cavitation inception. Work on confined jets has also been started at GTWT but no results are available yet.

Van der Meulen [55, 56, 57, 58, 59] has also investigated the influence of polymers on cavitation for two axisymmetric bodies: a hemisphere nose body and a "Schiebe" body. The Schiebe body is one of a series developed by placing a distributed source disc in a uniform flow and these bodies are characterized by having no laminar separation [88]. Van der Meulen injected polymer into the body boundary layer at the stagnation point. He found that polymer suppressed cavitation on a stainless steel hemisphere nose body but had little to no effect on a teflon hemisphere nose body. For the Schiebe body no change in the incipient cavitation index was measured.

To investigate why this different behavior should occur, van der Meulen and Oosterveld [57] developed a holographic technique to simultaneously visualize the viscous flow and cavitation inception. Experiments with the hemisphere nose body with 500 wppm Polyox showed that the polymer eliminated the laminar separation by apparently causing an early "transition" to occur. He did not however make any observations on the teflon hemisphere nose body but instead suggested that surface nuclei were responsible for the different behavior of the teflon hemisphere body. Observations on the "Schiebe" body substantiated that no laminar separation existed but instead a boundary layer with an attached laminar to turbulent transition was

present. The effect of the polymer injection on this body was to move the transition point upstream on the body but did not produce any measurable difference in the inception index.

Other investigations into the influence of drag-reducing polymers on cavitation have been carried out for different configurations. Hoyt [60,61] has studied jet cavitation with polymer additives. He found the addition of a few parts per million Polyox to the fluid reduced the incipient cavitation number by a factor of two. Walters [62] has found similar cavitation suppression on discs and White [63] noted that bubble production by a small propeller was reduced by the presence of 25 wppm Polyox. Substantial reductions in the cavitation number in flows of polymer through a venturi have been found by Vyažmenskii [64].

Associated with the suppression of cavitation inception in these experiments is a change in appearance of the developed cavitation. Ellis [50] noted that the developed cavity on a hemisphere became striated. Hoyt [65] found this in an earlier experiment and also noted that the cavity collapse was less violent in the polymer solution. Brennen [66] found very dramatic changes in the cavity appearance for cavitating spheres and cylinders with the addition of different polymers.

To explain these observed changes in cavitation appearance and the suppression effect two possible polymer-induced changes in the fluid behavior have been suggested. One possibility is that the presence of the polymer alters the dynamics of bubble growth and collapse. Fogler and Goddard [67] analyzed the collapse of a spherical cavity in a viscoelastic liquid and found that if the relaxation time of the liquid is much greater than the Rayleigh collapse time, the elasticity can

induce a prolonged vibrational motion of the cavity boundary. Ellis and Ting [68,69], however, found no change in growth or collapse rates of spark generated bubbles. Another possible mechanism is that the polymer modifies the viscous flow around the body and thus alters cavitation. The visual observations of van der Meulen [59] and the results of Arakeri and Acosta [41,42,44] suggest that this second explanation is the much more likely.

I. 10 Definition of Cavitation Inception

In the introduction of this chapter it was simply stated that cavitation inception occurred when cavities or bubbles became visible on or near the body surface. This definition is not always easily applied in practice. It has been the usual procedure to observe the test model under stroboscopic light and estimate inception by observing so many cavitation events per unit time. Recently a number of investigators have applied the same idea of counting cavitation events, but they have developed equipment to do the counting. At the present time there are two techniques for counting cavitation events, one acoustical and one optical. The group at St. Anthony Falls Hydraulic Laboratory have developed the acoustical technique [30]. A pressure transducer is located inside the test body. When a cavitation occurrence takes place on the surface of the body, a spike occurs in the output voltage. Cavitation inception occurs when the occurrence rate reaches a certain arbitrarily defined level.

Ellis [50] and Keller [12] have used optical techniques to determine cavitation inception. Using a 5mw He-Ne laser Ellis passed a

0.1 inch diameter beam through the test section. The beam was adjusted to just graze the body at the point where incipient cavitation had been observed to occur. A photocell was located at approximately 90 degrees to the laser beam. At incipient cavitation, bubbles in the beam would scatter light which was picked up by the photocell and the signal was recorded on an oscillograph. The sudden discontinuity on the oscillograph record was taken to be inception.

Keller focused the output from a strong lamp onto a point on either the top or the bottom of the body where inception was expected to occur. The light was collected on the other side of the test section and directed into a photocell. Whenever a bubble would pass through the focus point it would cause scattering and thus a drop in the light intensity received at the photocell. Cavitation inception was said to occur when five events would occur in a tenth of a second. It should be noted that the optical technique determines inception by the events at one particular spot on the body, whereas the acoustic method gathers information from the entire body surface.

The acoustic method is more useful in cases where noise is an important design factor or the geometry makes use of the optical technique difficult. The optical method has the advantage that it is not disturbed by cavitation events in other parts of the water tunnel. The advantages of these techniques is that they provide a method for consistent, repeatable measurement of inception. However, these techniques only apply to cavitation which is of the traveling bubble type and are not applicable to cases where band type or other attached forms of cavitation occur.

I. 11 Scope of Present Work

The liquid environment and the viscous flow are known to be major factors in the inception process. One purpose of this present work is to investigate two aspects of the environment on inception: free-stream turbulence level and freestream nuclei. To carry out this investigation the Low Turbulence Water Tunnel (LTWT) at Caltech was modified so that the axisymmetric test models could first of all be cavitated and secondly exposed to a series of freestream turbulence levels. The schlieren flow visualization technique was used to observe the effect of the turbulence level on the fully wetted flow. Of the two bodies tested, one was found to be completely insensitive to the turbulence level while the other was found to be very sensitive. Some cavitation tests were carried out at the higher turbulence levels.

To monitor the freestream nuclei population a pulsed ruby laser was obtained and a hologram reconstruction system built. The purpose of measuring freestream populations is two-fold: (1) to gather information about nuclei distributions in different facilities and (2) to investigate the effect of changing nuclei distributions on the type and occurrence of cavitation. It was found in the present investigation that the nuclei distribution obtained in the LTWT agree well with those measured in other facilities and that the presence of many large free-stream nuclei can alter the viscous flow past a body and cause traveling bubble type cavitation to occur.

As for the investigation of the polymer effect, the purpose of the present investigation was to determine whether or not alteration of the viscous flow was responsible for the observed cavitation suppression.

Polyox (WSR 301) was injected into the boundary layer at the stagnation point on two axisymmetric bodies: a hemisphere nose body and the NSRDC body. The schlieren flow visualization system was again used to observe simultaneously the fully wetted flow and cavitation inception. It was found that the presence of a small amount of drag-reducing polymer can cause an instability to develop which results in an early "transition" to turbulence with its subsequent removal of the laminar separation. This work, which began long before van der Meulen's results were available [59], confirms van der Meulen's findings at least on the hemisphere nose body.

Essentially then, the present work is an investigation into the combined effects of freestream nuclei and the fully wetted flow on cavitation inception, how they interact with one another, and the influence of factors which will change either the viscous flow or the nuclei population.

Chapter II

EXPERIMENTAL EQUIPMENT

II.1 Low Turbulence Water Tunnel

Two water tunnels were used in the present investigation — the Low Turbulence Water Tunnel (LTWT) and the High Speed Water Tunnel (HSWT). All the preliminary work and the bulk of the experiments were carried out in the LTWT; the HSWT only being used to obtain high Reynolds number data for the polymer tests on the hemisphere nose body.

Although the LTWT has been around for a number of years (completed in 1951), it has just recently become a "cavitation" facility. Since it is "new" in this respect and since it has a number of unique capabilities and advantages as compared to other facilities, it is worthwhile describing the LTWT circuit in detail. The LTWT was completed in the fall of 1951 and was built as part of a program to study the dynamics of particulates in fluid suspension [70, 71]. In particular, it was intended to study transportation and diffusion of particles in the atmosphere and thus it was designed to have a low freestream turbulence level in the test section — and thus its name. A schematic drawing of the tunnel circuit is shown in Fig. 6.

The working section of the tunnel is $8\frac{1}{3}$ feet long and expands from a 12 inch square cross-section at its entrance to a 12 inch by 14 inch cross-section at its exit — the constant dimension being the width. The test section is expanded in this fashion to compensate for boundary

layer growth on the test section walls and maintain a constant core velocity. The expansion is too much however, and the velocity decreases by about 4 percent over the length of the test section. The top and bottom test section windows are plexiglass and the side windows are glass.

When the flow leaves the test section, it enters a diffuser which expands the tunnel cross-section to 24 inches square; the included angle between opposite sides of the diffuser being 3 degrees and 13 minutes. At the end of the diffuser is a vaned 90 degree elbow which directs the flow into a vertical section. This vertical section makes a transition from the 24 inch square section to a 32 inch diameter section at the next elbow. This elbow, which is also vaned, is just upstream of the pump and carries the outer bearing for the pump shaft. The tunnel pump is a mixed flow type and is driven by a 30 horsepower D.C. electric motor through a V-belt drive. This combination of pump and motor provides a maximum test section velocity of about 25 feet per second.

The lower "leg" of the tunnel expands from the 32 inch diameter cross-section at the pump exit to a 48 inch square cross-section at the next elbow. This elbow has turning vanes made of $\frac{1}{4}$ inch steel plate with a chord length of 11 inches and are spaced $3\frac{1}{2}$ inches apart. After a short vertical section, there is another elbow which is "heavily" vaned—the vanes being only one inch apart. The leading edges of these turning vanes are rounded off to approximately a circular section and the trailing edges are tapered down to a $\frac{1}{8}$ inch thickness. These particular vanes have a chord length of $2\frac{7}{8}$ inches.

The section of the tunnel between this elbow and the tunnel nozzle is called the "stagnation" section. Two honeycombs and three turbulence damping screens are installed in this section. The purpose of the screens and honeycomb is to eliminate any large scale disturbances in the oncoming flow and produce a low turbulence level in the working section. Finally, as can be seen in Fig. 7, the tunnel cross section is reduced from the 48 inch square to the 12 inch square at the test section entrance by a nozzle with a 16:1 contraction ratio.

As already noted, honeycombs and screens are used in the stagnation section to control the freestream turbulence level. The configuration of these turbulence manipulators is shown in Fig. 8. The upstream honeycomb is located immediately downstream of the elbow and has equilateral triangular cells with a 1 inch altitude and is 7 inches deep. Approximately 9 inches downstream from the first honeycomb is another honeycomb. This one (see Fig. 9) is 2 inches deep and has $\frac{1}{8}$ inch hexagonal cells. Utilizing the results of Loehrke and Nagib [72], a screen is located immediately downstream of this honeycomb. Two more screens follow the first screen — the spacing between screens being about $1\frac{3}{4}$ inches. All three screens have 22 meshes per lineal inch and are woven with 0.0075 inch diameter stainless steel wire (see Fig. 10). These screens replace the original ones which were made of 0.018 inch diameter brass wire and had 18 meshes per lineal inch. These screens had an open area of only 48.3 percent (vs. 69.7 percent for the new screen) and were replaced for this reason. As is shown in Fig. 11, the second honeycomb and the three screens are removable.

The two honeycombs and three screens produce a low "reference"

turbulence level in the test section. Turbulence generating grids can be placed at the inlet to the test section to produce the desired test section turbulence levels (see Fig. 12). Four turbulence generating grids were used in the experiments thus providing five turbulence levels for study. The five configurations of turbulence manipulators are:

1. no turbulence generating grids
2. grid #1 — $\frac{1}{2}$ inch diameter bars with 2 inch mesh.
3. grid #2 — $\frac{1}{4}$ inch diameter bars with 1 inch mesh.
4. grid #3 — three 1 inch diameter horizontal bars on 3 inch centers.
5. grid #4 — 0.025 inch diameter fishing line with $\frac{3}{4}$ inch mesh.

Grids 1, 2 and 4 are located at the entrance to the test section. The distance from the grid location to the test model position is approximately 48 inches. Grid #3 is located in the stagnation section immediately after the final screen. Grid #3 has this particular configuration and location because (after much trial and error) it was found to produce a turbulence level which is close to the levels measured in a number of other facilities—see Table I. 1.

The turbulence level in the test section at each configuration of turbulence manipulators was measured as a function of velocity by a DISA constant temperature anemometer. A DISA wedge-shaped hot film probe (see Fig. 13) was firmly mounted on the tunnel center line (see Fig. 14) at the model location. The results of these measurements have been summarized and are presented in Fig. 15. Details of the turbulence measuring equipment and calculations are given in Appendix I.

Since the tunnel was originally designed and built without pressure control, a system to reduce the tunnel pressure so that the models could be cavitating had to be added. A Nash 5 hp vacuum pump was

connected by 2 inch PVC piping to two 5 gallon tanks mounted at the high points at each end of the tunnel. The tank at the upstream end of the tunnel and the two inch line to the vacuum pump can be seen in Fig.7. Pressure control is obtained by a bypass valve to atmosphere connected to the 2 inch vacuum line. With this system the lowest value of the cavitation number obtainable is approximately 0.30.

The tunnel velocity is determined from the pressure drop across the nozzle which is measured by a Statham differential pressure transducer and the tunnel test section static pressure is measured by a Statham absolute pressure transducer positioned at the entrance to the test section. Each transducer output is measured by a Ballantine digital voltmeter (two models are used, 8305 A and 8310 A). The two voltmeter displays can be frozen simultaneously by a remote switch. Each transducer was calibrated using a Hg-water manometer.

To inhibit corrosion in the LTWT a passivator (sodium chromate) has been added to the water. The concentration of this passivator is kept between 0.04 to 0.2 percent and the pH is adjusted to between 7.5 and 9.5 by the addition of KOH [73]. Addition of the inhibitor does not affect any properties of the water, but it does give it a yellow color.

Since the details of the HSWT are available in many other places (see, for example, Knapp et al [26]), no description of the tunnel will be made here.

II.2 Flow Visualization

To observe the fully wetted flow on the test bodies, the schlieren flow visualization technique was used. The schlieren system used in

the present experiments is shown schematically in Fig. 16 and is essentially the same as that developed by Arakeri [40]. However, a number of improvements were made on Arakeri's equipment to increase the system resolution. First, the spark-gap light source was replaced. The new light source, which can be seen in Figs. 17 and 19, has four 0.05 microfarad, 10 kilovolt capacitors connected in parallel across two stainless steel electrodes and is very similar to the unit described by Ková'sznay [74]. It provides a 0.040 inch diameter light source with a 2 microsecond duration (versus a 0.14 inch by 0.20 inch source with a 5 microsecond duration for the previous light source). Also, if required, the new unit can provide two flashes 0.5 milliseconds apart. Between the two electrodes is a 0.1 inch thick fiberglass disc with a 0.012 inch diameter hole in the center. The purpose of this disc is to confine the spark and produce a high intensity source. The discs are cut from circuit board blanks because it was found that it was the only readily available material that could withstand the high temperatures created by the discharge. For the same reason the trigger or tickler electrode is made from tungsten rod. Even with these precautions the disc would have to be replaced and the tickler reground after about 100 discharges to maintain the light intensity at the film plane when a magnification of 8 or greater was used. Maximum magnification obtainable is about 11, since at higher magnifications there is insufficient light.

The other change to the original system to improve the resolution was the replacement of the lenses. The original lenses were "simple" biconvex ones with a 17 inch focal length. The replacement lenses are high quality "complex," corrected lenses which were originally used in aerial cameras. The details of these lenses are given in Fig. 16 and

can be seen in the photographs of the schlieren system in Figs. 17 through 20. As in the original system [40], the prerequisite density gradient was produced by heating the body slightly with electric heaters. The subsequent schlieren effect was recorded on a 120 film format. This allowed the use of roll film and greatly facilitated film handling.

To obtain acceptable schlieren photographs in the HSWT it was necessary to add correction lenses to the side test section windows to compensate for the window curvature. Also, the windows did not have optically finished surfaces so it was necessary to put a thin film of glycerine between the correction lens and the tunnel window to reduce the resulting "orange peel" effect. No such problems were encountered in the LTWT since it has flat, good quality glass test section windows and excellent quality schlieren photographs were obtained. An example of a schlieren photograph obtained in the LTWT is shown in Fig. 21 and can be compared with a photograph obtained in the HSWT shown in Fig. 22.

One final note about the schlieren system that should be made is about the supporting structure. As can be seen in Fig. 20, the schlieren system at the HSWT was supported from the ceiling to isolate it from tunnel vibrations. This proved unnecessary at the LTWT and as can be seen in Fig. 18 the schlieren system was mounted directly on a table.

II.3 Injection System

Two methods for introducing the polymer into the flow have been used in the past. The first is to create a polymer "ocean" by adding polymer additive to the tunnel water; the second is to inject the polymer into the boundary layer from orifices in the body surface. Creating a

polymer ocean has the advantage that it eliminates concern over possible disturbances caused by the injection — but that is about the only advantage. Since the polymer degrades under mechanical action and with time [75], it is necessary to continuously monitor the state of the polymer. However, recalling Arndt et al's [54] experience, obtaining a valid correlation between monitor results and cavitation inhibition is not a trivial task. Further it is a major undertaking to change the polymer concentration since this involves draining the tunnel completely and flushing it at least once. Ellis [50] eased this particular difficulty by using a blowdown tunnel which required much less water than a closed circuit tunnel. Another difficulty with the polymer ocean approach is that anomalous readings are obtained from pressure taps as noted by Ellis [50] in his experiments and by Astarita and Nicodemo [76], Metzner and Astarita [77], and Smith et al [78] in other investigations of polymer effects.

The injection method, on the other hand, allows exact knowledge of the state of the polymer, the injection concentration can easily be changed, and there is no effect on tunnel instrumentation. However, the injection must be done carefully to prevent any permanent flow disturbance and also the tunnel water must be monitored for polymer build-up. However, from van der Meulen's experience [55] this does not seem to be a problem since the polymer is rapidly degraded by mechanical action in the circuit.

Jin Wu [79] has studied the effectiveness of various injection configurations and found that a porous injector gave the greatest initial mixing. However, the initial estimates of the polymer injection rates

required (based on van der Meulen's experiment) were too great to pass through a small porous injector — a porous injector would have to be kept small to avoid roughness effects. It was then decided to follow van der Meulen's example and inject the polymer into the boundary layer through a hole at the stagnation point.

As can be seen in Fig. 23, the injection system consists basically of a supply tank, a filter, a flowmeter and an injector. The supply tank, which has a capacity of about 75 liters, stores the mixed polymer solution until it is ready for use. A regulated air pressure of 80 psi is applied to the top of the supply tank to force the polymer solution into the injector. The polymer is removed from the tank through a fitting about six inches from the tank bottom. As is shown in Fig. 24, the polymer solution is then immediately filtered by a 5 micron fibre filter. A $\frac{3}{8}$ inch diameter Poly-Flo tube connects the filter through a metering valve to the rotameter. Finally, a $\frac{3}{16}$ inch O.D. by $\frac{1}{8}$ inch I.D. Tygon tube connects the output of the flowmeter to the injector. The rotameter was calibrated for each concentration used and interestingly it was found that the calibration curves did not depart much from each other or the water curve.

The first injector used simply consisted of a 0.085 inch I.D. copper tube which ran the length of the test body and emerged at the stagnation point. However, initial flow visualization tests of the injection at the stagnation point, at flowrates which at the time were considered necessary, found the flow there to be very unsteady. The hole size was then increased to 0.167 inch diameter to make the injection diameter to body diameter ratio the same as van der Meulen's. At the same

time, a rather more complex model injection configuration was made first to minimize any disturbances in the injection system which could get into the boundary layer and second to standardize the injection configuration inside the body so it could easily be fitted to other models.

The injector, shown assembled inside the hemisphere nose body, is presented schematically in Fig. 25. Figs. 26 and 27 show photographs of the partially assembled injector. The injector consists of first a settling section $\frac{1}{2}$ inch in diameter and $1\frac{1}{4}$ inches long. This section was packed with porous plastic foam held in place by a sintered brass disc. The purpose of this section is to disperse the jet entering the injector and provide a smooth flow into the 9:1 contraction which follows. After the smooth contraction there is a tube with a length to diameter ratio of 22. The end of this tube exits at the stagnation point.

The schlieren technique was used to visualize the injected flow and the maximum ratio of injected velocity to freestream velocity for stable injection was determined. Figs. 28 and 29 show examples of stable and unstable injectant flow respectively and the results of these tests are shown plotted in Fig. 30. When experiments were finally started, it was found that the required injectant rates were substantially less than initially thought. In fact schlieren photos at the lower injection rates showed no trace of an injectant standoff like those shown in Figs. 28 and 29. A similar check on the injection stability was carried out for the second body studied with results similar to those found on the hemisphere nose body. Thus for all test injection rates on both bodies, no disturbing effects came from the injection process.

Degradation of the polymer as it passed through the injection system was found to be minimal.

II.4 Models

Two axisymmetric models were tested in this program. The first is a brass hemisphere nose body 2 inches in diameter made specifically for these tests. The details of this body are shown in Figs. 4 and 25. The second model is a modified ellipsoidal or NSRDC body and again details are shown in Fig. 4. This body was provided by Peterson from NSRDC and is made of copper. It was modified so that the injector and the electric heaters could be installed.

The models were supported in the LTWT by a two-bladed sting such that the nose of the model was about six body diameters upstream of the sting. Misalignment from tunnel center-line in both the LTWT and the HSWT was measured to be about 0.2 degrees. In the HSWT the models were supported by a three-bladed sting with the nose of the model again about six body diameters upstream of the sting.

II.5 Nuclei Counter

As mentioned in Chapter I, the lack of a technique for the accurate appraisal of nuclei character, concentrations and size distributions has hampered the study of the role of freestream nuclei in the inception process. Morgan [80], in his review of nuclei measuring methods, enumerated the characteristics that such a nuclei counter should possess: it should measure both number and size distributions accurately and determine the type of nuclei (solid or bubble) in the test section under test

conditions, i.e. it should not be necessary to remove a sample from the test section to count it. Also, the counter should operate continuously, measure over a volume compatible with body size, and be direct i.e. the measurement should be independent of theoretical calculations involving many assumptions or extensive calibrations. Finally, it should do all this without disturbing the flow.

Until recently previous investigators have, at best, only been able to estimate nuclei distributions by measuring the amplitude attenuation of an acoustic pulse as it propagates across a water tunnel test section [29]. And, in general, most investigators have been forced to rely on measurements of total gas content as an indicator of nuclei concentrations. The first method relies on theoretical calculations for interpretation of the results and the second method satisfies none of the criteria of the "perfect" counter. However, with the development of laser technology two new techniques have been applied to this problem. Both methods offer large improvements over the previous methods, but they still do not satisfy all the requirements for the perfect counter.

The first technique that will be discussed is the light scattering technique employed by Keller [12] which is described in Chapter 1. The advantage of this technique is that it provides continuous and immediate results. The disadvantages being that it uses single particle scattering and thus has a small sample volume. Second, the results are dependent upon a calibration which has unknowns in it associated with the nucleus index of refraction. Third, because of the Gaussian intensity distribution in the laser beam and the small sample size, a particle passing through the edge of the volume will appear to have a

different size than if it passed through the center of the volume.

Fourth, the type of nuclei is not determined by this technique.

The second method is that of Fraunhofer holography. This technique was first developed for and applied to the problem of sizing particles in a dynamic aerosol [81]. Peterson [15] and Feldberg and Shlemenson [17] have taken this technique and applied it to the problem of cavitation nuclei with good success. The method involves a two-step image forming process. In the first step, a sample volume is illuminated by a collimated beam of coherent, quasi-monochromatic light. The interference between the coherent background and the particle-diffracted radiation is photographically recorded in the far field of the individual particles. This photographic record is called a Fraunhofer hologram because it records the far-field or Fraunhofer diffraction pattern. In the second step, the developed hologram is illuminated by another collimated beam of coherent, quasi-monochromatic light producing a three-dimensional image of the original volume. The reconstructed images of the particles can then be sized and counted at the investigator's leisure. If a more detailed account of the theory is desired, Thompson [82], or Parrent, Jr. [83] provide good starting points.

The advantage of this technique is that it is an absolute and direct method for determining nuclei distributions. And by recording a large volume it provides an accurate estimate of nuclei distributions. The disadvantages are that this technique is not continuous, does not provide immediate results and the reduction of data from the reconstructed holograms is very tedious.

II. 5. 1 Holocamera

As mentioned in the previous section, the first step of the process involves the making of a hologram. This is done by the use of a holocamera which is shown in detail in Fig. 31. It consists basically of three components: a light source, a beam-expander and a recording film. Since the nuclei are small (usually $< 100\mu$ in diameter) and moving with velocities of up to 8m/sec, a coherent light source capable of a very short duration, high energy output is required to "freeze" the particle motion. This type of output is readily available from a "Q-switched" ruby laser.

The ruby laser used in these experiments has a ruby rod approximately 10 cm long \times 0.6 cm in diameter which is "pumped" by a helical xenon flashlamp. The ruby rod-flashlamp assembly is located between two flat, dielectric mirrors which are spaced 1.5m apart and form an "optical cavity." Inside the cavity near each mirror is an iris which is adjusted to reduce the number of modes present in the laser output. Also inside the optical cavity is a spectrophotometer cell containing a saturable dye (cryptocyanine in acetone). By gradually increasing the concentration of cryptocyanine the output of the laser can be reduced to a single 20 nanosecond pulse (called Q-switching).

The ruby laser output first passes through a beamsplitter where a small fraction of the energy is reflected into a pin diode. The diode output is monitored on a CRT display and gives the output intensity as a function of time. It is used primarily as a check on Q-switching. The main portion of the beam then enters the beam-expander.

The beam-expander consists of a 1.6cm focal length lens which expands the beam, a 25μ pinhole located in the focal plane of the 1.6cm lens and a 43.2cm focal length lens which collimates the expanding beam. The purpose of the pinhole is to eliminate irregularities in the beam caused by the 1.6cm lens. The collimated beam, which is 6.35cm in diameter, is then turned through an angle of 90 degrees by a front surface mirror. The beam then passes through the water tunnel test section and finally onto the recording film. The holograms are recorded on 70mm AGFA GEVAERT 10E75 rollfilm. This is a high resolution film (2800 lines/mm) with maximum sensitivity at the wavelength of the laser (6943 \AA). The filmholder is a 70mm camera back clamped to a tripod and held against the test section window. Film exposure is controlled by neutral density filters placed between the beamsplitter and beam-expander.

II. 5.2 Reconstructor

The second step of the process involves the reconstruction of the original sample volume. A Spectra Physics 5mw He-Ne laser is used as the illumination source and as can be seen from Figs. 31 and 32, the beam is expanded in the same fashion as in the holocamera. The slide mounted hologram is transported on an X-Y-Z vernier carriage along the axis of the collimated beam. Reconstructed nuclei images are imaged through a 10X Wild microscope objective onto a videcon and displayed on a closed circuit television monitor. The total magnification from actual nuclei to the monitor is 160X. The particles are sized directly from the monitor by using a reticle on the screen.

Fig. 33 shows a photograph of the reconstruction system.

To obtain good estimates of nuclei concentrations over the recorded size range (10-500 μ diameter) two different size sample volumes from the reconstructed space are analyzed. For the more numerous small particles (< 50 μ diameter) a 2.0cm³ volume is examined, while for the more scarce large particles (> 50 μ diameter) a 36.9cm³ volume is studied. Typically, 200 particles per hologram are analyzed and this requires about one man-day. As was also found by Peterson [15], the limit of resolvability between a dirt particle and a gas bubble is 20-25 μ . Although the smallest nuclei that can be detected in the present system are 5 μ diameter, the background noise in the reconstruction system prevents any reliable estimate of nuclei concentrations for particles less than 10 μ diameter.

Chapter III

EXPERIMENTAL PROCEDURES AND REDUCTION OF DATA

III. 1 Preparation of Polymer Solutions

The polymer used in all the experiments is Polyox (WSR 301) and was obtained from Union Carbide. Before mixing, the polymer was first sifted through a U. S. Series Equivalent Mesh No. 45 wire screen which has a mesh opening of 0.0138 inches. This was done to remove any large aggregates in the powder because it was found that they usually did not dissolve. The polymer was then mixed according to the following procedure:

1. The polymer was put into suspension in a small beaker of alcohol.
2. The suspension was then slowly poured into a beaker of water which was being gently stirred. This forms a highly concentrated solution.
3. This concentrated solution was left to dissolve overnight.
4. At least one hour before the test, the concentrated solution was added to enough water to make a 100 liter batch.
5. Just before the test was to start the solution was siphoned from the mixing tank into the injection system holding tank.

The proportions for each concentration are given in the table below:

TABLE III. 1 Preparation of Polymer Solutions

<u>Conc'n.</u> (wppm)	<u>Polyox</u> (gm)	<u>Alcohol</u> (cc)	<u>Volume of Conc'd. Sol'n.</u> (liter)
20	2	25	4
50	5	50	4
100	10	125	4
500	50	500	16

Approximately 2 liters were taken from each batch and tested in a turbulent flow rheometer to monitor the consistency of the mixing technique. The turbulent flow rheometer [84] consists basically of a short length of tubing through which a given amount of polymer solution is forced. The time required to do this is measured and compared to the times of other batches of the same concentration.

III. 2 Preparation of Tunnel Water

Since the LTWT has no resorber, it was necessary to strongly deaerate the tunnel water before any cavitation tests could be done. If this were not done, tremendous numbers of freestream bubbles could be seen in the test section. The water was deaerated by pulling a vacuum on the tunnel with the Nash pump and at the same time slowly recirculating the water. By this method the total air content could be reduced from a saturated value of approximately 14 ppm to 7 ppm (the lowest value obtained) in about 16 hours of continuous operation. Air content level in the HSWT was reduced by lowering the tunnel pressure until the test body would supercavitate at a tunnel velocity of 30 fps. Every 15 minutes the tunnel would be stopped and the collected air

would be bled from the tunnel high points. By this method the air content was reduced to between 9-10 ppm and it remained constant for the duration of the tests. The air content was measured by a Delta Scientific 1010 dissolved oxygen meter which was occasionally checked with a van Slyke apparatus. The air content was checked before and after each day's testing.

In the LTWT, in which the bulk of the tests were done and which has a small capacity (5000 gallons), eventual contamination of the water by the polymer was a worry. Van der Meulen [55] used a turbulent flow rheometer similar to the one used in these experiments to monitor his tunnel water and his rheometer results indicated that the polymer had no effect on the tunnel water. Van der Meulen assumed this was due to rapid mechanical degradation of the polymer as it circulated through the tunnel. However, in light of Arndt et al's [54] finding that a test body experienced a drag reduction even though a rheometer test of the solution indicated no drag reduction, this method is suspect. Unfortunately, this finding did not come to my attention until after the completion of the experiments. But cavitation inception tests with no injection were performed each day of the testing and these values showed no downward trend. Also, schlieren photographs of the laminar separation showed no change over the duration of the tests. Thus the contamination of the tunnel water had no significant effect. Polymer contamination in the HSWT was not a problem since very little polymer was injected into the circuit (tests were held over a one week period vs a several month period for the LTWT) and the HSWT has a much larger capacity (70,000 vs 5000 gallons).

III. 3 Photography and Holography

Single exposure schlieren photographs were taken of the test model in silhouette at magnifications from 4 to 11. The low intensity light available at the film plane at magnifications of 8 or greater required the use of high speed film and special developing. Royal-X-Pan film with an ASA rating of 1250 was used and the film was "pushed" in the development by using Acufine developer. The holography film AGFA 10E75 had no special developing procedures except for a rather short development time (3 minutes).

III. 4 Test Procedure - LTWT

In a typical cavitation test involving polymer injection, the tunnel velocity and the injection rate were first adjusted to the desired values. The tunnel pressure was then lowered until inception took place. Inception was determined visually under stroboscopic light. At the instant of inception two switches were closed. When these switches close the schlieren spark source and the ruby laser are fired and the DVM readouts are frozen - all simultaneously. Thus at inception, a schlieren photograph is taken, a hologram made and the tunnel velocity and pressure recorded. The test had to take less than forty seconds because by that time bubbles generated at the pump would reach the test section and dramatically change the conditions in the working section. After each test the tunnel pressure was raised and the tunnel allowed to circulate for five minutes before the next test began. This recess between each test was required to let the ruby laser cool down and also let the air go back into solution or rise to the tunnel high

points and be removed.

III. 5 Test Procedure - HSWT

In the HSWT the same general procedure as used in the LTWT was followed. Toggle valves in the manometer lines were used to "freeze" the velocity and pressure readings at inception. After the readings were recorded, the pressure was increased until the cavitation disappeared (desinence) and the velocity and pressure readings were again frozen and recorded. Since no holograms were made and since the HSWT has a resorber, it was not necessary to wait five minutes between each test.

III. 6 Calculation of Tunnel Velocity and the Cavitation Number

As there is a boundary layer growth along the walls of the working section of the tunnel, it is necessary to calibrate the tunnel both bare and with the model installed in order to determine the static pressure and the velocity at the location of the model. Such calibrations have been done by Acosta and Hamaguchi [18] for the HSWT. Working formulas for the tunnel speed and cavitation number are given in the same reference and were used in the reduction of the raw data. Such information was not available for the LTWT and the calibrations had to be done. The results of the calibrations and the working formulas for working section velocity and pressure are given in Appendix II.

Chapter IV

PRESENTATION AND DISCUSSION OF THE FULLY WETTED RESULTS

As mentioned previously, the influence of freestream turbulence level and the presence of a drag-reducing polymer in the boundary layer upon the fully wetted flow about two axisymmetric bodies was studied by schlieren flow visualization. The effects of these factors upon the viscous flow were quantified by measuring the position, maximum height and the length of the laminar separation which existed on both bodies over their respective test Reynolds number ranges. The length of the separated bubble (L) was taken to be the distance from the position of separation to the point on the separated streamline where an oscillation first begins. The height of the separated bubble (H) was defined as the maximum bubble height. These quantities are defined in Fig. 34 and were measured directly from the negative of the schlieren photograph with the aid of a scale (or reference) negative. The definition of the position of transition on the separated streamline is the same as that for the "end" of the separation bubble, i. e. the end of the separated region and the position of transition coincide. The above quantities are illustrated in the schlieren photograph of Fig. 21.

IV.1 Freestream Turbulence Level - Presentation of Results

A sequence of photographs showing the laminar separation on the hemisphere nose body for a constant freestream velocity but gradually increasing turbulence level is presented in Fig. 35. Similar sequences for the NSRDC body are presented in Figs. 36 and 37. As can

be seen in Fig. 35, the laminar separation on the hemisphere nose body remained unchanged as the freestream turbulence level was increased. In Figs. 36 and 37, however, it can be seen that the viscous flow on the NSRDC body was drastically influenced by the increasing freestream disturbance level. The freestream velocity in Fig. 36 is about 9.7 feet per second ($Re_D = 1.6 \times 10^5$) and in Fig. 37 is approximately 15 feet per second ($Re_D = 2.5 \times 10^5$). The results of measurements of the laminar separation quantities (position, length, maximum height) are presented in Figs. 38 through 42. These quantities have been non-dimensionalized by the body diameter and plotted against body Reynolds number with freestream turbulence level as a parameter. Each plotted value is the average of at least three and usually four observations and the maximum scatter is approximately ± 25 percent of the mean.

It is readily apparent from the schlieren photographs that the hemisphere nose body is insensitive to these freestream disturbances while, by comparison, the NSRDC body is very susceptible. The lack of response of the flow about the hemisphere nose body to these imposed disturbances is surprising in view of the strong effect on the NSRDC body which is of a similar type. To see if this behavior would be expected, the recent literature on the influence of pressure gradient and freestream turbulence level upon boundary layer transition was consulted.

IV.2 Transition Prediction

There are two basic approaches to the prediction of laminar to turbulent boundary layer transition. In the first approach theory and

experiment have been combined to provide an empirical relation for transition prediction [for example see Ref. [45]]. The second approach is theoretical and involves the determination of the linear response of a laminar boundary layer to small usually two dimensional disturbances, i. e. the solution of the Orr-Sommerfeld equation. The advantage of the first approach is that it always gives a result, however the validity of that result is not always known. The second approach attempts to predict transition from first principles, however the lack of a full understanding of the mechanism of transition prevents meaningful calculations except in cases of simple freestream conditions and body geometries.

The available experimental data and empirical correlations pertaining to the combined influence of freestream turbulence level and pressure gradient upon transition have been reviewed by Hall and Gibbings [48]. They have summarized this information on a graph of the transition Reynolds number (Re_{θ}) versus the Polhausen parameter (λ_{θ}) for different freestream turbulence intensities. One correlation which is typical of the data presented in Hall and Gibbing's figure is that of van Driest and Blumer [85]. Using the correlation proposed by van Driest and Blumer, the critical Reynolds numbers (Re_c) for the present bodies were calculated for various turbulence levels.

Another correlation mentioned by Hall and Gibbings, which will be used extensively in this chapter, is that of Jaffe et al [45]. Basically this technique involves the calculation of the spatial growth of small disturbances in the boundary layer along the surface of the body. Transition is said to occur when the disturbance has been amplified by

a factor of e^7 . This method, however, does not take into account freestream disturbances and thus the results only apply to a zero turbulence level flow. The details of the application of this method to the present bodies is given in Appendix III.

IV.3 Results of Transition Calculations and Comparison with Present Experimental Results

Results of transition calculations using the correlations of Jaffe et al and van Driest and Blumer are presented in Fig. 43 along with the present experimental results and those of Arakeri and Acosta [41]. In this figure the value of the critical Reynolds number has been plotted vs. freestream turbulence level for both the NSRDC and the hemisphere nose body. The distinction between Eqs. 10 and 11 of van Driest and Blumer is that Eq. 10 was developed assuming a Polhausen velocity distribution while in Eq. 11 Falkner-Skan profiles were used.

For the NSRDC body the correlation of van Driest and Blumer agrees well with the present observed results for disturbance levels less than one percent. Above this disturbance level the agreement is very poor. For the hemisphere nose body the correlation predicts critical Reynolds numbers almost identical to those of the NSRDC body and thus varies substantially from the observed results. The Jaffe et al correlation prediction of the critical Reynolds number for the NSRDC body also agrees well with experiment. However, for the hemisphere nose body this correlation predicts a critical Reynolds number of 5×10^6 a factor of 10 greater than that predicted by the van Driest and Blumer correlation. Since Arakeri and Acosta [41] found the laminar

separation to still be present at a Reynolds number of 1×10^6 , it is believed the higher value is more near correct. The reason for the difference in the critical Reynolds number predicted by the two correlations for the hemisphere nose body is believed to be due to the local nature of the van Driest and Blumer correlation. This correlation does not take into account the stability or previous history of the boundary layer as the Jaffe et al correlation does. In view of the last statement it is believed that the good agreement between the van Driest and Blumer prediction of the critical Reynolds number and the experimentally observed value on the NSRDC body is fortuitous.

IV.4 Boundary Layer — Freestream Turbulence Interaction

Neither of the correlations predicted the lack of response of the hemisphere nose body to the increasing freestream turbulence level. The van Driest and Blumer correlation failed because it is inadequate and the Jaffe et al correlation does not include the effects of freestream turbulence level. As pointed out in the most recent review of boundary layer stability and transition (Reshotko [86], 1976), one of the basic problems in transition prediction is lack of full understanding of the mechanism by which freestream disturbances interact with the boundary layer. Further Reshotko emphasizes that a knowledge of the wave number and orientation spectra of the disturbance environment is of great importance. Wells and Spangler [47], for example, have shown that transition on a flat plate is sensitive both to the nature of the disturbance and its frequency content as well as the intensity. Unfortunately this type of information was not able to be obtained in the

present experiments. The best that can be done is to make an estimate of the ratio of the energy available at the respective critical boundary layer frequencies for each body. Using the approximate calculation technique of Jaffe et al [45] estimates of the critical boundary layer frequencies were made and are presented in Table IV.1. Making use of Tsuji's [87] measurements of turbulence spectra behind grids it was estimated from his power spectra that there is approximately 60 times as much energy available at the critical frequency of the NSRDC body than at the critical frequency of the hemisphere nose body at a Reynolds number of 2.5×10^5 .

Another factor which perhaps should be taken into consideration is the distance available for the growth of the disturbances on the body. On the NSRDC body, the distance from the point of neutral stability to the position of separation is 0.42 diameters, whereas for the hemisphere nose body it is 0.07 diameters! Thus the distance available for growth on the NSRDC body is six times that on the hemisphere nose body since both bodies have the same diameter. Using values of phase velocities calculated by Wazzan* for a Schiebe body [88] and assuming the values for the NSRDC and the hemisphere nose bodies are about the same, the growth rates of disturbances were calculated. It was estimated that a 5 percent growth in amplitude per wavelength for the NSRDC body and an 18 percent growth in amplitude per wavelength for the hemisphere nose body would be required to produce transition at the separation point at a Reynolds number of 2.5×10^5 . Whereas at

* Private Communication

each body's estimated critical Reynolds number with no freestream disturbances, only a 1-2 percent growth in amplitude per wavelength is required. The above calculations, however, must be viewed sceptically since the small disturbance parallel flow theory is undoubtedly invalid at these amplification rates. However, the results do indicate that the freestream energy available and the time available for the growth of disturbances is much less for the hemisphere nose than the NSRDC nose and these reasons probably account for the insensitivity of the hemisphere nose body to the freestream turbulence levels in the present experiments. Yet, the above discussion is still highly speculative in view of lack of understanding about the interaction of freestream disturbances with the boundary layer.

In this section the influence of freestream turbulence level upon the fully wetted flow has been discussed. In the next section the influence of small quantities of polymer in the boundary layer upon the fully wetted flow will be discussed.

IV.5 Influence of Polymer Injection on the Fully Wetted Flow —

Presentation of Results

Before conducting any polymer experiments, the effect of the injection itself upon the flow was tested. The sequences of schlieren photographs presented in Figs. 44 and 45 show the effects of water injection upon the laminar separation on the hemisphere nose and NSRDC bodies. It is readily observed in these photographs that the injection process has no effect on the viscous flow at the injection rates used in the polymer tests.

Sequences of schlieren photographs showing the effects of gradually increasing injection rate on the laminar separation on the hemisphere nose body for two different concentrations are given in Figs. 46 and 47. Similar sequences are given in Figs. 48 and 49 for the NSRDC body at the same concentration but two different velocities. In each sequence the transition point is seen to move upstream as polymer is added. The forward movement of the transition point on the free shear layer causes a reduction in size of the laminar separation. When the injection rate is such that the transition and separation points coincide, the laminar separation is eliminated and replaced by a turbulent boundary layer. If the injection rate is increased beyond this level, the position of transition moves further upstream as can be seen in photographs 47(e) and 49(c). However, when this happened the position of transition could not be detected because of the limited resolution of the present schlieren system. Summaries of the separation dimensions are presented in Figs. 49 through 54. The separation dimensions have been nondimensionalized by the body diameter and plotted against the body Reynolds numbers for various values of the parameter "G". This parameter is the ratio of the mass flowrate of polymer in the boundary layer to the boundary layer mass flowrate calculated at the position of separation, i. e. :

$$G = \frac{c\dot{Q}}{U_{\infty}\delta_s^*}$$

where c is the polymer concentration in wppm, \dot{Q} is the polymer

solution injection rate, U_{∞} is the freestream velocity, and δ_s^* is the boundary layer displacement thickness at the position of separation. Why this parameter was used will be explained in the next chapter.

IV.6 Comparison of Present Results with Those of van der Meulen

Since the present experiments are closely related to those of van der Meulen [59], it would be informative to compare the fully wetted results of these two separate investigations. Van der Meulen studied the influence of dilute polymer solutions upon the fully wetted flow and upon cavitation inception for two axisymmetric bodies. As in the present case, the polymer was injected into the boundary layer at the stagnation point. The two bodies studied were a 10 mm diameter hemisphere nose body and a blunt nose body of the series described in Schiebe's report [88] having a final diameter of 9.88 mm and a minimum pressure coefficient of -0.75. The test Reynolds number range was 1.2×10^5 to 2.6×10^5 .

To observe the flow van der Meulen used pulsed ruby layer holography. However, to make the flow visible he added salt to the polymer solution. The injected liquid was then a 2 percent - 500 wppm Polyox (WSR 301) solution. However, the density stratification produced in the boundary by the injection of this solution is known to be destabilizing on the curved sections of these bodies (see for example Ref. [89]). The magnitude of the effect relative to that of the polymer is unknown. However, the good agreement between the laminar separation dimensions on the hemisphere nose body measured by Arakeri [40] and those obtained by van der Meulen when he injected a

salt solution suggests that the effect is small on the hemisphere nose body. The magnitude of the effect on the "Schiebe" body is unknown and should be kept in mind when examining the results on that body.

On the hemisphere nose body van der Meulen observed that the injection of the salt-polymer solution eliminated the laminar separation by causing an early transition to a turbulent non-separating boundary layer. On the "Schiebe" body, on which no laminar separation was observed, the laminar to turbulent transition point was found to move to a new position upstream of the no-injection position. Comparison of quantitative data is, however, not very fruitful. Van der Meulen always injected at a rate such that the injection layer thickness at the tangent point on the body was between 2 and 4 microns (i.e. values of G between 40×10^{-6} and 70×10^{-6}). At these injection rates the laminar separation on the hemisphere nose was always eliminated and thus no comparison of laminar separation dimensions with polymer present could be made. Since the "Schiebe" body geometry was not tested in the present experiments, no quantitative comparison can be made.

The results of the present experiments confirm van der Meulen's observations (on the hemisphere nose body at least) that the presence of small quantities of Polyox in the boundary layer causes a destabilizing effect. Such an effect is rather contrary to the general impression obtained from the available literature on the effects of drag-reducing polymer on fluid friction (see, for example, Hoyt [90]). For this reason we summarize here from the literature the influence of these polymers on flow past bodies having either a laminar or turbulent separation or an attached laminar to turbulent separation.

IV.7 Other Work

The influence of drag-reducing polymers upon separation has been investigated mainly in drag-reduction experiments with spheres and cylinders. Sarpkaya et al [91] have reviewed the available literature on this topic; it is worthwhile to mention a few of these investigations here — especially those in which some flow visualization was done. Lang and Patrick [92] observed the flow about freely falling spheres, cylinders and cones in solutions of Polyox in water. They found the drag on a sphere in the subcritical Reynolds number range was considerably reduced by the addition of polymer. Flow visualization by dye showed that the laminar boundary layer separation was moved further downstream and that wake size was decreased. White [93] also carried out free-fall experiments with spheres in a polymer solution and, like Lang and Patrick, noted a large drag reduction at subcritical Reynolds numbers. He also concluded that a delayed separation and a smaller wake size were responsible for the reduction. Brennen [66] studied the influence of polymer on fully developed cavity flow past two spheres and a cylinder. He observed that the polymer caused a distortion in the separation line and also on the cavity surface for all three bodies. However, whereas the separation line on the spheres moved downstream, the separation line on the cylinder did not change position. Brennen attributed the above observations to a polymer induced instability in the wetted surface flow around the headform which, upon convection, dramatically altered the cavity surface appearance. Sarpkaya et al [91] investigated the influence of polymer solutions on flow past cylinders. Using dye injection to visualize the flow

it was observed that the separation point moved downstream slightly and became distorted. Sarpkaya also claimed that the dye visualization tests revealed a laminar to turbulent transition just ahead of separation.

In each of the above experiments a delay in separation was observed. However, it is not clear that this delay is due to an early polymer-induced transition to a more separation-resistant turbulent boundary layer. The distortion of the separation line noted by Brennen and Sarpkaya et al suggest that this may be the case. To obtain additional information about the influence of polymer on separations, we turn to the effect of polymer solutions on the flow past hydrofoils.

IV.8 Flow of Polymer Solutions Past Lifting Surfaces

The flow field about a lifting surface can be changed substantially by changing the angle of attack of the foil and thus provides a better opportunity to study polymer effects on separation and transition than does a cylinder or sphere. Most investigators [94, 95, 96, 97, 98] have found that the presence of polymer decreases the performance of a lifting surface. Latta and Czaban [99] found, however, an increase in turbomachinery performance with the addition of polymer. Lehman and Suessmann [100], who did both polymer injection and polymer "ocean" tests with hydrofoils, found the lift could be either increased or decreased depending on the injection process and the drag, although generally reduced, could in some circumstances actually be increased. Fruman et al [101, 102] also did injection tests on a hydrofoil with results qualitatively similar to Lehman and Suessmann.

In the above experiments flow visualization had a low priority and consequently very little was learned about any polymer-induced modifications in the basic flow field.

In an attempt to untangle the above observations and gain insight into what the polymer was actually doing, Sarpkaya [103] tested six different hydrofoils (NACA 0006, 0012, 0024, 4412, 66₁-012 and 65006) in a recirculating water tunnel filled with a polymer solution. He found that the NACA 0012, 0024, 4412, and 66₁-012 foils showed a decrease in lift and an increase in drag whereas the NACA 0006 and 0065 foils showed an increase in lift and a decrease in drag. Flow visualization by means of dye injection showed that the position of laminar separation on the upper side moved forward slightly and that the separation line was distorted and oscillated back and forth. Sarpkaya explains these results as follows: the NACA 0006 and 0065 foils possess a forward laminar separation. Subsequent transition on the free shear layer and reattachment as a turbulent boundary layer give rise to a separation bubble. If this bubble is long, as is the case for NACA 0006 and 0065, it will increase the drag and reduce the lift. For these types of foils, Sarpkaya says "the instability and the transition to turbulence brought about by the polymer help to replace the long bubble by a turbulent boundary layer and partly restore the lift otherwise lost due to the bubble. Furthermore, the relative decrease in the apparent size of the foil as well as the friction reduction with polymer, in turbulent flow over the upper and lower sides of the foil, results in a Reynolds-number-dependent drag reduction." Presumably by "apparent size" Sarpkaya is referring to the foil thickness.

As for the remaining foils, Sarpkaya explains as follows: on the NACA 0012, 0024 and 4412 foils, which have a turbulent separation near the trailing edge, the early polymer-induced transition to a turbulent boundary layer causes a thicker boundary layer at the trailing edge and thus a thicker wake. This thicker wake, it is claimed, will cause a reduction in lift and the thicker boundary layer will cause an increase in effective foil size and thus a larger drag. This speculation by Sarpkaya is supported by the results of Tagori et al [104]. They studied the flow past NACA 0012 and 66₁-012 foils in a water solution of polyacrylamide (separan AP-300) and used air bubbles injected into the freestream to visualize the flow. These results clearly show a thickened turbulent boundary layer when the polymer is present.

It is clear from the present experiments and the ones just discussed that the presence of a drag-reducing polymer can greatly modify the laminar boundary layer including the features of separation and transition. Some indications of what may happen for separation have been sketched above. We now review what little information on the stability of a laminar boundary layer is available with a view of obtaining more ideas as to the effects to be expected for transition.

IV.9 Stability of Polymer Flows — Experimental

As would be expected, a large fraction of the experimental work on the laminar to turbulent transition in dilute polymer solutions has been done in pipe flows. The majority of the studies indicate a delay in transition [90]. An example of this is given by Castro and Squire [105] who measured the "intermittency" (ratio of length of time

the flow is turbulent to the length of time the flow is laminar) of the flow through a pipe. In tests on a number of different molecular weight polymers, they found the presence of polymer decreased both the intermittency and the intensity of the turbulent flashes. Giles and Pettit [106] used dye to visualize the transition process in glass tubes. They found very large delays in the occurrence of transition and the delay increased with polymer concentration. White and McEligot [107] made studies of transition in small tubes for mixtures of polymers with different molecular weights. They also found delays in the occurrence of transition with the delay being influenced most by the polymer with the highest molecular weight.

However, there are some studies which found no delay, and in a few cases an even earlier transition is found than for pure water. Virk et al [108] tested five polyethylene oxides in pipe flows and found in the majority of the tests no delay in transition occurred. Goldstein et al [109] used a laser doppler anemometer to investigate turbulent and transitional pipe flows. They found that although the presence of the polymer did not alter the longitudinal turbulent intensity, an unsteady flow existed at Reynolds numbers for which the water flow is normally laminar. More recently Paterson and Abernathy [110] have studied laminar to turbulent transition in pipe flows of dilute solutions of polyethylene in which both a smooth and an abrupt inlet section were used. For the high disturbance or abrupt inlet case the polymer was found to have no effect on transition. Whereas for the low disturbance or smooth inlet case the polymer was found to cause an earlier transition to occur.

Besides pipe flows, investigations into the stability of flow between

two concentric cylinders with relative rotation have been carried out. However, since these flows are dominated by secondary fluid motions and do not have a laminar to turbulent transition, those investigations will not be discussed here. As for flows over flat plates and discs, Hoyt [90] has reviewed the available information. However in these investigations the main effort was to measure drag reduction in a turbulent boundary layer and few attempts were made to see what was happening to the pre-existing laminar boundary layer.

The experimental findings reviewed above are certainly contradictory and confusing. This confusion is mainly due to a lack of understanding of the basic mechanism by which the polymer interferes with the original flow and thus an incomplete understanding of the variables affecting the polymer behavior. Another factor contributing to the confusion is the precise determination of the laminar to turbulent transition. In the works just reviewed, three methods were used: the "break point" in the pipe friction factor curve, measurement of the "intermittency" and flow visualization. Use of the break point to define transition is misleading since both Paterson and Abernathy [110] and Goldstein et al [109] found unsteady flow to exist for Reynolds numbers in the laminar portion of the pipe friction factor curve for dilute polymer solutions. Flow visualization is a better technique but it has the disadvantage of being dependent on the observer. The concept of intermittency appears to be best because an arbitrary value can be given to the intermittency factor and applied to all experiments. Further it is not observer dependent.

Since the experimental investigations (into the laminar to turbulent transition in polymer flows) are so inconclusive, it was hoped

that the theoretical investigations would yield more consistent results. A brief review of some of these theoretical works now follows.

IV.10 Stability of Polymer Flows — Theoretical

In the theoretical works reviewed, the approach to the problem of determining laminar to turbulent transition is the same as for Newtonian fluids, i.e. solution of the Orr-Sommerfeld equation. The only modification to the equation to account for the presence of the polymer is to change the constitutive relation to include viscoelastic effects.

Fong and Walters [111] used a model of a slightly viscoelastic fluid to investigate the stability of plane Poiseuille flow. Their solutions predicted a destabilization due to the presence of elasticity. Since they felt this result was in contradiction to experimental observations, they repeated the analysis using another constitutive relation which also included a variation in viscosity with the rate of shear [112]. Again their solutions predicted a destabilizing influence. They then returned to the original constitutive relation and analyzed the stability of a laminar boundary layer. This time they found the presence of elasticity to have a stabilizing effect. Gupta [113] investigated the flow of a viscoelastic liquid flowing down an inclined plane. He found the presence of elasticity caused the flow to be unstable at any Reynolds number! Craik [114] showed that this unsatisfactory result was due to an inadequate fluid model. More recently Mook [115] found elasticity to be stabilizing in combined Couette-Poiseuille flow and also in a flat plate boundary layer flow.

In these studies it has been assumed that the stability of two dimensional disturbances will control transition as in the case of Newtonian flow [116]. However, Lockett [117] suggests that the viscoelasticity may make it necessary to study the full three dimensionality of the flow. This is substantiated somewhat by Brennen's [66] observations of three-dimensional instabilities on fully developed cavity surfaces in a drag-reducing flow past spheres and cylinders. Kundu [118] using an energy method studied the stability of two and three dimensional disturbances in plane Couette flow of a second-order fluid. He found the presence of elasticity to be stabilizing to two dimensional disturbances but three dimensional disturbances could be either stabilized or destabilized depending on the constants in the constitutive relation.

From all this work it seems then that theoretical calculations are hampered by the lack of the "correct" constitutive relation and perhaps the need for a full three dimensional consideration of disturbances. A summary of both the experimental and the theoretical investigations can at best say that the influence of a drag-reducing additive upon laminar to turbulent transition may be stabilizing or destabilizing depending upon the flow geometry, type of polymer and its concentration.

IV.11 A Correlation Between Disturbance Amplification and G

It had been hoped that a review of the literature would indicate a practical modification to the approximate stability calculation method of Jaffe et al [45] that would make it applicable to polymeric flows. However, from the preceding review no such simple modification is yet possible with the present theoretical means. Yet, there is some

advantage to calculating the added disturbance amplification due to the presence of the polymer and see if this can be related to the amount of polymer present. For a given Reynolds number the actual amplification at the position of laminar separation was estimated by the method of Jaffe et al [45]. Then using the e^7 criterion the extra amplification required to produce transition at the position of separation was calculated. This added amplification plotted against the value of G at which the laminar separation first disappears is shown in Fig. 55. Comparison of these results with those of van der Meulen [59] was not possible since he always injected polymer solution at a rate such that the laminar separation was eliminated.

As can be seen in Fig. 55, there is a good deal of scatter but a correlation does seem to exist. But perhaps it is only fortuitous since the calculations based on two-dimensional small disturbance theory are almost certainly invalid at the Reynolds numbers of the present experiments. Moreover, it is likely [66] that the disturbances are three-dimensional although this remains to be confirmed in fully wetted flow.

IV.12 Polymer Mechanism

The previous sections have discussed the modifications to the laminar to turbulent transition produced by the presence of polymer, but no mention of a mechanism to explain these effects has been made. Hoyt [90] has reviewed the existing mechanisms proposed to explain friction reduction, but these theories are based mainly upon observation from turbulent pipe flow of polymer solutions. First it is not clear that the polymer acts the same in a laminar boundary layer as in a

turbulent one and second, established turbulent pipe flow is quite different from the flow over spheres, cylinders, etc. There are, nevertheless, a few topics gained from experience in pipe flows that may be discussed with respect to the present experiments:

One of these is that of a critical or onset shear stress. It has been noted in pipe flows of drag reducing polymer solutions that no effect is observed until the wall shear stress reaches a certain critical value. The maximum shear stresses on the NSRDC and hemisphere nose bodies were calculated for various values of the Reynolds number and compared to the critical value of 2.1 dynes/cm^2 for Polyox (WSR 301) [90]. In all cases the calculated shear stress was much greater than the critical value. However, in the present experiments no tests were done for which the maximum shear stress was less than the critical value, so no definitive conclusion about the significance of the shear stress effect in activating the polymer can be made for these experiments.

A concept, which has arisen to try to explain these various polymer effects in laminar and turbulent flow, is the idea of molecular stretching. Tulin [119] and Lumley [120, 121] tried to explain the turbulent drag-reduction by suggesting that if the polymer molecules were stretched from their naturally coiled condition they could become large enough to interfere with turbulent eddies. Brennen [66] has used this idea in a somewhat different way to forward an explanation for the observed destabilization of the boundary layer.

Brennen proposed that the highly favorable pressure gradient on the forward portions of spheres and cylinders stretches the long chain

molecules out of their naturally coiled state. Once past the minimum pressure point an adverse pressure gradient exists and the polymer molecule is allowed to relax. As the molecule relaxes, it would put energy into the boundary layer and if the boundary layer could be sufficiently energized, transition could occur upstream of the position at which it normally occurs. Essentially then the molecule is considered as a spring which is first stretched and then released as it passes over the body. If this analogy is applicable, then it would be expected that the molecule would oscillate when released at a frequency equal to the reciprocal molecular relaxation time. For Polyox (WSR 301) this is 1000 Hz [50]. Now it is known from solutions of the Orr-Sommerfeld equation that a certain range of disturbance frequencies is amplified in the boundary layer to a much greater extent than other frequencies. In particular there is one frequency (called the critical frequency) at which maximum amplification occurs. Using the approximate calculation technique [45] the critical frequencies for the present bodies were calculated for several different Reynolds numbers and are presented in the table below.

TABLE IV.1 Critical Boundary Layer Frequencies
(at separation)

Re_D	Hemisphere Nose Body (Hz)	NSRDC Body (Hz)
1.67×10^5	1070	670
2.50×10^5	1800	1060
3.33×10^5	2140	1780
4.17×10^5	3350	2100

Comparison of these critical boundary layer frequencies with the resonant frequency of the molecule indicates that the boundary layer would be particularly responsive to disturbances imposed on it by oscillations of the polymer molecule. The NSRDC body would seem especially susceptible to polymer influence since its critical frequencies are very near the polymer frequency and also the boundary layer is highly amplified to begin with. This was substantiated by experiment in that for a given Reynolds number and concentration a lower injection rate was required for the NSRDC body than for the hemisphere nose body to eliminate the separation, eg. see Figs. 50, 51. Thus the "stretching" hypothesis seems to be a plausible mechanism by which the laminar boundary layer could be destabilized. However, in view of the lack of direct evidence that polymer stretching actually does occur in the present flows, this mechanism must still be regarded as being a hypothetical one.

In summary then there is substantial experimental evidence that the presence of drag-reducing polymers causes a destabilization of the laminar boundary layer. Theoretical evidence is less clear and predicts either a stabilization or destabilization of the laminar boundary layer can occur.

Chapter V

PRESENTATION AND DISCUSSION OF CAVITATION RESULTS

V.1 Freestream Turbulence Level and Cavitation Inception - Presentation of Results

The cavitation inception characteristics of the hemisphere nose body were studied in the HSWT and the LTWT at its lowest turbulence level. The NSRDC body was tested in the LTWT only and it was tested at two freestream velocities and two freestream disturbance levels.

V.1.1 Visual Observations - Hemisphere Nose Body

The cavitation inception sequence upon the hemisphere nose body was the same in both the HSWT and the LTWT and has already been described in detail in section I.7. A photograph illustrating the appearance of developed cavitation on this body can be seen in Fig. 58a.

V.1.2 Visual Observations - NSRDC Body

At the low turbulence level (0.05 percent), band type cavitation inception always occurred with no initial appearance of steady bubble type cavitation. At the high turbulence level (0.65 percent) cavitation was of the same type and occurred at the same value of the cavitation number. However, at the low disturbance level, the subsequent developed cavitation was steady whereas the developed cavitation at the high disturbance level was unsteady. At the 0.65 percent disturbance level the separation line became very irregular and erratic and

occasionally portions of the body would become rewetted. This difference in behavior between the low and high turbulence levels is demonstrated in the photographs of Fig. 56.

V.2 LTWT Limitations

Before discussing the cavitation experiments, we need to explain their limited test range. Only a small velocity range is available since the LTWT has a maximum test section velocity of only 25 feet per second and the lowest velocity at which bodies of the present shape can be made to cavitate is about 18 feet per second. Hence, tests were carried out at two velocities only. There is another limitation. Although five freestream turbulence levels are available, only two could be used — the 0.05 and 0.65 percent levels. This is so because turbulence grids located at the entrance to the test section would cavitate before the test model and thus three of the turbulence levels were eliminated from consideration. With these restrictions then, the experiments conducted in the LTWT to determine the influence of freestream turbulence level upon cavitation inception were: for the hemisphere nose, $Re_D = 3.0 \times 10^5$ and 3.8×10^5 at 0.05 percent turbulence level; and for the NSRDC body, $Re_D = 3.3 \times 10^5$ and 3.8×10^5 at 0.05 percent and $Re_D = 3.3 \times 10^5$ at 0.65 percent turbulence level.

V.3 Discussion

The results of the cavitation tests on the NSRDC body are presented in Fig. 57 where the cavitation inception index has been plotted versus Reynolds number with the freestream disturbance level as a

parameter. Included in Fig. 57 for comparison are cavitation data obtained on the same model in the NSRDC facility. The cavitation results for the hemisphere nose body in both the LTWT and the HSWT have been included in Fig. 60. As mentioned earlier, the high disturbance level caused no change in the inception value on the NSRDC body but it did produce a dramatic change in the appearance of the developed cavitation. Schlieren visualization of the fully wetted flow at the 0.65 percent disturbance level showed only a slight reduction in size of the laminar separation region. Comparison of the scatter in the measured laminar separation dimensions between the low and the high disturbance levels show only slightly higher scatter at the higher level — thus suggesting that the laminar separation is only slightly more unsteady at the high turbulence level than at the low turbulence level. However, the cavitation indicates that the freestream disturbances influence the viscous flow to a greater extent than would be predicted from only the above schlieren observations. Or, perhaps the explanation is that the developed cavity is more sensitive to freestream disturbances than the fully wetted shear layer. If this were so, the value of the cavitation number at inception would not change, but the appearance of the developed cavity would.

V.4 Comparison with Other Investigations

In general the main purpose of the investigation of freestream turbulence level upon cavitation occurrence and type was to determine if it could be a contributing factor in the differences in cavitation results on identical bodies tested in different facilities. In particular we

wanted to know if the observed differences in cavitation on the same NSRDC body when tested in the NSRDC facility versus the HSWT at CIT could be explained by different turbulence levels in these facilities.

It had been observed [122] that in the NSRDC facility the critical velocity for this body was 9.3 feet per second. All cavitation tests were carried out at supercritical velocities and cavitation was always of the traveling bubble type. In the HSWT the same body was found to have a critical velocity of 30 feet per second and the type of cavitation depended on velocity (see Section I.7). It was recognized that the different viscous flows on the two bodies was at least partially responsible for the differences in cavitation. However, it was not known why the critical velocity in the NSRDC facility was so low compared to the HSWT. It was suspected [44] that the freestream turbulence level might be responsible and thus the tests in the LTWT were carried out.

At the lowest turbulence level (0.05 percent) in the LTWT the laminar separation was found to be still present at a velocity of 24 feet per second and thus supports the result in the HSWT (measured turbulence level is 0.25 percent*). And also, band type inception always occurred. To reduce the critical velocity to 10 feet per second in the LTWT required a turbulence level of 3.6 percent. As can be seen from Table I.1, this is an exceptionally high turbulence level in a water tunnel test section. Initially it was thought unlikely that the disturbance level in the NSRDC facility is this high. However, after inspecting a drawing of the NSRDC facility (Fig. 2.3, Knapp et al [26]), this result

* Private Communication

does not seem so unlikely. The bulk of the circuit is 18-inch diameter pipe with turning vanes in only one corner; it has a small (6.25:1) contraction ratio and only one honeycomb, located immediately after the tunnel pump. This type of water tunnel would be expected to have a high turbulence level and in view of the changes in cavitation made by a 0.65 percent disturbance level, it seems likely that the freestream turbulence is responsible for the low critical velocity and thus partially responsible for the differences in cavitation results. However, it is believed differences in freestream nuclei populations between these facilities must also be included in a discussion of this topic and will be done so in the next chapter.

V.5 Polymer Additives and Cavitation Inception

V.5.1 Visual Observations - Hemisphere Nose Body

As in the fully wetted flow visualization experiments, the effect of the polymer caused a significant change in the flow and here in particular the appearance of the cavitation on the hemisphere nose body was strongly dependent on the amount of polymer present in the boundary layer. For a fixed concentration and freestream velocity the following changes were observed to take place as the injection rate was increased: At zero injection rate, incipient band type cavitation always occurred. At injection rates less than the critical value at which the separation would disappear, incipient band type inception would still occur but as can be seen in Fig. 58b the surface of the developed cavity has a definite wave structure and the separation line has become very irregular. Inspection of schlieren photographs of the fully wetted

flow at this injection rate showed a reduced laminar separation region with transition on the free shear layer having moved upstream from the no-injection case. With a further increase in the injection rate to values near the critical rate, different types of cavitation were observed depending upon the facility. In the HSWT band type inception would occur in patches with irregular separation lines and surfaces as is shown in Figs. 58c,d. Furthermore this type of cavitation would occur in an intermittent fashion. At even higher injection rates above the critical one, a similar behavior was observed but with the flow altering between fully wetted and patchy band cavitation more rapidly. A decrease in cavitation number at this injection condition would make this type of activity more violent, but no steady attached cavitation could be obtained. At this same injection rate, the fully wetted observations showed the laminar separation to be eliminated for the most part with only an occasional reappearance. That is, the fully wetted flow is almost always turbulent in this region of interest. If then at this stage the injection rate was suddenly reduced to zero, a large steady cavity would quickly form on the body. In the LTWT the same sequence of cavitation development would take place. However, in this facility traveling bubble type and band type cavitation would occur simultaneously when polymer was injected into the boundary layer unlike the HSWT where no bubble type cavitation was observed. We will return to this important difference in Chapter VI.

V.5.2 Visual Observations — NSRDC Body

The NSRDC body was tested in the LTWT only and it too was

observed to go through a sequence of cavitation development similar to that described above for the hemisphere nose body in the LTWT; namely, that the injection of polymer at subcritical rates changed the original band type cavitation into alternating band and bubble type. And at supercritical injection rates this intermittency became more rapid and no attached cavitation could be sustained. Examples of these types of cavitation on the NSRDC body are shown in Fig. 59 wherein it may be seen that the polymer injection has an equally dramatic effect as on the hemisphere nose body. This is demonstrated particularly well in Fig. 59d where only one cavitation bubble can be seen at the extremely low cavitation number of 0.34!

V.6 Discussion

Results of the cavitation tests with polymer injection are summarized in Figs. 60 and 61 where the values of the inception cavitation number are plotted versus Reynolds number for various values of the parameter G . We pause here to discuss the parameter G : In Fig. 62 the inception cavitation number has been plotted against the polymer injection rate for two concentrations, but in Fig. 63 the same data have been replotted against the factor G instead of the injection rate. It may be seen there that both sets of data have collapsed onto one curve. A similar result was also found for the laminar separation dimensions when plotted versus G . We may recall from the definition of G (Chapter IV) that for a fixed freestream velocity and body size, G becomes proportional to the mass flowrate of the polymer in the boundary layer. So the correlation of the cavitation index with G implies

that the polymer "effectiveness" is proportional only to the amount present within the boundary layer. Evidently from this finding, the amount present can either be controlled by the concentration or the injection rate, and hence it does appear that only G is significant for the injection effect.

Returning to the results of Figs. 60 and 61 then, it can be seen that increasing amounts of polymer in the boundary layer produce an increasing suppression in cavitation inception. There is a limit, however, beyond which no further increase in cavitation suppression occurs; in the present case on the hemisphere nose body $G \doteq 7 \times 10^{-6}$ and by observation of the schlieren photographs, this limit concurs with the removal of the laminar separation. Van der Meulen [59] injected a 500 wppm salt-polymer solution in the range $40 \times 10^{-6} \leq G \leq 72 \times 10^{-6}$ and for all of these conditions and test velocities the laminar separation was found to have been removed. These and the present results are compared in Fig. 64 where the maximum percent reduction in cavitation index has been plotted versus the Reynolds number. The agreement is believed to be reasonably good for experiments of this type. Values from Baker et al [52], Holl et al [53] and Ellis et al [50] who did polymer "ocean" tests on hemisphere nose bodies are also shown. However, the information from their reports is limited and all that can be said is that they give values approximately the same as those noted in the present study.

During their cavitation tests Baker et al [52] and Holl et al [53] noted a change in the appearance of the developed cavitation. From photographic observations of these changes Holl, Baker et al speculated

that the cavitation attenuation was due to a "flow reorientation in the region of the laminar separation bubble." They further speculated [54] that the amount of attenuation would depend on the ratio of the molecular relaxation time (T) to a flow time scale based on the free-stream velocity and the boundary layer displacement thickness at separation (δ_s^*) i.e. ($T \cdot U_\infty / \delta_s^*$). This idea is equivalent to that of a critical shear stress discussed in Chapter IV. The work of van der Meulen [59] and the present investigation verify the first speculation about flow reorientation. However, no correlation of the present results with the parameter $T \cdot U_\infty / \delta_s^*$ could be obtained. The absence of a suppression effect on an eight inch diameter nose model observed by Arndt et al [54] is believed to be due to the laminar separation being very much reduced in size or eliminated by natural transition. The Reynolds number of the test was 4×10^6 [54] and the freestream turbulence level has been reported to be about 0.8 percent [49]. The critical Reynolds number for this type of body has been estimated to be 5×10^5 at a zero freestream turbulence level [41].

V.7 Comparison with Boundary Layer Trip Experiments

The suppression of cavitation upon these bodies is a result of the elimination of the laminar separation by the polymer. It is worthwhile to compare the present results with those in which the separation is eliminated by another method. Arakeri and Acosta [41] did a series of tests with a hemisphere nose body and the ITTC body using boundary layer trips to reduce the critical Reynolds number. They found, with the trip present and at velocities above the new critical

velocity, that the occurrence of cavitation was significantly suppressed and that at higher velocities the tunnel would choke before the body could be made to cavitate. The present polymer tests show a very large effect on inhibiting cavitation but not as dramatic as the tripped tests, particularly at the higher velocities. Since in each case the schlieren photographs showed the laminar separation had been eliminated, some other factor must be the controlling influence in the present experiments. One possibility is that the injected solution itself supplied nuclei to initiate cavitation. Even though the polymer solution is mixed with deaerated tunnel water, it is under an air pressure of 80 psi in the holding tank and may therefore, eventually become saturated at a higher pressure. However, if this were the case, some traveling bubble type cavitation would be expected to occur. The photographs in Fig. 58 show that no bubble type cavitation occurs and in fact the appearance of the cavitation is much the same as that observed on the tripped bodies [41].

Another explanation is that the body, when installed in the HSWT, has a slight positive angle of attack. This angle of attack would result in a somewhat uneven distribution of the polymer tending to send more over the top portion of the body. From the photographs of the physical appearance of the cavitation on the hemisphere nose body presented in Fig. 58 it can be seen that the cavitation first disappears on the top of the model. This trend was repeatable and supports the above speculation. Further support is provided by Arakeri and Acosta's [43] observations of the viscous flow on a 1.5 calibre ogive body in the HSWT. Schlieren flow visualization showed a laminar separation to be present

on top of the body at a velocity of 65 feet per second whereas on the bottom side no separation was visible — thus suggesting a slight positive angle of attack.

Up to this point the influence of viscous effects upon the type and occurrence of cavitation have been emphasized. For a complete understanding of the inception process, the nature, number and size distributions of cavitation nuclei and how they interact with the viscous flow past the body must be known. The next chapter presents some measurements of nuclei populations obtained in the LTWT and discusses their interaction with the flow past the present bodies.

Chapter VI

FREESTREAM NUCLEI AND CAVITATION INCEPTION

VI. 1 Presentation of Results

Some typical results of nuclei population measurements made during cavitation tests in the LTWT are presented in Fig. 65. Included there for comparison are nuclei distributions measured in other facilities by different investigators. The nuclei histograms from these investigations (including the present one) have been reduced to the number density function, $N(R)$, by the following approximation:

$$N\left(R = \frac{R_1 + R_2}{2}\right) =$$

$$\frac{\text{number of nuclei with radii between } R_1 \text{ and } R_2 \text{ per unit volume}}{(R_2 - R_1)}$$

Estimates of the slopes of the lines through the data have been made and are given in Table VI. 1 shown on the following page.

VI. 2 Comparison of Nuclei Distributions

As can be seen in Table VI. 1, most of the distributions have slopes between -3.0 and -4.0 over at least some portion of the distribution. That the slope varies so little is rather surprising in view of the many different sets of environmental conditions (ambient pressure, air content, velocity) existing in these facilities when the measurements were made. For example, Gavrilov [123] measured the nuclei distribution in quiescent tap water whereas in the present study in the

TABLE VI. 1 Estimated Slopes of the Number Density Functions

<u>Investigator</u>	<u>Slope</u>
Feldberg and Schlemenson [17]	-1.9
Arndt and Keller [32]	-2.1 $0 \leq R \leq 50\mu$ -5.8 $R > 50\mu$
Keller and Weitendorf [31]	-4.0
Peterson et al [16] scattering	-4.2
Peterson et al [16] holography	-3.7
Present study: high air content	-3.1 $0 \leq R \leq 50\mu$ -1.9 $R \geq 50\mu$
low air content	-3.2 $R \geq 50\mu$
Gavrilov [123]	-3.5 $4\mu \leq R \leq 34\mu$

LTWT the water had a velocity of approximately 20 feet per second, had an air content of about 7 ppm and experienced an ambient pressure of about 2 psia. The relative insensitivity of the slope to these dramatic changes in the environment implies that, although the nuclei population can change by several orders of magnitude, the distribution of the nuclei sizes remains constant! Whether or not this constancy of slope is always true or for what range of nuclei sizes it is valid will require many more data than are presently available.

VI.3 Freestream Nuclei and Cavitation Inception Tests in the LTWT

Aside from Keller's work [12] no systematic study of the effects of these different nuclei distributions on cavitation inception has been done. And, although the main purpose of the present nuclei counting was to obtain an accurate estimate of nuclei distributions in the LTWT, a number of interesting observations made during cavitation tests on both bodies prompted a few experiments in which it was deliberately attempted to modify the nuclei distribution. First, these observations will be described and then the results of some experiments designed to explain these observations will be discussed.

As will be recalled from Chapter III, the LTWT has no resorber. This necessitates collecting cavitation data before the freestream bubbles created at the pump reach the test section. On a number of occasions the cavitation on the body was deliberately maintained and the freestream gas bubbles from the pump allowed to pass through the test section. As the number of free gas bubbles increased, the initially occurring band type cavitation was gradually destroyed and replaced by

traveling bubble type cavitation. If the tunnel pressure was lowered so that the body does not cavitate but the pump still does and again the freestream bubble population allowed to increase with time, the body would eventually cavitate — inception then always being of the traveling bubble type. Also, the models could be made to cavitate at almost any value of the cavitation number (but not above $\sigma = -c_{p_{\min}}$) by merely allowing the number of freestream bubbles to increase.

To try to determine the reasons for the above behavior, the effect of many freestream bubbles upon the fully wetted flow was investigated by the schlieren technique. Also, nuclei populations were measured when band type inception occurred and when bubble type inception occurred (deliberately promoted by the technique described in the previous paragraph) and compared. The influence of freestream nuclei on the fully wetted flow was accomplished by circulating water, which was saturated with air, at a slightly reduced tunnel pressure and using the schlieren technique to visualize the flow. The results of the schlieren study are presented in Fig. 66 and the measured nuclei distributions are given in Fig. 67.

VI. 4 Discussion of Nuclei Tests in the LTWT

Steady light source schlieren observation showed that as the number of freestream nuclei increased, the laminar separation on the hemisphere nose body became very unsteady and was finally eliminated. The schlieren photographs in Fig. 66 were taken at random as the nuclei population increased and clearly show the effect of the bubbles on

the laminar separation. The mechanism by which these gas bubbles effect this change is unknown. It has been speculated that the presence of the freestream bubbles could produce a high freestream disturbance level and thus promote an early laminar to turbulent transition on the body. However, in light of the results of the turbulence level tests on the hemisphere nose body presented in Chapter IV this seems an unlikely mechanism. In any event, whatever the mechanism may be, the observed elimination of the laminar separation by the freestream gas bubbles helps explain the observations described in the previous section.

In the case where band type inception is already present, the increasing freestream bubble population removes the laminar separation and thus causes a change from band type cavitation to well developed traveling bubble type cavitation. For the case where the tunnel pressure was held at an initially non-cavitating level for the body, the increasing number of freestream nuclei again remove the laminar separation and thus traveling bubble type inception occurs without any previous appearance of band type cavitation. In the latter case nuclei distributions were obtained at the instant inception occurred and two of these distributions ($\sigma_1 = 0.58, 0.73$) are compared in Fig. 67 with two distributions ($\sigma_1 = 0.44$) obtained when band type inception occurred, i. e. with the laminar separation present. As can be seen in this figure, for nuclei with radii less than 100 microns all the distributions are essentially the same whereas for nuclei greater than 100 microns in radius the bubble type inception distributions have many more nuclei than the band type inception ones. Thus in those facilities in which the laminar separation has been removed either by many freestream bubbles

or a high freestream turbulence level, traveling bubble type inception will occur and the value of the cavitation number at which it occurs will depend on the nuclei population. To see if these ideas are consistent with experiment consider the results of the cavitation tests on the NSRDC body in the NSRDC facility and the LTWT. (In these tests the same body was tested in facilities for which nuclei distributions are known.)

In the NSRDC facility at all test velocities the laminar separation was not present and traveling bubble type inception occurred at values of the cavitation index between 0.6 and 0.8. In the LTWT, when bubble type inception was deliberately promoted, the laminar separation was also absent and inception took place at values of the cavitation index between 0.58 and 0.73. Using the static stability analysis for a spherical gas bubble, the critical bubble size was calculated for the given values of the cavitation number and freestream velocity. Then, using the measured nuclei distributions, the number of "cavitatable" nuclei per cubic centimeter was estimated. The results of these calculations are presented in the Table VI.2 shown on the following page. The nuclei distributions for the NSRDC tests were also obtained by holography [12] and an example of one of the distributions is given in Fig. 67.

It can be seen that with the exception of the one test in the LTWT ($\sigma_i = 0.58$) that good agreement (for these types of experiments) is obtained between the two facilities. If we now follow Johnson and Hsieh's example [39] and assume that only nuclei within ± 0.01 body radii of the body centerline are possible candidates for cavitation sites,

TABLE VI.2 Cavitation Event Rates

<u>Facility</u>	<u>Model Mat'l.</u>	σ_i	U_∞ (ft./sec)	R_c (microns)	<u>Cavitatable Nuclei/cm³</u>	<u>Calculated Events/sec</u>	<u>Measured Events per sec</u>
NSRDC	CU	0.62	29.86	12	0.5	0.9	1.0
	CU	0.66	29.86	15	1.8	3.2	1.0
	AU-Plated	0.65	29.86	14	2.1	3.8	1.0
	DELRIN	0.69	29.86	18	0.5	0.9	1.0
	DELRIN	0.71	29.86	21	2.4	4.3	1.0
LTWT	CU	0.58	20.15	21	8.9	10.7	-----
	CU	0.64	20.10	29	2.0	2.4	-----
	CU	0.66	20.15	32	0.9	1.1	-----
	CU	0.73	20.25	58	1.7	2.0	-----

the number of cavitation events per second can be calculated and the results of these calculations are also given in Table VI. 2. Peterson measured the actual number of events for the NSRDC tests by an acoustic method and chose the value of one event per second to be inception since at this rate good agreement was obtained with the "visual call" of inception. In the LTWT inception was determined visually and no measurements of event rates were made.

Comparing the calculated event rate between the two facilities, it can be seen that again good agreement is obtained. This implies for one thing that the different experimenters give the same "visual call" of inception and this is good to know. Comparing the calculated event rates to measured rates it can be seen that the calculated rate is in general higher. This is attributed to the fact that not all the calculated "cavitatable" nuclei actually cavitate. This relates back to the question of what the nuclei actually are and the relative importance of the different types as cavitation nuclei (e. g. particulates versus gas bubbles).

The results of these experiments suggest, in those cases in which viscous effects do not control inception, traveling bubble type cavitation will occur and the value of the cavitation index at inception will depend on the nuclei distribution and the critical nuclei size.

It has been proposed earlier by Silberman and Schiebe [88, 129, 130, 131] that by measuring the number of cavitation events per unit time on a standard body as a function of the cavitation number the cavitation "susceptibility" of the facility water could be determined. This proposal is the reverse of the method used in the present investigation in which the nuclei population was first determined and then the

cavitation event rate inferred. By using Silberman's technique a distribution is obtained of only those nuclei which actually "cavitate" instead of the entire nuclei spectrum and thus presumably a better correlation between calculated and measured event rates would be achieved. The results of the present experiments and those of Peterson [15] tend to support Silberman et al's proposal provided of course that the standard body have no laminar separation and that inception is not controlled by the laminar to turbulent transition.

VI. 5 Cavitation Nuclei and Boundary Layer Interaction

In the preceding section the nuclei distributions were discussed with reference to traveling bubble type cavitation inception on bodies which do not have a laminar separation. As has been mentioned before, in cases where the laminar separation is present a good correlation can be made between the incipient cavitation number and the pressure coefficient at the position of the separation [41]. For the case of an attached laminar to turbulent transition, Arakeri [42] found good agreement between the pressure coefficient at the calculated position of transition and the desinent cavitation data of Parkin and Holl [46] for a 1.5 calibre ogive body. However, how the nuclei interact with these viscous effects and cause the cavitation to occur is not fully understood [3]. For example, on the hemisphere nose body it was found that $\sigma_i \geq -c_{p_s}$ whereas on the ITTC body $\sigma_i \leq -c_{p_s}$ [40]. No explanation for this behavior has been proposed. Another unexplained observation concerning the interaction between the freestream nuclei and the viscous flow was made in the present experiments, i. e. in both

the HSWT and the LTWT, cavitation tests on the NSRDC body produced band type cavitation inception at approximately the same value of the cavitation number (0.40 in the HSWT and 0.44 in the LTWT). Based on the cavitation tests in the HSWT on a tripped hemisphere nose body it is estimated that the nuclei distribution in the HSWT is 3 to 4 orders of magnitude less than that in the LTWT. Yet both facilities exhibited the normal band type of inception at subcritical Reynolds numbers at about the same inception index! Since band type inception is controlled by the presence of a laminar separation, it is speculated that the nuclei population in the separated bubble is substantially different from that in the freestream. However, at the present time no measurements of nuclei distributions in the separated bubble are available and the above speculation must await experimental verification.

In summary then the following observations were made about freestream nuclei and cavitation inception:

1. Nuclei populations appear to have a "universal" size distribution although the absolute concentrations may vary by several orders of magnitude.
2. If there are many large nuclei in the freestream they may substantially alter the fully wetted flow and thus change the value of the cavitation number and the type of inception.
3. Band type inception appears to be insensitive to freestream nuclei populations (provided of course that the population is not so large as to remove the separation).

Chapter VII

SUMMARY AND CONCLUSIONS

The influence upon the basic viscous flow on two axisymmetric bodies of freestream turbulence intensity and small amounts of a drag-reducing polymer in the boundary layer was investigated. The effects of the resulting modifications to the viscous flow upon cavitation inception were then studied. At the same time freestream nuclei populations were measured and preliminary tests carried out to determine the influence of different distributions on inception.

This investigation produced the following results: first, the viscous flow on the hemisphere nose body was insensitive to the present freestream disturbances. The NSRDC body, by comparison, was very susceptible to the freestream turbulence intensity having its critical Reynolds number reduced from 5×10^5 at 0.04 percent turbulence level to 1.6×10^5 at 3.75 percent. In the cavitation tests the NSRDC body was studied at two turbulence levels (0.04 and 0.65 percent). It was found that, although the inception index did not change, the developed cavitation became very unsteady at the higher turbulence level.

Second, the injection of small quantities of a drag-reducing polymer into the boundary layer was found to also lower the critical Reynolds number but, unlike the freestream turbulence level, the polymer was effective on both bodies. The "effectiveness" of the polymer in lowering the critical Reynolds number was found to be approximately proportional to the amount of polymer present. The subsequent

cavitation tests showed a large suppression in the inception index and a change from band type inception to simultaneously occurring traveling bubble and "rough" band type.

Third, the measured nuclei distributions were found to be in general accordance with other populations in similar facilities. It was found that, if there were many freestream gas bubbles, the normally present laminar separation was eliminated and traveling bubble type cavitation occurred — the value of the inception index then depended upon the nuclei population. In cases where the separation was present it was found that the value of the inception index was insensitive to the freestream nuclei populations.

The conclusions are then: both the increased freestream turbulence level and the injection of Polyox remove the laminar separation by destabilizing the laminar boundary layer and promoting an early transition to a turbulent non-separating one. However, the mechanisms by which either the turbulence level or the polymer interact with the laminar boundary layer are not understood and thus no explanation for the lack of effect of the turbulence intensity on the hemisphere nose body is forwarded.

On the present bodies in the LTWT and the HSWT the type of cavitation and the value of the inception index are determined by the presence of a normally occurring laminar separation. Elimination of the separation by freestream turbulence, by the injection of Polyox or by the presence of many free gas bubbles in the incoming flow causes a change in the type of inception from band to travelling bubble type. The value of the cavitation number at inception is then determined by

the freestream nuclei population.

It was found that when traveling bubble type inception occurs that it is very desirable to have first a universally accepted definition of inception based on the number of cavitation events per unit time per unit of surface area and second a standard procedure for counting the number of events.

In cases where the viscous effects control inception it is the interaction between these viscous effects (e.g. laminar separation, attached transition) and the nuclei which determine inception. How these interactions take place is not fully understood; however, in the particular case when a laminar separation occurs, it is believed that the insensitivity to freestream nuclei populations is due to a substantially different population in the separated region where inception begins. This speculation awaits experimental verification.

REFERENCES

1. Plesset, M.S., "The Tensile Strength of Liquids", Cavitation State of Knowledge, ASME 1969, pp. 15-25.
2. Holl, W.J., "Limited Cavitation", Cavitation State of Knowledge, ASME 1969, pp. 26-63.
3. Acosta, A.J. and Parkin, B.R., "Cavitation Inception—A Selective Review", Journal of Ship Research, Vol. 19, No. 4, Dec. 1975, pp. 193-205.
4. Lindgren, H. and Johnsson, C.A., "Cavitation Inception on Head Forms ITTC Comparative Experiments", Publications of the Swedish State Shipbuilding Experimental Tank, No. 58, 1966. (Also presented at the Eleventh ITTC Meeting in Tokyo, 1966.)
5. Johnsson, C.A., "Cavitation Inception on Head Forms, Further Tests", 12th International Towing Tank Conference, Rome 1969, pp. 381-392.
6. Hoyt, J.W., "The Influence of Polymer-Secreting Organisms on Fluid Friction and Cavitation", Naval Ordnance Test Station Rep. TP-4364.
7. Epstein, P.S. and Plesset, M.S., "On the Stability of Gas Bubbles in Liquid-Gas Solutions", The Journal of Chemical Physics, Vol. 18, No. 11, Nov. 1950, pp. 1505-1509.
8. Fox, F.E. and Herzfeld, K.F., "Gas Bubbles with Organic Skin as Cavitation Nuclei", The Journal of the Acoustical Society of America, Vol. 26, No. 6, Nov. 1954, pp. 984-989.
9. Pease, D.C. and Blinks, L.R., "Cavitation from Solid Surfaces in the Absence of Gas Nuclei", Journal of Physical and Colloidal Chemistry, Vol. 51, 1947, pp. 556-567.
10. Holl, J.W., "Nuclei and Cavitation", Journal of Basic Engineering, Dec. 1970, pp. 681-688.
11. Harvey, E.N., Barnes, D.K., McElroy, W.D., Whiteley, A.H., Pease, D.C., and Cooper, K.W., "Bubble Formation in Animals I, Physical Factors", Jr. Cellular and Comp. Physiol., Vol. 24, No. 1, Aug. 1944, pp. 1-22.
12. Keller, A.P., "The Influence of the Cavitation Nucleus Spectrum on Cavitation Inception, Investigated with a Scattered Light Counting Method", Journal of Basic Engineering, Dec. 1972, pp. 917-925.

13. Keller, A.P., "Investigations Concerning the Modeling of Flow Cavitation", The University of Michigan Cavitation and Multiphase Flow Laboratory, Rep. No. UMICH 01357-28-T, Mar. 1973.
14. Knapp, R.T., "Cavitation and Nuclei", Trans. of the ASME, Aug. 1958, pp. 1315-1324.
15. Peterson, F.B., "Hydrodynamic Cavitation and Some Considerations of the Influence of Free Gas Content", 9th Symposium on Naval Hydrodynamics, Paris, 1972.
16. Peterson, F.B., Daniel, F., Keller, A., and Lecoffe, Y., "Determination of Bubble and Particulate Spectra and Number Density in a Water Tunnel with Three Optical Techniques", 14th ITTC, 1975.
17. Feldberg, L.A. and Shlemenson, K.T., "The Holographic Study of Cavitation Nuclei", Discussion to Proceedings IUTAM Symposium on Non-Steady Flow of Water at High Speeds, Leningrad, USSR (English version; Moscow, 1973), pp. 106-111.
18. Acosta, A.J. and Hamaguchi, H., "Cavitation Inception on the ITTC Standard Head Form", Rep. No. E-149.1, Hydrodynamics Laboratory, California Institute of Technology, Mar. 1967.
19. Holl, J.W. and Treaster, A.L., "Cavitation Hysteresis", Journal of Basic Engineering, Trans. ASME, Series D, Vol. 88, No. 1, Mar. 1966, pp. 199-212.
20. Holl, J.W., "Sources of Cavitation Nuclei", Presented at the 15th American Towing Tank Conference, Ottawa, Canada, June 1968.
21. Reed, R.L., "The Influence of Surface Characteristics and Pressure History on the Inception of Cavitation", M.S. Dissertation, Dept. of Aerospace Engineering, The Pennsylvania State University, Mar. 1969.
22. Gupta, S.K., "The Influence of Porosity and Contact Angle on Incipient and Desinent Cavitation", M.S. Dissertation, Department of Aerospace Engineering, Pennsylvania State University, Dec. 1969.
23. Van der Meulen, J.H.J., "Incipient and desinent cavitation on hemispherical nosed bodies", International Shipbuilding Progress, Vol. 19, No. 209, Jan. 1972, pp. 21-32.
24. Van der Meulen, J.H.J., "Cavitation on hemispherical nosed teflon bodies", International Shipbuilding Progress, Vol. 19, No. 218, Oct. 1972, pp. 333-341.
25. Peterson, F.B., "Cavitation Originating at Liquid-Solid Interfaces", Rep. 2799, Naval Ship Research and Development Center, Sept. 1968.

26. Knapp, R. T., Daily, J. W., and Hammitt, F. G., Cavitation, McGraw-Hill 1970.
27. Knapp, R. T. and Hollander, A., "Laboratory Investigations of the Mechanism of Cavitation", Trans. ASME, Vol. 70, 1948, pp. 419-435.
28. Ripken, J. F. and Killen, J. M., "Gas Bubbles: Their Occurrence, Measurement, and Influence in Cavitation Testing", Proceedings of IAHR-Symposium, Sendai, Japan, 1962, pp. 37-57.
29. Killen, J. M. and Ripken, J. F., "A Water Tunnel Air Content Meter", University of Minnesota, St. Anthony Falls Hydraulic Laboratory, Project Rep. No. 70, February 1964.
30. Schiebe, F. R., "The Influence of Gas Nuclei Size Distribution on Transient Cavitation Near Inception", University of Minnesota, St. Anthony Falls Hydraulic Laboratory, Project Rep. No. 107, May 1969.
31. Keller, A. P. and Weitendorf, E. A., "Influence of Undissolved Air Content on Cavitation Phenomena at the Propeller Blades and on Induced Hull Pressure Amplitudes", Proceedings of IAHR-Symposium, Paris, 1976, pp. 65-76.
32. Arndt, R. E. A. and Keller, A. P., "Free Gas Content Effects on Cavitation Inception and Noise in a Free Shear Flow", Proceedings of IAHR-Symposium, Paris, France, 1976, pp. 3-16.
33. Parkin, B. R., "Scale Effects in Cavitating Flow", Ph. D. Dissertation, California Institute of Technology, 1952.
34. Plesset, M. S., "The Dynamics of Cavitation Bubbles", Journal of Applied Mechanics, Vol. 16, Sept. 1949, pp. 277-338.
35. Parkin, B. R. and Kermeen, R. W., "Incipient Cavitation and Boundary Layer Interaction on a Streamlined Body", California Institute of Technology, Hydrodynamics Laboratory Rep. No. E-35.2, Dec. 1953.
36. Holl, J. W. and Kornhauser, A. L., "Thermodynamic Effects on Desinent Cavitation on Hemispherical Nosed Bodies in Water of Temperatures from 80 Degrees F to 260 Degrees F", presented at Joint Conference of Applied Mechanics and Fluids Engineering Divisions, ASME, Northwestern University, June 1969. ASME Paper No. 69-FE-1.
37. Van der Walle, F., "On the Growth of Nuclei and the Related Scaling Factors in Cavitation Inception", Fourth Symposium on Naval Hydrodynamics, August 27-31, 1962 (sponsored by ONR).
38. Oshima, R., "Theory of Scale Effects on Cavitation Inception on

- Axially Symmetric Bodies", *Journal of Basic Engineering*, Trans. ASME, Series D, No. 3, Vol. 83, Sept. 1961, pp. 379-398.
39. Johnson Jr., V.E. and Hsieh, T., "The Influence of the Trajectories of Gas Nuclei on Cavitation Inception", Sixth Symposium on Naval Hydrodynamics, Sept. 1966 (Sponsored by ONR).
 40. Arakeri, V.H., "Viscous Effects in Inception and Development of Cavitation on Axi-Symmetric Bodies", Ph.D. dissertation, California Institute of Technology, 1973.
 41. Arakeri, V.H. and Acosta, A.J., "Viscous Effects in Inception of Cavitation on Axisymmetric Bodies", *Journal of Fluids Engineering*, Dec. 1973, pp. 519-526.
 42. Arakeri, V.H., "A Note on the Transition Observations on an Axisymmetric Body and Some Related Fluctuating Wall Pressure Measurements", *Journal of Fluids Engineering*, ASME, Vol. 97, Series 1, No. 1, Mar. 1975, pp. 82-87.
 43. Arakeri, V.H. and Acosta, A.J., "Some Transition and Cavitation Inception Observations on a 1.5 Calibre Ogive," presented at the 17th American Towing Tank Conference, Pasadena, California, 1974.
 44. Arakeri, V.H. and Acosta, A.J., "Cavitation Inception Observations on Axisymmetric Bodies at Supercritical Reynolds Numbers", *Journal of Ship Research*, Vol. 20, No. 1, Mar. 1976, pp. 40-50.
 45. Jaffe, N.A., Okamura, T.T., and Smith, A.M.O., "Determination of Spatial Amplification Factors and Their Application to Predicting Transition", *AIAA Journal*, Vol. 8, No. 2, Feb. 1970, pp. 301-308.
 46. Parkin, B.R. and Holl, J.W., "Incipient Cavitation Scaling Experiments for Hemispherical and 1.5 Calibre Ogive Nosed Bodies", Rep. Nord 7958-264, Ordnance Research Laboratory, The Pennsylvania State University, May 1954.
 47. Spangler, J.G. and Wells Jr., C.S., "Effects of Freestream Disturbances on Boundary Layer Transition", *AIAA Journal*, Vol. 6 1968, pp. 543-545.
 48. Hall, D.J. and Gibbings, J.C., "Influence of Stream Turbulence and Pressure Gradient Upon Boundary Layer Transition", *Journal of Mechanical Engineering Science*, Vol. 14, No. 2, 1972, pp. 134-146.
 49. Summary of Replies to Questionnaire on Water Tunnel Experiment Methods, 12th ITTC Cavitation Committee.

50. Ellis, A.T., Waugh, J.G., and Ting, R.Y., "Cavitation Suppression and Stress Effects in High-Speed Flows of Water with Dilute Macromolecular Additives", *Journal of Basic Engineering*, Sept. 1970, pp. 459-466.
51. Arndt, R.E.A., "Cavitation Inception: The Influence of Roughness Turbulence and Polymer Additives", *Ordnance Research Laboratory Technical Memorandum TM 71-195*, The Pennsylvania State University, Aug. 1971.
52. Baker, C.B., Arndt, R.E.A., and Holl, J.W., "Effect of Various Concentrations of WSR-301 Polyethylene Oxide in Water Upon the Cavitation Performance of 1/4-Inch and 2-Inch Hemispherical Nosed Bodies", *Applied Research Laboratory Technical Memorandum TM 73-257*, The Pennsylvania State University, Sept. 1973.
53. Holl, J.W., Arndt, R.E.A., Billet, M.L., and Baker, C.B., "Cavitation Research at the Garfield Thomas Water Tunnel", *Applied Research Laboratory Technical Memorandum 74-62*, The Pennsylvania State University, Mar. 1974.
54. Arndt, R.E.A., Billet, M.L., Holl, J.W., and Baker, C.B., "A Note on the Inhibition of Cavitation in Dilute Polymer Solutions", *Applied Research Laboratory Technical Memorandum 75-285*, The Pennsylvania State University, Nov. 1975.
55. Van der Meulen, J.H.J., "Cavitation Suppression by Polymer Injection", *ASME Cavitation and Polyphase Flow Forum*, New York, 1973, p. 48.
56. Van der Meulen, J.H.J., "The Influence of Polymer Injection on Cavitation", *Conference on Cavitation*, Paper No. C 149/74, Edinburgh, Scotland, Sept. 1974.
57. Van der Meulen, J.H.J. and Oosterveld, N.B., "A Holographic Study of Cavitation Inception on a Hemispherical Nosed Body", *Symposium of High Powered Propulsion of Large Ships*, Wageningen, the Netherlands, N.S.M.B. Publication No. 490, Dec. 1974.
58. Van der Meulen, J.H.J., "Holographic Study of Polymer Effect on Cavitation", *ASME Polyphase Flow and Cavitation Forum*, New Orleans, 1976.
59. Van der Meulen, J.H.J., "A Holographic Study of Cavitation on Axisymmetric Bodies and the Influence of Polymer Additives", *Doctoral Thesis*, Netherlands Ship Model Basin, 1976.
60. Hoyt, J.W., "Effect of Polymer Additives on Jet Cavitation", *Trans. 16th ATTC*, Sao Paulo, Brazil, Vol. 1, 1971, p. 70.

61. Hoyt, J.W., "Jet Cavitation in Polymer Solutions", ASME Cavitation and Polyphase Flow Forum, ASME, p.44.
62. Walters, R.R., "Effect of High-Molecular Weight Polymer Additives on the Characteristics of Cavitation", Advanced Technology Center, Inc., Dallas, Report No. B-94300/s TR-32, 1972.
63. White, J.R., "Propeller Cavitation in Solutions of Polyethylene Oxide", M.S. Thesis, Naval Postgraduate School, Monterey, California, 1971.
64. Vyaz'menskii, B. E., "Effect of Polymer Additives on Cavitation", Journal of Engineering Physics, Vol. 25, July 1, 1975, pp. 1536-1538. (Russian Original — Vol. 25, No. 6, December 1973).
65. Hoyt, J.W., "Effects of High-Polymer Solutions on a Cavitating Body", Proceedings, 11th ITTC, Tokyo, 1966.
66. Brennen, C., "Some Cavitation Experiments with Dilute Polymer Solutions", Journal of Fluid Mechanics, Vol. 44, Part 1, 1970, pp. 51-63.
67. Fogler, H.S. and Goddard, J.D., "Collapse of Spherical Cavities in Viscoelastic Fluids", The Physics of Fluids, Vol. 13, No. 5, May 1970, pp. 1135-1141.
68. Ellis, A.T. and Ting, R.Y., "Bubble Dynamics in Drag Reducing Polymer Solutions", University of California, San Diego, Department of Aeronautical and Mechanical Engineering, Final Rep. under NUC Contract N66001-70-0237, 1970.
69. Ting, R.Y. and Ellis, A.T., "Bubble Growth in Dilute Polymer Solutions", Physics of Fluids, Vol. 17, No. 7, July 1974, pp. 1461-1462.
70. Vanoni, V.A., Hsu, E., and Davies, R.W., "Dynamics of Particulate Matter in Fluid Suspensions", Hydrodynamics Laboratory Report No. 71.1a, California Institute of Technology, Nov. 1950.
71. Vanoni, V.A. and Hsu, E.Y., "The Dynamics of Particulate Matter in Fluid Suspensions", Hydrodynamics Laboratory Rep. E-34. California Institute of Technology, Dec. 1951.
72. Loehrke, R.I. and Nagib, H.M., "Experiments on Management of Freestream Turbulence", AGARD Rep. No. 598., Sept. 1972.
73. Uhlig, H.H., Corrosion and Corrosion Control, 2nd Edition, John Wiley and Sons Inc., 1971.
74. Kovaszny, L.S.G., "High Power Short Duration Spark Discharge"

The Review of Scientific Instruments, Vol. 20, No. 9, Sept. 1949, pp. 696-697.

75. Brennen, C. and Gadd, G.E., "Aging and Degradation in Dilute Polymer Solutions", *Nature*, Vol. 215, No. 5108, Sept. 23, 1967, pp. 1368-1370.
76. Astarita, G. and Nicodema, L., "Velocity Distributions and Normal Stresses in Viscoelastic Turbulent Pipe Flow", *AIChE Journal*, Vol. 12, 1966, p. 478-484.
77. Metzner, A.B. and Astarita, G., "External Flow of Viscoelastic Materials: Fluid Property Restrictions on the Use of Velocity-Sensitive Probes", *AIChE Journal*, Vol. 13, 1967, p. 550-555.
78. Smith, K.A., Merrill, E.W., Mickley, H.S., and Virk, P.S., "Anomalous Pitot Tube and Hot Film Measurements in Dilute Polymer Solutions", *Chemical Engineering Science*, Vol. 22, 1967, p. 619-626.
79. Wu, J., "Some Techniques of Ejecting Additive Solutions for Drag Reduction", *Hydronautics, Inc.*, Technical Rep 7101-1, Feb. 1971.
80. Morgan, W.B., "Air Content and Nuclei Measurement", 13th ITTC, 1972, Rep. of Cavitation Committee.
81. Thompson, B.J. and Ward, J.H., "Particle Sizing — the First Direct Use of Holography", *Scientific Research*, Vol. 1, No. 10, Oct. 1966, pp. 37-40.
82. Thompson, B.J., Ward, J.H., and Zinky, W.R., "Application of Hologram Techniques for Particle Size Analysis", *Applied Optics*, Vol. 6, No. 3, 1967, pp. 519-526.
83. Parrent, Jr., G.B. and Thompson, B.J., "On the Fraunhofer (far field) Diffraction Pattern of Opaque and Transparent Objects with Coherent Background", *Opt. Acta.*, No. 11, 1964, pp. 183-193.
84. Debrule, F.M., "Friction and Heat Transfer Coefficients in Smooth and Rough Pipes with Dilute Polymer Solutions", Ph.D. Thesis, California Institute of Technology, 1972.
85. Van Driest, E.R. and Blumer, C.B., "Boundary Layer Transition: Freestream Turbulence and Pressure Gradient Effects", *AIAA Journal*, Vol. 1, No. 6, June 1963, pp. 1303-1306.
86. Reshotko, E., "Boundary-Layer Stability and Transition", *Annual Review of Fluid Mechanics*, Vol. 8, 1976, pp. 311-349.

87. Tsuji, H., "Experimental Studies on the Spectrum of Isotropic Turbulence Behind Two Grids", *Journal of Physical Society of Japan*, Vol. 11, No. 10, 1956, pp. 1096-1104.
88. Schiebe, F.R., "Measurement of the Cavitation Susceptibility of Water Using Standard Bodies", St. Anthony Falls Hydraulic Laboratory Project Rep. No. 118, University of Minnesota, Feb. 1972.
89. Turner, J.S., Buoyancy Effects in Fluids, Cambridge University Press, 1973, pp. 108-111.
90. Hoyt, J.W., "The Effect of Additives on Fluid Friction", *Trans. ASME Journal of Basic Engineering*, June 1972, pp. 258-285.
91. Sarpkaya, T., Rainey, P.G., and Kell, R.E., "Flow of Dilute-Polymer (Polyox WSR-301) Solutions About Circular Cylinders", Naval Postgraduate School Rep. 59SL72072A, July 1972. See also *JFM*, Vol. 57, 1973, pp. 177-208.
92. Lang, T.G. and Patrick, H.V.L., ASME preprint 66-WA/FE-33, 1966.
93. White, A., "Drag of Spheres in Dilute Polymer Solutions", *Nature*, Vol. 216, Dec. 1967, pp. 994-995.
94. Kowalski, T., "Effect of Polymer Additives on Propeller Performance", *Journal of Hydronautics*, 5, 1, Jan. 1971, pp. 11-14.
95. Wu, J., "Lift Reduction in Additive Solutions", *Journal of Hydro-nautics*, Vol. 3, No. 4, Oct. 1969, pp. 198-200.
96. Wolf, J. and Cahn, R., "Lifting Surface in Polymer Solutions," NSRDC Rep., No. 3653, May 1971.
97. Sarpkaya, T., "Lift and drag measurements on a hydrofoil in dilute polyox solutions", *Nature*, 241, No. 5385, Nov. 1973, pp. 114-115.
98. Sanders, J.V., Henderson, L.H., and White, R.J., "Effects of polyethylene oxide solutions on the performance of a small propeller", *Journal of Hydronautics*, 7, 2, July 1973, pp. 124-128.
99. Latta, B. and Czaban, J., "On the Performance of Turbomachinery in the Presence of Aqueous Polymer Solution", International Conference on Drag Reduction, Sept. 1974.
100. Lehman, A.F. and Suessmann, R.T., "An Experimental Study of the Lift and Drag of a Hydrofoil with Polymer Injection", *Oceanics Rep. No. 72-94*, Nov. 1972.

101. Fruman, D.H., Sundaram, T.R., and Daugard, S.J., "Effect of Drag-Reducing Polymer Injection on the Lift and Drag of a Two-Dimensional Hydrofoil", Hydronautics Technical Rep. 7101-4, Sept. 1974.
102. Fruman, D.H., Tulin, M.P., and Liu, H.L., "Lift, Drag, and Pressure Distribution Effects Accompanying Drag-Reducing Polymer Injection on Two-Dimensional Hydrofoil", Hydronautics Technical Rep. 7101-5, Oct. 1975.
103. Sarpkaya, T., "On the Performance of Hydrofoils in Dilute Polyox Solutions", International Conference on Drag Reduction, 4-6th, Sept. 1974.
104. Tagori, T., Masunaga, K., Okamoto, H., and Suzuki, M., "Visualization of Flow of Dilute Polymer Solutions around Two-Dimensional Hydrofoils", 2nd Symposium on Flow Visualization, ISAS, University of Tokyo, July 1974, pp. 83-88.
105. Castro, W. and Squire, W., "The Effect of Polymer Additives on Transition in Pipe Flow", Appl. Sci. Res., 18, Sept. 1967, pp. 81-96.
106. Giles, W.B. and Pettit, W.T., "Stability of Dilute Viscoelastic Flows", Nature, Vol. 216, Nov. 1967, pp. 470-472.
107. White, W.D. and McEligot, D.M., "Transition of Mixtures of Polymers in a Dilute Aqueous Solution", Journal of Basic Engineering, Trans. of the ASME, Sept. 1970, pp. 411-418.
108. Virk, P.S., Merrill, E.W., Mickley, H.S., Smith, K.A., and Mollo-Christensen, E.L., "The Toms Phenomenon: Turbulent Pipe Flow of Dilute Polymer Solutions", JFM, Vol. 30, 1967, pp. 305-328.
109. Goldstein, R.J., Adrian, R.J., and Kreid, D.K., "Turbulent and Transition Pipe Flows of Dilute Aqueous Polymer Solutions", I&EC Fundamentals, Vol. 8, No. 3, Aug. 1969, pp. 498-502.
110. Paterson, R.W. and Abernathy, F.H., "Transition to Turbulence in Pipe Flow for Water and Dilute Solutions of Polyethylene Oxide", JFM, Vol. 51, 1972, pp. 177-185.
111. Fong, C.F. Chan Man and Walters, K., "The Solution of Flow Problems in the Case of Materials with Memory. Part II — The Stability of Plane Poiseuille Flow of Slightly Viscoelastic Liquids", Journal de Mecanique, Vol. 4, No. 4, 1965.
112. Jones, D.T. and Walters, K., "Some Remarks on the Stability of Parallel Flow of Non-Newtonian Fluids", AIChE Journal, Vol. 14, No. 4, 1968, pp. 658-659.

113. Gupta, A.S., "Stability of a Visco-elastic Liquid Film Flowing Down an Inclined Plane", JFM, Vol. 28, 1967, pp. 17-28.
114. Craik, A.D.D., "A Note on the Static Stability of an Elastico-Viscous Fluid", JFM, Vol. 33, 1968, pp. 33-38.
115. Mook, D.T., "Stability of Parallel Flows of Second Order Liquids", The Physics of Fluids, Vol. 15, No. 2, 1972, pp. 219-223.
116. Squire, H.B., "On the Stability of Three-Dimensional Distribution of Viscous Fluid Between Parallel Walls", Proc. Roy. Soc, London, A142, 1933, pp. 621-628.
117. Lockett, F.J., "Fluid Dynamics Approach to the Toms Effect", Nature, Vol. 222, 1969, pp. 937-939.
118. Kundu, P.K., "Investigation of Stability of Plane Couette Flow of a Second-Order Fluid by the Energy Method", Trans. of the Society of Rheology, 18:4, 1974, pp. 527-539.
119. Tulin, M.P., "Hydrodynamics Aspects of Macromolecular Solutions", Proceedings 6th Symposium on Naval Hydrodynamics, 1966.
120. Lumley, J.L., "The Toms Phenomenon: Anomalous Effects in Turbulent Flow of Dilute Solutions of High Molecular Weight Linear Polymers", Applied Mechanics Review, Vol. 20, 1967, pp. 1139-1149.
121. Lumley, J.L., "Drag Reduction in Turbulent Flow by Polymer Additives", J. Polymer Science: Macromolecular Reviews, Vol. 7, 1973, pp. 263-290.
122. Brockett, T., "Some Environmental Effects on Headform Cavitation Inception", NSRDC Report 3974, 1972.
123. Gavrilov, L.R., "Free Gas Content of a Liquid and Acoustical Techniques for its Measurement", Soviet Physics - Acoustics, Vol. 15, No. 3, 1970, pp. 285-295.
124. Vanoni, V.A. and Brooks, N.H., "A Study of Turbulence and Diffusion Using Tracers in a Water Tunnel", Hydrodynamics Laboratory Rep. No. E-46, January 31, 1955, California Institute of Technology.
125. Thwaites, B., "Approximate Calculation of the Laminar Boundary Layer", Aeronautical Quarterly, 1, 1949, pp. 245-280.
126. Crabtree, L.F., Küchemann, D., Sowerby, L., "Three-Dimensional Boundary Layers", in Laminar Boundary Layers, edited by L. Rosenhead, 1963, pp. 430-432.

127. Wazzan, A.R., Okamura, T.T., and Smith, A.M.O., "Spatial and Temporal Stability Charts for the Falkner-Skan Boundary Layer Profiles", DAC 67086, McDonnell Douglas Corp., Sept. 1, 1968.
128. Kermeen, R.W., "Some Observations of Cavitation on Hemispherical Head Models", Hydrodynamics Rep. No. E-35.1, June 1952, California Institute of Technology.
129. Silberman, E., Schiebe, F., and Mroska, E., "The Use of Standard Bodies to Measure the Cavitation Strength of Water", St. Anthony Falls Hydraulic Laboratory, Rep. 141, University of Minnesota, 1973.
130. Silberman, E. and Schiebe, F., "A Method for Determining the Relative Cavitation Susceptibility of Water", Presented at Conference on Cavitation, Institute of Mechanical Engineers, Edinburgh, Scotland, 1976.
131. Silberman, E., "Discussions of the Report of Cavitation and Propulsion Committee", 17th American Towing Tank Conference, June 1974.

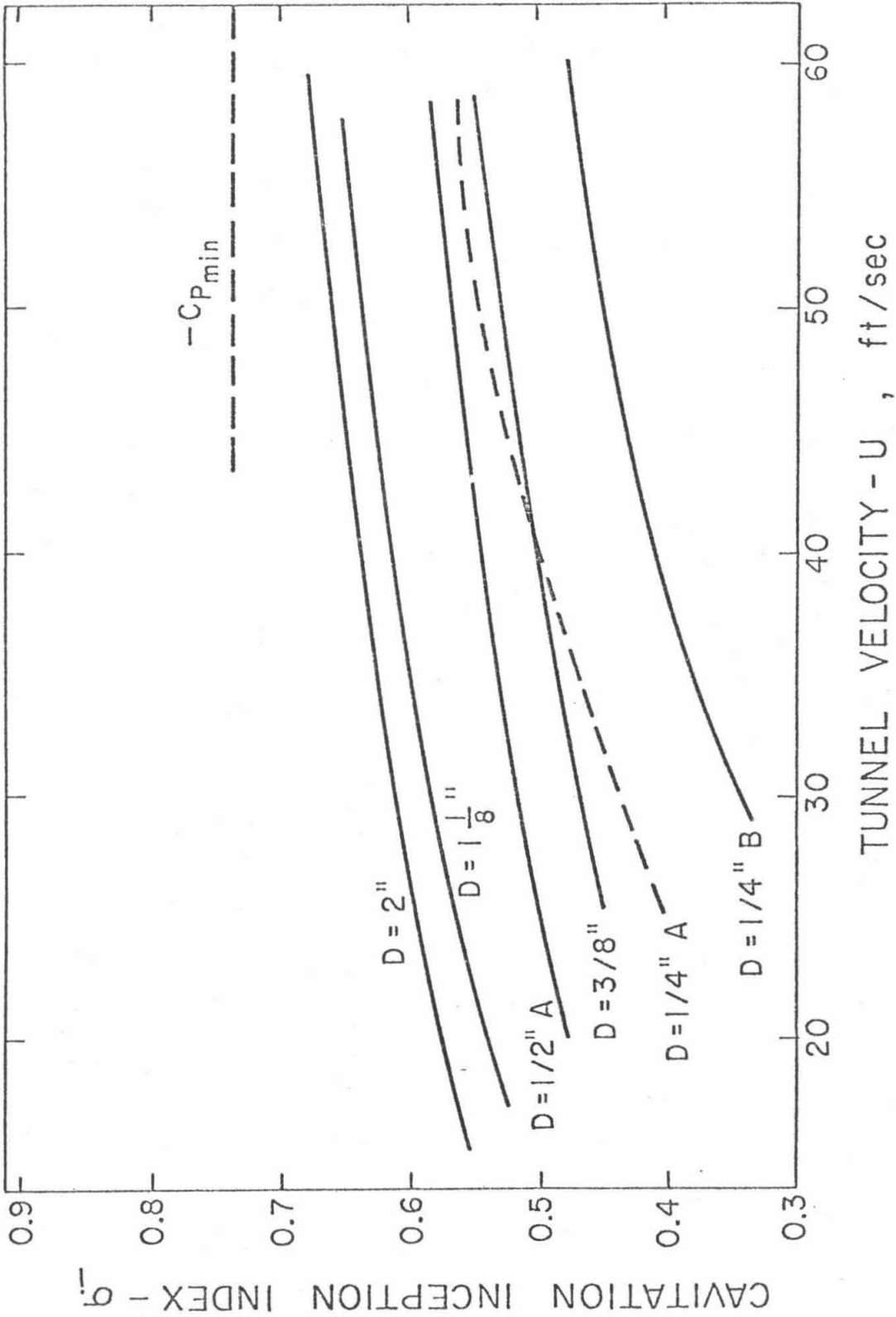


Fig. 1 Cavitation inception number versus velocity for a series of six hemisphere nose bodies. (Ref. 128)

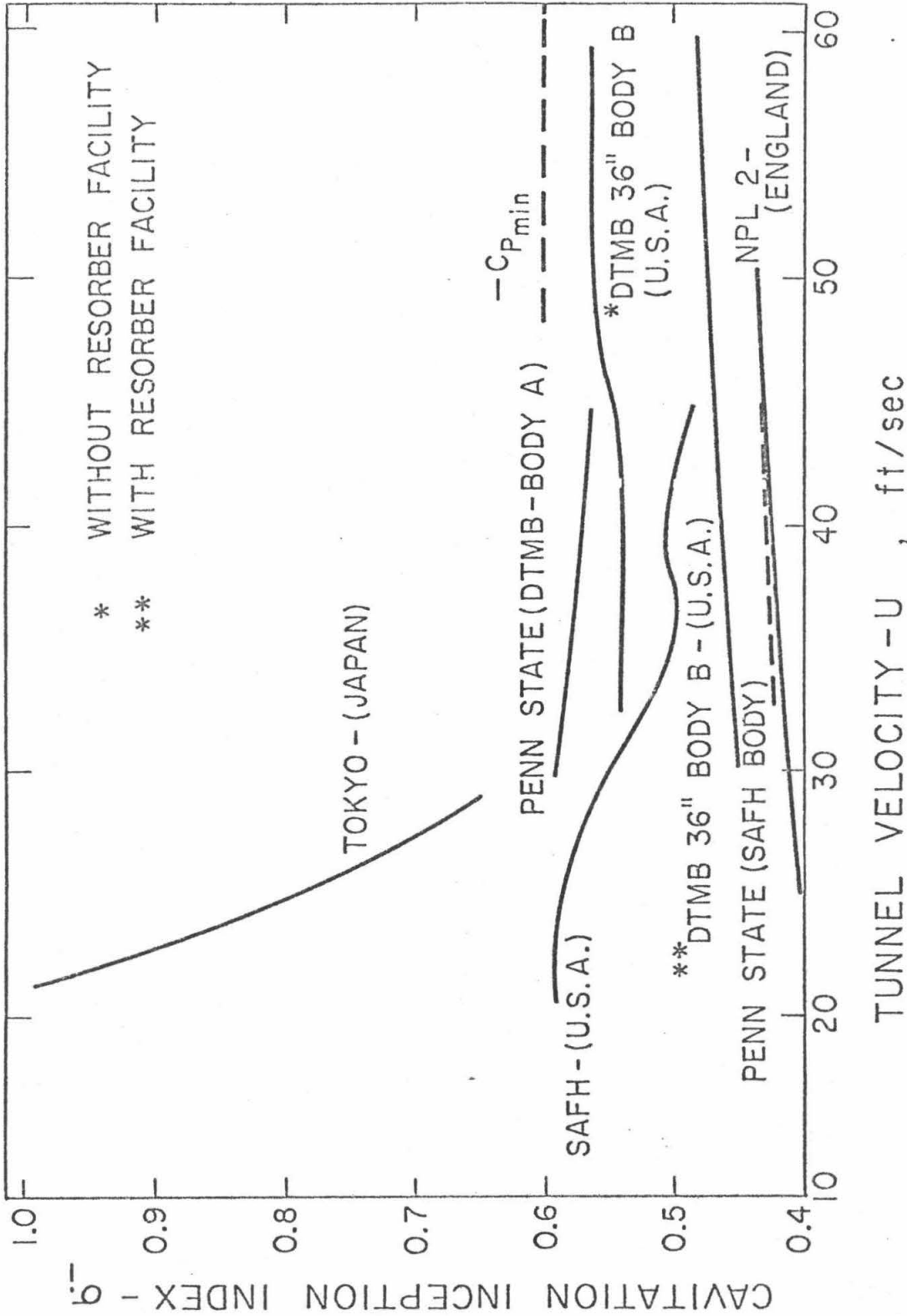


Fig. 2. Results of a comparative cavitation inception test on a modified ellipsoidal headform sponsored by the International Towing Tank Conference. Taken from Fig. 8 of Ref. 4.

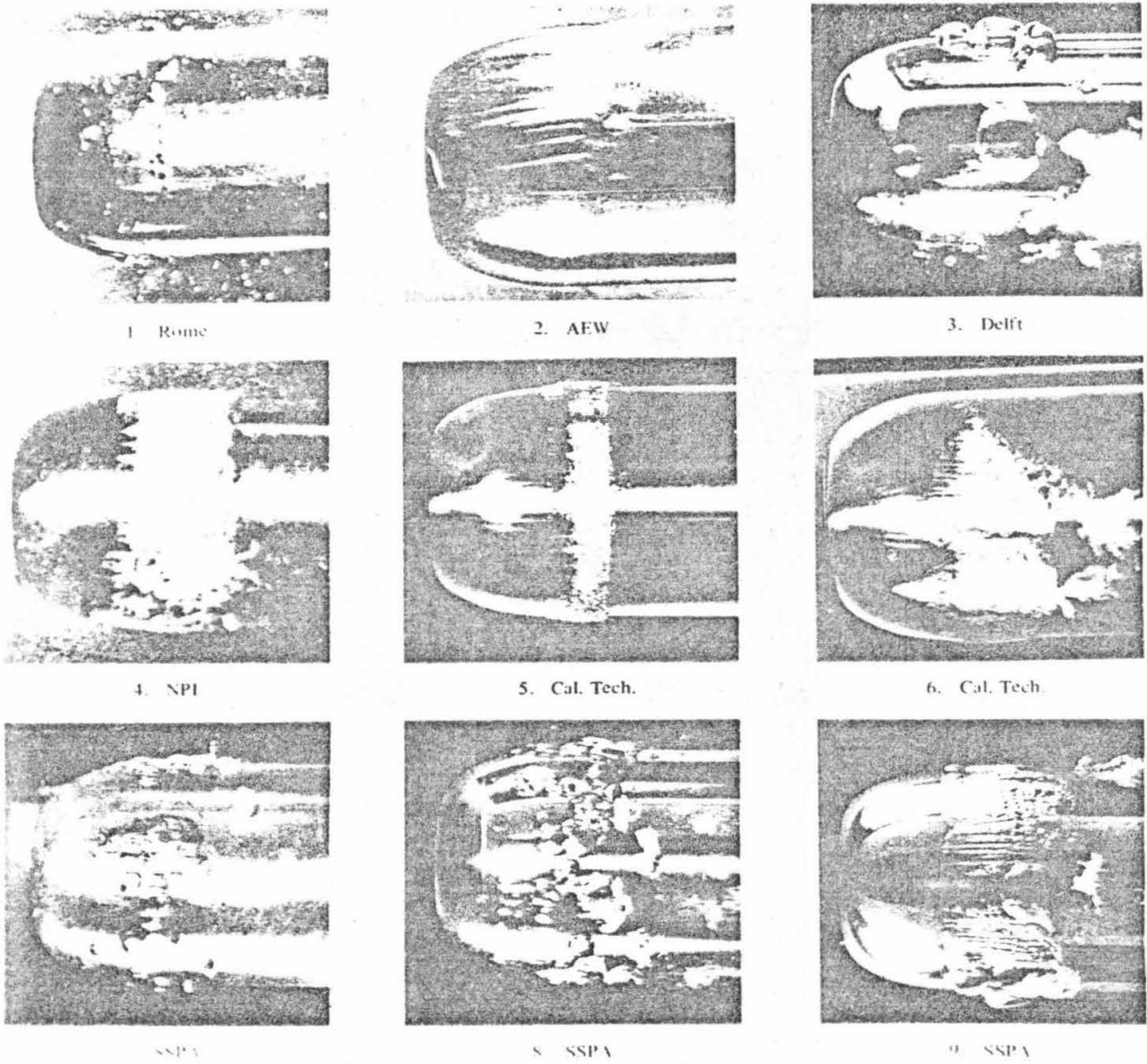
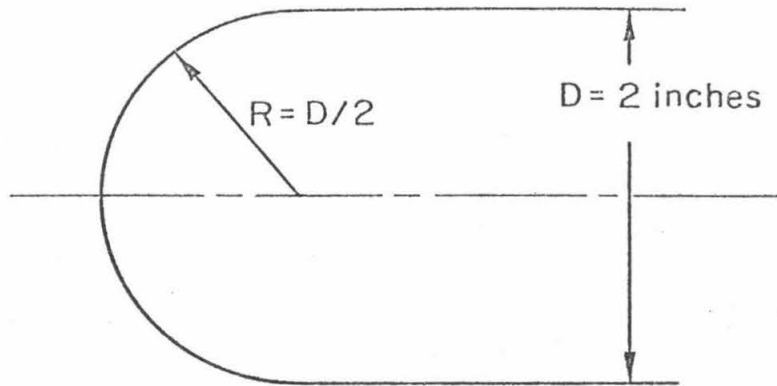


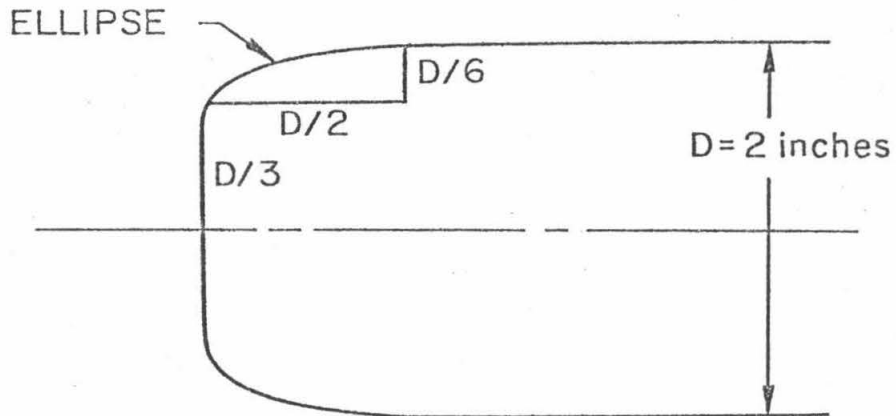
Fig. 3. Photographs of incipient cavitation on the ITTC headform in various facilities. Taken from Ref. 5.



MATERIAL - BRASS
AXISYMMETRIC

SURFACE FINISH - SMOOTH

(a)

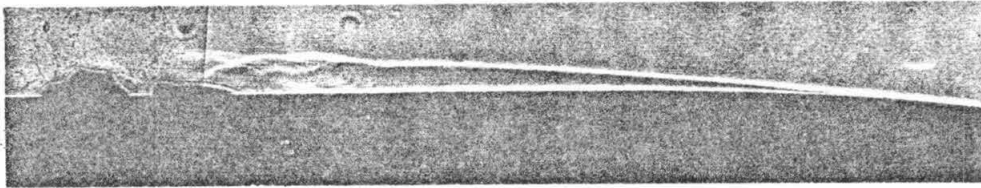


MATERIAL - COPPER
AXISYMMETRIC

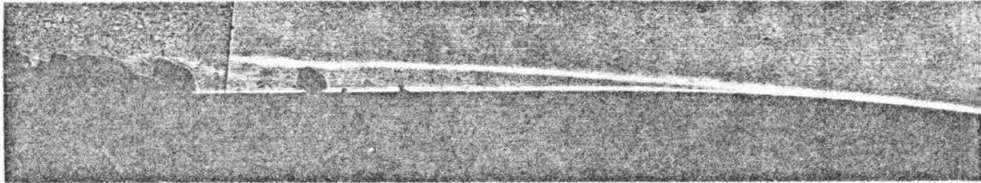
SURFACE FINISH - SMOOTH

(b)

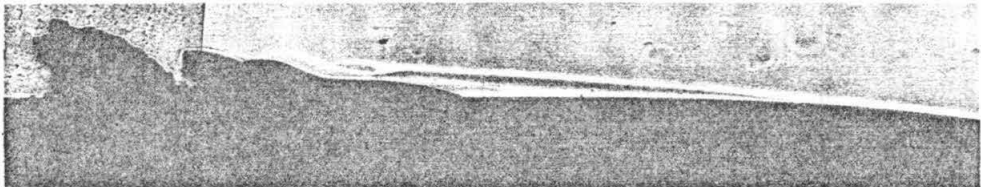
Fig. 4. Diagrams of the test bodies showing the geometric details.
(a) hemisphere nose body
(b) NSRDC body



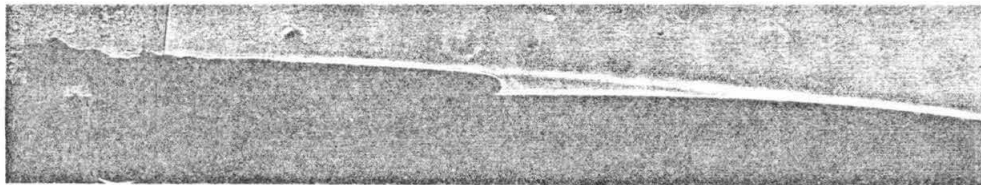
(a)



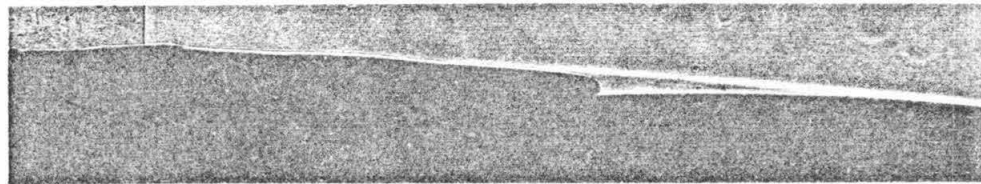
(b)



(c)



(d)



(e)

Fig. 5 Schlieren photographs of the laminar separation and cavitation inception on the hemisphere nose body. The photographs illustrate the development of cavitation from "steady bubble" type to "band type" cavitation. Inception can clearly be seen to start in the reattachment zone of the separation. Flow is from right to left. $Re_p = 3.3 \times 10^5$, $\sigma = 0.66$ for each photograph.

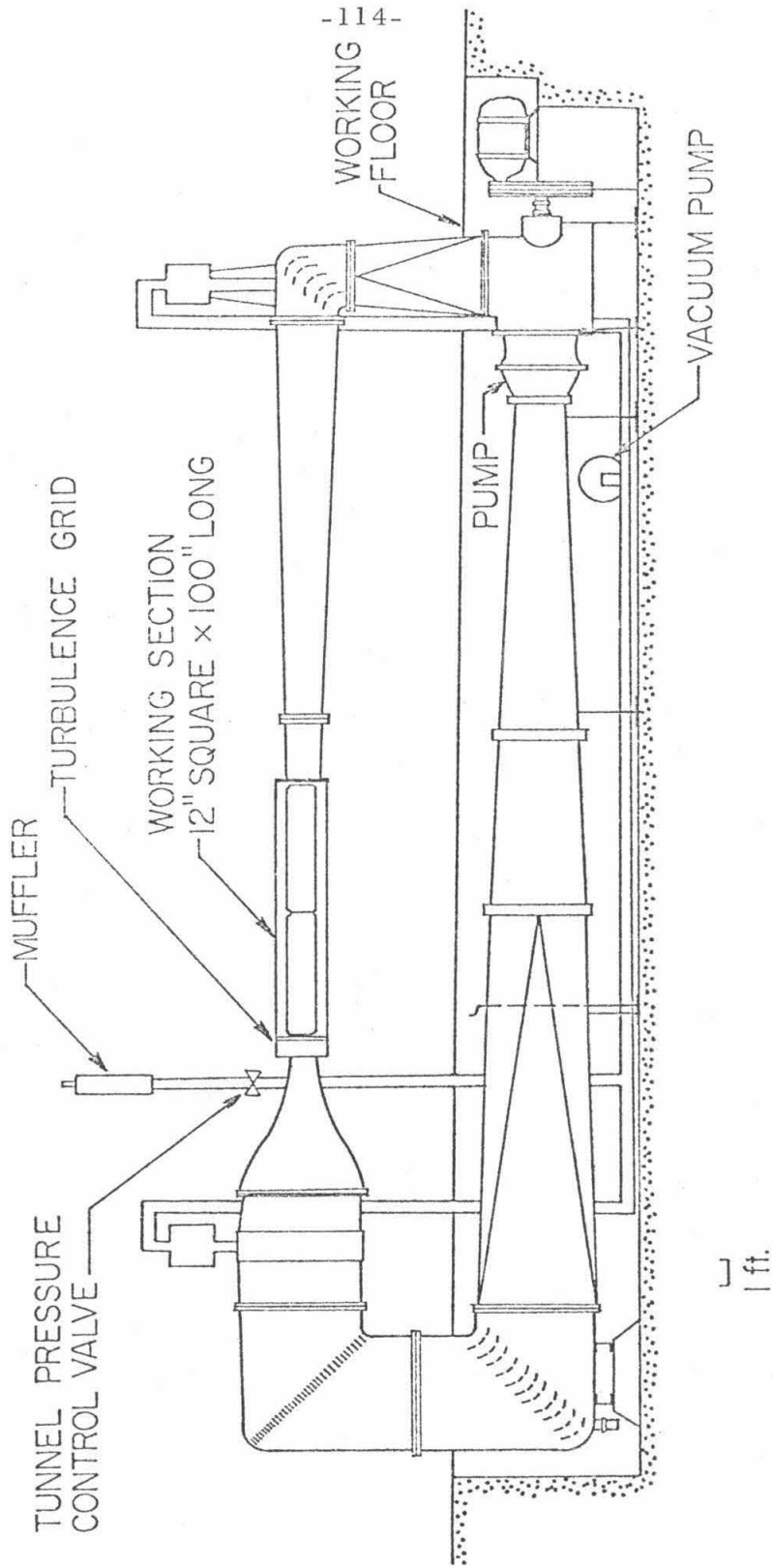


Fig. 6. Schematic diagram of the LTWT.

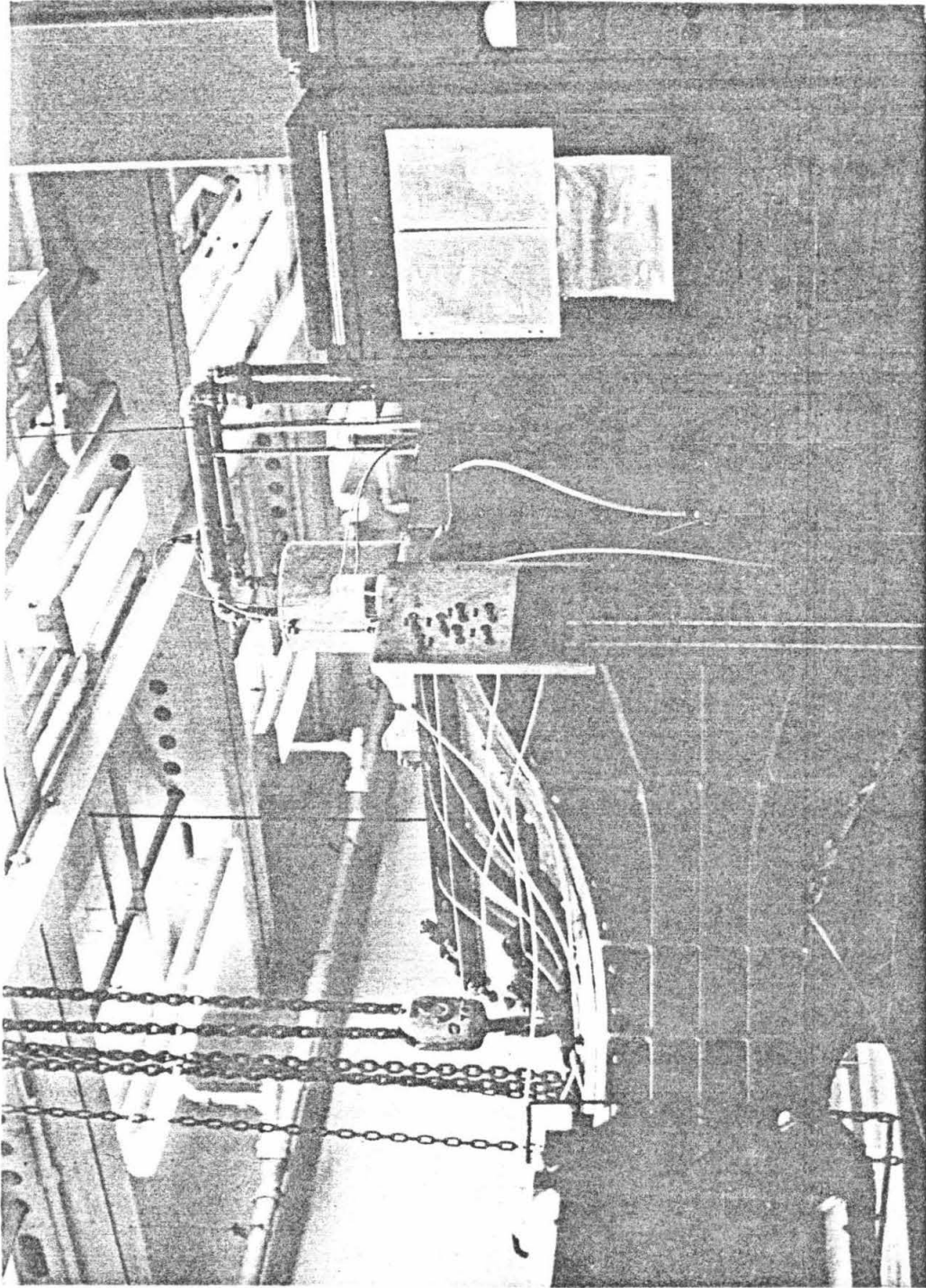
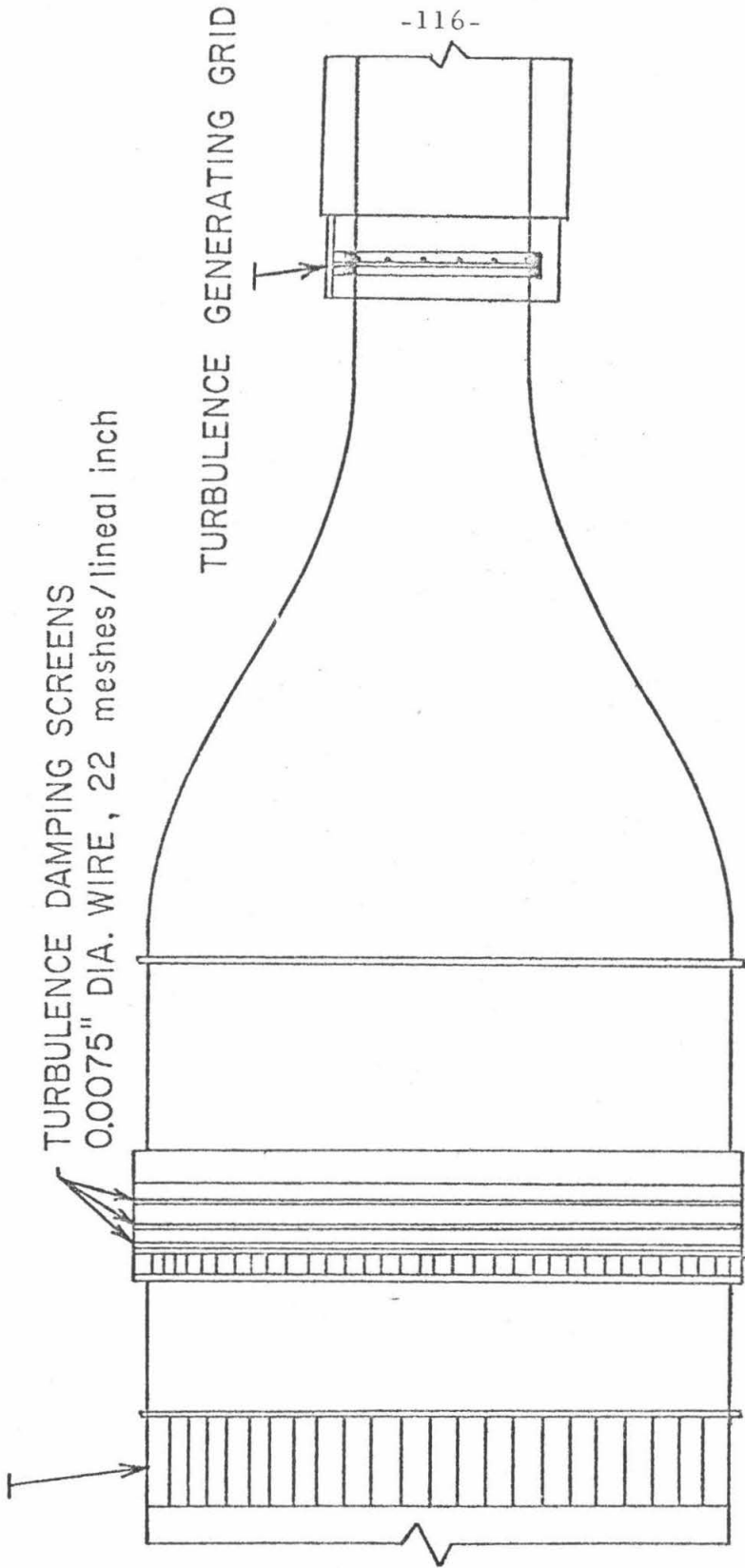


Fig. 7. Photograph of nozzle and stagnation section of the LTWT. Panels in the lower right of the picture are the tunnel power and velocity controls. On top of the stagnation section is the expansion pot and the piping to the vacuum pump and drain.

HONEYCOMB

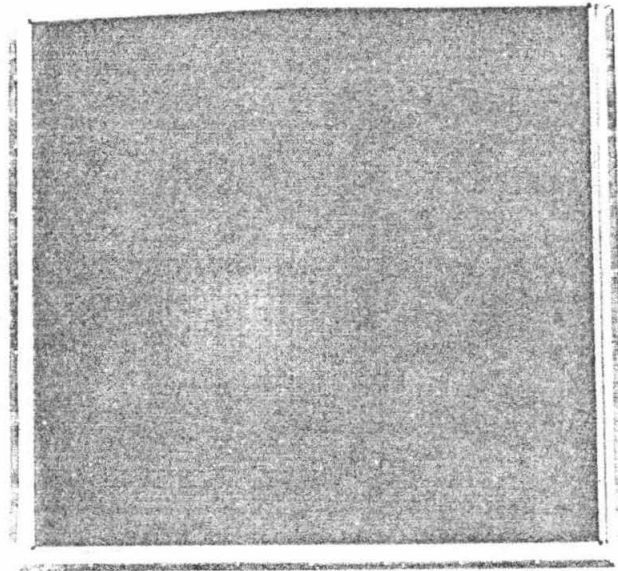
1" X 7" TRIANGULAR CELLS (1" ALTITUDE, EQUILATERAL)



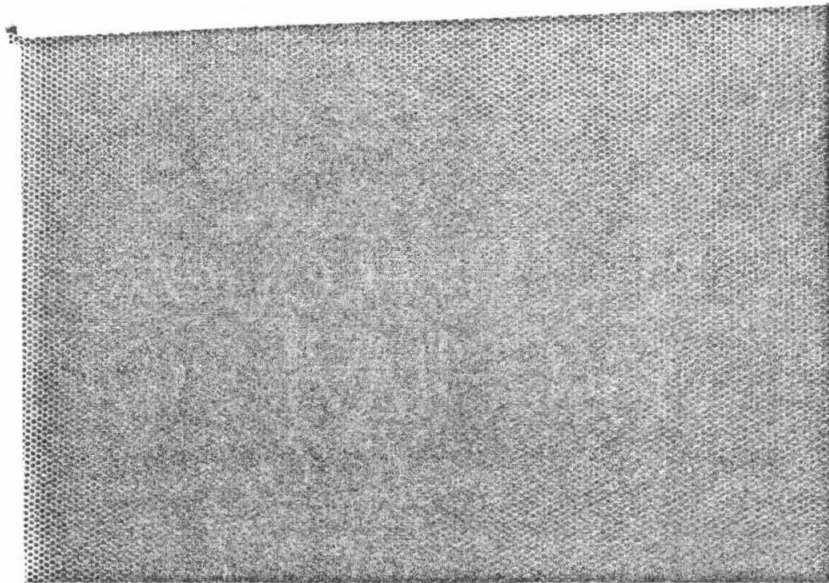
SCALE : 1 ft

SECOND HONEYCOMB
1/8" X 2" HEXAGONAL CELLS

Fig. 8. Schematic diagram of the details and positions of the turbulence manipulators in the Low Turbulence Water Tunnel.

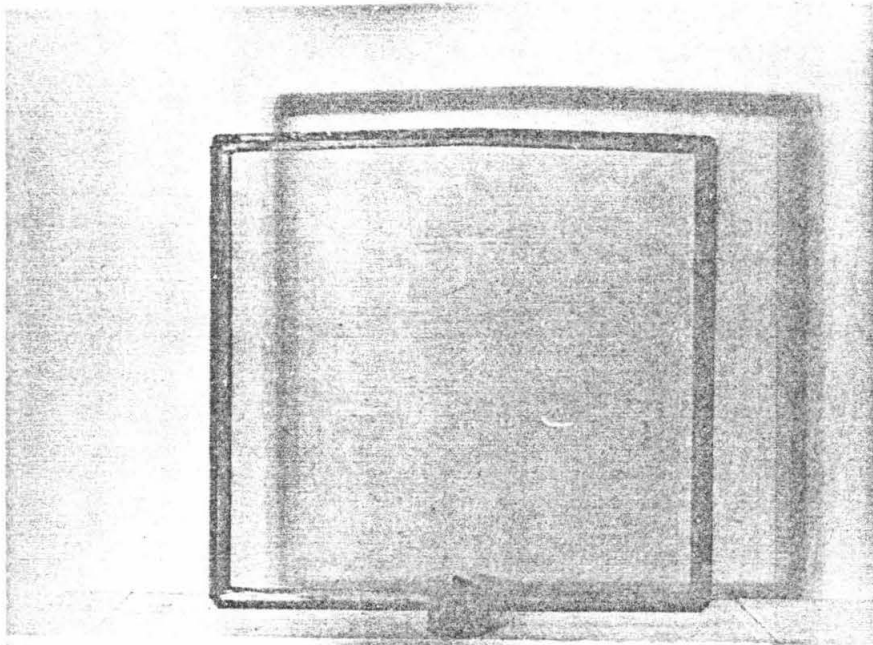


(a)

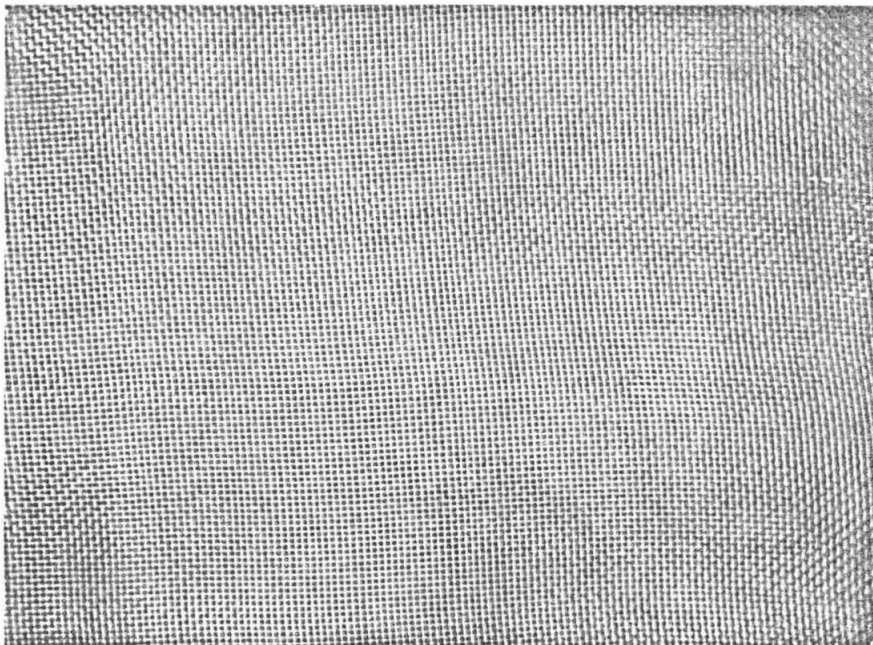


(b)

Fig. 9. The second honeycomb located in LTWT stagnation section. (a) View of honeycomb in its supporting frame. Honeycomb is $4' \times 4' \times 2''$ deep. (b) Close-up view of $1/8''$ hexagonal cells.



(a)



(b)

Fig. 10. One of the three turbulence damping screens located in the stagnation section of the LTWT. (a) View of screen on its frame. Screen is $4' \times 4'$. (b) Close-up view of screen. Screen is made of 0.0075" diameter stainless steel wire and has 22 mesh/lineal inch.

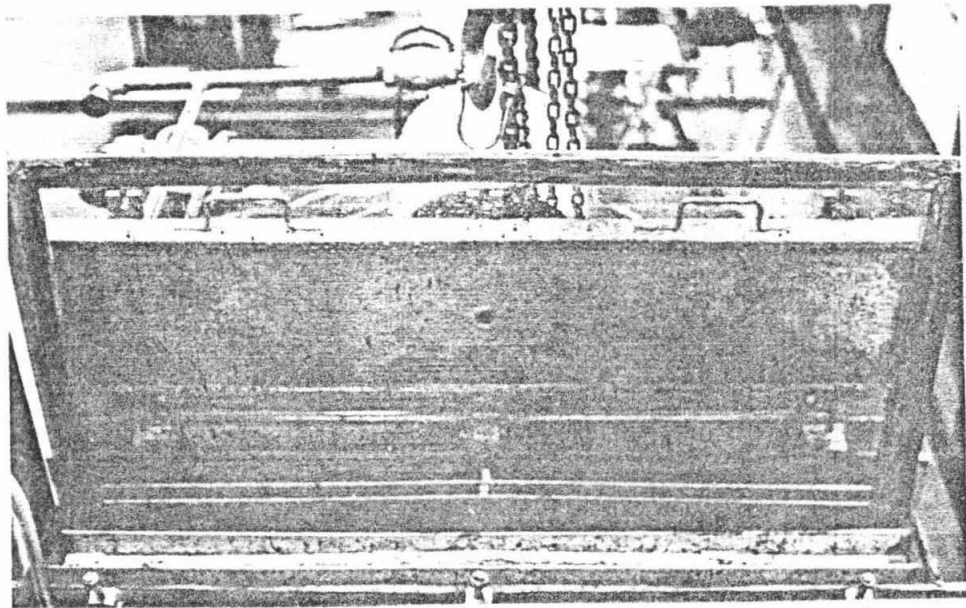


Fig. 11. Photograph of turbulence damping screen being installed in the stagnation section of the LTWT.

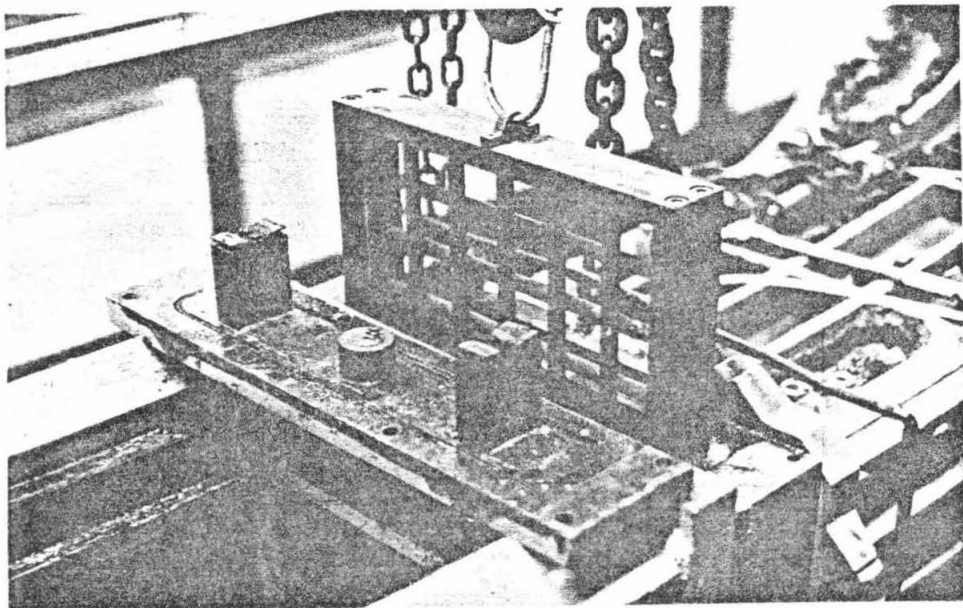


Fig. 12. Photograph of turbulence generating grid being installed in the test section entrance of the LTWT.

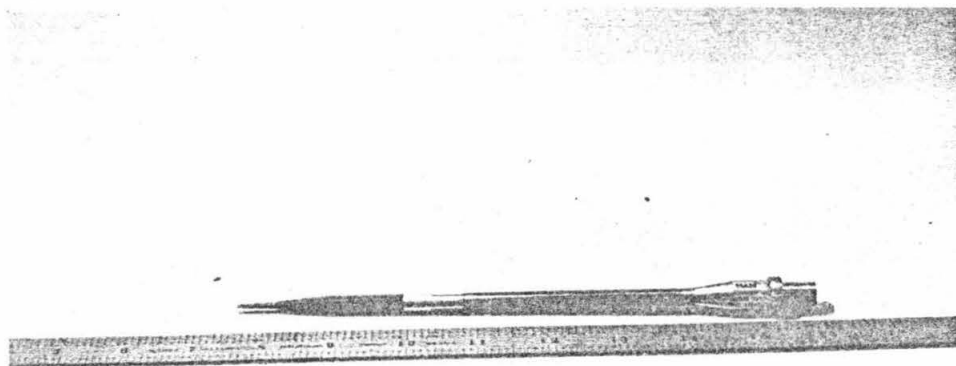


Fig. 13. Photograph of the Disa hot-film probe used to measure turbulence levels in the LTWT.

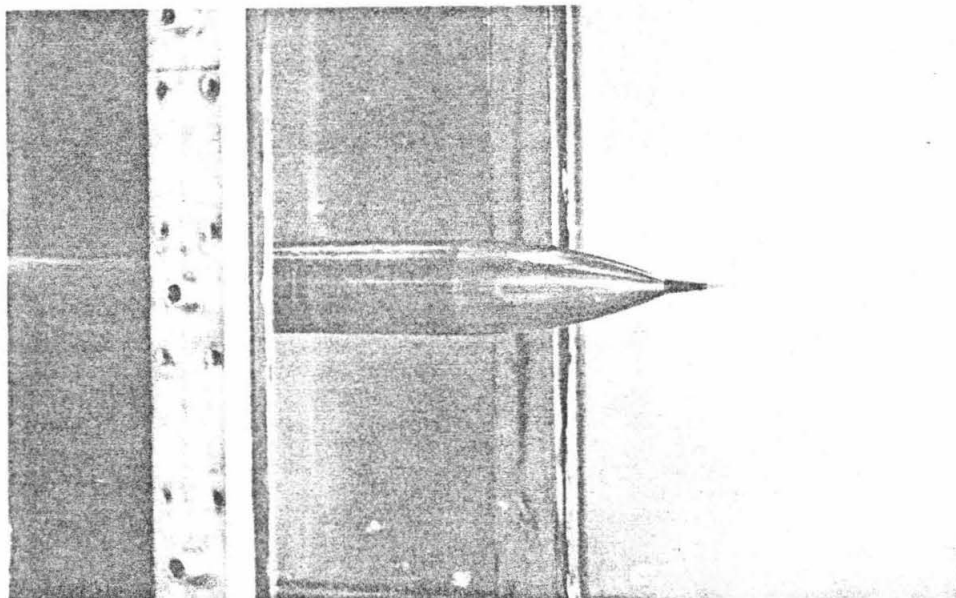


Fig. 14. Photograph of the hot-film probe mounted in the LTWT. Flow is from right to left.

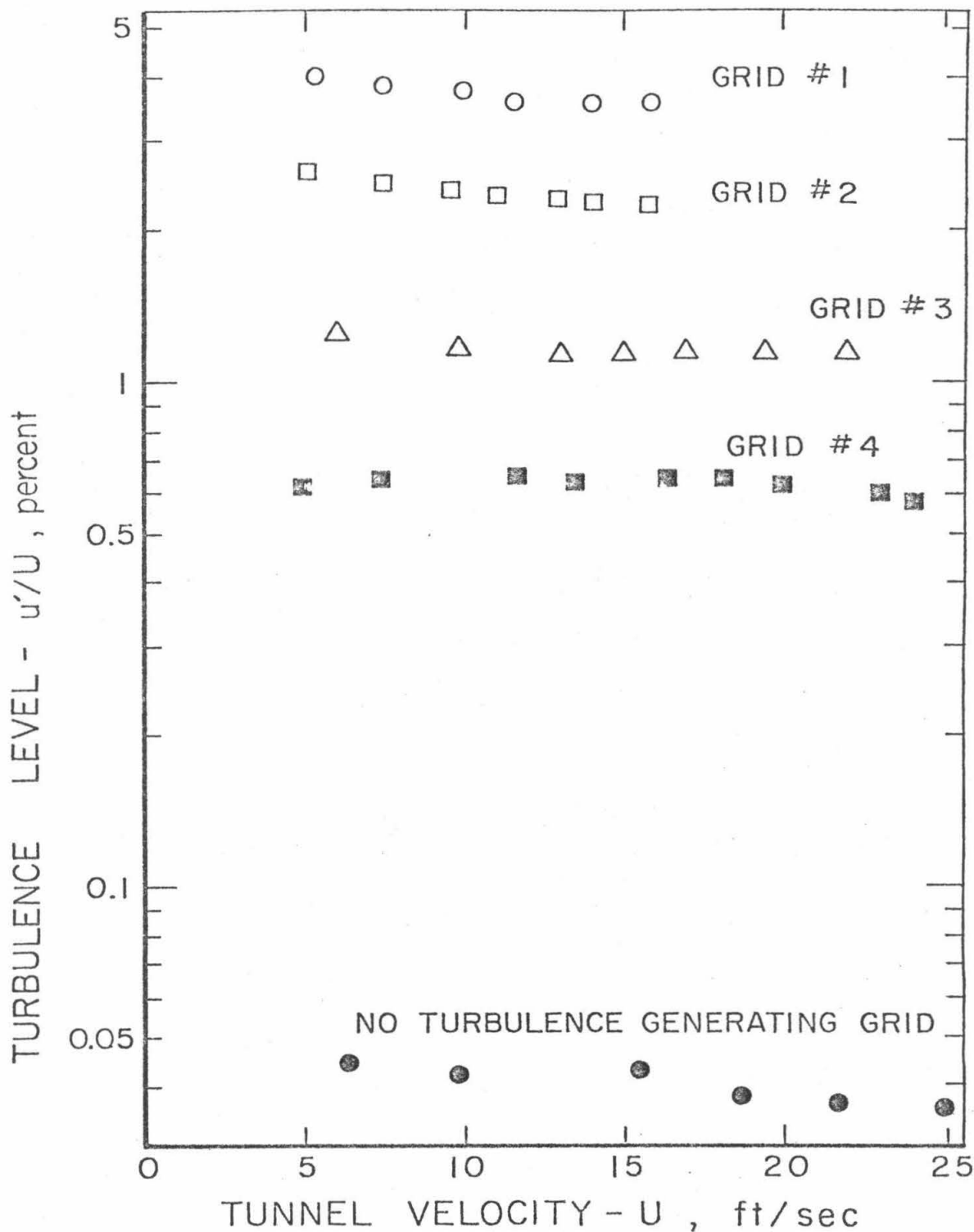


Fig. 15. Summary of the turbulence level measurements in the LTWT.

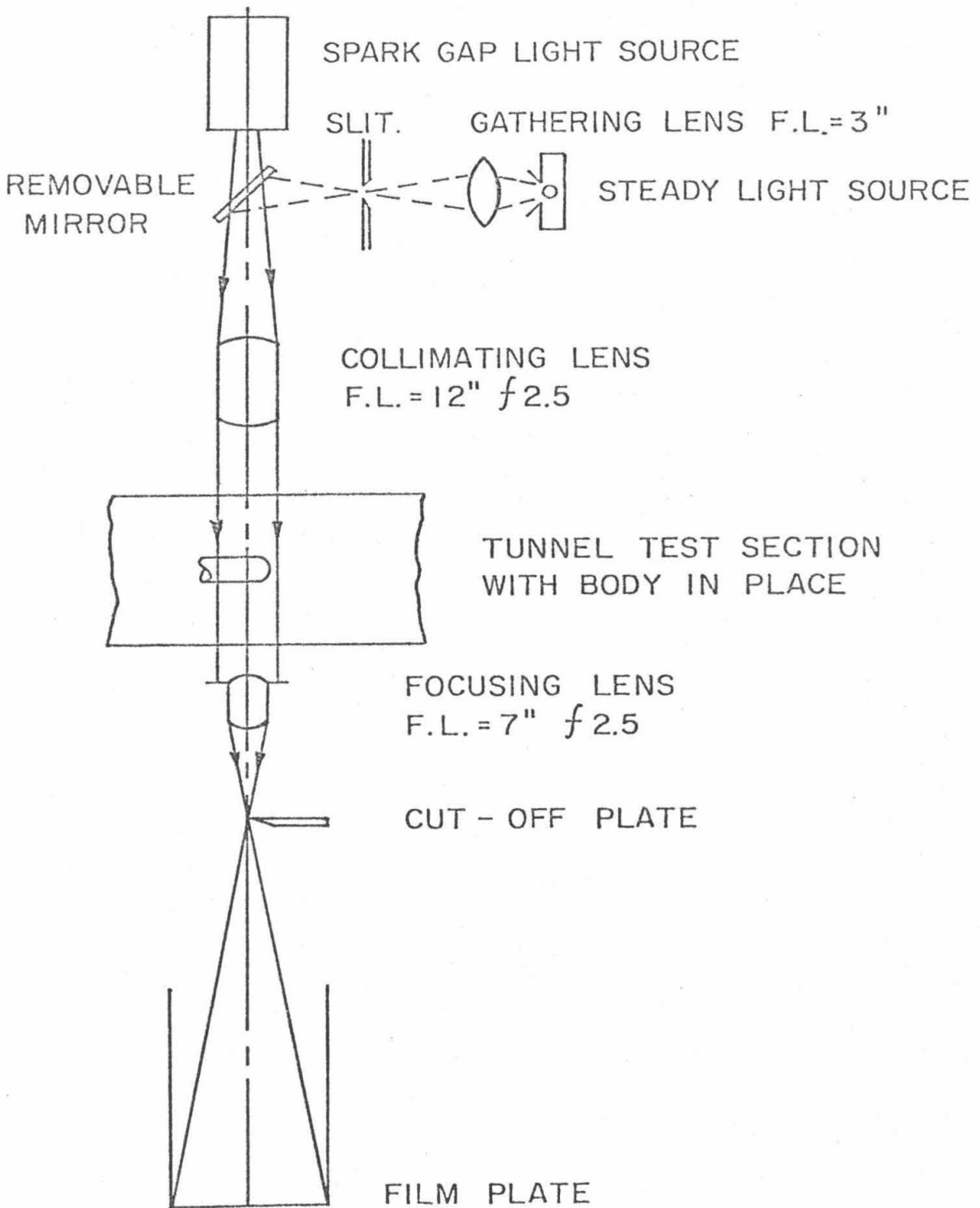


Fig. 16. Schematic diagram of the schlieren flow visualization system.

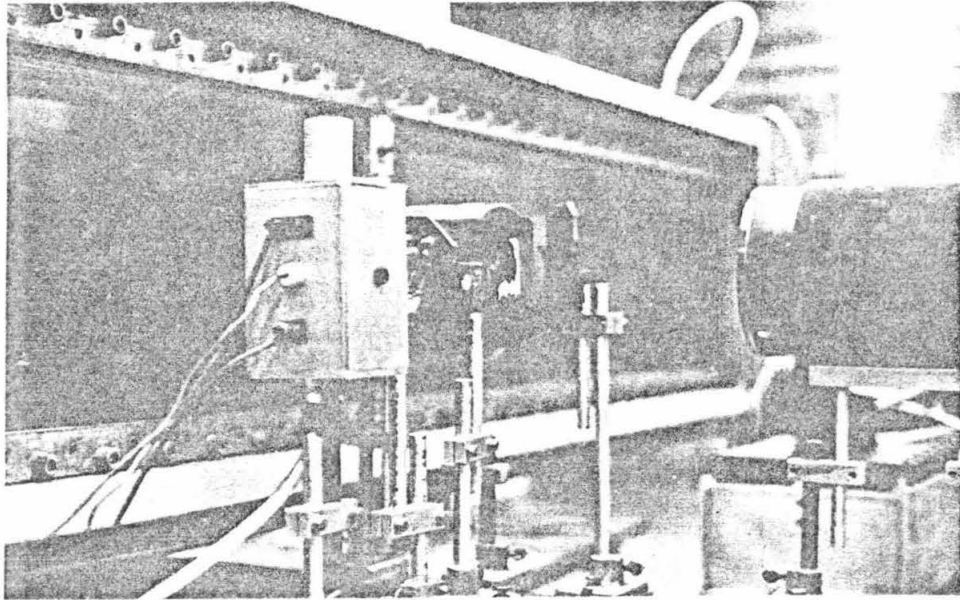


Fig. 17. Photograph of the schlieren light sources. The silver box is a Hg arc lamp used for steady observation. The removable mirror reflects the light along the optical axis of the schlieren system. The black cylinder in the right of the photograph is the spark gap light source.

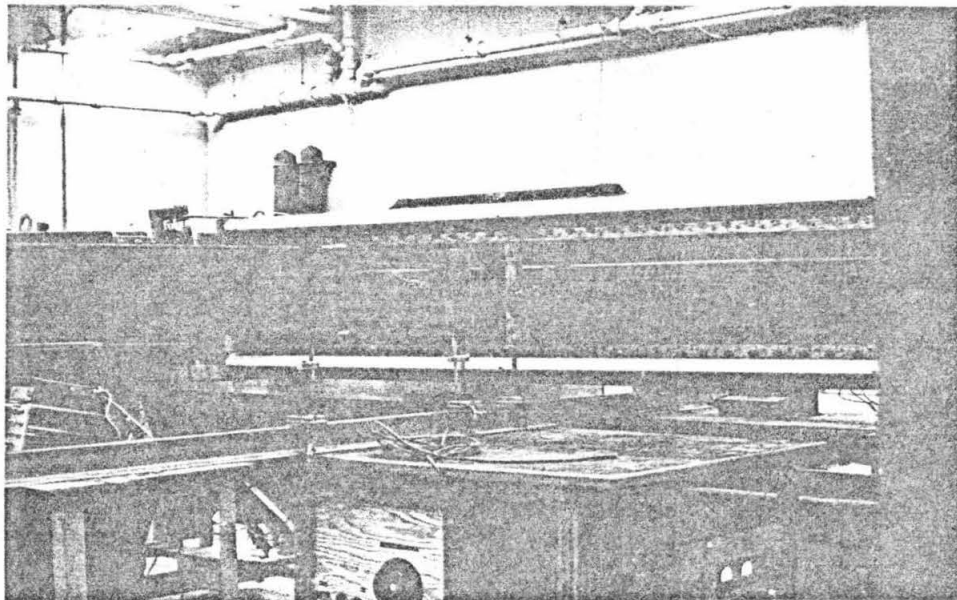


Fig. 18. The camera side of the schlieren system. The lens simultaneously focuses the collimated beam on the knife edge and the image of the model on the film. The camera box is about 80 inches long giving an overall magnification of about 8 times.

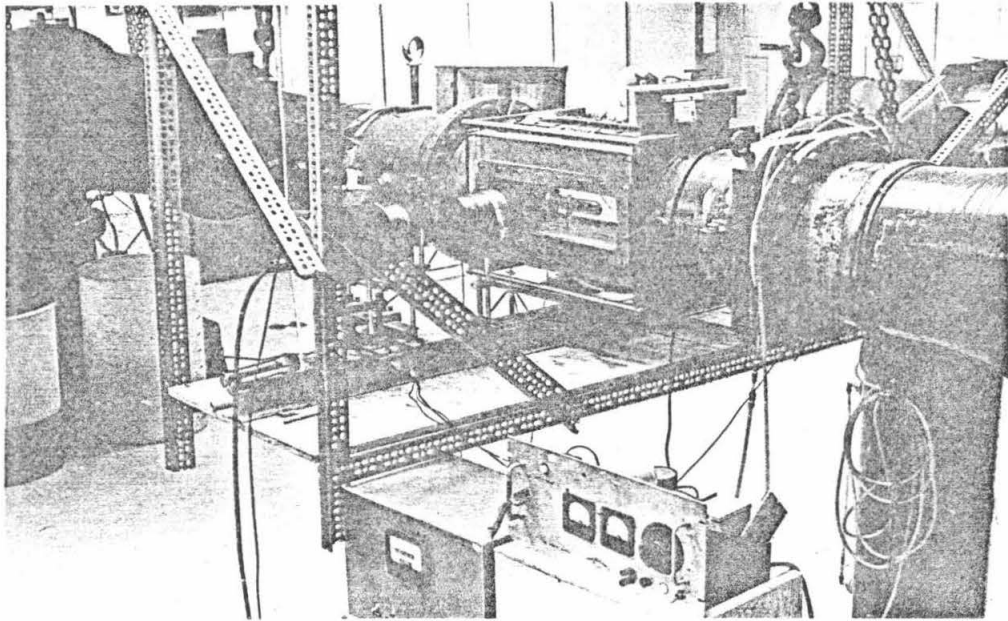


Fig. 19. Light source side of schlieren system mounted at HSWT.

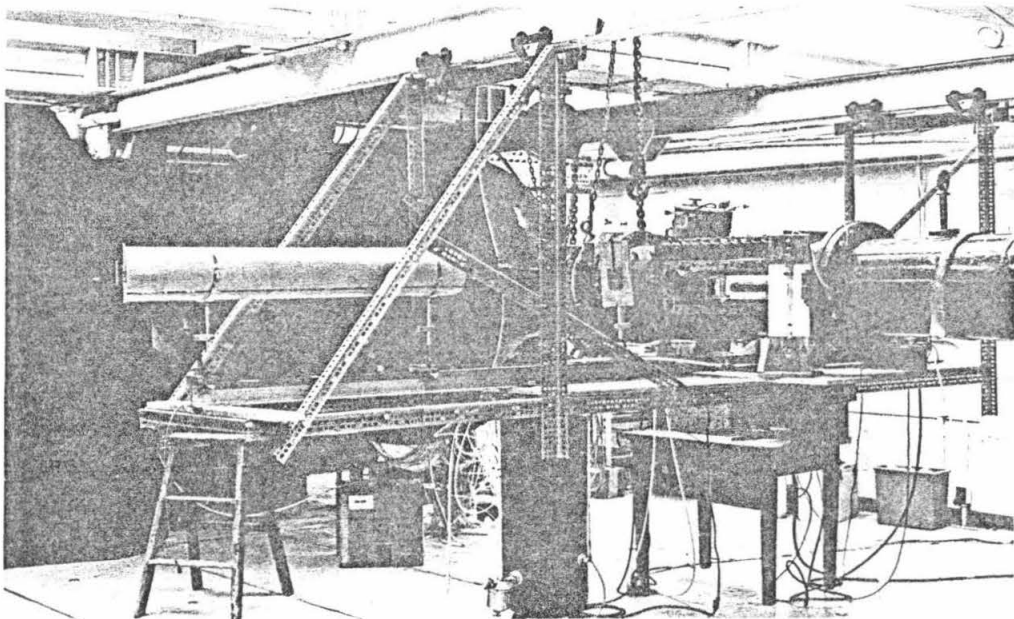


Fig. 20. Camera side of schlieren system mounted at HSWT. System is suspended from ceiling to isolate it from tunnel vibration.

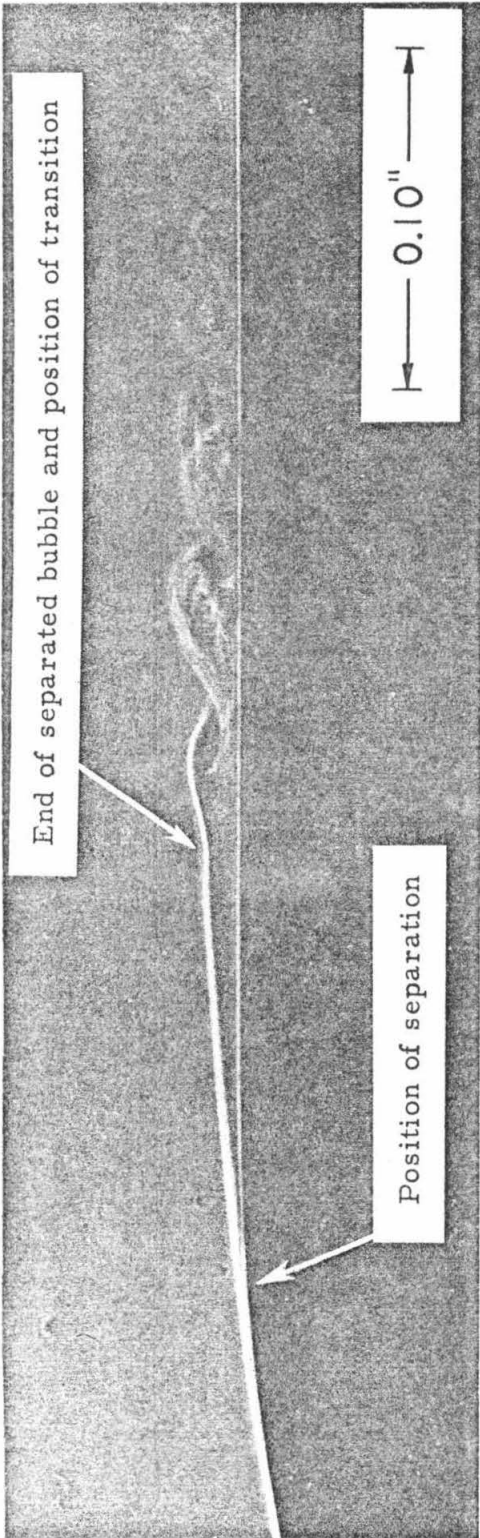


Fig. 21. Example of quality of schlieren photography obtained in LTWT which has flat glass test section windows. Flow is from left to right on hemisphere nose body. $Re_0 = 2.6 \times 10^5$.

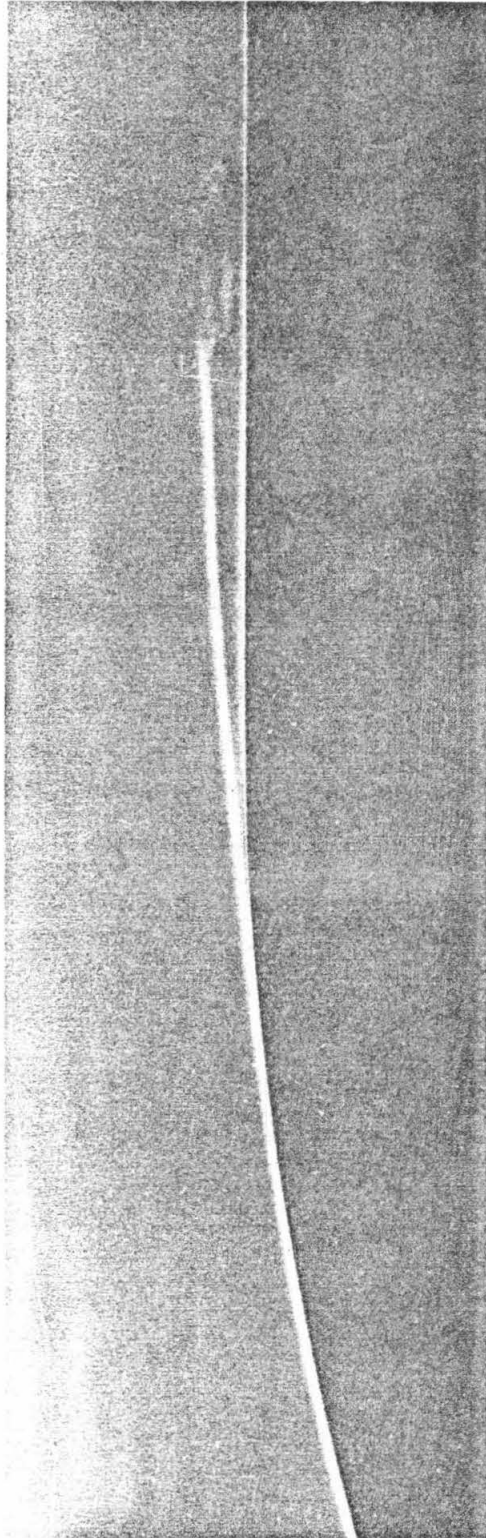


Fig. 22. Example of quality of schlieren photography obtained in HSWT which has curved plexiglass test section windows. Note loss of detail in reattachment zone as compared to Fig. 21. Flow is from left to right on a hemisphere nose body. $Re_0 = 4.2 \times 10^5$.

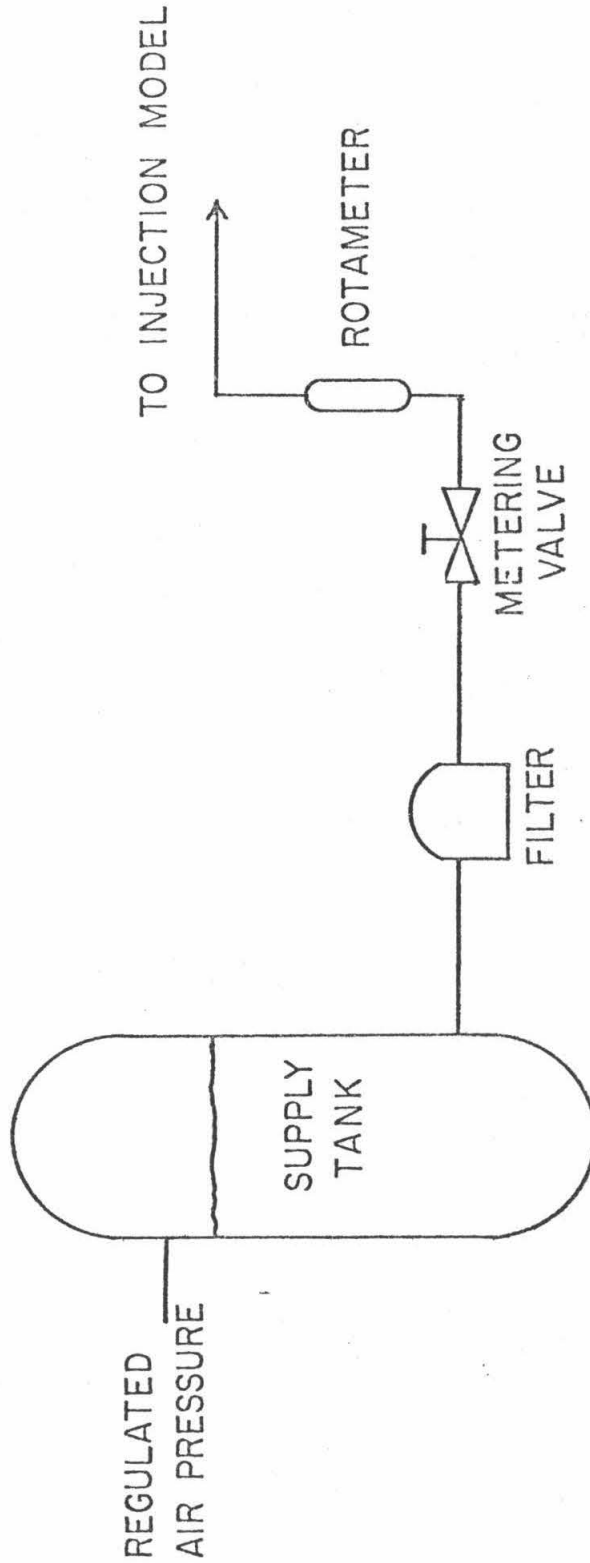


Fig. 23. Schematic diagram of the injection system.

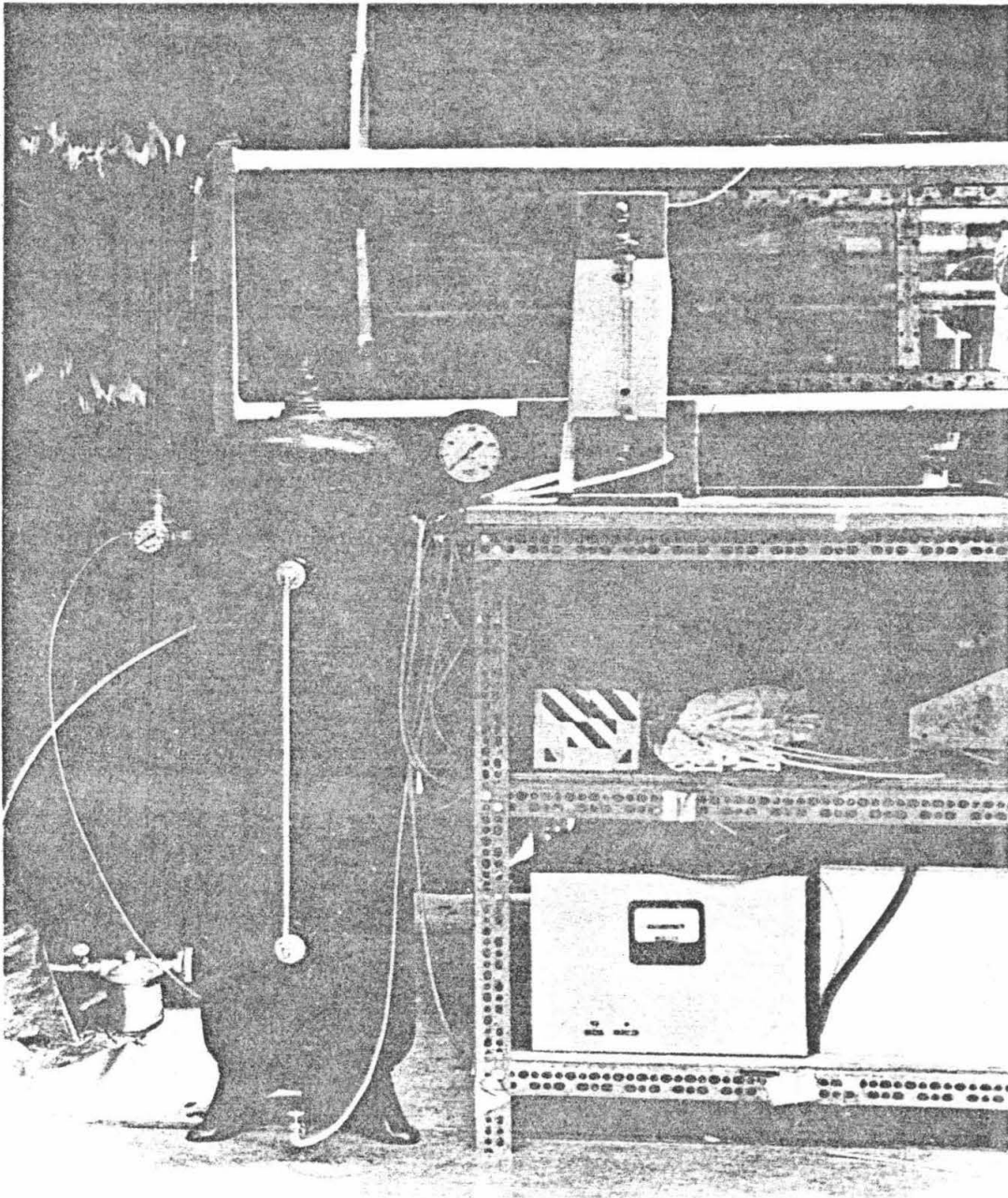


Fig. 24. Photograph of the injection system at the LTWT showing the holding tank and the flowmeter.

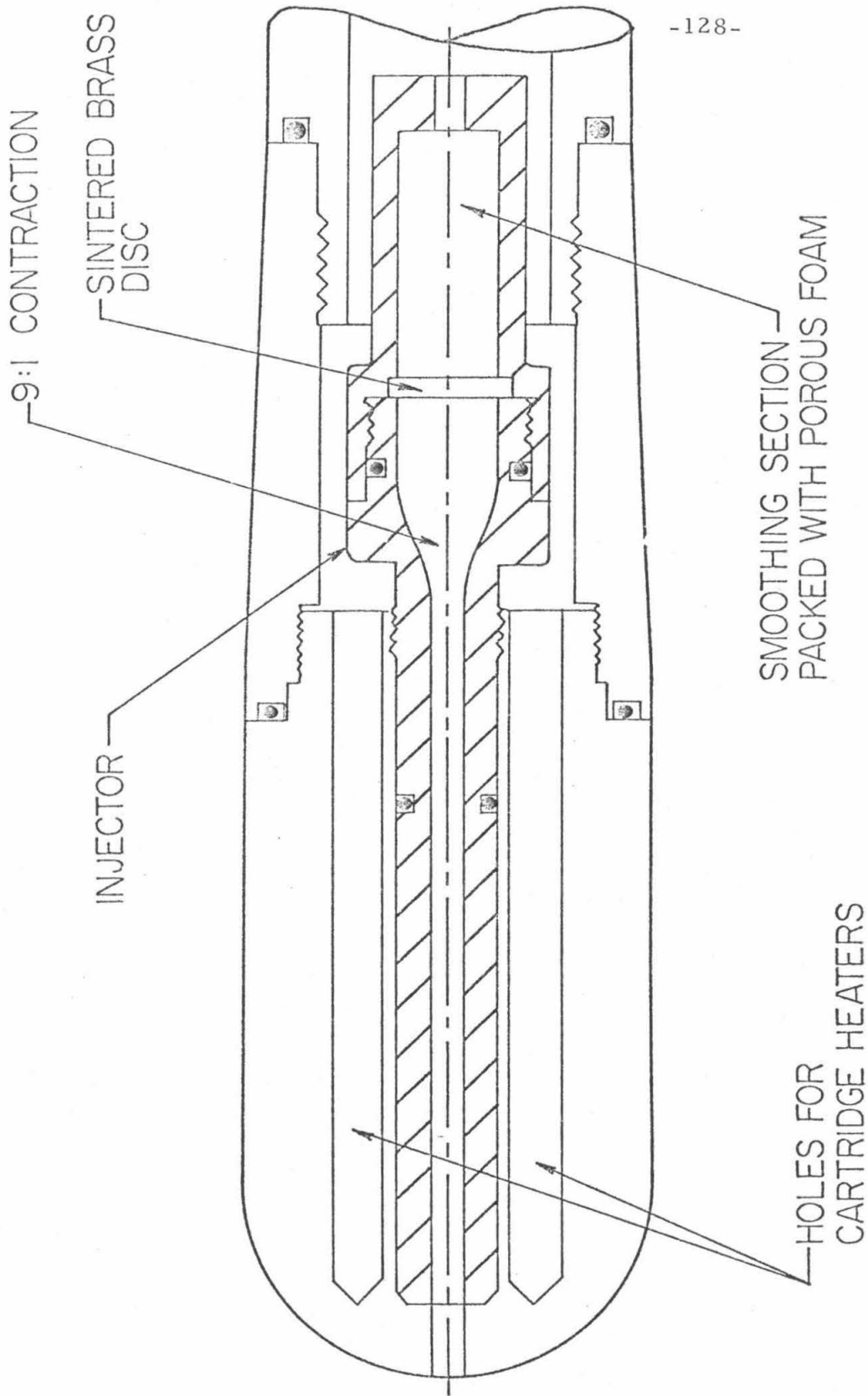


Fig. 25. Schematic drawing showing the injector mounted inside the hemisphere nose body.

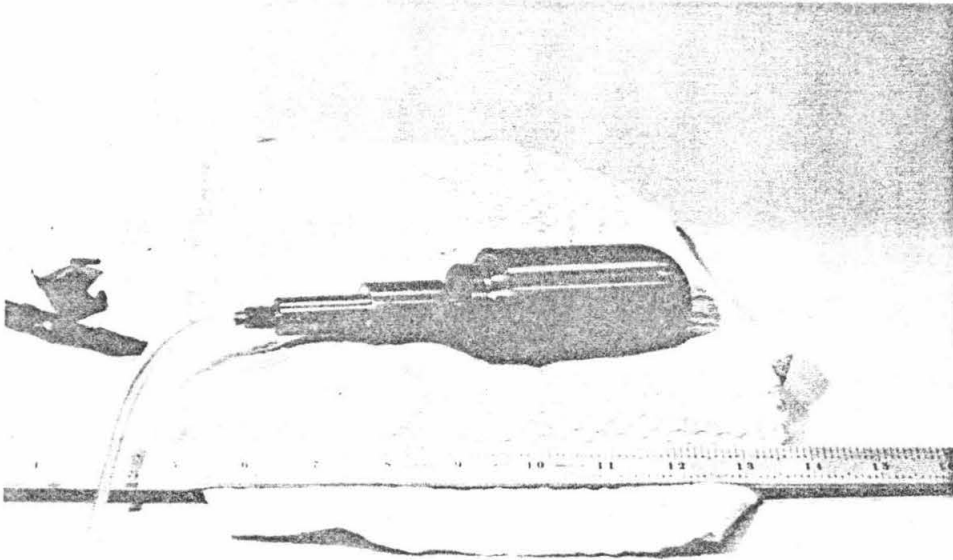


Fig. 26. Photograph of injector installed in hemisphere nose body.

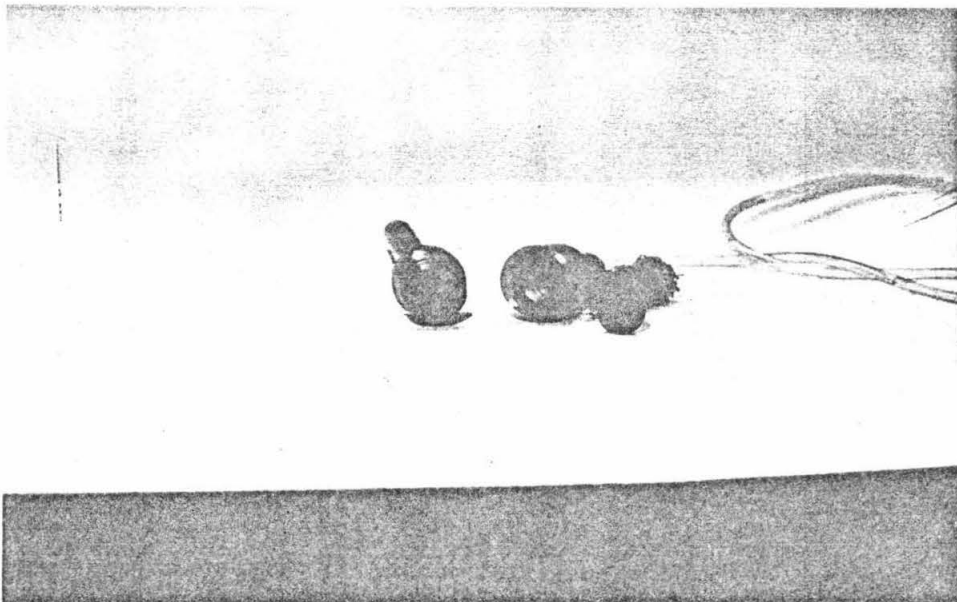


Fig. 27. Photograph of dismantled injector showing porous foam and sintered disc used to help smooth the injection flow.

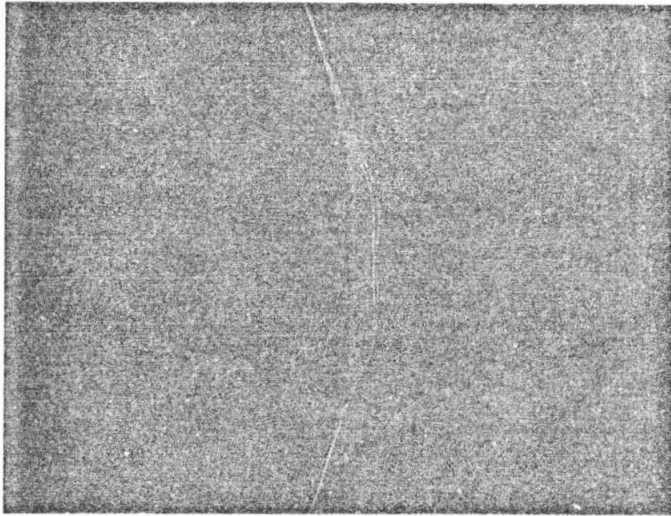


Fig. 28. Schlieren photograph of an example of stable injection of water at stagnation point of hemisphere nose body. $U_1/U_\infty = 0.16$, $U_\infty = 12.2$ feet per second. Freestream flow is from right to left.

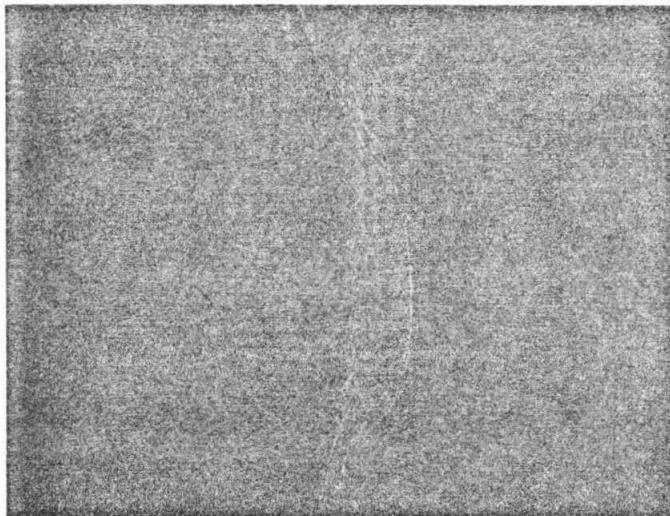
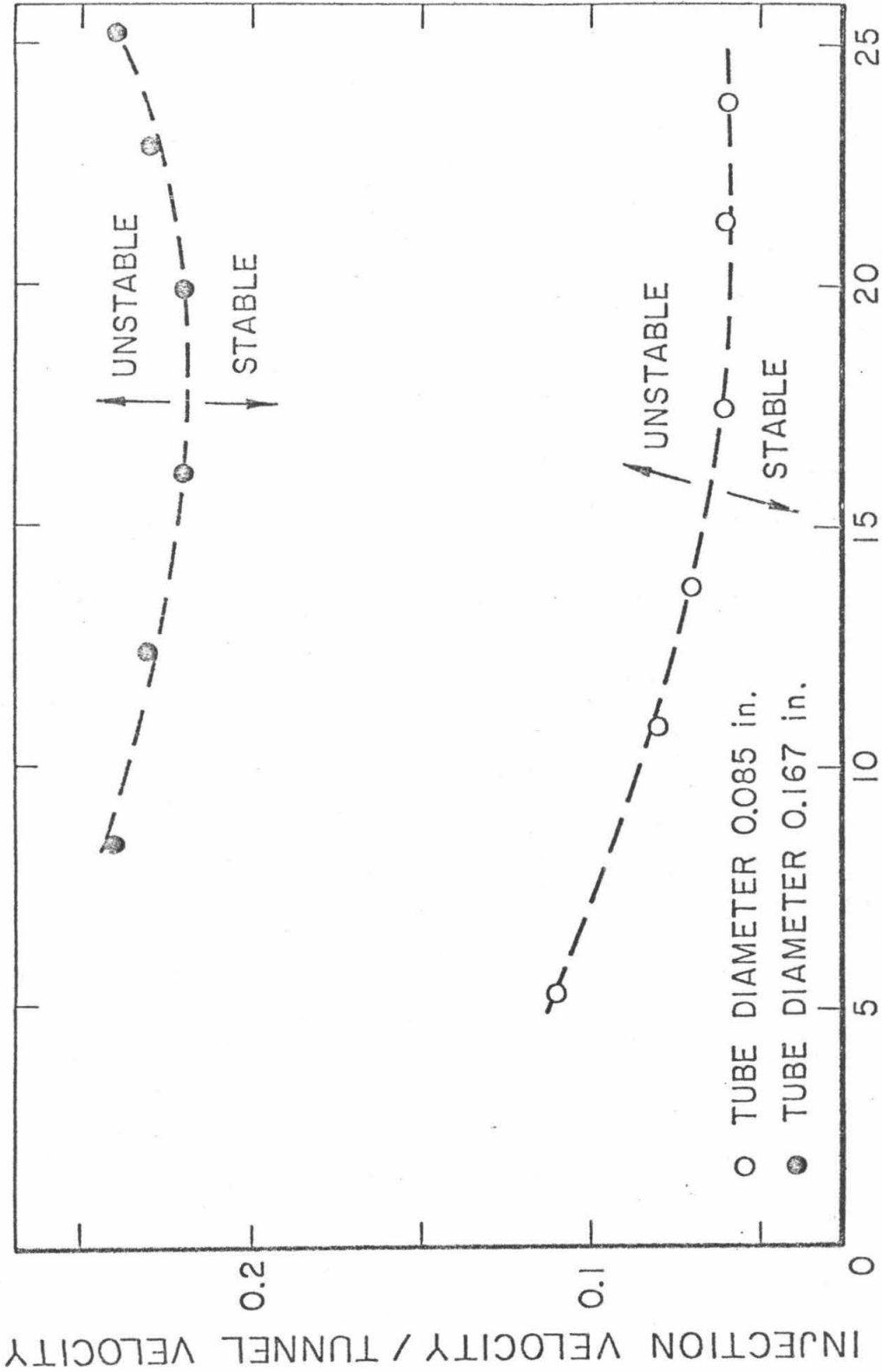


Fig. 29. Schlieren photograph of an example of unstable injection of water at stagnation point of hemisphere nose body. $U_1/U_\infty = 0.29$, $U_\infty = 12.2$ feet per second. Freestream flow is from right to left.



TUNNEL VELOCITY - U , ft/sec

Fig. 30. Plot of the regions of stable and unstable injection with water on the hemisphere nose body for two injection tube diameters.

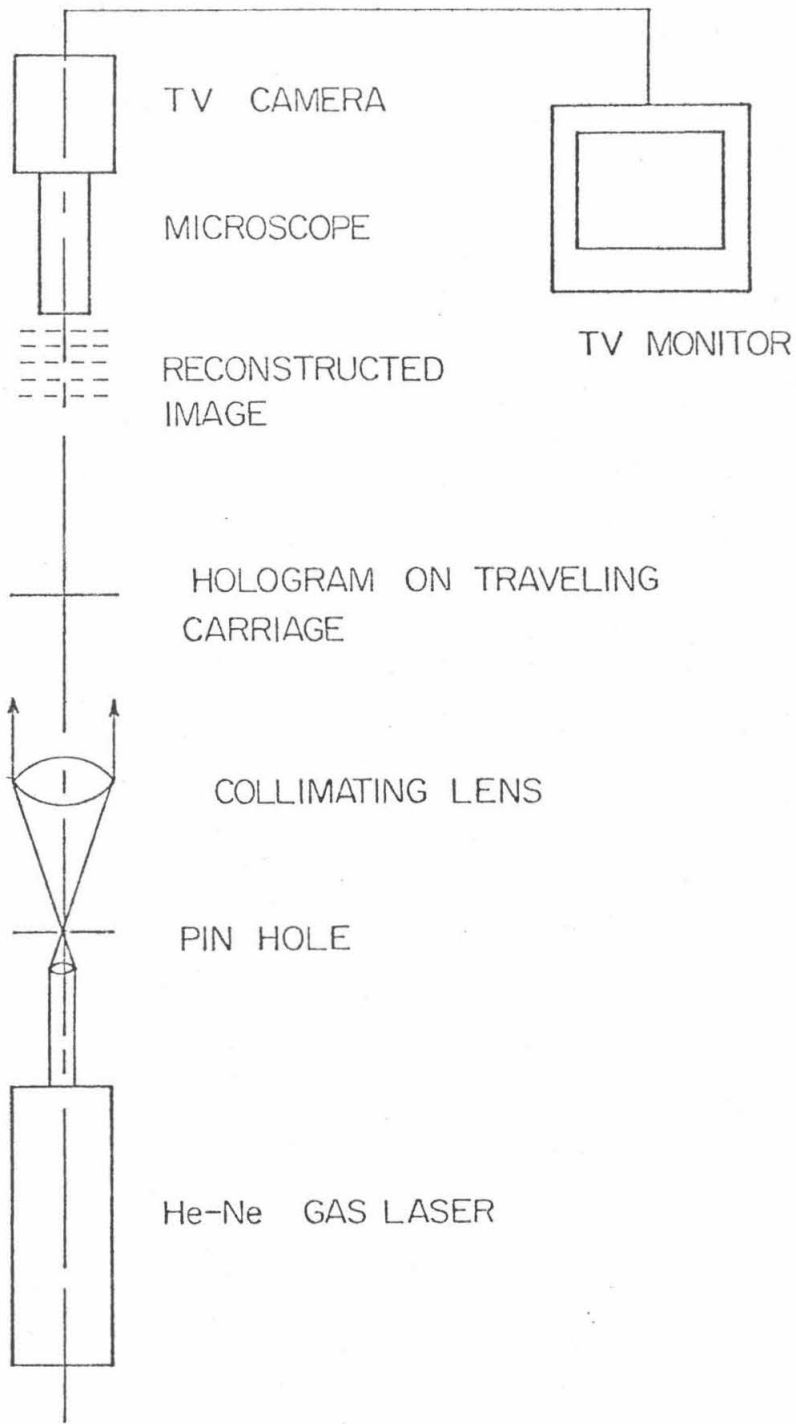
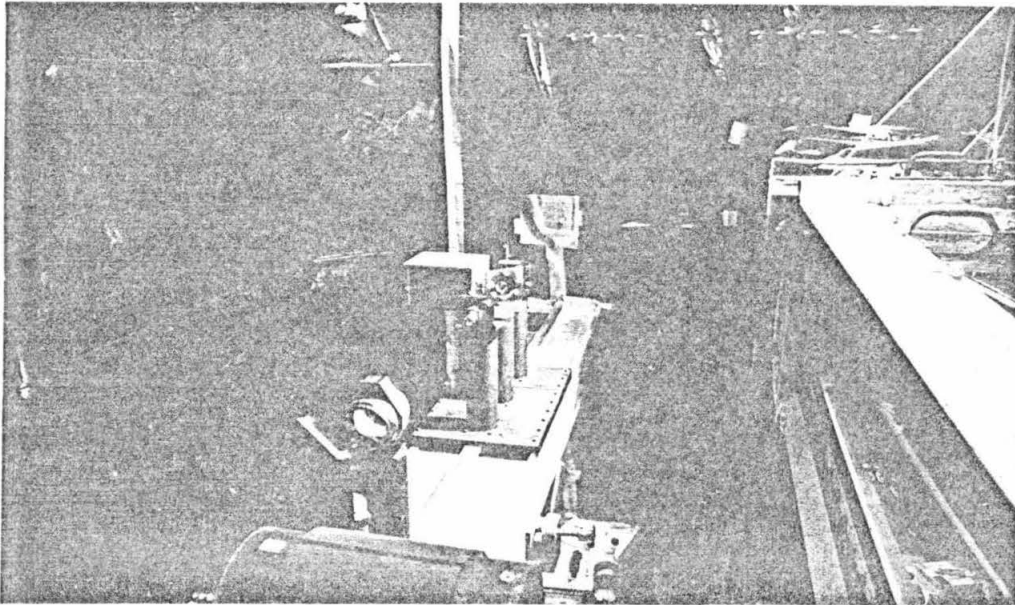
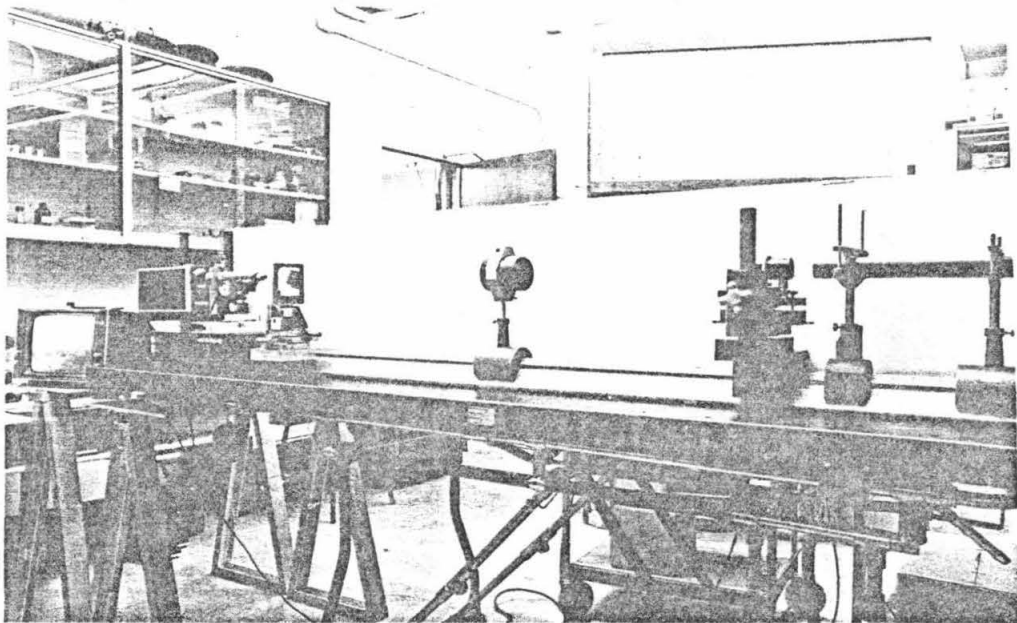


Fig. 32. Schematic drawing of the reconstruction system.

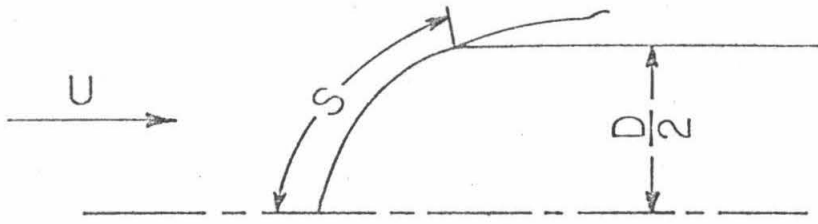


(a)

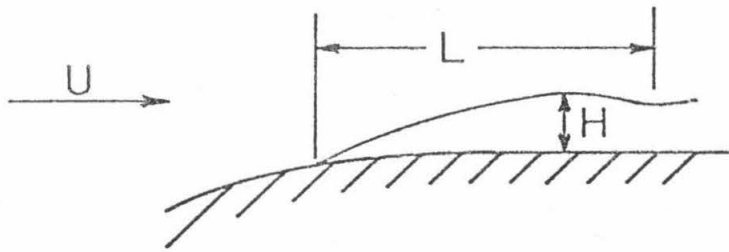


(b)

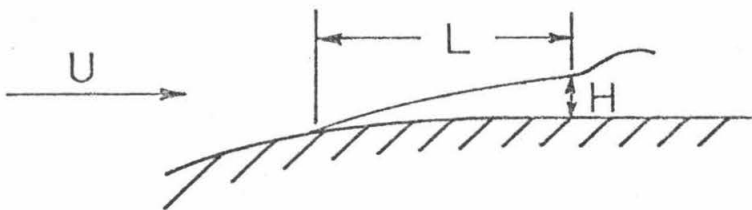
Fig. 33. Photographs of the components of the nuclei counting system. (a) holocamera set-up at the LTWT. (b) the reconstruction system. On the monitor screen can be seen the reconstructed images of some 100μ diameter polystyrene spheres.



(a) POSITION OF LAMINAR SEPARATION

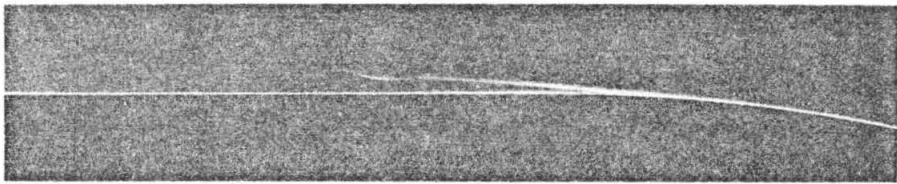


(b) LENGTH AND HEIGHT OF SEPARATED REGION.
TYPE I

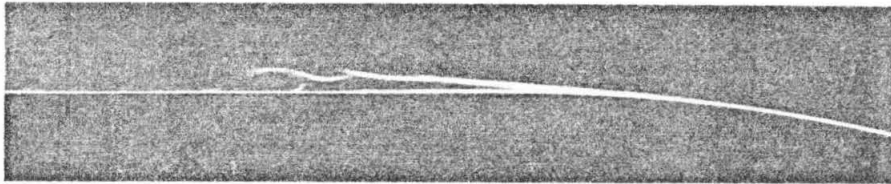


(c) LENGTH AND HEIGHT OF SEPARATION REGION.
TYPE II

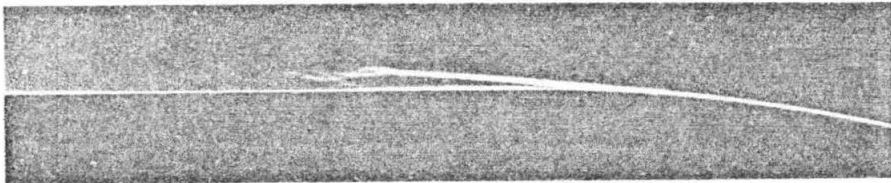
Fig. 34. Schematic drawings showing the definitions of the laminar separation dimensions.



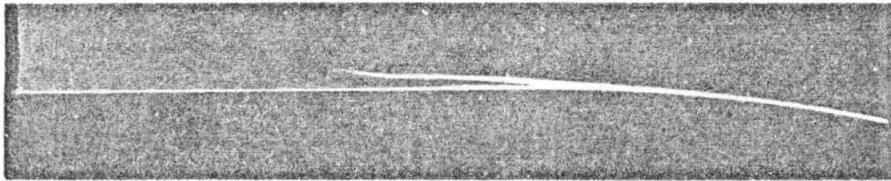
(a)



(b)

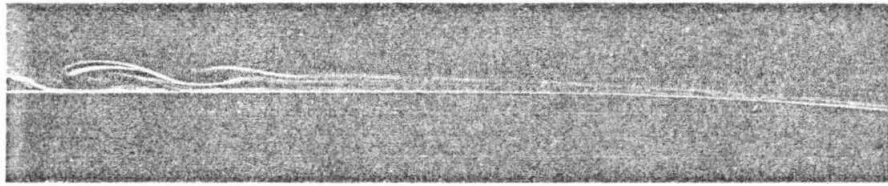


(c)

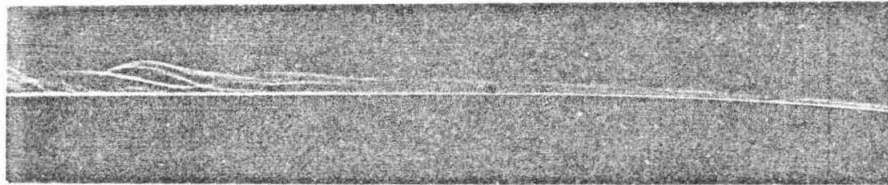


(d)

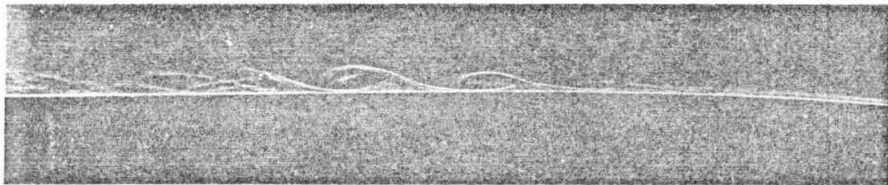
Fig. 35. Effect of freestream turbulence level upon laminar separation on hemisphere nose body. Flow is from right to left. $Re_D = 2.6 \times 10^5$.
(a) $u'/U = 0.05\%$
(b) $u'/U = 1.2\%$
(c) $u'/U = 2.3\%$
(d) $u'/U = 3.6\%$



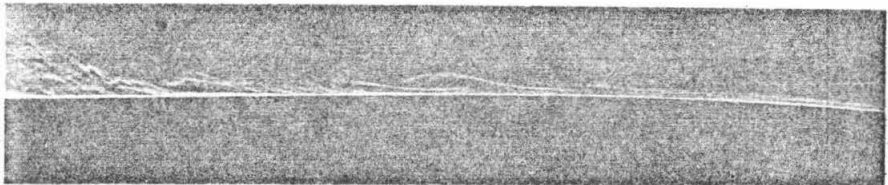
(a)



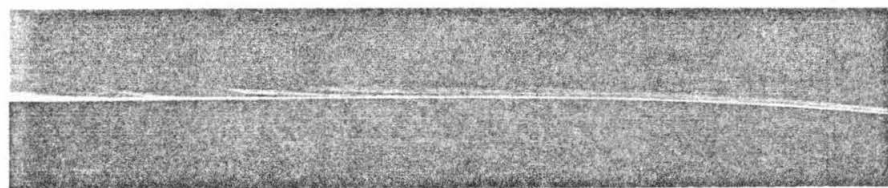
(b)



(c)



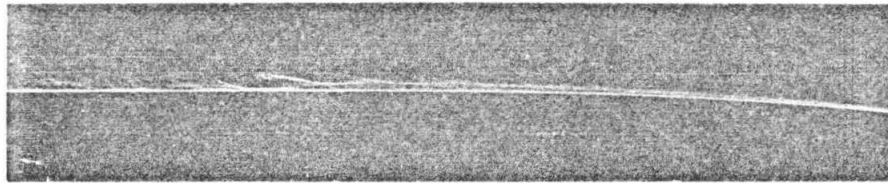
(d)



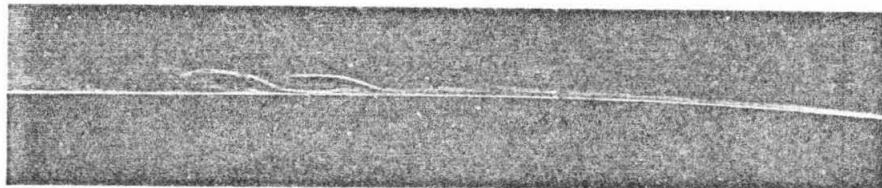
(e)

Fig. 36 Effect of freestream turbulence level on the laminar separation on the NSRDC body. Flow is from right to left. $Re_0 = 1.6 \times 10^5$.

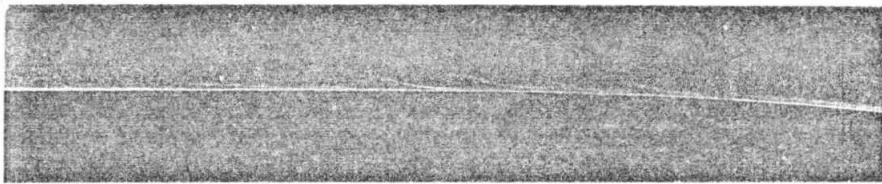
- (a) $u'/U = 0.05\%$
- (b) $u'/U = 0.65\%$
- (c) $u'/U = 1.1\%$
- (d) $u'/U = 2.3\%$
- (e) $u'/U = 3.6\%$



(a)



(b)



(c)



(d)



(e)

Fig. 37 Effect of freestream turbulence level upon the laminar separation on the NSRDC body. Flow is from right to left. $Re_0 = 2.5 \times 10^5$.

(a) $u'/U = 0.05\%$

(b) $u'/U = 0.65\%$

(c) $u'/U = 1.1\%$

(d) $u'/U = 2.3\%$

(e) $u'/U = 3.6\%$

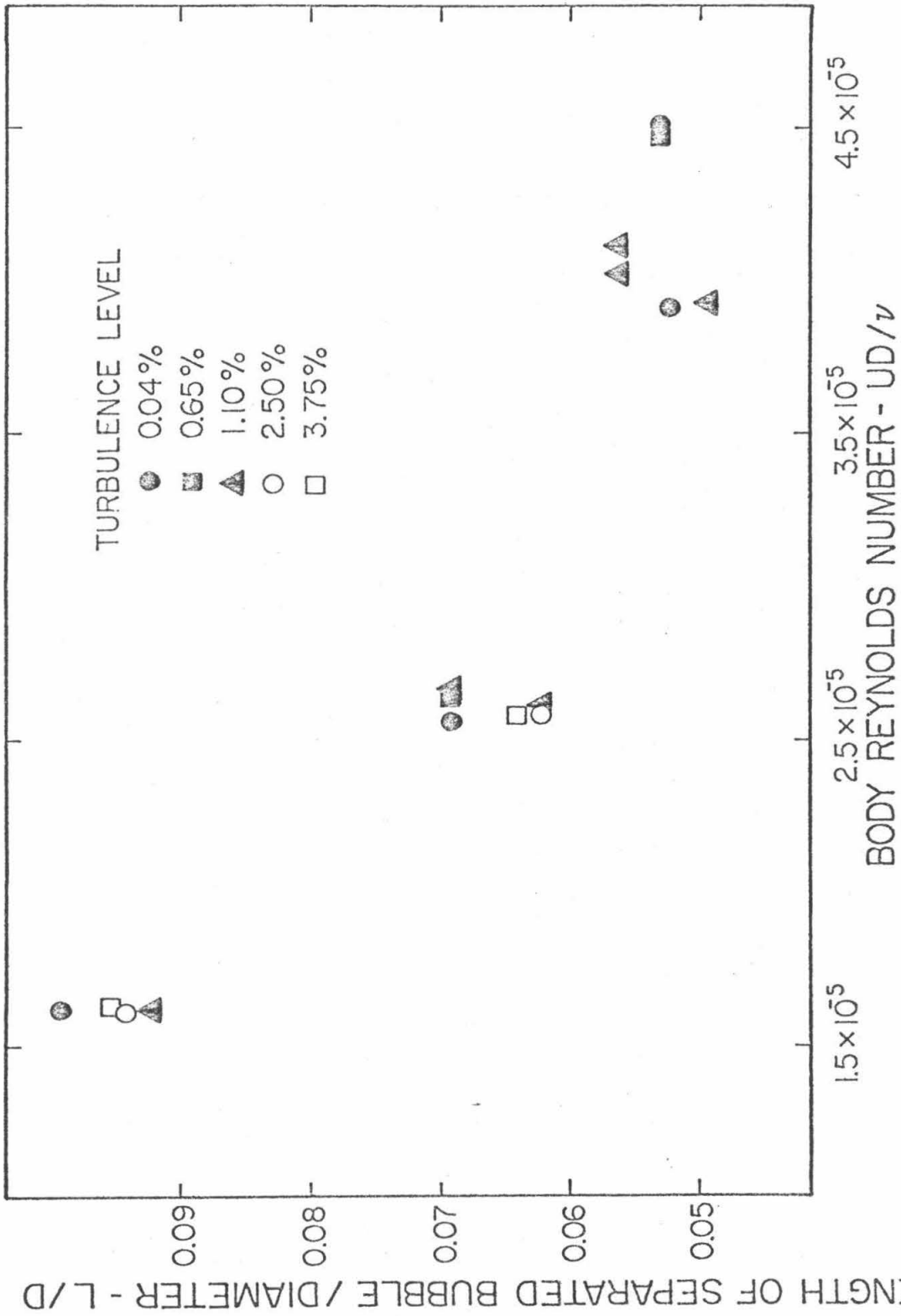


Fig. 38. Effect of freestream turbulence level on the length of the separated region on the hemisphere nose body.

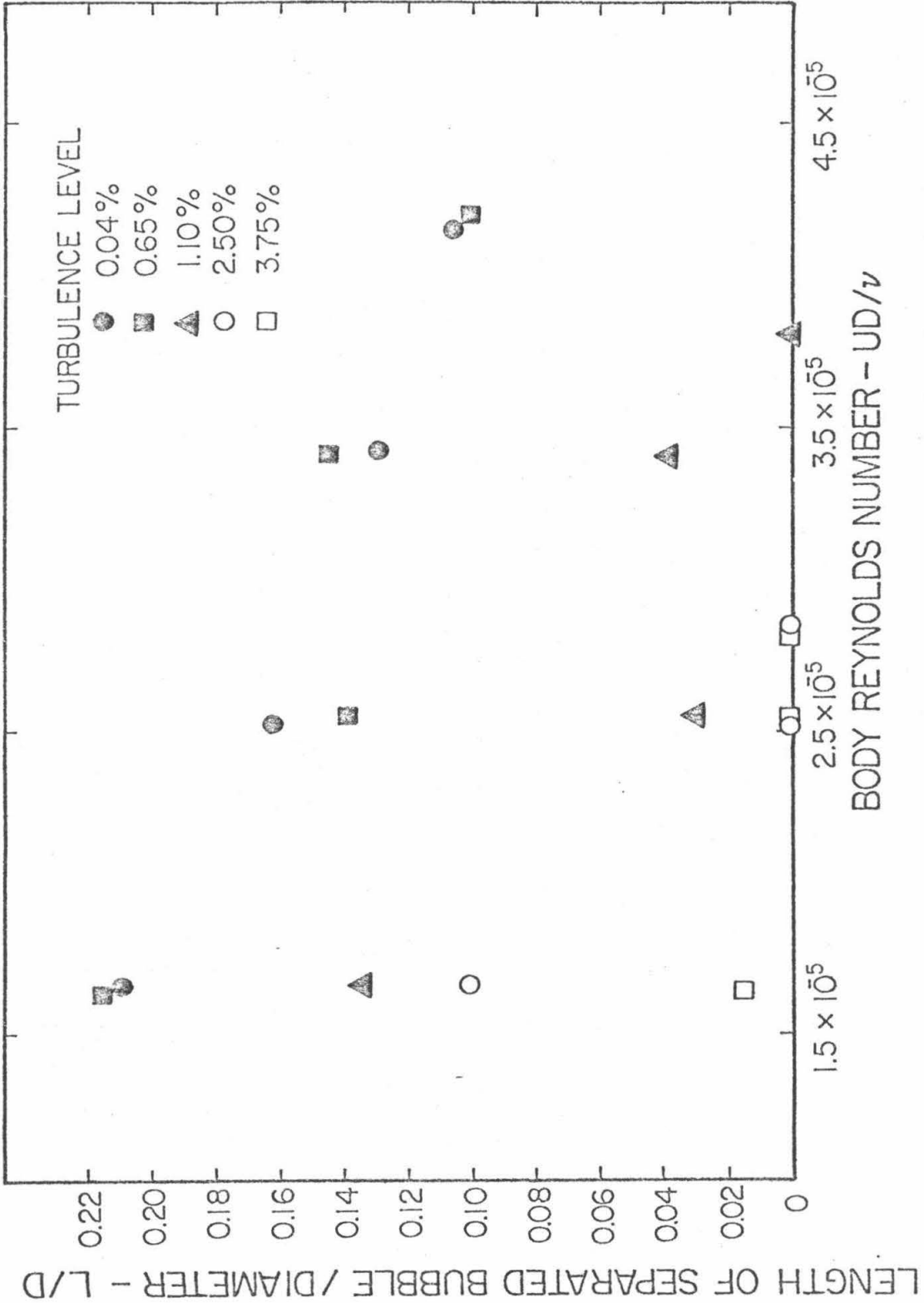


Fig. 39. Effect of freestream turbulence level on the length of the laminar separation on the NSRDC body.

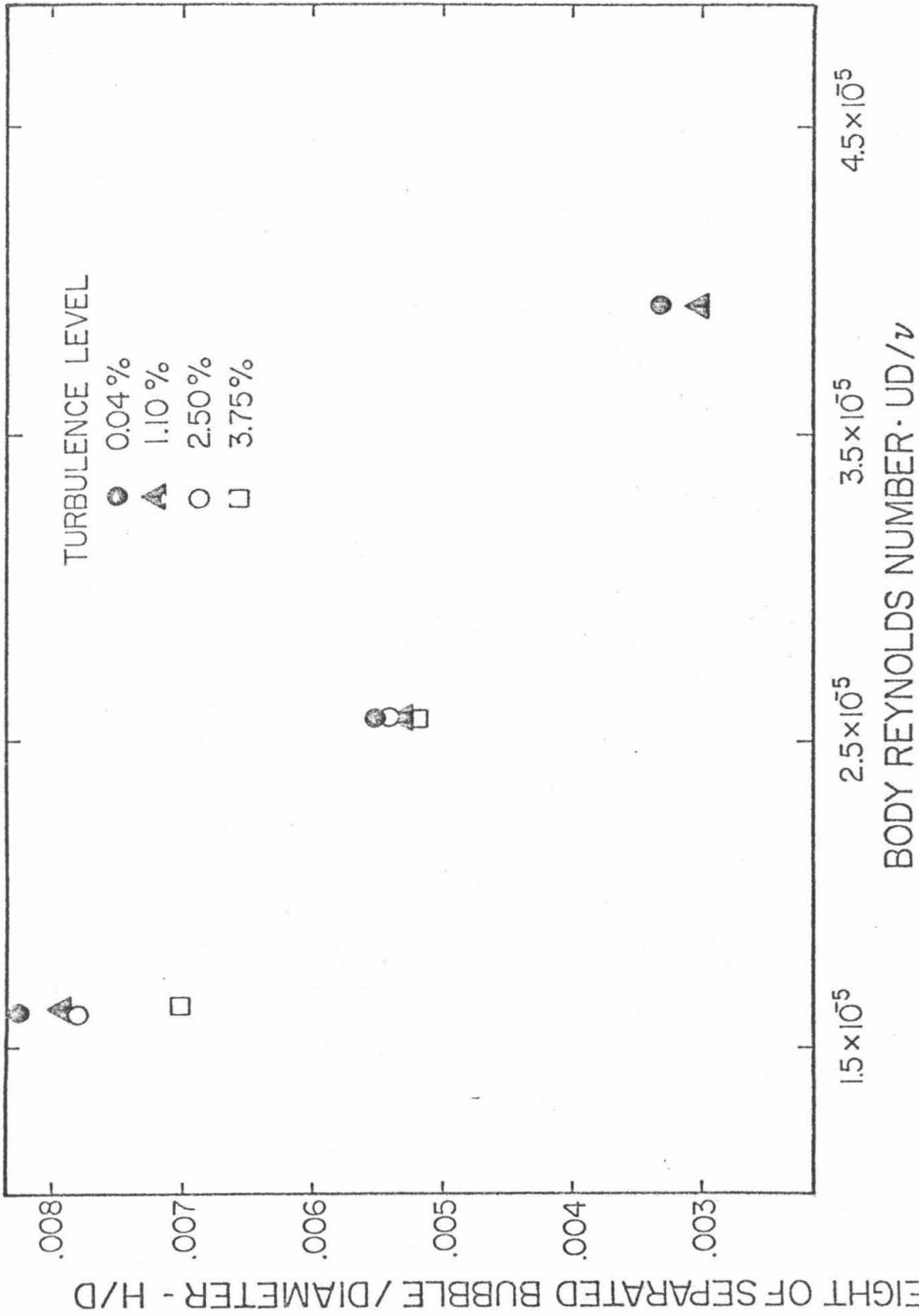


Fig. 40. Effect of freestream turbulence level on the height of the separated region on the hemisphere nose body.

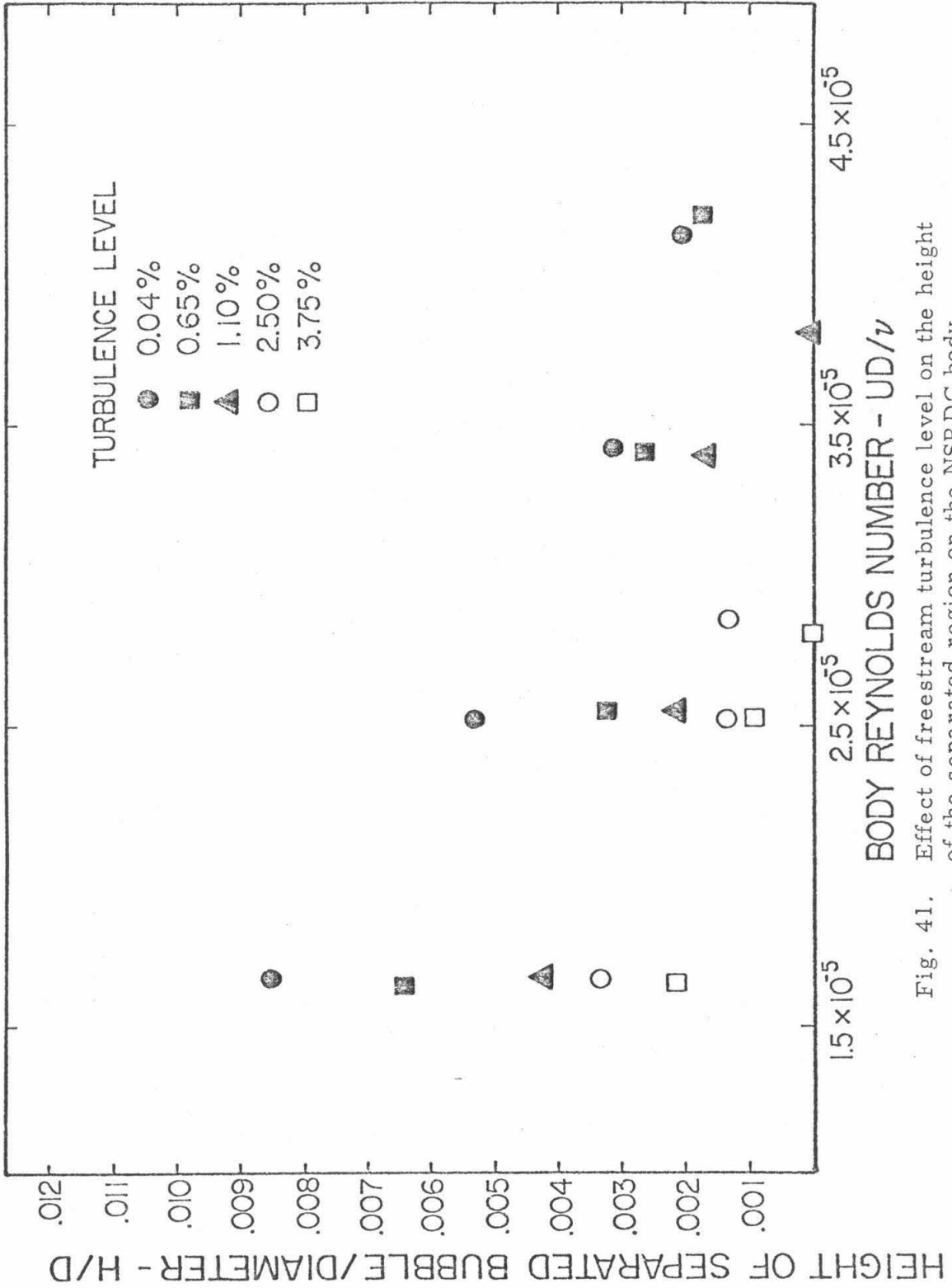


Fig. 41. Effect of freestream turbulence level on the height of the separated region on the NSRDC body.

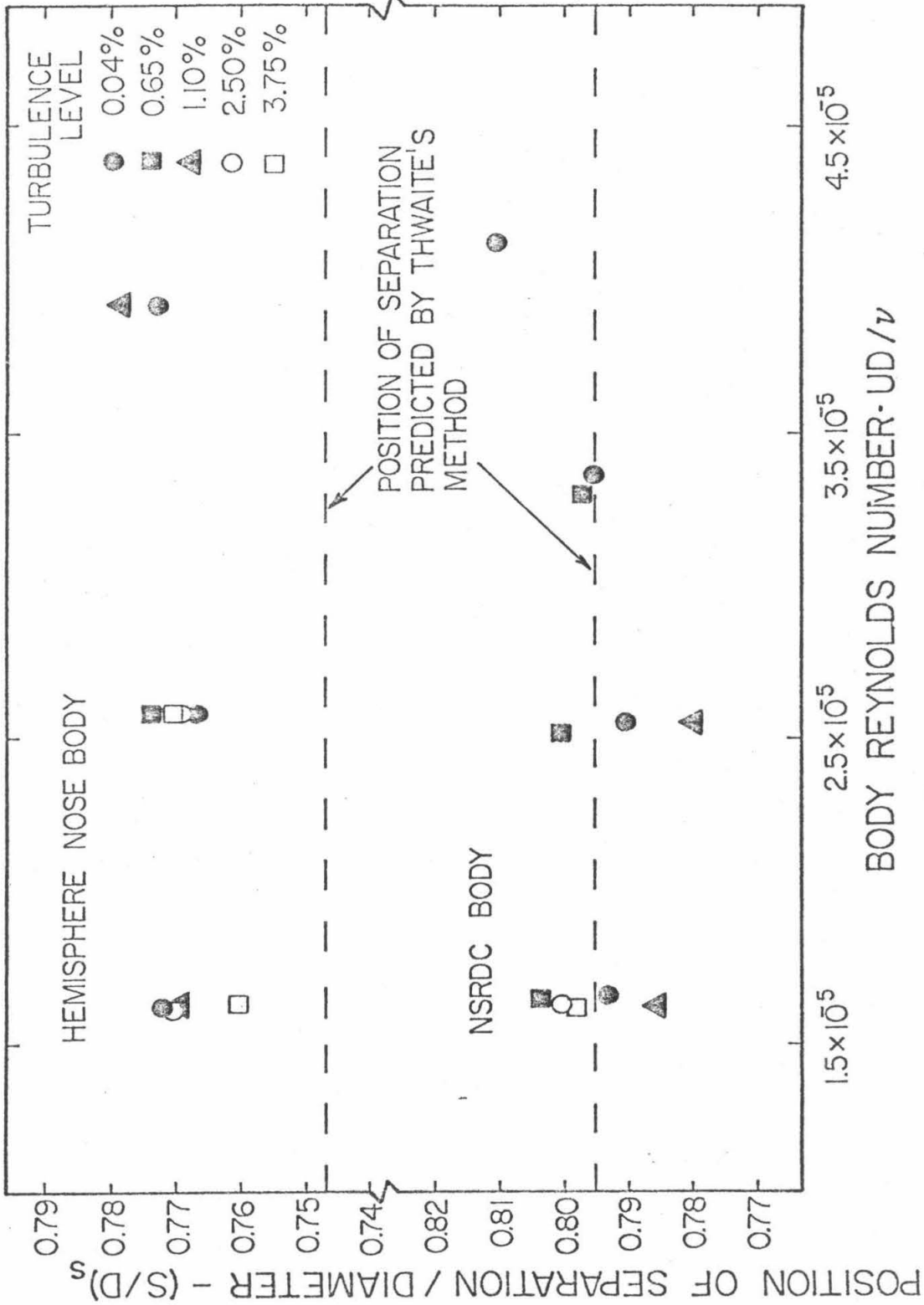


Fig. 42. Effect of freestream turbulence level on the position of separation for both the hemisphere nose body and the NSRDC body.

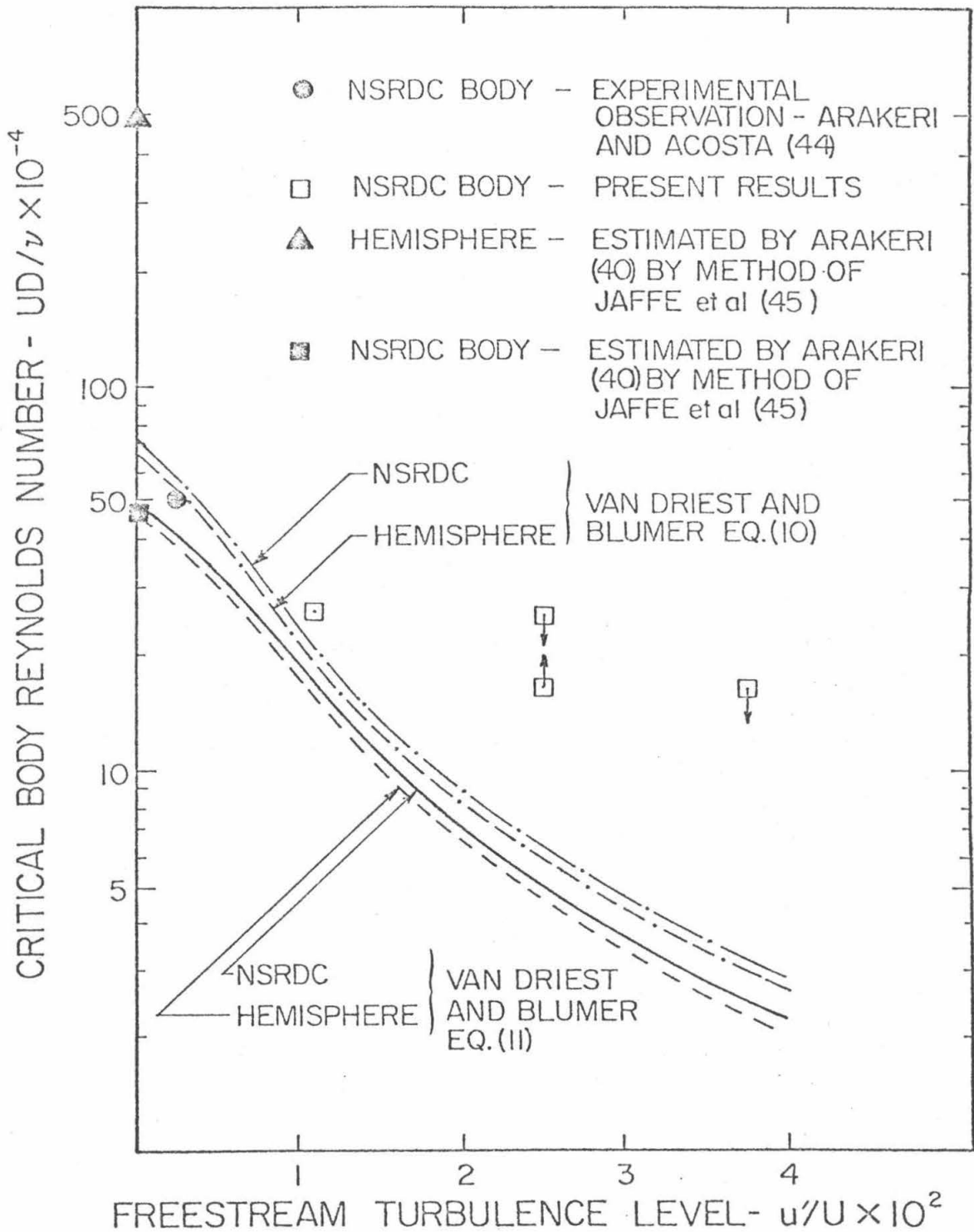
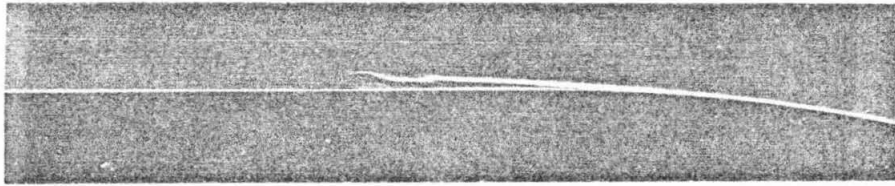
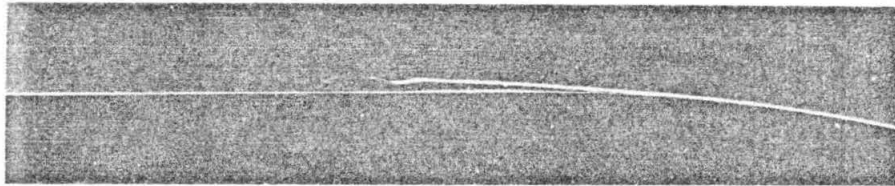


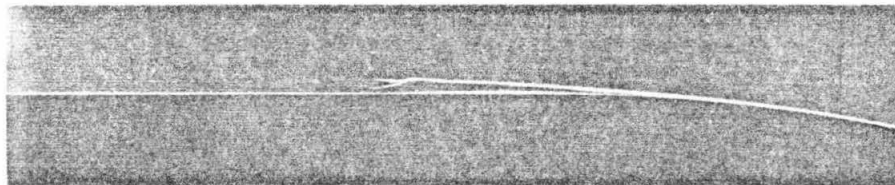
Fig. 43. Comparison of calculated and measured values of the critical Reynolds number for the hemisphere nose and NSRDC bodies.



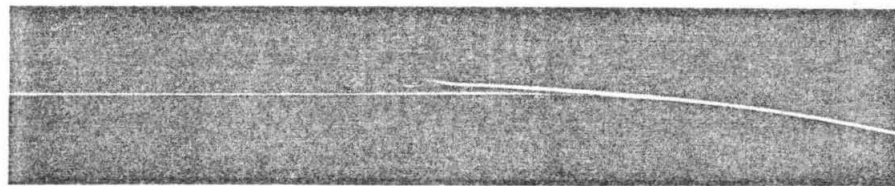
(a)



(b)



(c)

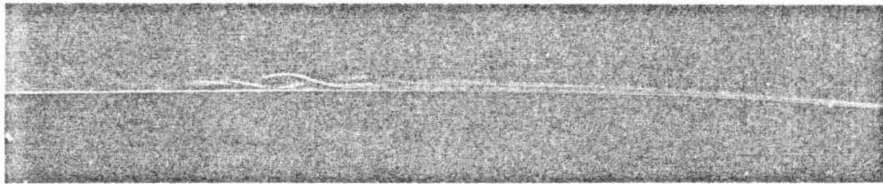


(d)

Fig. 44 Effect of injection of water on the laminar separation on the hemisphere nose body. Flow is from right to left. $Re_D = 3.9 \times 10^5$.
(a) \dot{Q} (injection rate) = 0.0 ml/sec
(b) $\dot{Q} = 3.57$ ml/sec
(c) $\dot{Q} = 8.35$ ml/sec
(d) $\dot{Q} = 13.21$ ml/sec



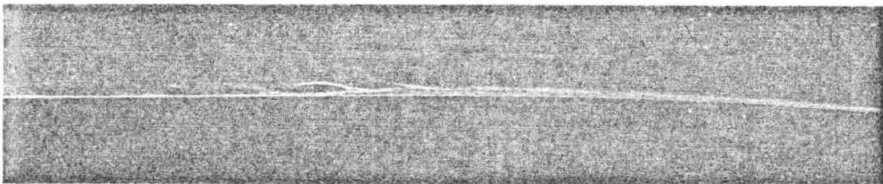
(a)



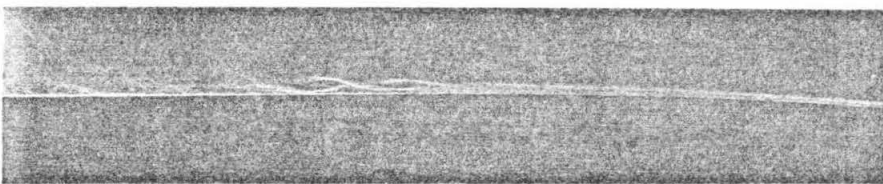
(b)



(c)



(d)



(e)

Fig. 45 Effect of injection of water on the laminar separation on the NSRDC body. Flow is from right to left.

$Re_p = 3.2 \times 10^5$.

(a) \dot{Q} (injection rate) = 0.0 ml/sec

(b) $\dot{Q} = 1.80$ ml/sec

(c) $\dot{Q} = 3.60$ ml/sec

(d) $\dot{Q} = 6.60$ ml/sec

(e) $\dot{Q} = 9.80$ ml/sec

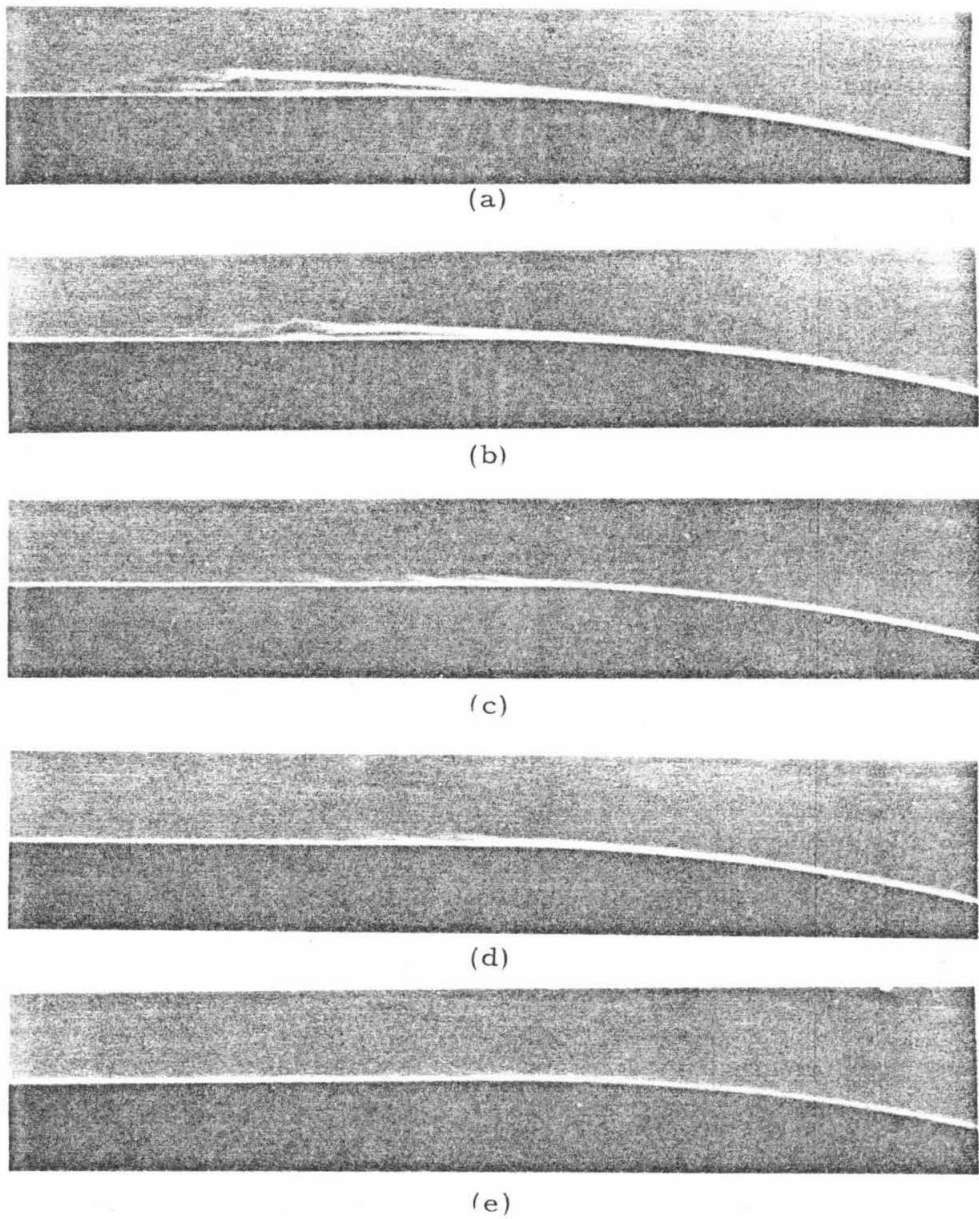


Fig. 46. Effect of injection of Polyox (WSR 301) on the laminar separation on the hemisphere nose body. Flow is from right to left. $Re_D = 4.2 \times 10^5$. Concentration = 500 wppm.

- (a) \dot{Q} (injection rate) = 0.0, $G = 0.0$
- (b) $\dot{Q} = 0.1$ ml/sec, $G = 0.47 \times 10^{-6}$
- (c) $\dot{Q} = 0.3$ ml/sec, $G = 1.40 \times 10^{-6}$
- (d) $\dot{Q} = 0.5$ ml/sec, $G = 2.34 \times 10^{-6}$
- (e) $\dot{Q} = 2.0$ ml/sec, $G = 9.35 \times 10^{-6}$

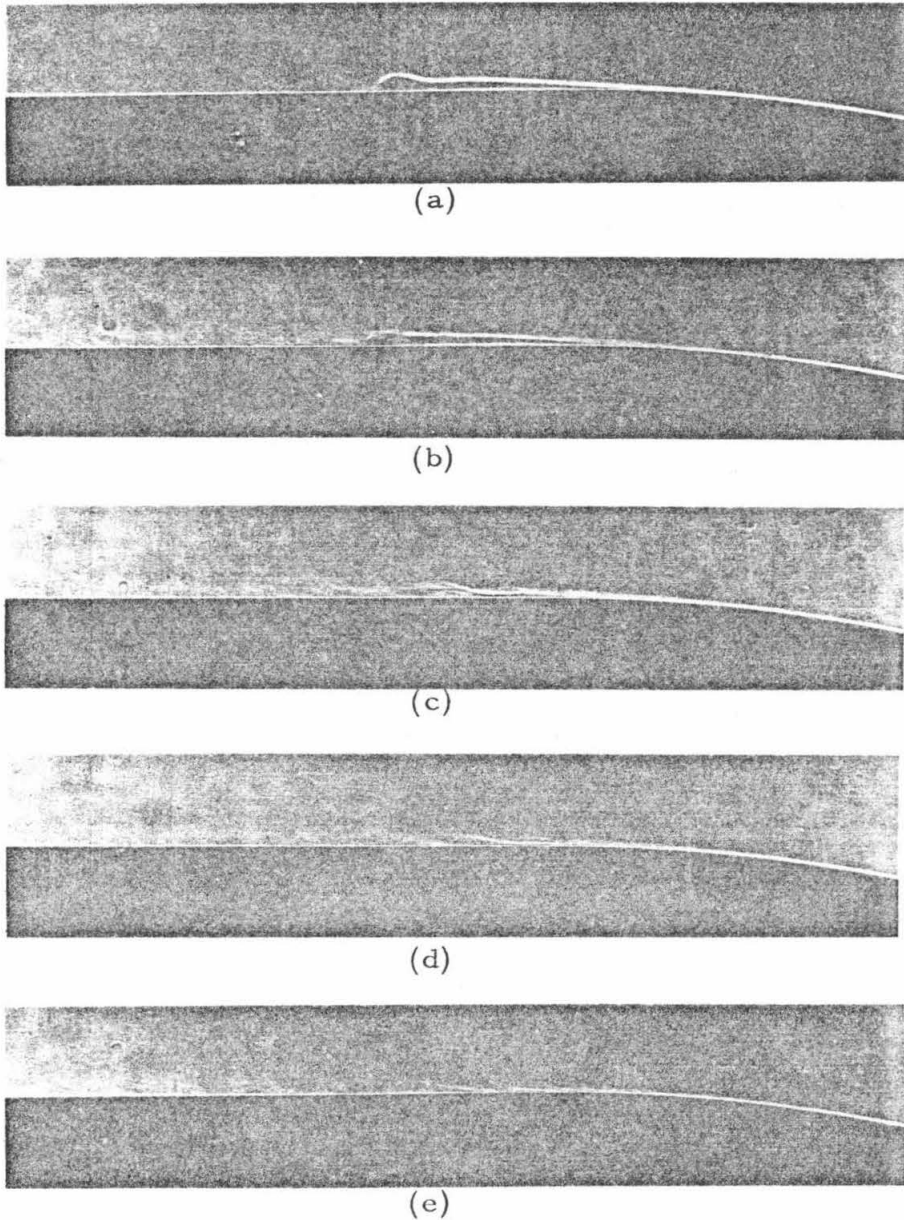


Fig. 47 Effect of injection of Polyox (WSR 301) on the laminar separation on the hemisphere nose body. Flow is from right to left. $Re_D = 3.9 \times 10^5$. Concentration = 100 wppm.

- (a) \dot{Q} (injection rate) = 0.0 ml/sec, $G = 0.0$
- (b) $\dot{Q} = 0.53$ ml/sec, $G = 0.5 \times 10^{-6}$
- (c) $\dot{Q} = 1.10$ ml/sec, $G = 1.1 \times 10^{-6}$
- (d) $\dot{Q} = 1.75$ ml/sec, $G = 1.7 \times 10^{-6}$
- (e) $\dot{Q} = 3.00$ ml/sec, $G = 2.9 \times 10^{-6}$



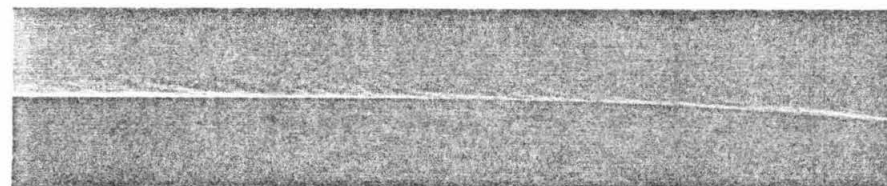
(a)



(b)

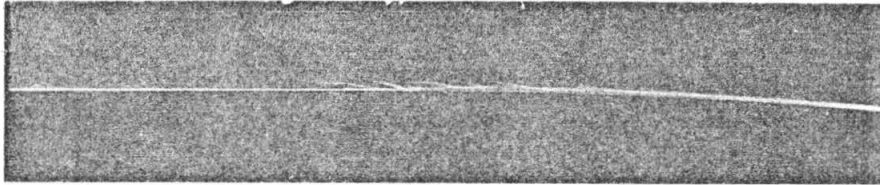


(c)

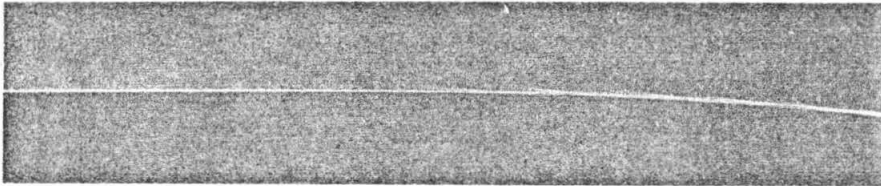


(d)

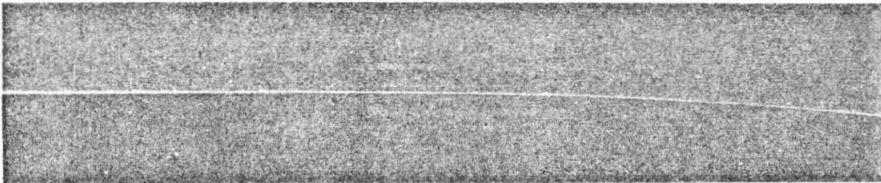
Fig. 48 Effect of injection of Polyox (WSR 301) on the laminar separation on the NSRDC body. Flow is from right to left. $Re_D = 1.6 \times 10^5$. Concentration = 500 wppm.
(a) \dot{Q} (injection rate) = 0.0 ml/sec, $G = 0.0$
(b) $\dot{Q} = 0.1$ ml/sec, $G = 0.5 \times 10^{-6}$
(c) $\dot{Q} = 0.3$ ml/sec, $G = 1.5 \times 10^{-6}$
(d) $\dot{Q} = 0.5$ ml/sec, $G = 2.5 \times 10^{-6}$



(a)



(b)



(c)

Fig. 49 Effects of injection of Polyox (WSR 301) on the laminar separation on the NSRDC body. Flow is from right to left. $Re_D = 3.4 \times 10^5$. Concentration = 500 wppm.
(a) \dot{Q} (injection rate) = 0.0 ml/sec, $G = 0.0$
(b) $\dot{Q} = 0.1$ ml/sec, $G = 0.36 \times 10^{-6}$
(c) $\dot{Q} = 0.3$ ml/sec, $G = 1.08 \times 10^{-6}$

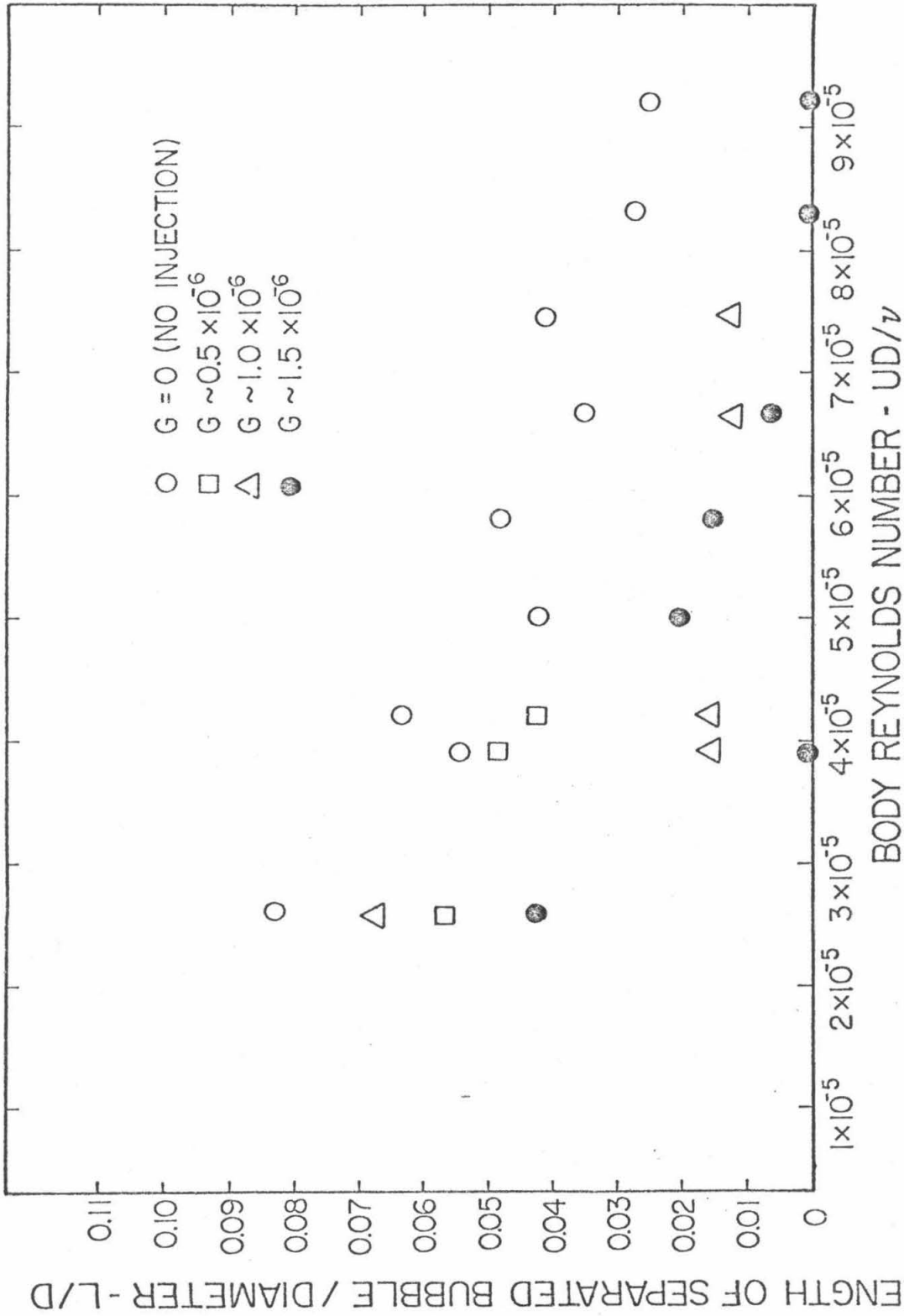


Fig. 50. Effect of injection of Polyox (WSR 301) on the length of the laminar separation on the hemisphere nose body.

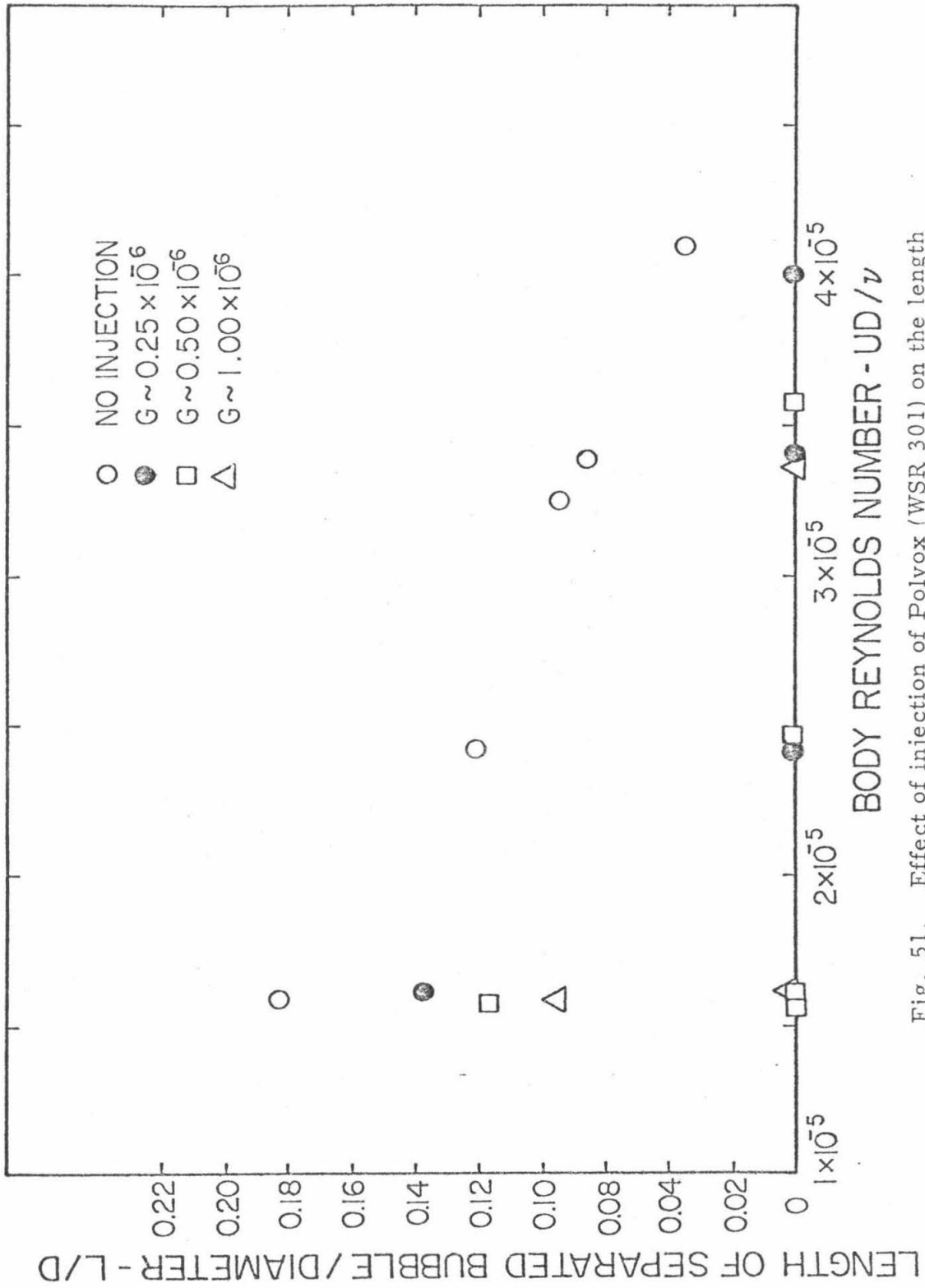


Fig. 51. Effect of injection of Polyox (WSR 301) on the length of the laminar separation on the NSRDC body.

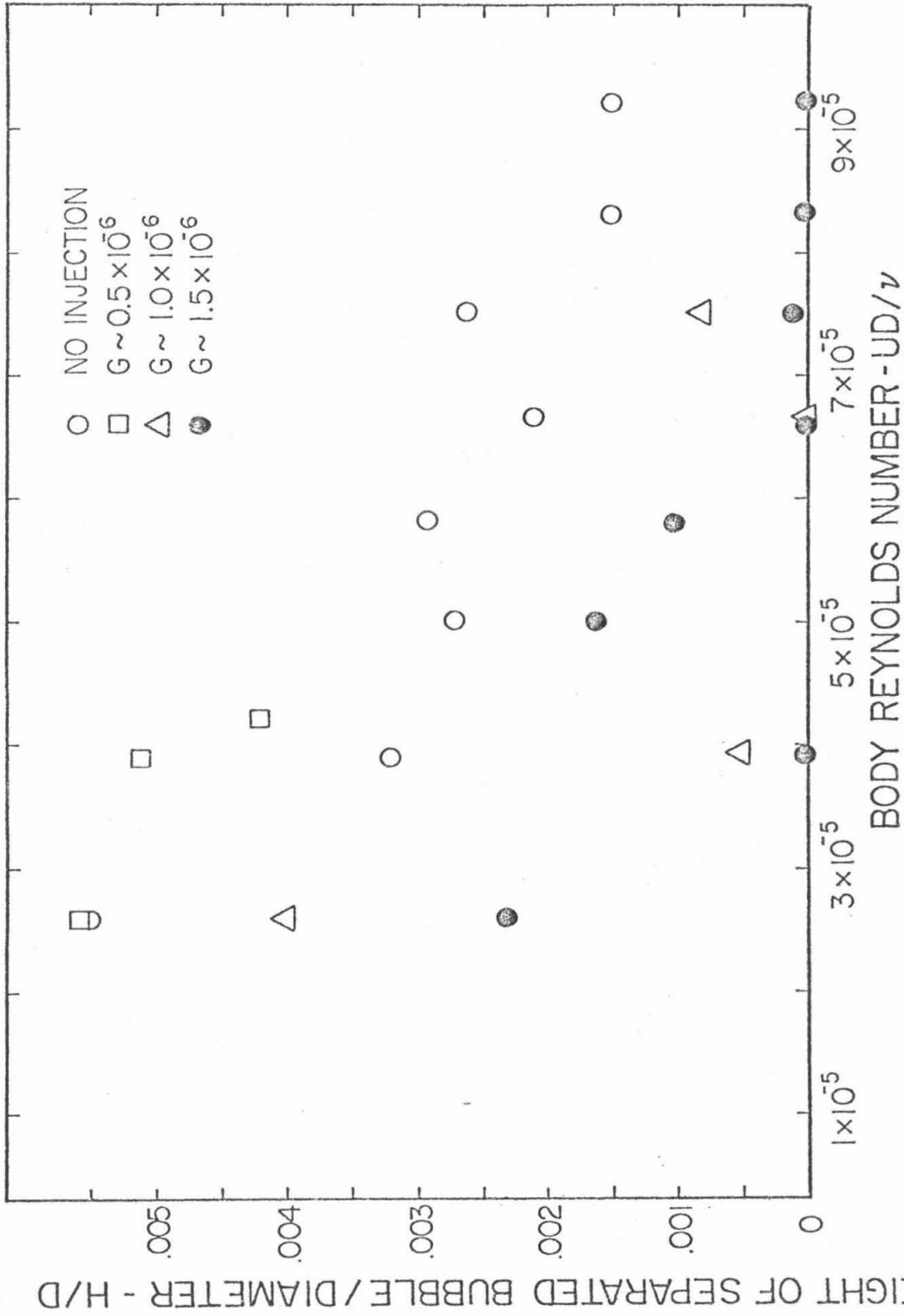


Fig. 52. Effect of injection of Polyox (WSR 301) on the height of the laminar separation on the hemisphere nose body.

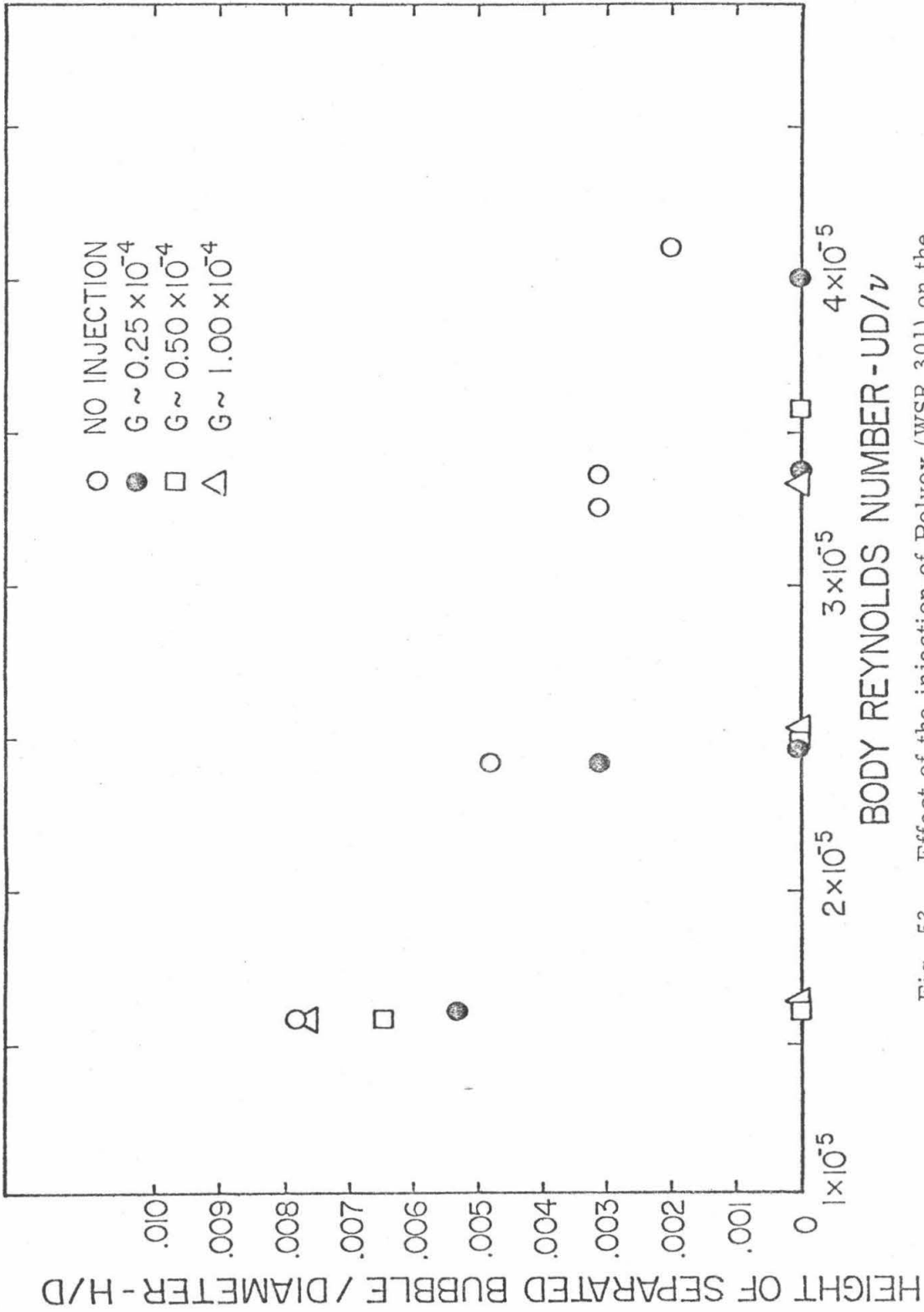


Fig. 53. Effect of the injection of Polyox (WSR 301) on the height of the laminar separation on the NSRDC body.

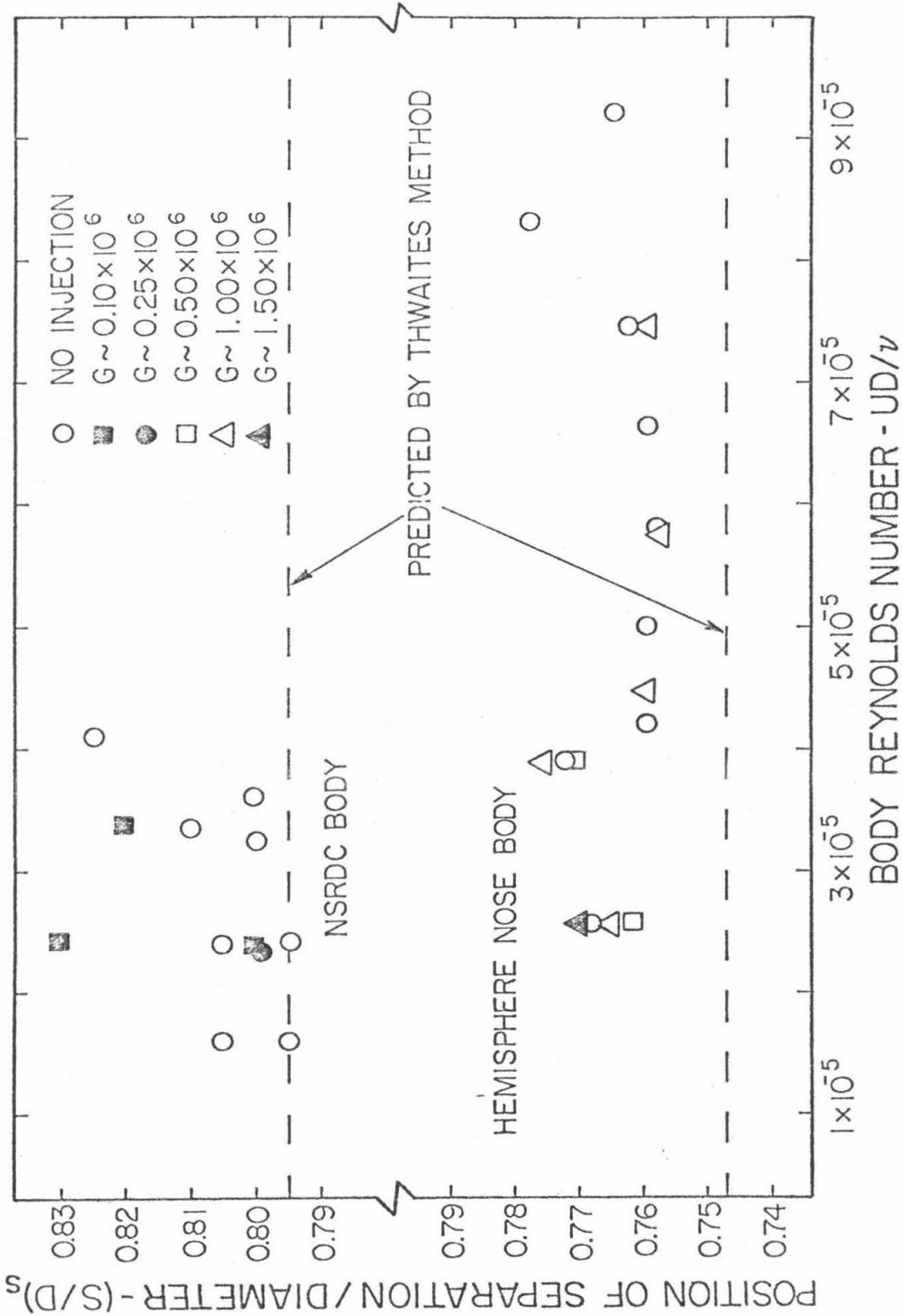


Fig. 54. Effect of injection of Polyox (WSR 301) on the position of separation on both the hemisphere nose and the NSRDC bodies.

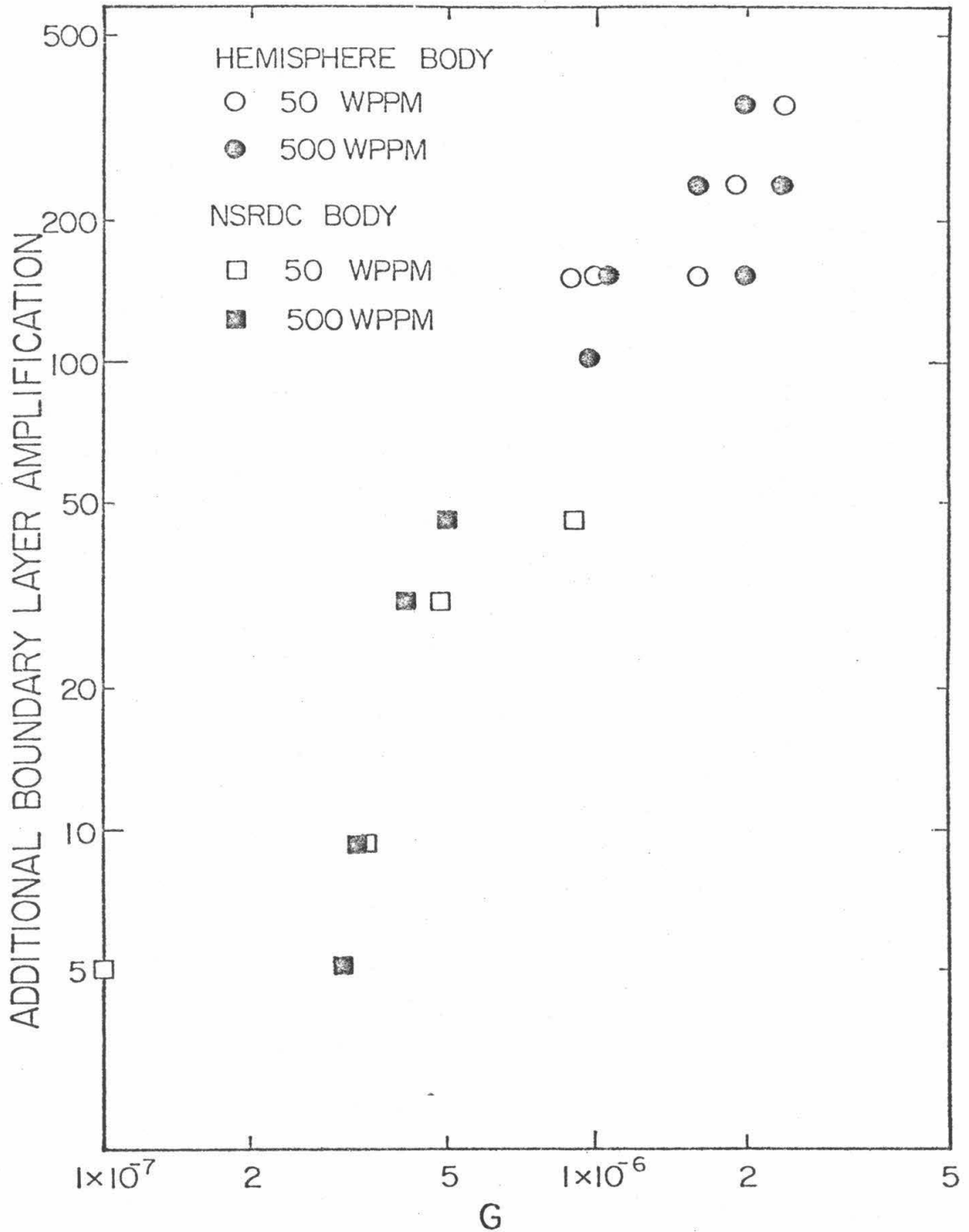


Fig. 55. The estimated additional boundary layer disturbance amplification caused by the presence of Polyox (WSR 301).

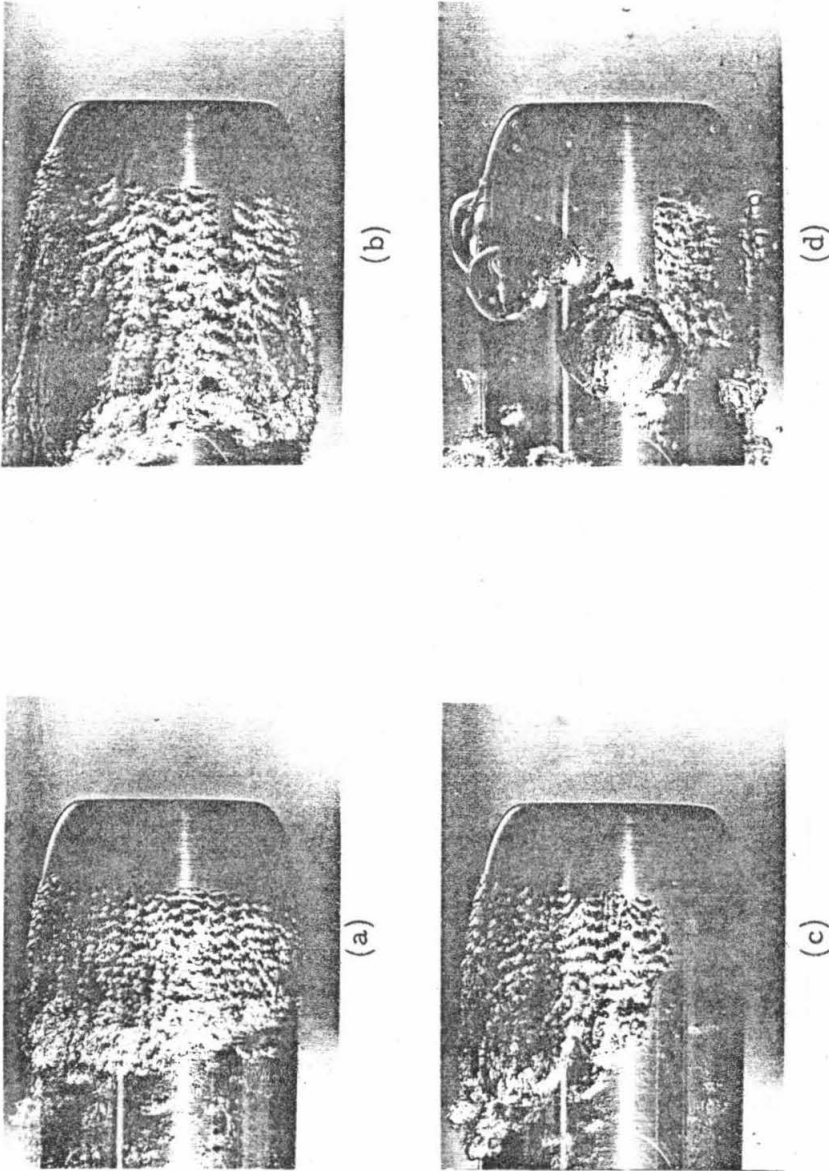


Fig. 56 Photographs of the physical appearance of cavitation on the NSRDC body at two turbulence levels. Flow is from right to left. $Re_D = 3.4 \times 10^5$.

(a) $u'/U = 0.05\%$, $\sigma = 0.44$
(b) $u'/U = 0.65\%$, $\sigma = 0.36$
(c) $u'/U = 0.65\%$, $\sigma = 0.36$
(d) $u'/U = 0.65\%$, $\sigma = 0.35$

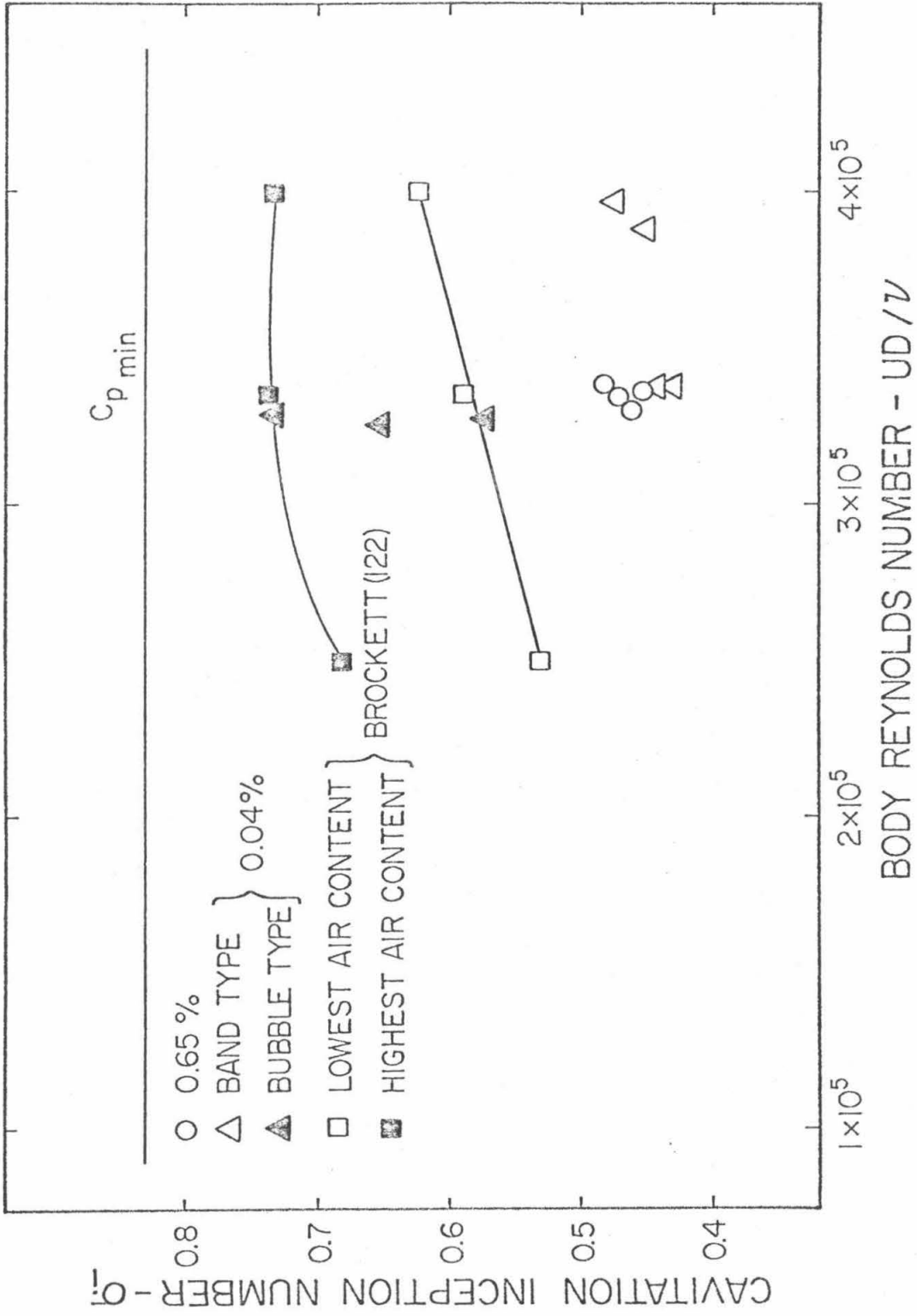


Fig. 57. The effect of freestream turbulence level upon the cavitation inception number on the NSRDC body.

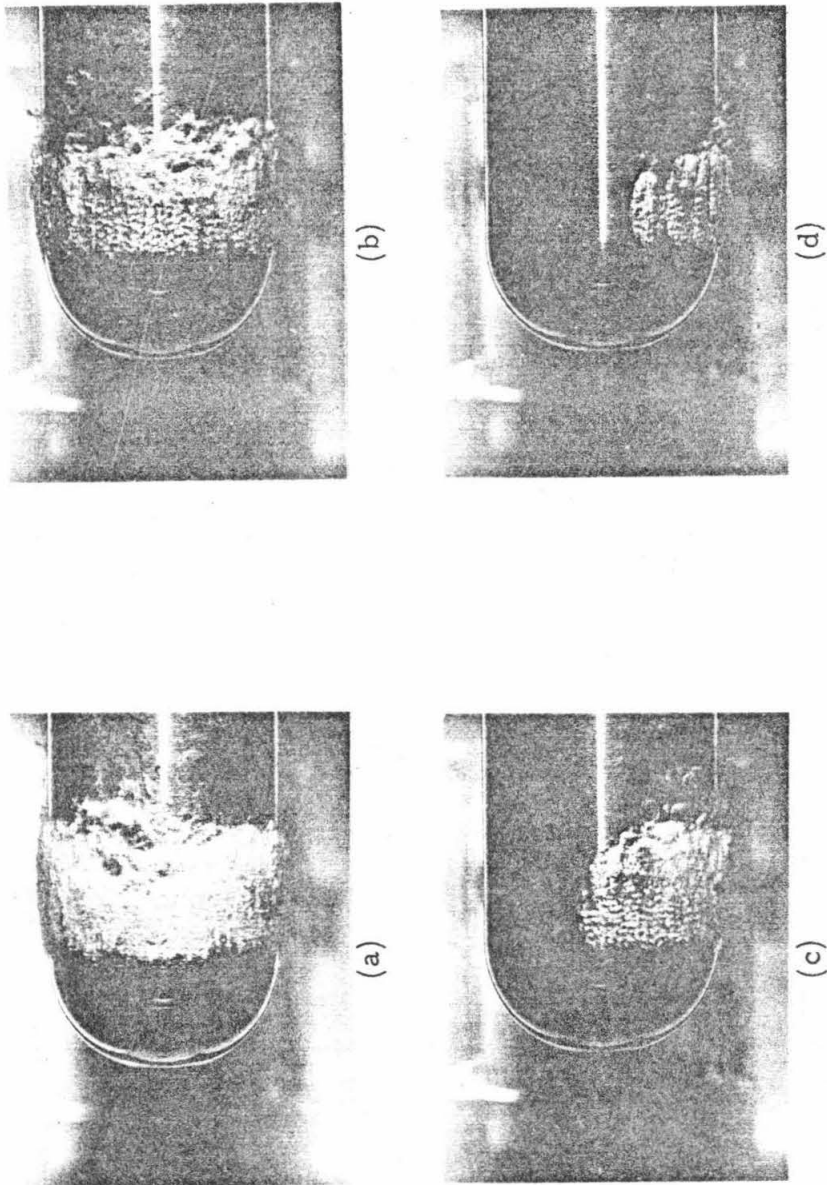


Fig. 58 Photographs of the physical appearance of cavitation on the hemisphere nose body with polymer injection. Flow is from left to right. $Re_0 = 6.7 \times 10^5$, $\sigma = 0.59$. Concentration = 500 wppm.

(a) $Q(\text{injection rate}) = 0.0 \text{ ml/sec}$, $G = 0.0$

(b) $Q = 0.51 \text{ ml/sec}$, $G = 1.88 \times 10^{-6}$

(c) $Q = 1.12 \text{ ml/sec}$, $G = 4.14 \times 10^{-6}$

(d) $Q = 1.42 \text{ ml/sec}$, $G = 5.24 \times 10^{-6}$

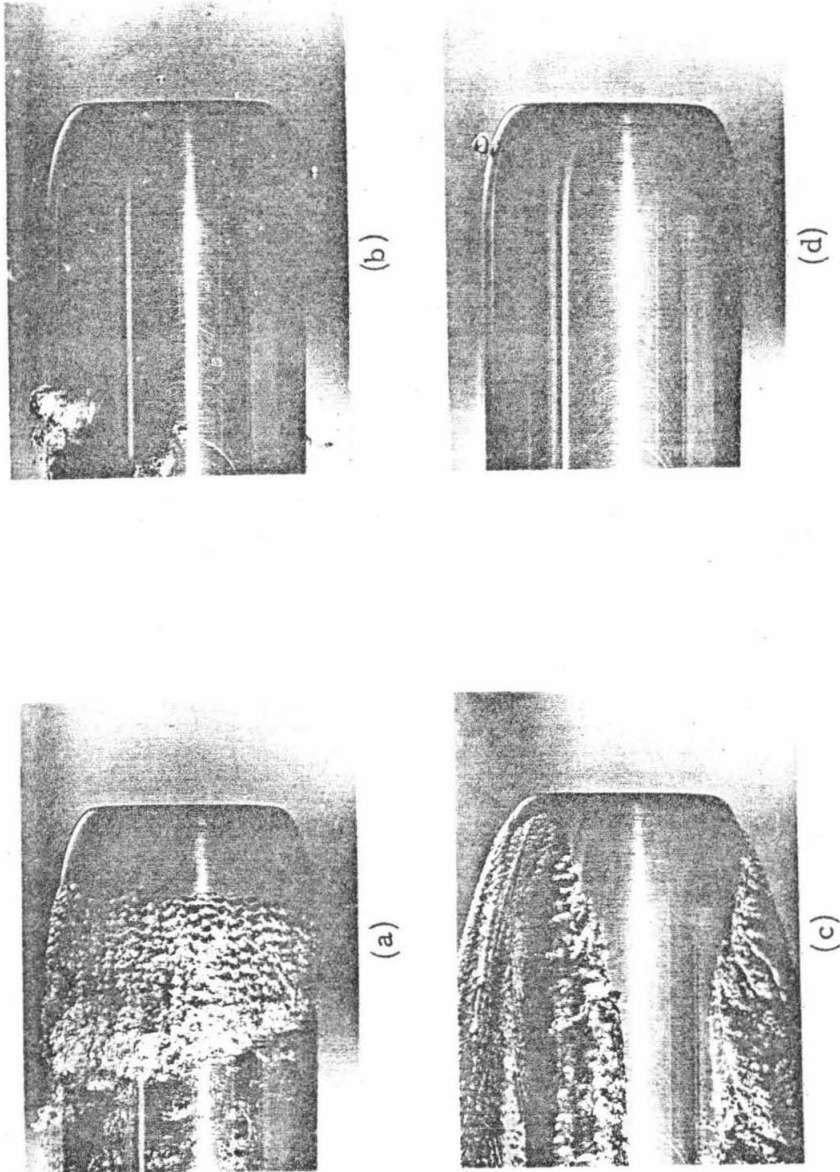


Fig. 59 Photographs of the physical appearance of cavitation on the NSRDC body with polymer injection. Flow is from right to left. $Re_0 = 3.4 \times 10^5$.

(a) \dot{Q} (injection rate) = 0.0 ml/sec., $G = 0.0$, $\sigma = 0.44$
(b) $\dot{Q} = 2.40$ ml/sec., c (concentration) = 20 wppm, $G = 0.34 \times 10^{-6}$, $\sigma = 0.45$
(c) $\dot{Q} = 2.40$ ml/sec., $c = 20$ wppm, $G = 0.34 \times 10^{-6}$, $\sigma = 0.34$
(d) $\dot{Q} = 2.00$ ml/sec., $c = 500$ wppm, $G = 7.11 \times 10^{-6}$, $\sigma = 0.34$

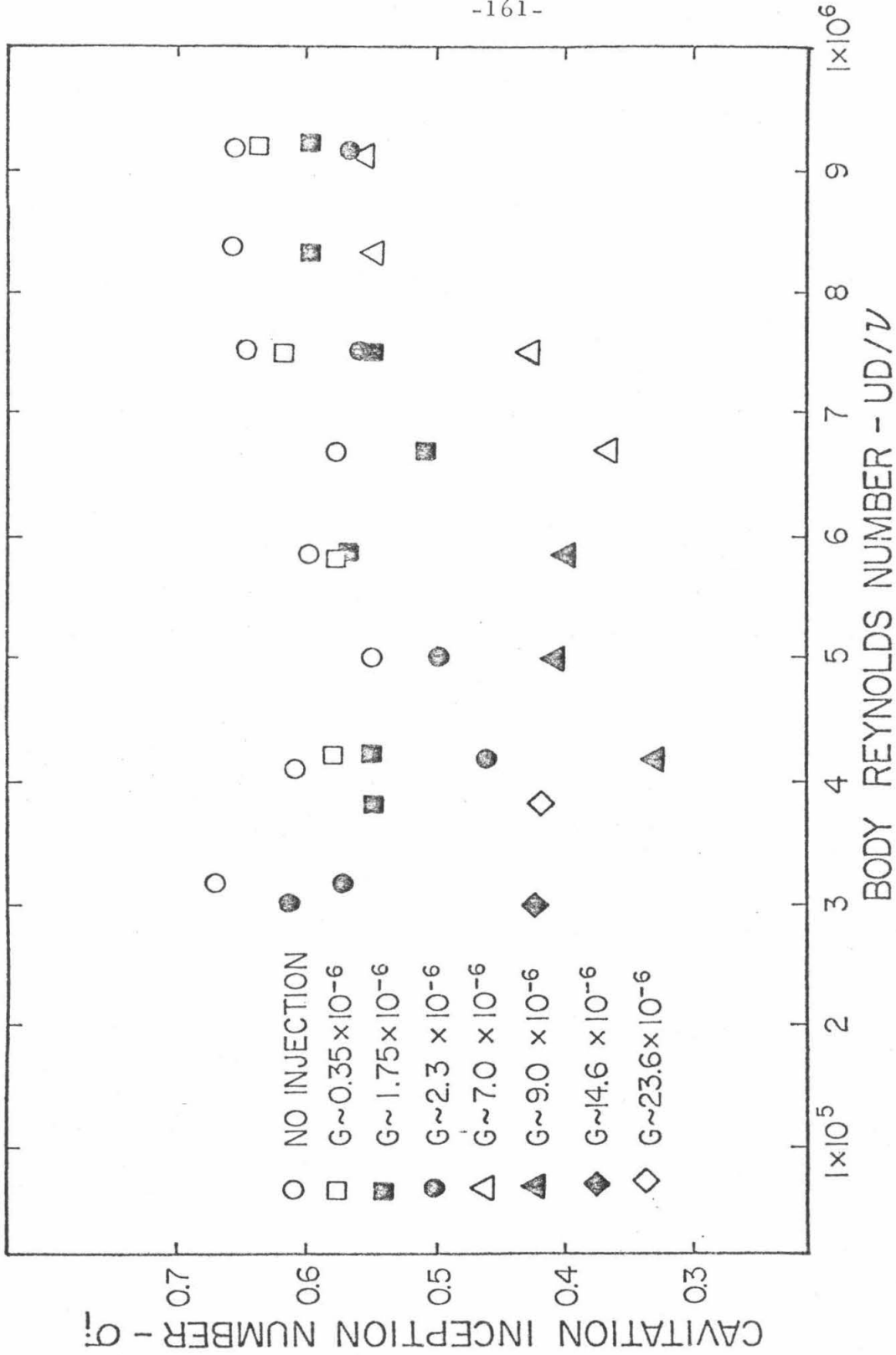


Fig. 60. The effect of injection of Polyox (WSR 301) upon cavitation inception number on the hemisphere nose body.

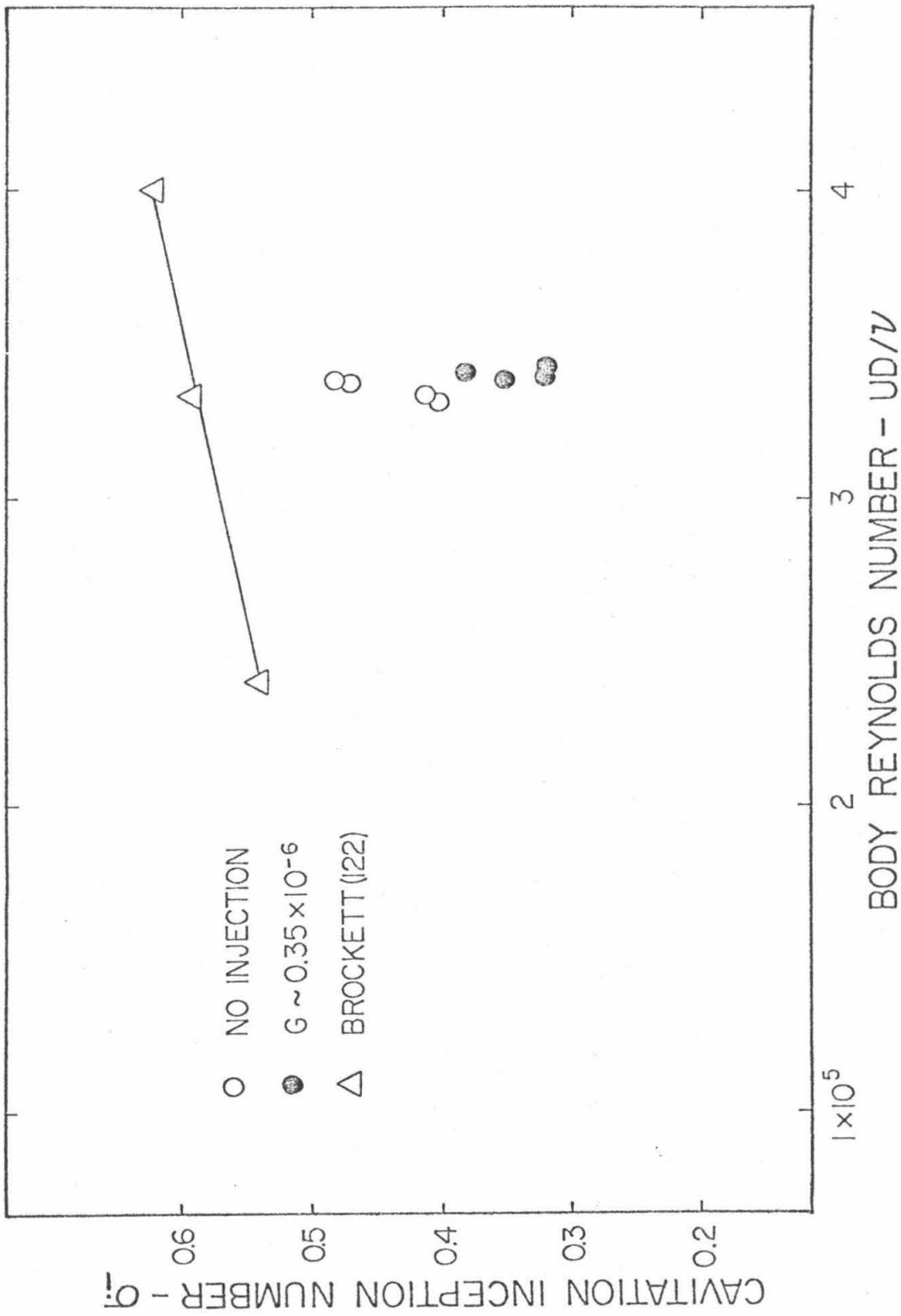


Fig. 61. The effect of injection of Polyox (WSR 301) on the cavitation inception number on the NSRDC body.

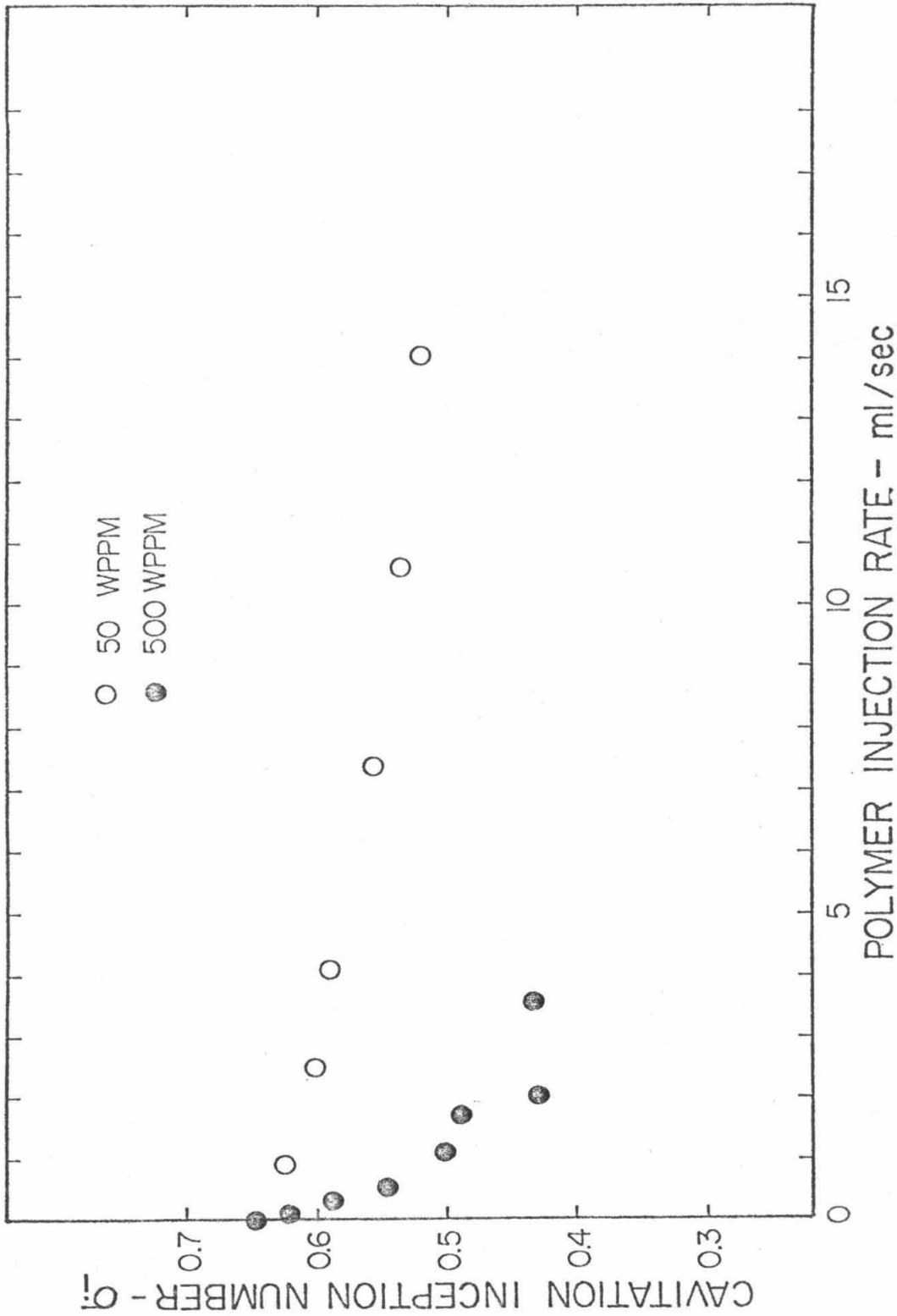


Fig. 62. The effect of injection of Polyox (WSR 301) on the cavitation inception number on the hemisphere nose body as a function of injection rate for two concentrations. $Re_p = 7.5 \times 10^5$.

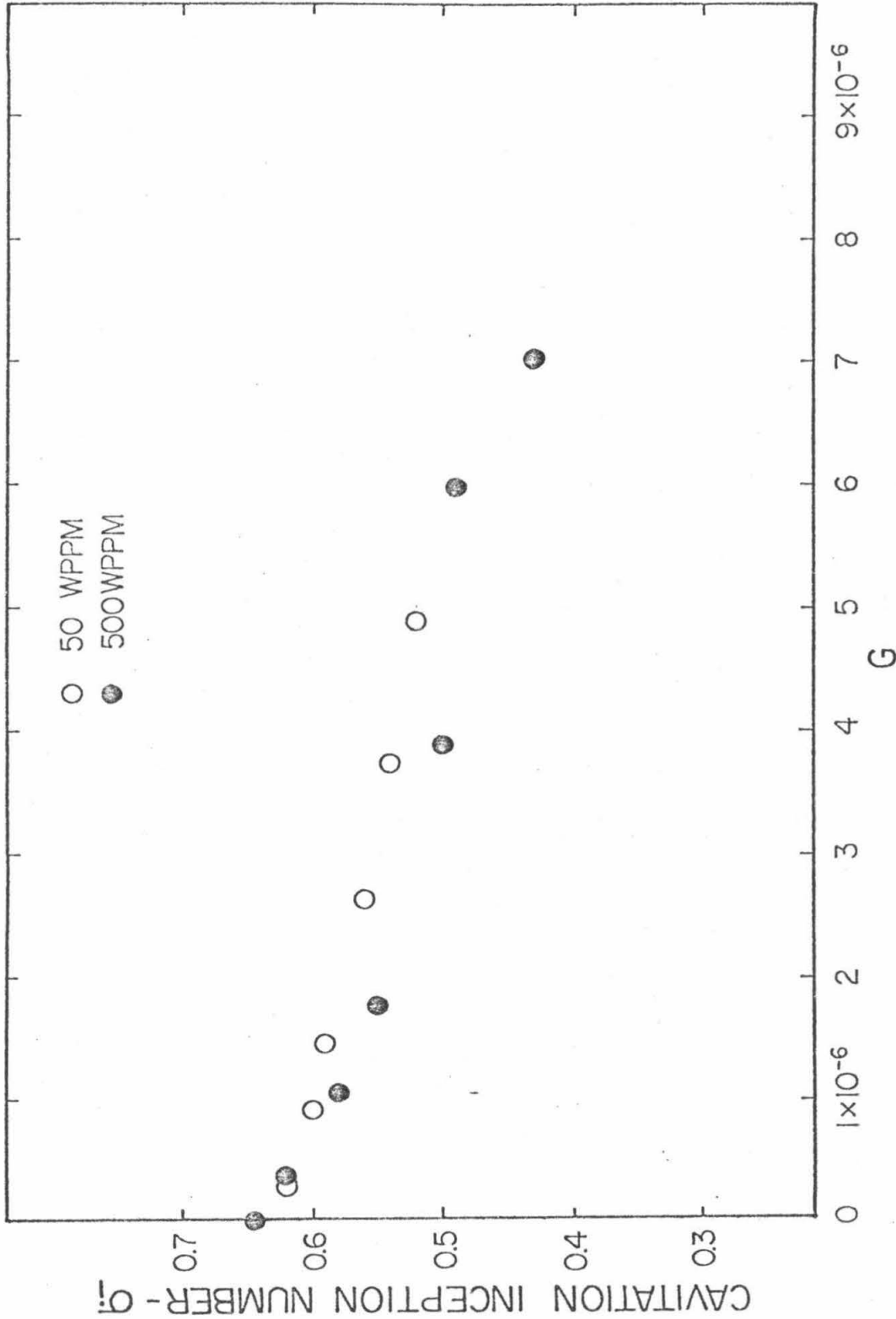


Fig. 63. The same data as presented in Fig. 62 but now plotted versus the parameter G to show the correlation of the cavitation suppression with the amount of polymer injected into the boundary layer.

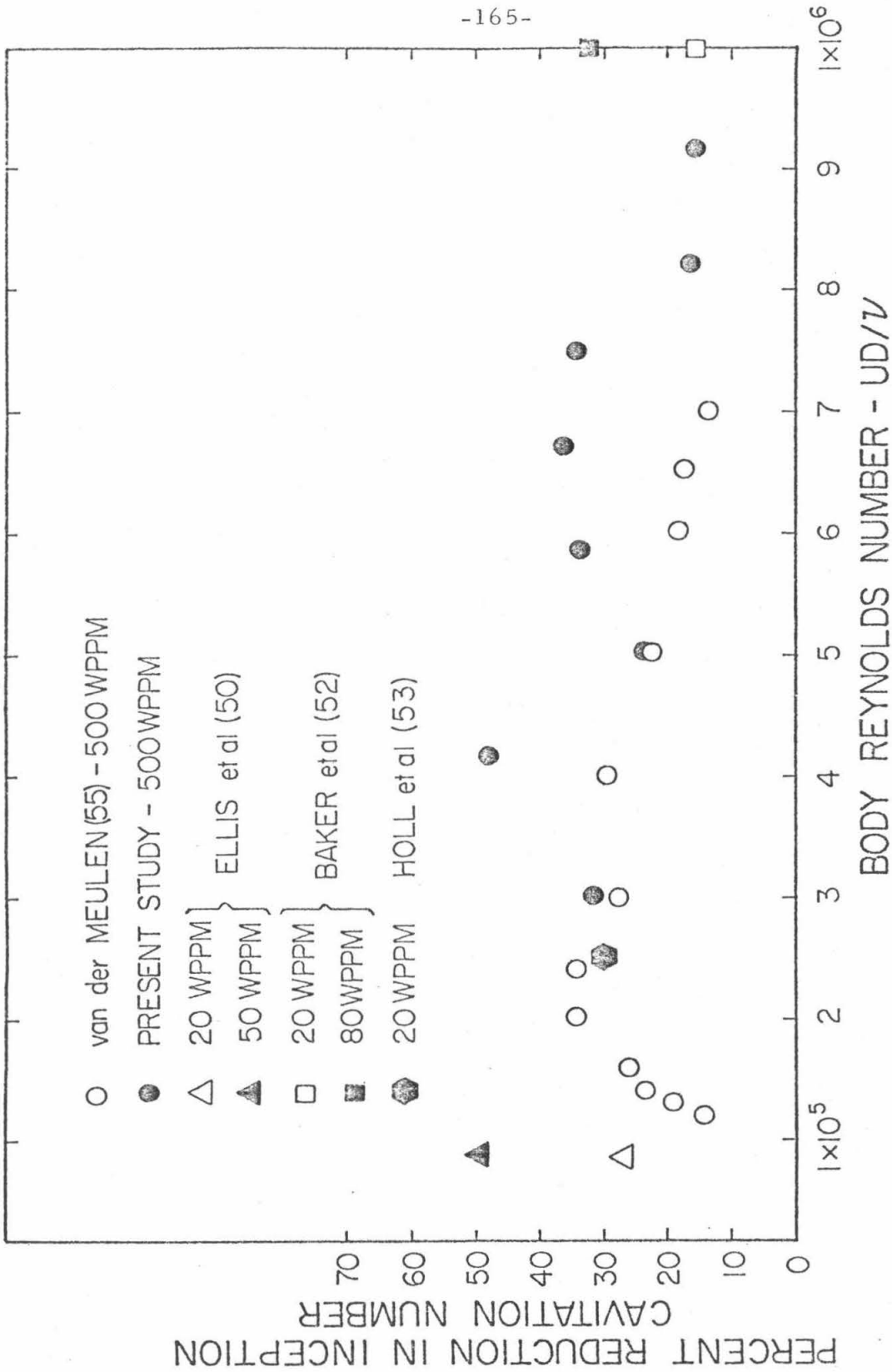


Fig. 64 Comparison of the cavitation suppression results of the present study with those of several other investigations.

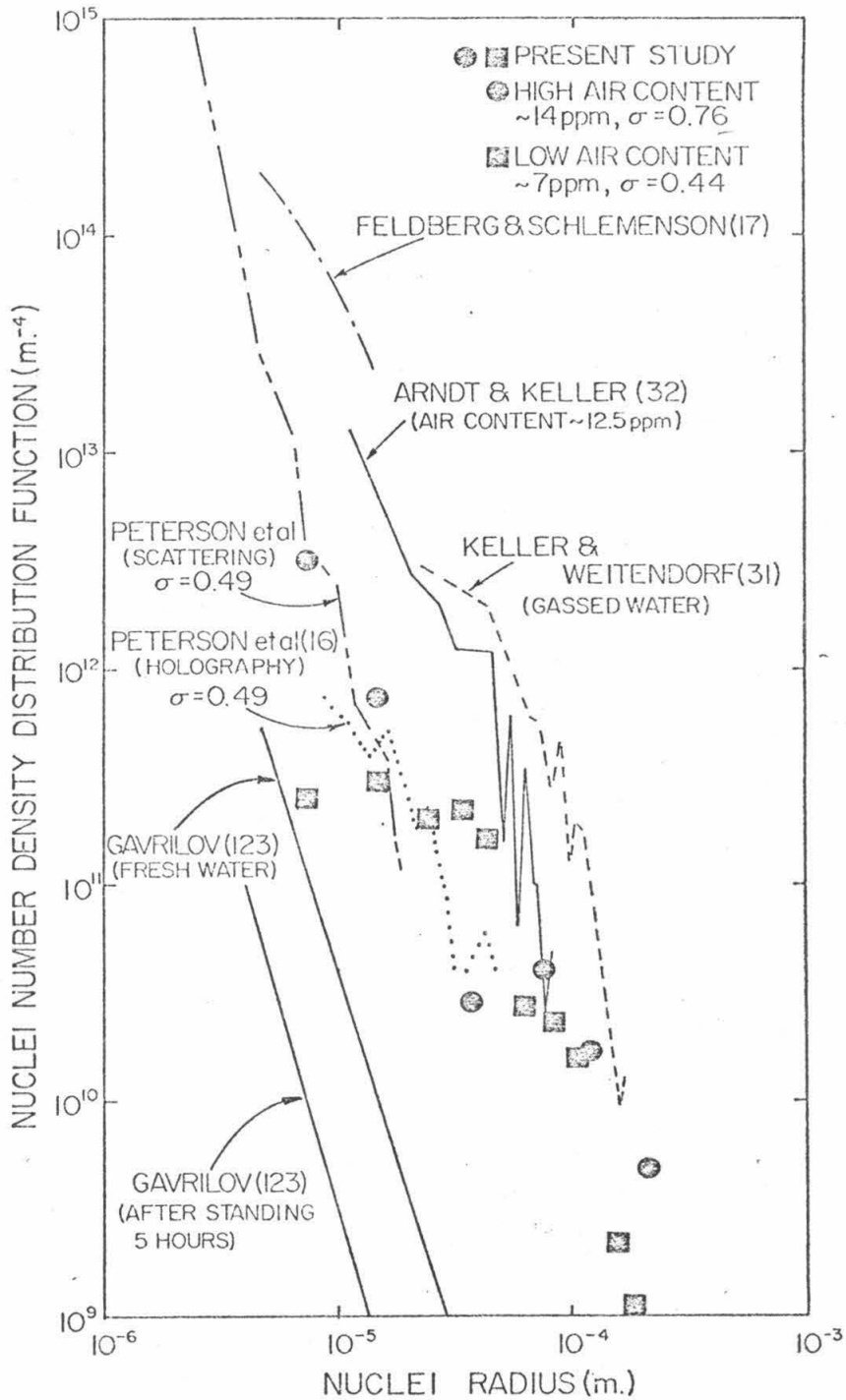


Fig. 65. Comparison of nuclei number density distribution functions derived from the experimental results of several investigations.

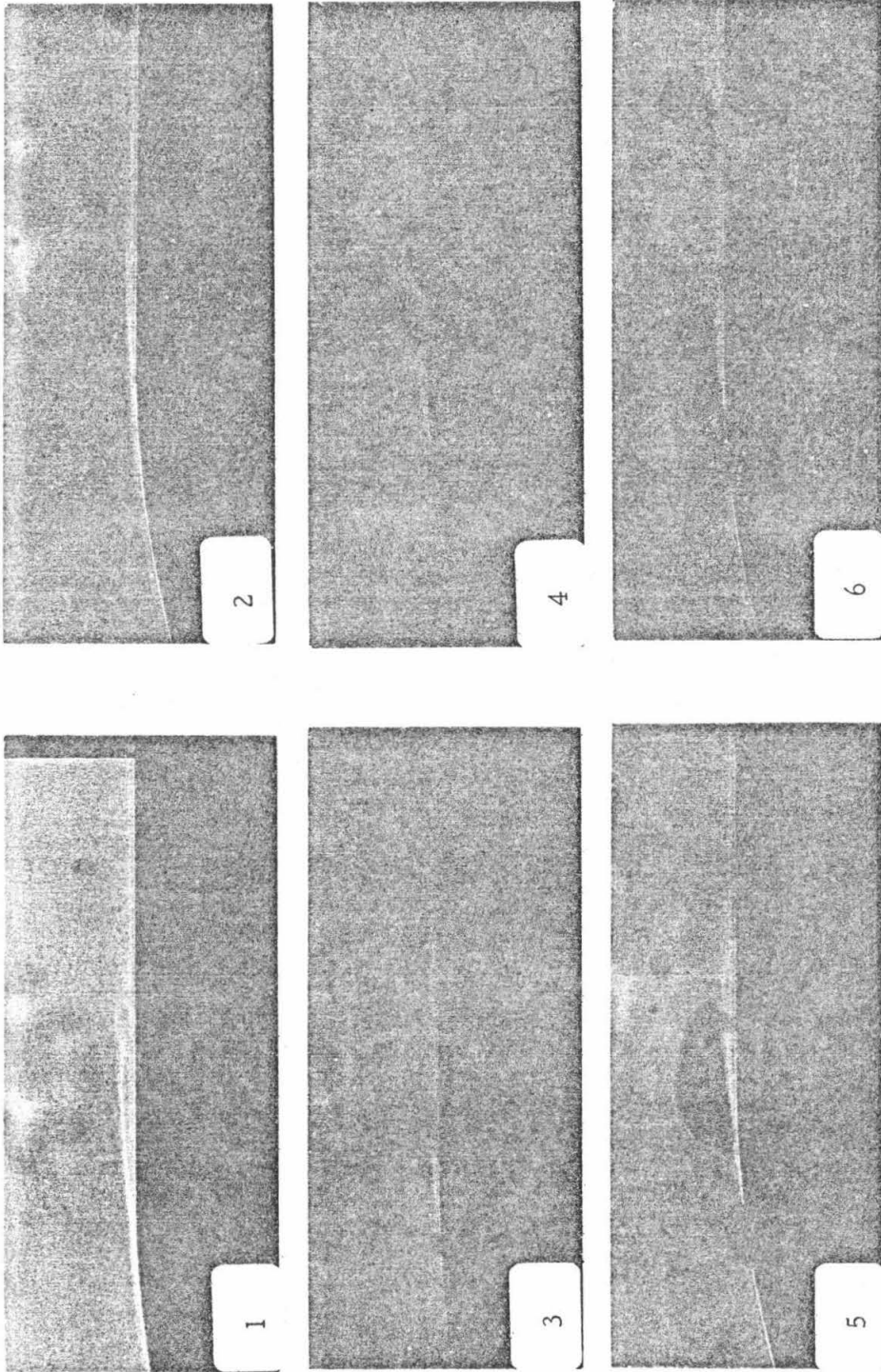


Fig. 66. Schlieren photographs of the effect of increasing numbers of freestream bubbles on the laminar separation on the hemisphere nose body. Flow is from left to right. $Re_D = 3.5 \times 10^5$.

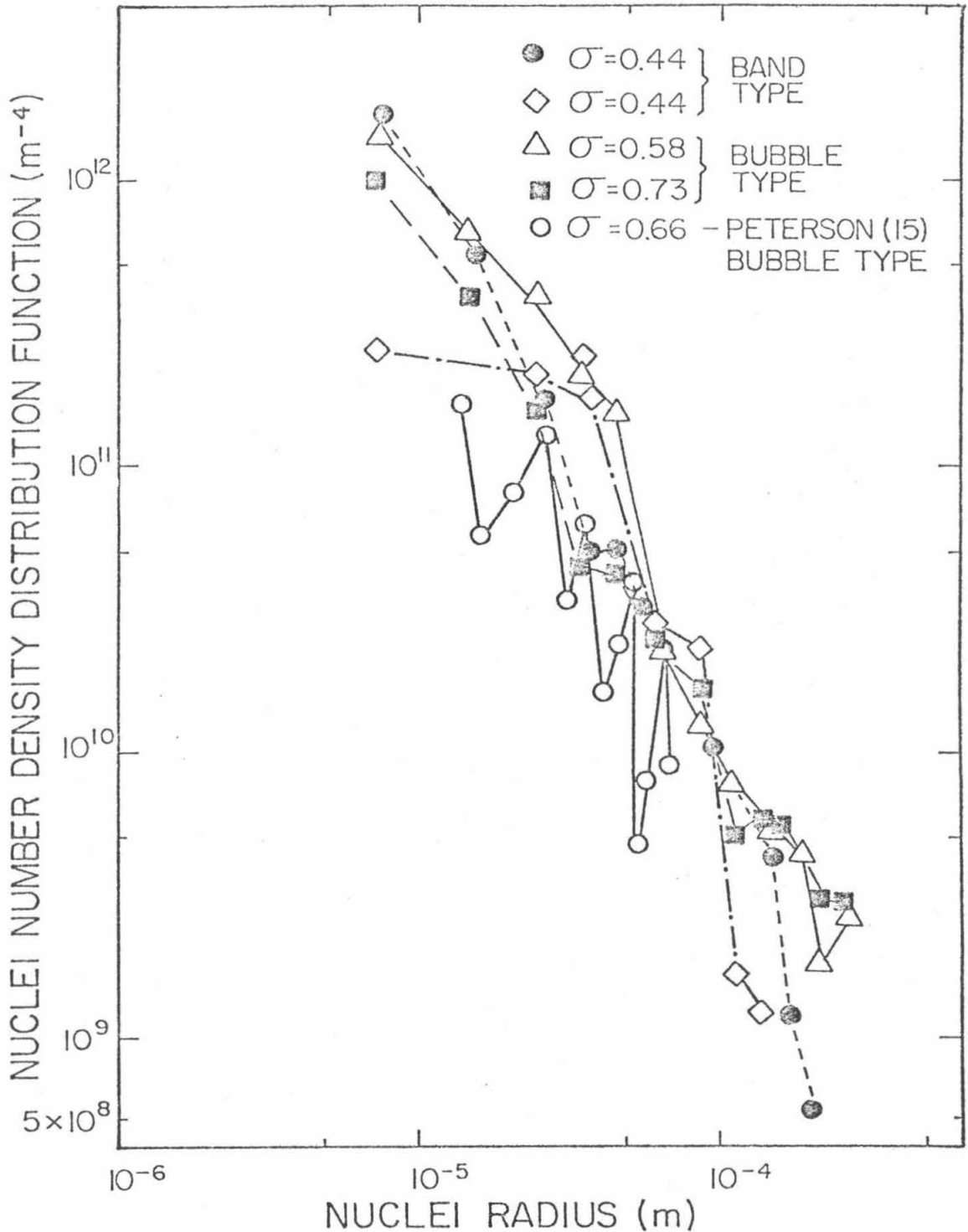


Fig. 67 Some nuclei distributions obtained in the LTWT during the present investigations and one distribution obtained in the NSRDC facility by Peterson [15]. The holographic technique was used in both investigations.

Appendix I

MEASUREMENT OF FREESTREAM TURBULENCE
LEVEL IN THE LTWT

I.1 Flow Measuring Equipment

The test section longitudinal velocity component was measured using a DISA 55D05 constant temperature hot film anemometer. The anemometer consists basically of a bridge circuit with a feedback amplifier. The probe, which forms one arm of the bridge, was a DISA wedge-shaped film type. Two types of probes were used: a 90 degree hot film probe (55R36) and a straight hot film probe (55R32). Initially it had been desired to measure the velocity and turbulence profiles across the test section. For this purpose, the 90 degree probe was purchased. This probe was mounted in the top test section window and was "swept" from the tunnel center-line up to the window. However, it was found that the resultant signal was so dominated by the vibration of the probe that no useful information could be extracted. Subsequently the straight probe was purchased and firmly held on the tunnel center-line by a sting support. Photographs of the 180 degree probe itself and the probe mounted in the tunnel are presented in Figs. 13 and 14 of the main text.

Normally this DISA anemometer is a battery operated unit. However, because of the high probe currents required for measurements in water, it was necessary to use an auxiliary power supply instead of the batteries. A Hewlett-Packard constant voltage power

supply (HP 6216A) was used. The output signal from the anemometer was first low-pass filtered by a simple RC circuit to remove high frequency noise from the anemometer feedback amplifier. A circuit diagram and the measured frequency response of this filter are given in Figs. I. 1 and I. 2 respectively. The filtered signal was then divided into its D. C. and A. C. components. A Keithley digital multimeter (model 171) was used to extract the D. C. component while a Hewlett-Packard true rms voltmeter (model 3400A) measured the A. C. component. Since it was very difficult to follow the fluctuating needle readout on the true rms meter, use was made of the output provided by this meter. The true rms meter provides a D. C. voltage from zero to one volt which is proportional to the needle deflection. This output was connected to a Hewlett-Packard integrating D. C. voltmeter (Counter-DMV model 5326B) which averaged the signal over a ten second time period.

Spectral analysis of the signal was performed by a Hewlett-Packard spectrum analyzer (model 3580A). The results were shown on a cathode ray tube display which was photographed for permanent record. Also photographed at the same time was the anemometer signal as displayed on an oscilloscope. Examples of both the signal and its spectrum are presented in Figs. I. 3 and I. 4 respectively. Figure I. 5 is a block diagram of the turbulence level measuring system and Fig. I. 6 is a photograph of the system.

I. 2 Data Recording

Turbulence levels were measured at a fixed location on the tunnel center-line as a function of velocity for a given configuration of turbulence manipulators. At the beginning of each test, the probe

cold resistance and zero flow D. C. voltage were recorded. If the probe was new, a frequency response adjustment was also made. The velocity was then gradually increased in increments of two to three feet per second. At each velocity, the D. C. component voltage and ten ten-second averages of the true rms value of the fluctuating component voltage were recorded. Also, the pressure drop across the nozzle was recorded. At the conclusion of each test (which usually consisted of eight velocities), the probe cold resistance and zero flow D. C. voltage were checked to see that no change had occurred during the test.

I.3 Data Reduction

First, the freestream velocity was calculated from pressure drop data across the nozzle. Then, on log-log paper, the freestream velocity was plotted versus the difference between the anemometer D. C. voltage and the anemometer zero flow D. C. voltage. As expected from theory, this gave a straight line the slope of which was measured directly from the graph. Next, the ten recorded true rms values of the fluctuating component were averaged. Then, since the fluctuating values were small in comparison with the D. C. or mean value, the turbulent intensity was calculated by the following relation:

$$\frac{u'}{U} = \frac{\overline{V}_{\text{rms}}}{\Delta V} \times \text{SLOPE}$$

where

u' = the rms value of the fluctuating component of the longitudinal velocity.

U = mean value of the longitudinal velocity.

\bar{V}_{rms} = average of the true rms values of the fluctuating component of the anemometer signal.

ΔV = the anemometer D. C. voltage minus the anemometer zero flow D. C. voltage.

SLOPE = slope of the log-log plot of velocity versus ΔV .

This value was then converted to percent and plotted versus freestream velocity. And thus a graph was obtained for each configuration of turbulence manipulators. The summary of the results are presented in Fig. 15 of the main text.

I. 4 Comparison of Results

The only other measurements of freestream turbulence level in the LTWT were carried out by Vanoni and Brooks [124]. They photographed the trajectories of neutrally buoyant particles and estimated the turbulence level from the position and time coordinates of the particles. It is very difficult to accurately determine the turbulence intensity by this method and they estimated that their measurement procedure would produce a turbulence level of 0.4 percent even if the actual level were zero! However, at the higher disturbance levels where this error is minimized, good agreement between the present values and those of Vanoni and Brooks is obtained if the injector of the neutrally buoyant particles was located in the grid and not in a strut (see Fig. I. 7).

I. 5. Estimate of the Error in the Turbulence Level Measurements

At the low turbulence level (0.05 percent) it is believed that

"noise" from the anemometer feedback amplifier dominates, so no estimate of the error is possible. However, at the higher turbulence levels where other errors dominate, an estimate can be made.

Recall:

$$\frac{u'}{U} = \frac{\bar{V}_{rms}}{\Delta V} \times \text{SLOPE} \quad .$$

Error in ΔV :

The specifications for the Keithley multimeter give the accuracy as ± 0.02 percent of reading + 0.01 percent of range. However, this was not the major concern in measuring the D. C. voltage. At the higher turbulence levels the D. C. voltage could vary as much as 0.03 volts because of the turbulent fluctuations, but only one value was recorded. Also, the D. C. level could change this much because of changing probe resistance. So ΔV could be in error by as much as ± 0.03 volts. At lower velocities where the D. C. voltage was approximately 3 volts this implies an error of:

$$\frac{0.06}{3.00} \times 100 = 2 \text{ percent}$$

while at high velocities where the D. C. voltage was approximately 6 volts the error would be:

$$\frac{0.06}{6.00} \times 100 = 1 \text{ percent.}$$

Error in \bar{V}_{rms} :

Specifications of the true rms meter give the accuracy of the A. C. to D. C. conversion as ± 5 percent for the frequency range of interest. The integrating voltmeter is accurate to ± 0.04 percent. So the

limitation here is the A. C. to D. C. conversion taking place inside the true rms meter.

Error in Slope:

The estimation of the slope was found to be not better than ± 5 percent. This figure was arrived at by (i) drawing several best fit lines and (ii) comparison with the slope of a least squares fit line.

So the error in turbulent intensity is:

$$\frac{(1 \pm 0.05) \bar{V}_{\text{rms}}}{(1 \pm 0.02) \Delta V} \times (1 \pm 0.05) \text{SLOPE} \Rightarrow \pm 12 \text{ percent}$$

at low velocities, and:

$$\frac{(1 \pm 0.05) \bar{V}_{\text{rms}}}{(1 \pm 0.01) \Delta V} \times (1 \pm 0.05) \text{SLOPE} \Rightarrow \pm 11 \text{ percent}$$

at high velocities.

The majority of the error is introduced by the error in the estimate of the slope of the velocity versus ΔV line.

Repeatability of measured turbulence levels was found to be better than 5 percent.

LIST OF FIGURE CAPTIONS — APPENDIX I

- Fig. I. 1. Circuit diagram of the low-pass filter.
- Fig. I. 2. Frequency response of the RC filter as determined with a signal generator. Maximum frequency available from the signal generator is 2 KHz.
- Fig. I. 3. Example of the oscilloscope trace of the anemometer signal. Freestream velocity is 9.33 feet per second and the turbulence level is 0.65 percent. Vertical scale is 10mv/cm. Horizontal scale is 10 msec/cm.
- Fig. I. 4. Example of the spectrum of the anemometer signal. Freestream velocity is 9.81 feet per second and the turbulence level is 0.65 percent. Horizontal scale is 200 Hz/cm.
- Fig. I. 5. Block diagram of the turbulence measuring system and the signal reduction equipment.
- Fig. I. 6. Photograph of the turbulence level measuring equipment. The anemometer is on the table beside the spectrum analyzer. The equipment in the rack is used to determine the A. C. and D. C. components of the anemometer signal.
- Fig. I. 7. Comparison of present turbulence level measurements with those of Vanoni and Brooks [124].

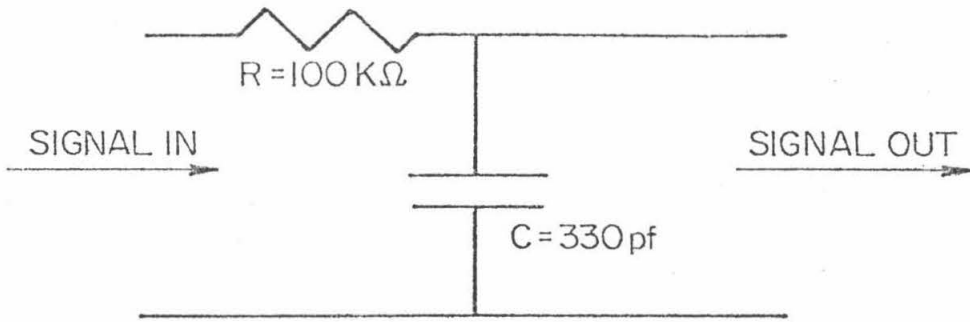


Fig. I.1 Circuit diagram of low-pass filter.

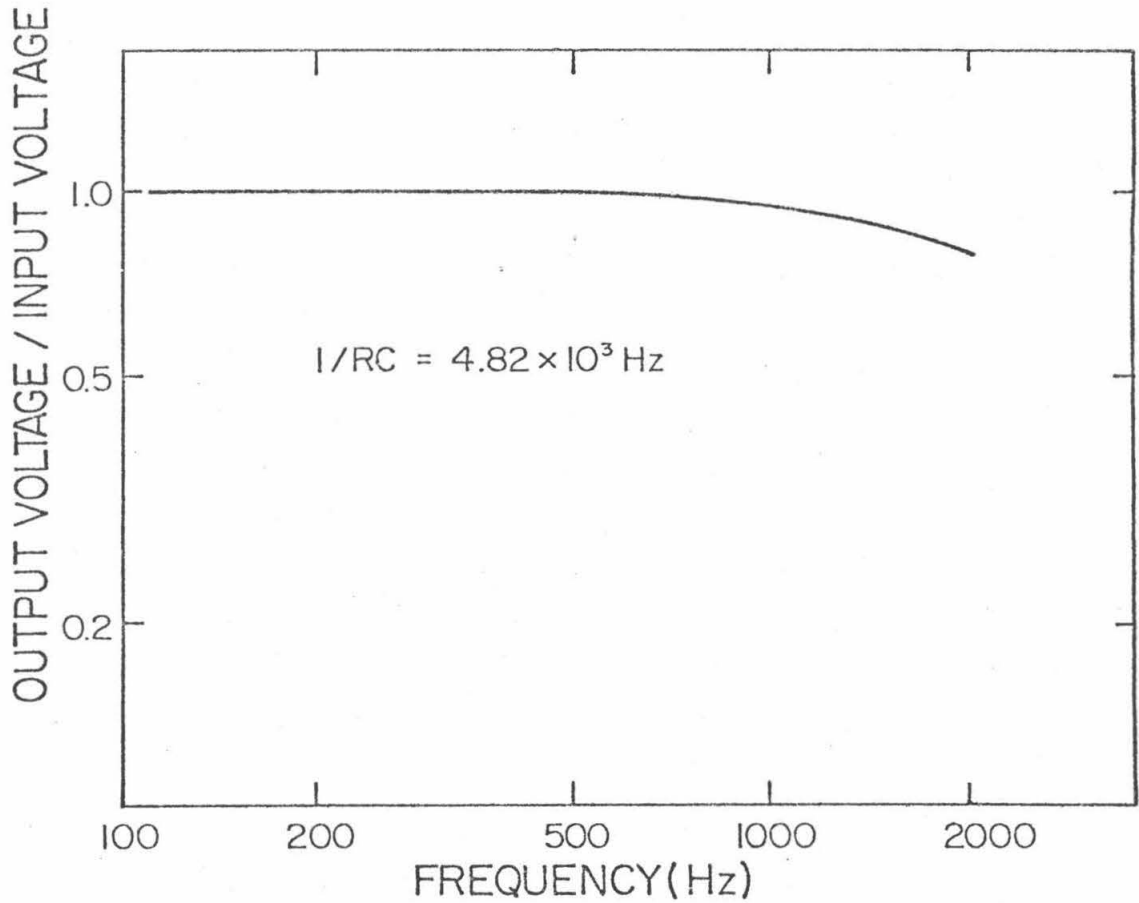


Fig. I.2 Frequency response of the RC filter as determined with a signal generator. Maximum frequency available from the signal generator is 2 KHz.

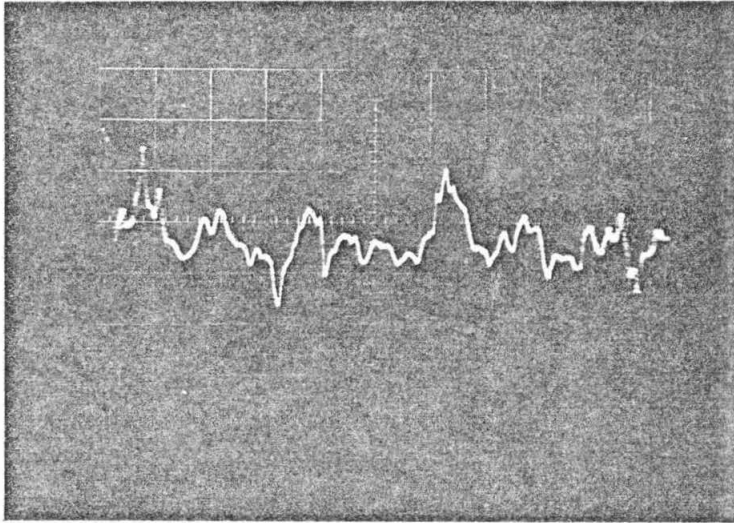


Fig. I.3 Example of the oscilloscope trace of the signal from the hot film anemometer. Freestream velocity is 9.33 feet per second and the turbulence level is 0.65 percent. Vertical scale is 10 mv/cm. Horizontal scale is 10 msec/cm.

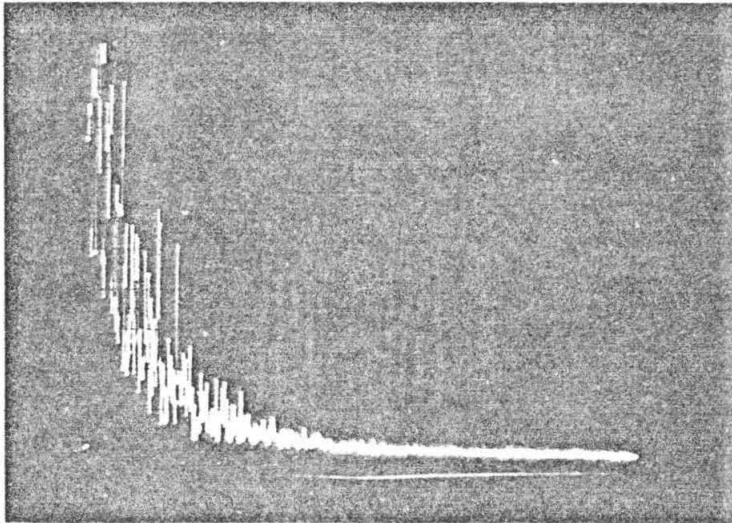


Fig. I.4 Example of the spectrum of the anemometer signal. Freestream velocity is 9.81 feet per second and the turbulence level is 0.65 percent. Horizontal scale is 200 Hz/cm.

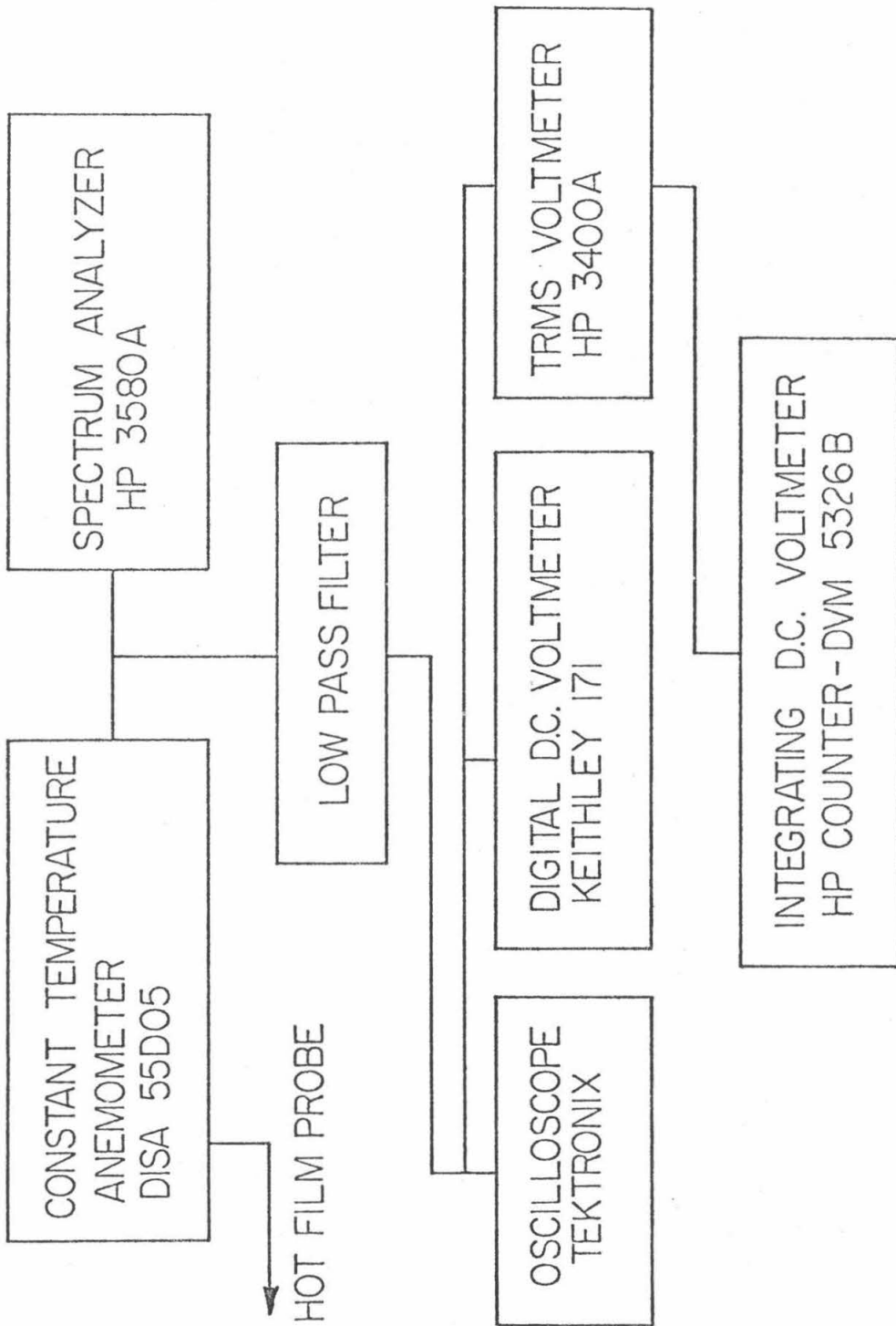


Fig. I.5 Block diagram of the turbulence measuring system and the signal reduction equipment.

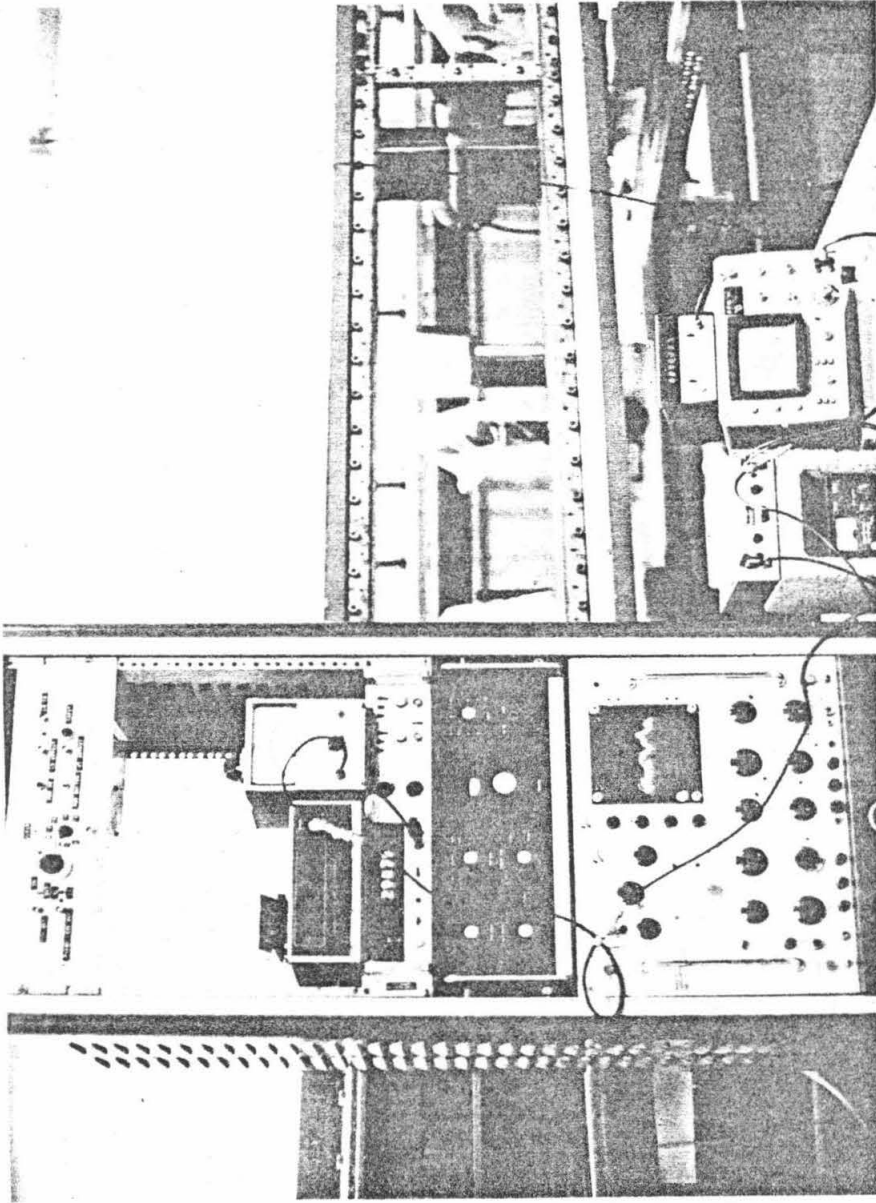


Fig. I.6 Photograph of the turbulence level measuring equipment. The anemometer is on the table beside the spectrum analyzer. The equipment in the rack is used to determine the A. C. and D. C. components of the anemometer signal.

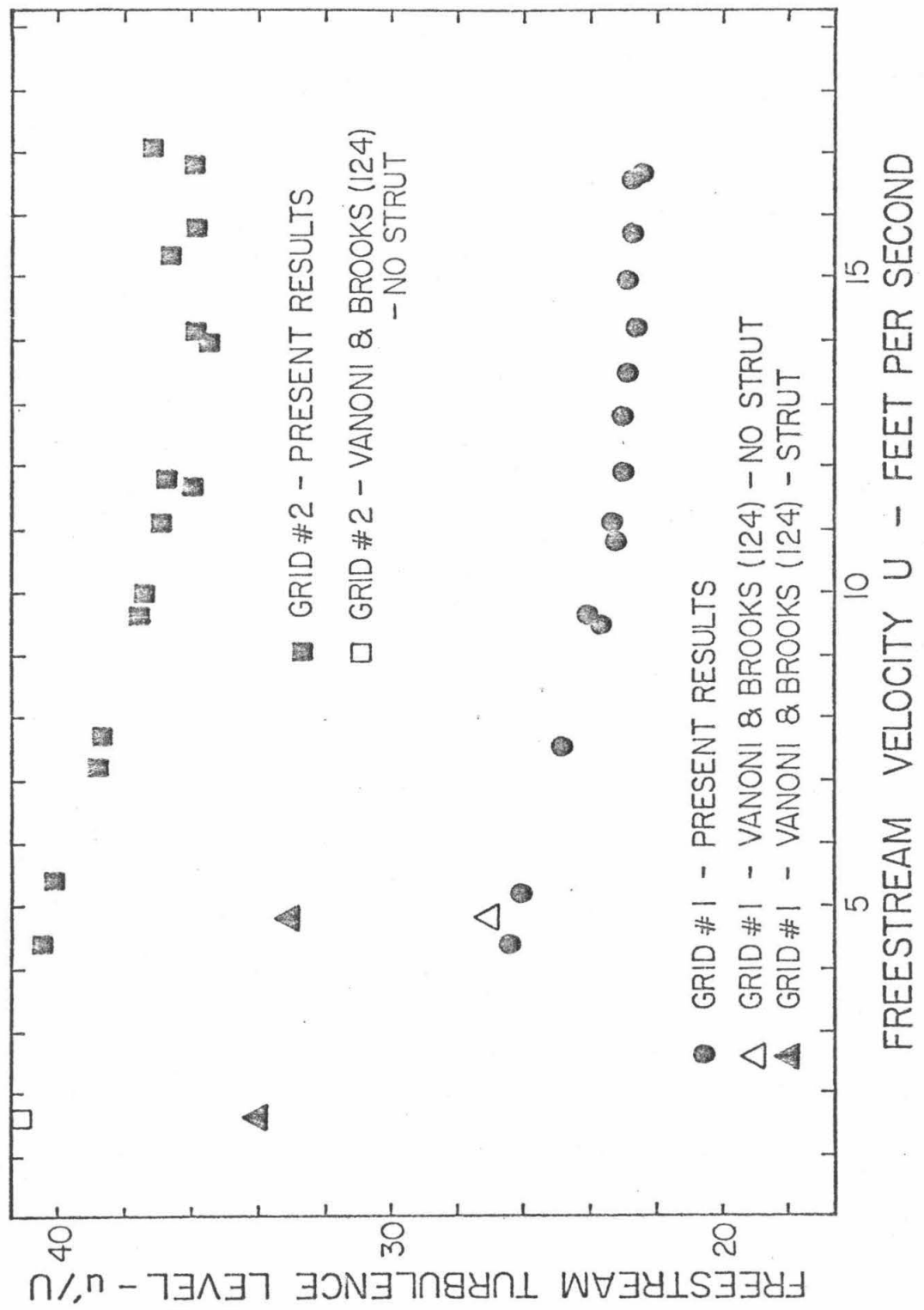


Fig. I. 7 Comparison of present turbulence level measurements with those of Vanoni and Brooks [124].

Appendix II

TUNNEL CALIBRATION PROCEDURE

As there is a boundary layer growth along the tunnel walls, it is necessary to calibrate the tunnel both bare and with a model installed in order to determine the static pressure and the velocity at the location of the model. Figure II.1 is a schematic diagram showing the location of the pressure taps used to determine the static pressure at the model location. Pressure p_1 is the pressure at the entrance to the nozzle. Pressure p_2 is the pressure at the entrance to the test section and is the average of four pressure taps in a piezometer ring. Pressure p_∞ is the pressure at the model location; it consists of a single orifice 0.030 inches in diameter drilled in a brass window plug.

The calibration consists of measuring the pressure differences $p_1 - p_2$, $p_1 - p_\infty$ and $p_\infty - p_2$ as a function of tunnel velocity. The difference $p_1 - p_2$ was measured by a mercury-water manometer; the difference $p_1 - p_\infty$ by a differential pressure transducer and the difference $p_\infty - p_2$ by a water manometer. This was done for the bare tunnel at two turbulence levels (0.05 percent and 0.65 percent) and with the NSRDC body installed at one turbulence level (0.65 percent).

These pressure differences were then converted into pressure coefficients as follows:

$$C_{p_n} = \frac{p_n - p_\infty}{p_1 - p_2}, \quad n = 1, 2 \quad .$$

These coefficients were then plotted versus $p_1 - p_2$, the pressure drop across the nozzle, and are presented in Figs. II.2 and II.3.

We now list the working formulas for the tunnel speed and cavitation number.

The working formula for the tunnel speed U is:

$$U = \sqrt{\frac{p_1 - p_\infty}{\frac{1}{2} \rho} + U_1^2}$$

which is obtained by applying the Bernoulli equation between the model location and the entrance to the nozzle. By applying the Bernoulli equation and continuity across the nozzle, we get:

$$U_1^2 = \frac{p_2 - p_1}{\frac{1}{2} \rho \left[1 - \left(\frac{A_1}{A_2} \right)^2 \right]}$$

where A_1/A_2 is the nozzle area contraction ratio. Substituting this into the equation for U :

$$U = \sqrt{\frac{p_1 - p_2}{\frac{1}{2} \rho} \frac{p_1 - p_\infty}{p_1 - p_2} + \frac{1}{\left(\frac{A_1}{A_2} \right)^2 - 1}}$$

For the LTWT $(A_1/A_2)^2 = 14.535$, so

$$U = \sqrt{\frac{p_1 - p_2}{\frac{1}{2} \rho} (C_{p1} + 0.005)}$$

The working formula for the cavitation number σ is:

$$\sigma = \frac{P_{\infty} - P_v}{\frac{1}{2} \rho U^2}$$

where p_v is the vapor pressure. Or

$$\sigma = \frac{P_{\infty} - P_2}{\frac{1}{2} \rho U^2} + \frac{P_2 - P_v}{\frac{1}{2} \rho U^2}$$

which upon substitution for U gives:

$$\sigma = \frac{\left[-C_{P_2} + \frac{P_2 - P_v}{P_1 - P_2} \right]}{\left[C_{P_1} + 0.005 \right]}$$

In carrying out the actual calculations, those values of C_{P_1} and C_{P_2} corresponding to the bare tunnel were used. Thus no account of tunnel blockage is made in determining either the cavitation parameter or the tunnel velocity.

LIST OF FIGURE CAPTIONS — APPENDIX II

- Fig. II.1 Schematic drawing showing the location of the pressure taps used to calibrate the LTWT.
- Fig. II.2 Plot of the calibration factor C_{p_1} versus the pressure drop across the nozzle.
- Fig. II.3 Plot of the calibration factor $-C_{p_2}$ versus the pressure drop across the nozzle.

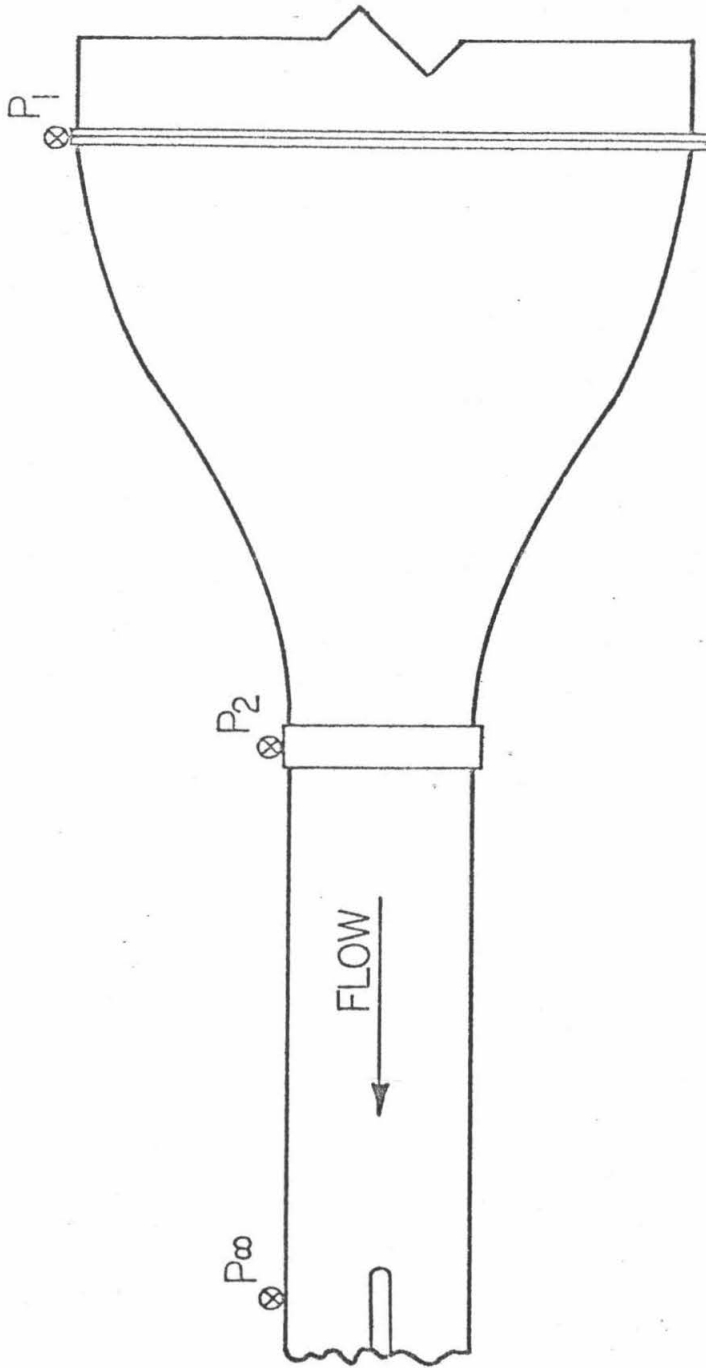


Fig. II.1 Schematic drawing showing the location of the pressure taps used to calibrate the LTWT.

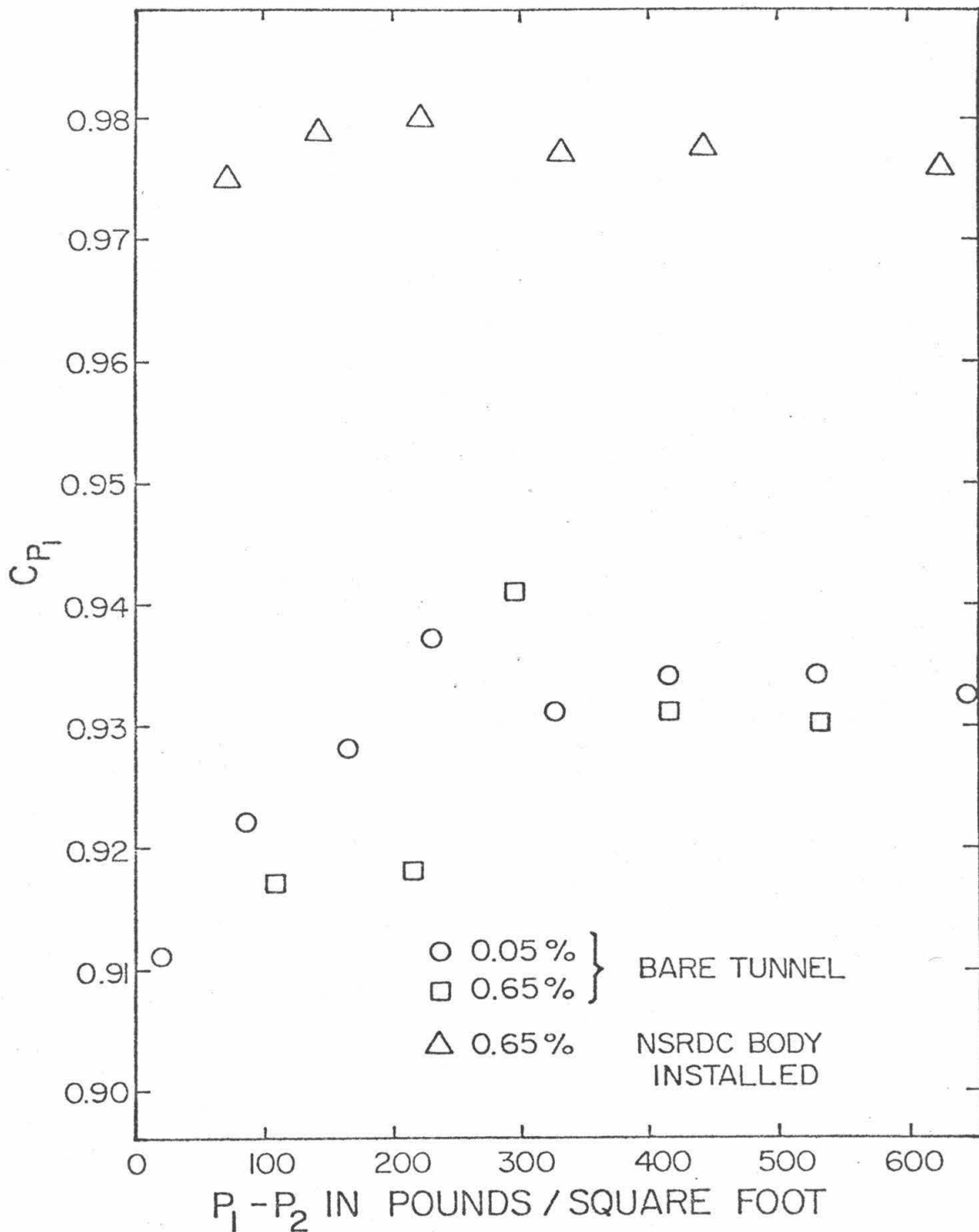


Fig. II. 2 Plot of the calibration factor C_{p_1} versus the pressure drop across the nozzle.

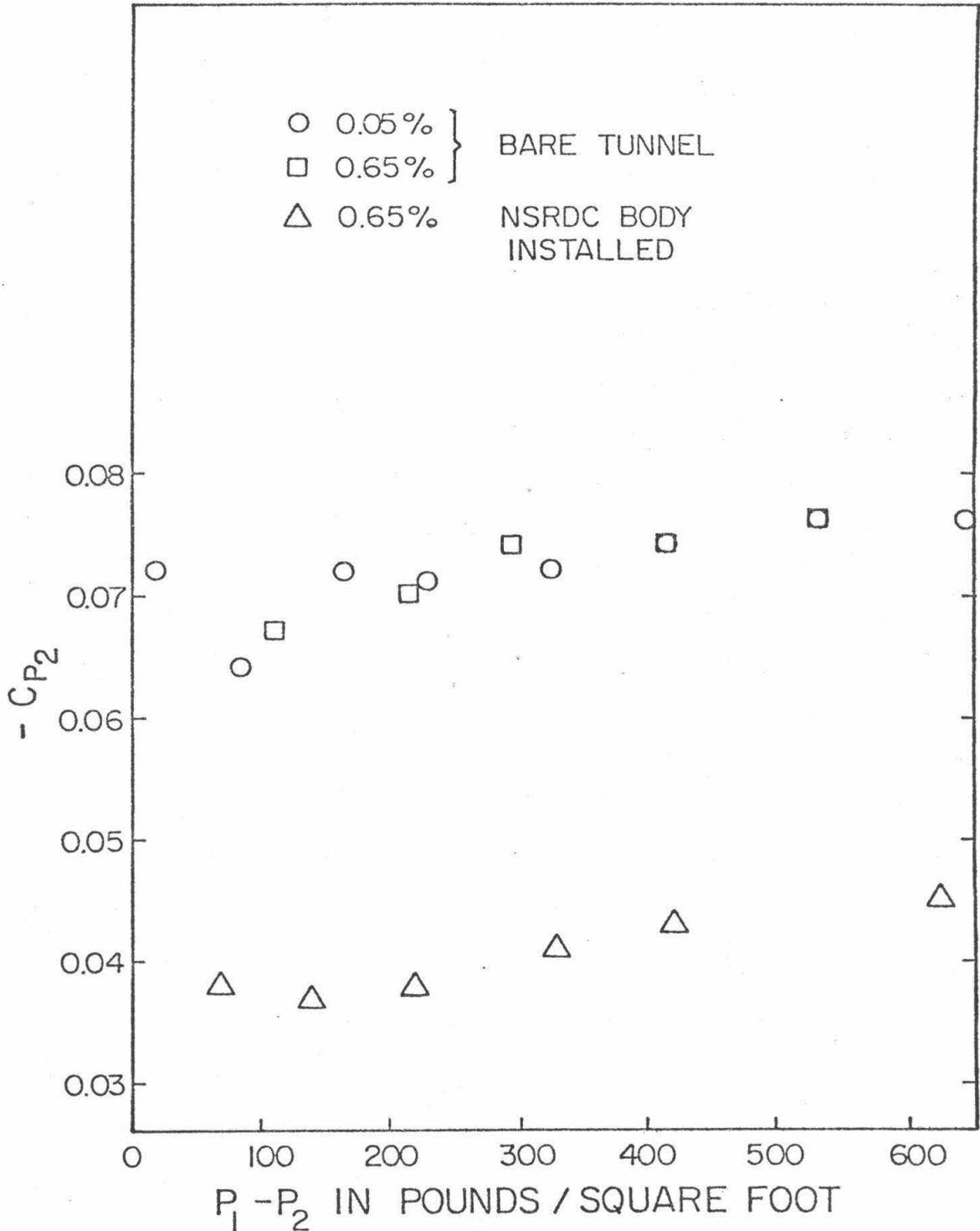


Fig. II.3 Plot of the calibration factor $-C_{p_2}$ versus the pressure drop across the nozzle.

Appendix III

BOUNDARY LAYER CALCULATIONS

III. 1 Laminar Boundary Layer Growth

The growth of the laminar boundary layer was estimated by Thwaites method which is detailed in Ref. [125] for two dimensional bodies and in Ref. [126] for axisymmetric bodies. Application of the Thwaites method requires the evaluation of the parameter λ which is defined as:

$$\lambda = \frac{\theta^2 U'_e}{\nu} ,$$

where θ is the boundary layer momentum thickness, U'_e is the local velocity gradient at the edge of the boundary layer and ν is the kinematic viscosity. It is determined by evaluating the following expression:

$$\lambda = \frac{0.45 U'_e}{r_0^2 U_e^6} \int_0^s r_0^2 U_e^5 ds \quad \text{(III. 1)}$$

Where s is the coordinate measured along the surface of the body, r_0 is the local radius of revolution and U_e is the local velocity at the edge of the boundary layer — s and r_0 are shown defined in Fig. III. 1. For the purposes of evaluation, Eq. III. 1 was made non-dimensional:

$$\lambda = \frac{0.45}{r_0^2} (-dC_p/d(s/D)) \cdot \frac{1}{2\sqrt{1-C_p}} \cdot \frac{1}{(1-C_p)^3} \int_0^{(s/D)} r_0^2 [1-C_p]^{5/2} d(s/D) \quad (\text{III.2})$$

where the velocity has been non-dimensionalized by U_∞ which is the velocity far from the body and the distances have been non-dimensionalized by the body diameter D . Also, the relationship $U_e/U_\infty = \sqrt{1-C_p}$ where C_p is the local pressure coefficient and is defined by $C_p = (p - p_\infty)/(1/2 \rho U_\infty^2)$ has been used. P_∞ is the static pressure far from the body and ρ is the liquid density.

The necessary pressure distribution was computed numerically with a Douglas-Neumann potential flow program. Pressure distributions calculated with this program for the hemisphere nose body and the NSRDC body are presented in Fig. III. 2. Equation (III. 2) was then evaluated on a high speed computer using Simpson's rule to evaluate the integral and a spline interpolating routine to determine derivatives of the pressure distribution. Then, knowing λ and θ as a function of s/D , reference to the table on page 306 of [126] provides values of the shape factor H_s as a function of s/D which thus provides the displacement thickness δ^* .

The position of laminar separation was determined by finding the value of s/D at which $\lambda = -0.09$. Comparison of the calculated position of separation and the observed position for the hemisphere nose and NSRDC bodies can be made in Fig. 42 of the main text. The maximum error is about 3 percent.

III.2 Approximate Calculation of Spatial Amplification of Boundary Disturbances

Calculation of the position of transition on the present axisymmetric bodies was carried out by using the semi-empirical method proposed by Smith and presented in Ref. [45]. Essentially Smith's method states that transition from a laminar to a turbulent boundary layer occurs when the amplitude of an initial boundary layer disturbance has been increased by a factor of between e^7 and e^9 . In the present calculations the factor e^7 was used.

The spatial amplification of an initial boundary layer disturbance was calculated from the spatial stability charts computed by Wazzan et al [127] for Falkner-Skan velocity profiles. The results of their calculations are presented in the form of curves of constant $\alpha_i \delta^* / Re_{\delta^*}$ on a plot of dimensionless frequency (ω_r) versus Reynolds number (Re_{δ^*}) where α_i is the imaginary part of the dimensional wave number associated with a Tollmien-Schlichting disturbance. There is a plot for each Falkner-Skan profile (i. e. for each value of the Hartree β) used in the calculation.

Then, if s_N denotes the position of neutral stability (the position from which disturbances begin to grow) the amplification (A) at any point downstream of s_N is given by:

$$\ln A \Big|_{s/D} = - \int_{s_N/D}^{s/D} (\alpha_i \delta^* / Re_{\delta^*}) (U_e / U_\infty) (Re_D) d(s/D) \quad (III. 3)$$

for a fixed value of the reduced frequency ω_r .

III. 2. 1 Present Computational Method

Fix the Reynolds number Re_D . From the Thwaites calculation, the local Reynolds number based on displacement thickness Re_{δ}^* and the shape parameter H_s are known as a function of s/D . Corresponding to each H_s a value of β is obtained from Fig. III.3. Fix a value of the reduced frequency ω_r . Then from the stability chart in Ref. [127] corresponding to the calculated β and fixed ω_r , a value of $\alpha_i \delta^*/Re_{\delta}^*$ is obtained at each value of s/D . And thus the value of the integrand in Eq. (III.3) is known as a function of s/D and the integration may be carried out numerically. This has to be done for different values of ω_r until the value producing the maximum amplification at the desired position is found.

Some of the calculations made by this method on the hemisphere and NSRDC bodies are presented in Figs. III.4 and III.5.

LIST OF FIGURE CAPTIONS — APPENDIX III

- Fig. III. 1 Schematic diagram showing the definitions of the body coordinates s and r_0 .
- Fig. III. 2 Pressure distributions for the hemisphere nose and NSRDC bodies calculated by the Douglas-Neumann potential flow program for a body Reynolds number of 4.17×10^5 .
- Fig. III. 3 Relationship between the Hartree β and the shape parameter H_s .
- Fig. III. 4 Estimated maximum disturbance amplification as a function of the streamwise coordinate for several Reynolds numbers on the hemisphere nose body.
- Fig. III. 5 Estimated maximum disturbance amplification as a function of the streamwise coordinate for several Reynolds numbers on the NSRDC body.

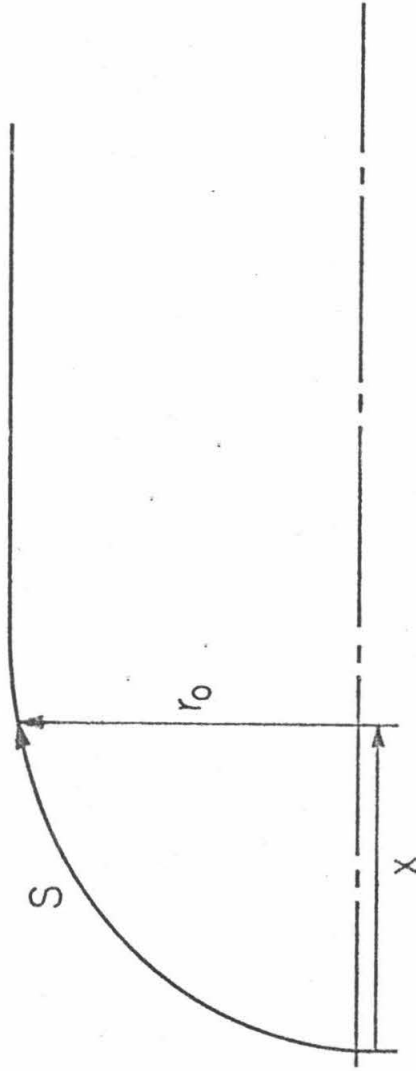
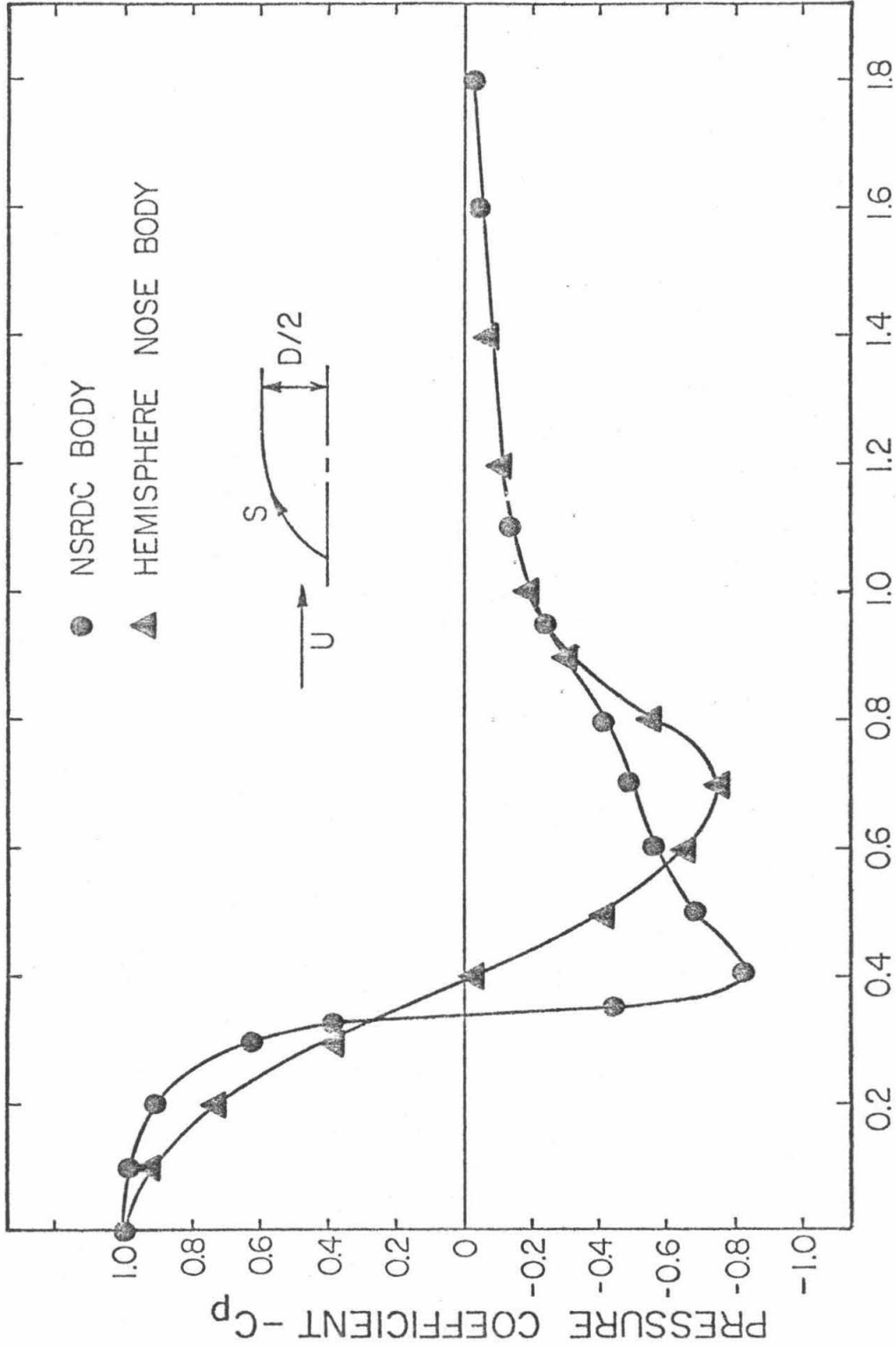


Fig. III. 1 Schematic drawing showing the definitions of the body coordinates s and r_0 .



STREAMWISE DISTANCE TO DIAMETER - S/D
Fig. III.2 Pressure distributions on the hemisphere nose and NSRDC bodies calculated by the Douglas-Neumann potential flow program for a body Reynolds number of 4.17×10^6 .

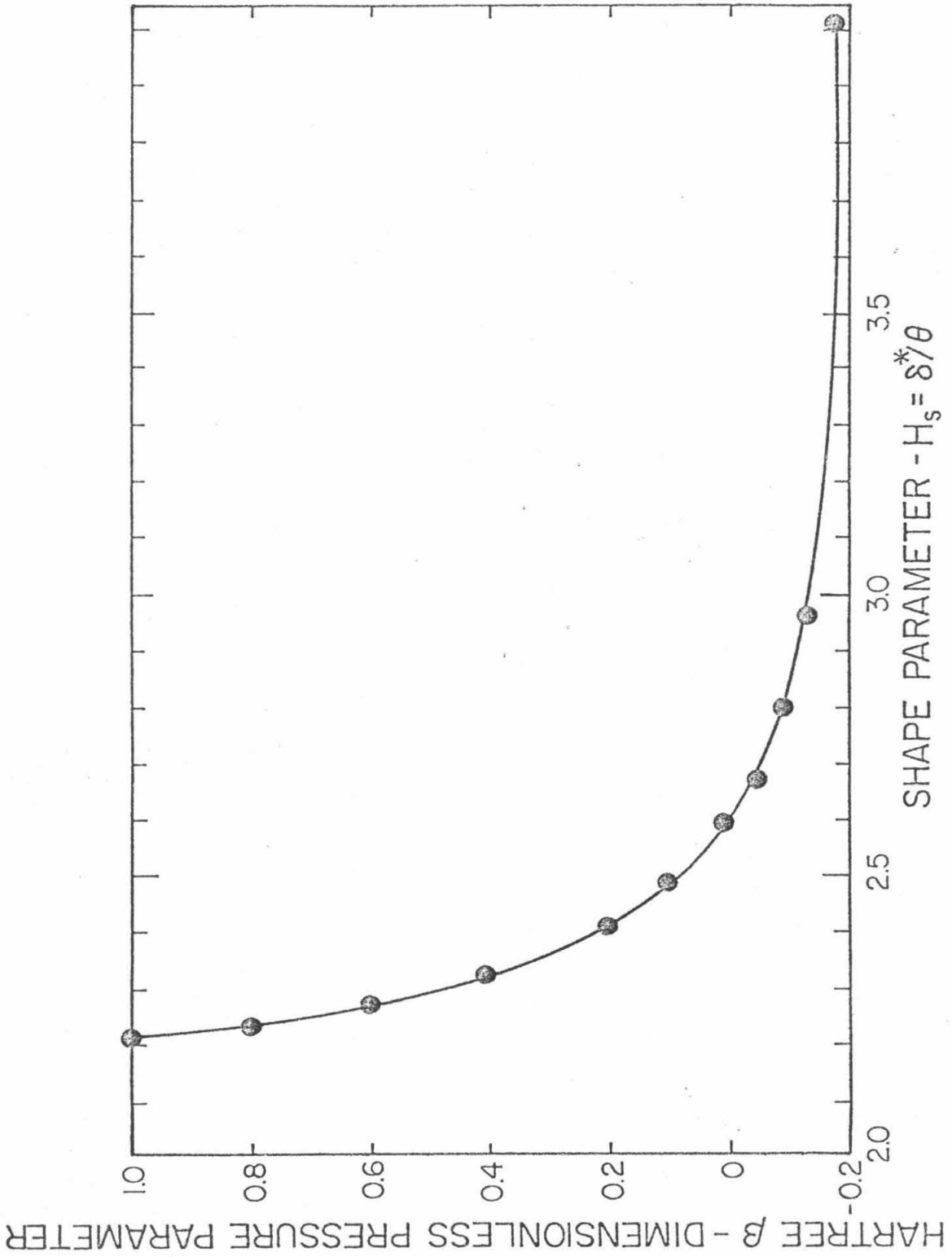


Fig. III.3 Relationship between the Hartree β and the shape parameter H_s .

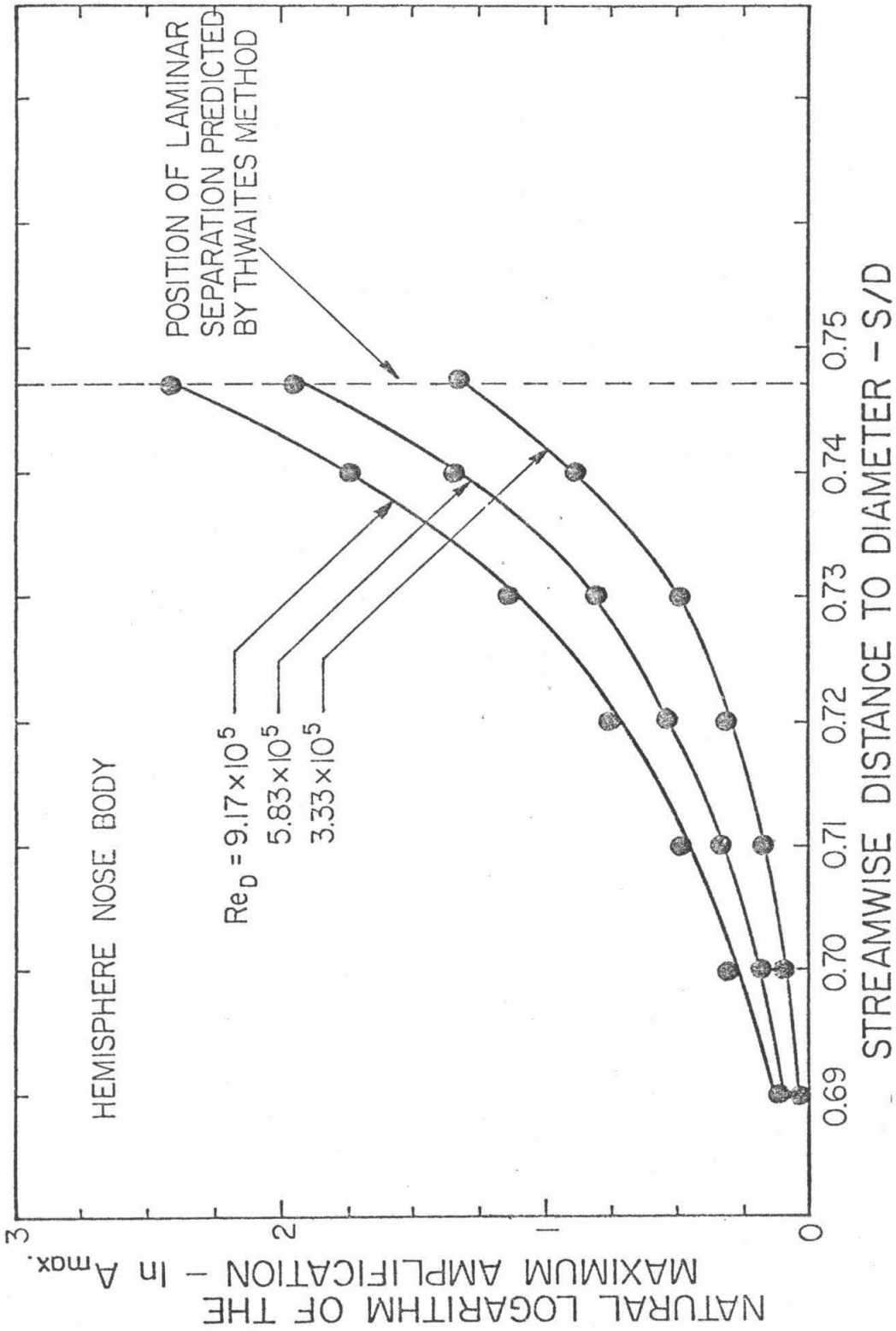


Fig. III.4 Estimated maximum disturbance amplification as a function of the streamwise coordinate for several Reynolds numbers on the hemisphere nose body.

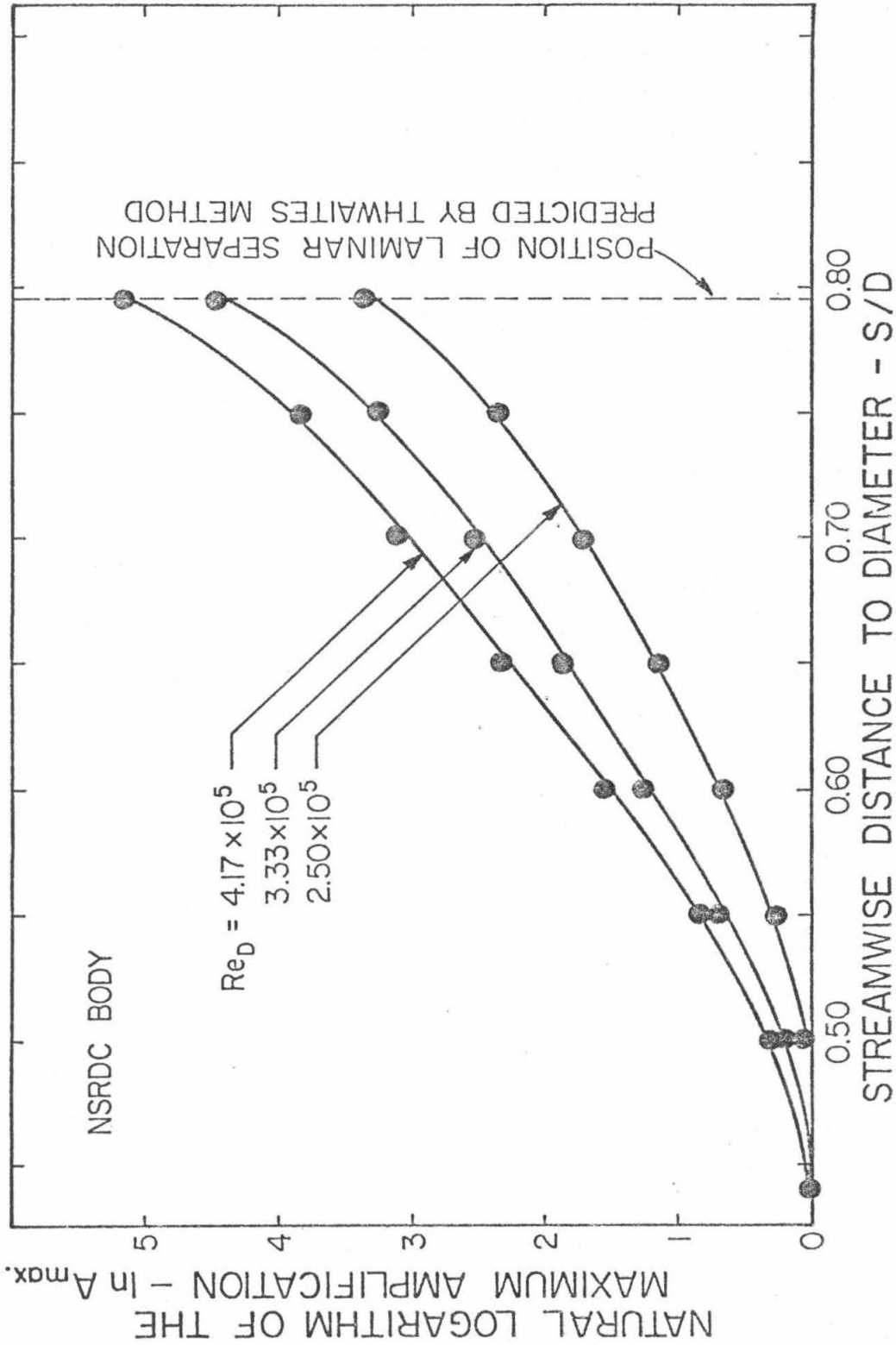


Fig. III. 5 Estimated maximum disturbance amplification as a function of the streamwise coordinate for several Reynolds numbers on the NSRDC body.